FUNCTIONALIZATION OF CARBON NANOTUBES

A DISSERTATION SUBMITTED TO
THE DEPARTMENT OF PHYSICS
AND THE INSTITUTE OF ENGINEERING AND SCIENCE
OF BILKENT UNIVERSITY
IN PARTIAL FULFILLMENT OF THE REQUIREMENTS
FOR THE DEGREE OF
DOCTOR OF PHILOSOPHY

By
Sefa Dağ
June, 2005

I certify that I have read this thesis and that in my opinion it is fully adequate, in scope and in quality, as a dissertation for the degree of doctor of philosophy.

Prof. Dr. Salim Çıracı(Supervisor)

I certify that I have read this thesis and that in my opinion it is fully adequate, in scope and in quality, as a dissertation for the degree of doctor of philosophy.

Prof. Dr. Atilla Erçelebi

I certify that I have read this thesis and that in my opinion it is fully adequate, in scope and in quality, as a dissertation for the degree of doctor of philosophy.

Prof. Dr. Atilla Aydınlı

I certify that I have read this thesis and that in my opinion it is fully adequate, in scope and in quality, as a dissertation for the degree of doctor of philosophy.

Prof. Dr. Şefik Süzer

I certify that I have read this thesis and that in my opinion it is fully adequate, in scope and in quality, as a dissertation for the degree of doctor of philosophy.

Prof. Dr. Şakir Erkoç

Approved for the Institute of Engineering and Science:

Prof. Dr. Mehmet B. Baray
Director of the Institute

ABSTRACT

FUNCTIONALIZATION OF CARBON NANOTUBES

Sefa Dağ
PhD in Physics
Supervisors: Prof. Dr. Salim Çıracı
June, 2005

Carbon nanotubes, in which two-dimensional hexagonal lattice of graphene is transformed to a quasi one-dimensional lattice that conserves the local bond arrangement, provide several structural parameters to engineer novel structures with desired properties allowing ultimate miniaturization. Most of the effort has gone to reveal various physical properties of nanotubes and to functionalize them by external agents. This thesis covers the investigation of electrical, mechanical, magnetic and contact properties of single wall carbon nanotubes functionalized with deformation, doping, coating, *etc.* All investigations in this thesis are based on the first principles calculations.

At the beginning, the adsorption of individual atoms and molecules on the semiconducting and metallic single-walled carbon nanotubes (SWNT) has been investigated. First calculations cover an extensive and systematic analysis of the oxygenation of semiconducting and metallic single-wall carbon nanotubes. The physisorption of oxygen molecules, chemisorption of oxygen atoms and formation of an oxide, as well as the equilibrium binding geometry and corresponding electronic energy structure have been treated. Apart from oxygen, the stable adsorption geometries and binding energies have been determined for a large number of foreign atoms ranging from alkali and simple metals to the transition metals and group IV elements. We found that the character of the bonding and associated physical properties such as electronic, magnetic and mechanical properties strongly depend on the type of adsorbed atoms, in particular, on their valence electron structure.

Nanotube coverage is one of the important phenomena to produce metallic nanowires and high-conducting interconnects in nanoelectronics. We were interested in preparing decorated nanotubes by using transition-metal atoms onto nanotube surfaces. We have shown that a semiconducting SWNT can only be

covered uniformly by titanium atoms and form a complex but regular atomic structure. The circular cross section of the tube changes to a square-like form, and the system becomes metallic with high state density at the Fermi level, and with high quantum ballistic conductance. Even more interesting is that uniform titanium covered tubes have magnetic ground state with significant net magnetic moment. Other than Ti, Ga is also shown to be a potential element that can make good conducting wires through coverage of SWNTs.

We report the crossed junctions which are modelled by two-dimensional grids of zigzag SWNTs. The atomic and electronic structure, stability, and energetics of the junctions are studied for different magnitudes of contact forces pressing the tubes towards each other and hence inducing radial deformations. The intertube conductance through such a junction diminish because of finite potential barrier intervening between the tubes. On the other hand, our study of the contact between a semiconducting SWNT and metal electrodes shows that the electronic structure and potential depend strongly on the type of metal.

Because of high surface-volume ratio nanotubes are also considered important systems for hydrogen storage. We demonstrated that hydrogen molecule can not bind to SWNT surface. But the character of the bonding changes dramatically when SWNT is functionalized by the adsorption of Pt atom. Single H_2 is chemisorbed to Pt atom on the SWNT either dissociatively or molecularly. If Pt-SWNT bond is weakened either by displacing Pt from bridge site to a specific position or by increasing number of the adsorbed H_2, the dissociative adsorption of H_2 is favored. Present results reveal the important effect of transition metal atom adsorbed on SWNT and advance our understanding of the molecular and dissociative adsorption of hydrogen for efficient hydrogen storage. In particular, they led to the study of Ti adsorbed SWNT on the adsorption of hydrogen. It is reported that a single Ti atom coated on a SWNT binds up to four hydrogen molecules. The first H_2 adsorption is dissociative with no energy barrier while the other three adsorptions are molecular with significantly elongated H-H bonds. We carried the adsorption of H_2 on the innerwall of SWNT to increase the storage capacity further. These results advance our fundamental understanding of dissociative adsorption of hydrogen in nanostructures and suggest new routes to better storage and catalyst materials.

Keywords: Carbon Nanotube, *Ab-initio*, Density Functional Theory, Functionalization, Transition Metal, Hydrogen Storage, Contact.

ÖZET

KARBON NANOTÜPLERİN FONKSİYONELLEŞTİRİLMESİ

Sefa Dağ
Fizik, Doktora
Tez Yöneticisi: Prof. Dr. Salim Çıracı
Haziran, 2005

Karbon nanotüpler, grafitin iki boyutlu hekzagonal örgünün silindirik, bir boyutumsu örgüye dönüşmüş halidir. Bu dönüşüm esnasında yerel bağ düzeni korunur. Bu yapılar, en aşırı minyatürleştirme ile arzu edilen özelliklerde alışılmadık yapıların tasarlanabilmesini sağlayacak çok farklı yapısal niteliklere sahiptir. Günümüzde bu konuda yapılan çalışmalar, nanotüplerin fiziksel özelliklerini ortaya çıkarma ve dış etkenler yardımıyla nasıl fonksiyonel hale getirilebileceğini anlamaya yöneliktir. Bu tez çalışması, esas olarak, karbon nanotüplerin katkılama ve kaplama etkisi ile yapısal, elektronik, manyetik, ve iletkenlik özelliklerinin birinci dereceden (*ab-initio*) hesaplar yardımı ile incelenmesini içermektedir.

Önce tek tek atom ve moleküllerin yarıiletken ve metalik tüp üzerinde soğurulmaları incelenmiştir. Bu konuda yapılan ilk çalışmalar yarıiletken ve metalik tüplerin oksitlenmesinin ayrıntılı ve sistematik analizleridir. Bu çalışma oksijen molekülünün fiziksel soğurulmasını, oksijen atomlarının kimyasal soğurulmasını ve oksitlenmenin oluşumunu kapsamaktadır. Ayrıca dengede bulunan sistemin elektronik enerji yapısı da incelenmiştir. Bunun yanısıra, geçiş elementlerinden grup IV elementlerine kadar geniş aralıkta bütün atomların ayrı ayrı soğurulma özellikleri incelenmiş, bağlanma enerjileri ve etkileri hesaplanmıştır. Bağlanma karakteristiği soğurulmuş atomun özelliklerine, özellikle değerlik elektron yapısına bağlı olmaktadır.

Nanotüplerin kaplanması metalik nanoteller ve aşırı iletken bağlantı noktaları elde etmek için önemli bir olgudur. Bu bağlamda nanotüplerin geçiş elementleri ile süslenmesi ile ilgilenmekteyiz. Çalışmamızda yarıiletken tek duvarlı

nanotüplerin sadece titanyum atomları ile düzgün ve homojen biçimde kaplanabileceğini gösterdik. Burada dairesel kesit alanının yapısal optimizasyon sonunda kare biçimli kesit alanına dönüştüğünü, sistemin Fermi düzeyinde çok yüksek durum yoğunluğu gösterdiğini ve yüksek kuvantum balistik iletime sahip olduğunu gösterdik. Daha da önemli ve ilginç olan, homojen biçimde titanyum ile kaplanmış tüpün manyetik taban durumuna sahip olması ve net manyetik moment vermesidir. Öte yandan, galyum elementinin de çok iyi kaplama malzemesi olabileceğini ve yüksek elektriksel iletime sahip olan malzeme yapmak için olası bir element olduğunu gösterdik.

Diğer bir çalışmada ise çapraz tüp-tüp eklemleri, zigzag tek duvarlı nanotüp kullanılarak modellenmiştir. Bu eklemlerin, tüpler arasındaki farklı kontak kuvvetleri etkisi altında ve farklı radyal deformasyonlarda atomsal, elektronik yapıları, kararlılık durumları, ve enerjileri incelenmiştir. Çapraz tüp-tüp kontaklarında tüpler arasındaki potansiyel engel sebebiyle tüpler arasında iletkenlik yok olmaktadır. Diğer bir taraftan nanotüp ile metal yüzeyi arasındaki kontak özellikleri incelenmiş ve burada elde edilen kontak özelliklerinin kullanılan metal yüzeyindeki atomların yüzey dağılımına ve metal özelliklerine bağlı olduğu birinci dereceden hesaplar ile gösterilmiştir.

Son olarak nanotüplerin hidrojen depolamada kullanılabilecek önemli yapılar olduğunu ortaya koyduk. Hidrojen molekülü nanotüp ile kuvvetli bağ yapmamaktadır. Ancak aradaki etkileşim, tek boyutlu nanotüpün Pt atomunun soğurulması sonucunda fonksiyonelleştirilmesi ile değişmektedir. Tek bir H_2 molekülü SWNT üzerine soğurulmuş Pt ile kimyasal bağ yapmakta bunun sonucunda Pt' nin yüzey üzerindeki konumuna göre ya molekül ya da parçalanmış halde bulunmaktadır. Eğer Pt-SWNT arasındaki bağ zayıflarsa (bu durum Pt nin C-C köprü bağı üzerindeki konumundan başka bir belirgin noktaya gitmesiyle, ya da soğurulmuş H_2 sayısının değişimiyle mümkündür) H_2'nin parçalanarak soğurulması mümkün olmaktadır. Bu çalışmada bulunan sonuçlar, SWNT tarafından soğurulmuş geçiş elementlerinin ne kadar önemli bir özelliğe sahip olduğunu göstermekte ve hidrojen depolama için gerekli olan hidrojen soğurma işlemini anlamamıza yardım etmektedir. En önemlisi elde edilen sonuçlar SWNT üzerine soğurulan titanyum elementinin yüksek hidrojen depolama kapasitesine sahip olabileceğinin gösterilmesine yol açmıştır. SWNT'nin iç cidarlarına soğurulmuş Ti atomunun H_2 depolama özellikleride araştırılarak H_2 depolamada öngörülen kapasitenin daha da artırılması beklenmektedir.

Anahtar sözcükler: nanotüp, İlk elden, Yoğunluk Fonksiyoneli Kuramı, Fonksiyonelleştirme, Hidrojen Depolama, Eklem.

Acknowledgement

The work presented in this thesis is the conclusion of the theoretical-computational work that I have been engaged in for the last 4 year. Through computational work, I have demonstrated several new physical properties of carbon nanotubes.

First of all, I would like to express my deepest gratitude to *Prof. Salim Ciraci* for his supervision, guidance and understanding throughout the preparation of this thesis during last six years. Dr. Ciraci is really patient, fair and an enthusiastic scientist. During the time that I worked with him, he showed me the way to become a good scientist. He taught me that qualified scientist must have following: respect your job, be patient, tolerate the great pains in doing your job, believe in yourself, do not hesitate working very hard and "*never put off till tomorrow what maybe done today*!". I hope that I will keep all his doctrines to become a good scientist. I worked in lots of projects with him. He knew how to keep me alive. I kept my concentration with his assistance. He helped me to keep up my morale. I can say that it has not been very easy. Most of the time I had to work very hard. Sometimes I have complained about that but I knew that this was really necessary for me. There is a proverb: **Strike while the iron is hot**. Besides, I had to be efficient. We have published more than 25 articles. Sometimes when I look back I can not believe how we did these! He had a vision and he helped me to open my eyes and see further. I appreciate what Prof. Ciraci has provided me.

Dr. Ciraci sent me to the United States to collaborate with Prof. C. Y. Fong in University of California at Davis. I had a chance to work with him for 6 months. After that, I continued to work with him occasionally. He had also great contributions to construct my background. I was not his PhD student. Despite this, he approached me like as a supervisor. He was a wonderful scientist. When I discussed with him, he knew how to direct me to solve my scientific problems. I would like to thank him for helping me with his guidance and morale supports.

I would like to thank Dr. Oğuz Gülseren, Dr. Taner Yıldırım, and Dr. Tuğrul

Senger. They were like friends for me. When I collaborate with them, I feel that I am really working with a good team. I took their helps in lots of problems which extend in a large spectrum, from computer to science, and physics to my personal problem. I am really lucky to have worked with them. We made a good teamwork.

I could not forget my friends Engin Durgun and Sefaattin Tongay. They were home mates and office mates of me. We supported each other. We helped each other. While we shared our works, we were never selfish and jealous. I really thank my friends for their valuable discussion about science. We behaved each other like brothers. Thank you Engin. Thank you Sefaattin.

I would like to thank all of my friends in Physics department.

My father, my mother and my sisters are everything of my life and my grandmother (She passed away!). During whole of my life, they were with me. Now I am not living with them but they always live in my heart. They have grown me. They helped me to develop my personality. They did not hesitate to give their moral and financial support.

I would like to dedicate my work to my father Necmettin, my mother Şükran, and my deceased grand mother Şevkiye (God rest her soul!) and my sweet sisters Şevkiye and Tülin.

Contents

0.1 Abbreviations

- **DFT** Density Functional Theory
- **DOS** Density of States
- **HM** Half Metal
- **GGA** Generalized Gradient Approximations
- **LDA** Local Density Approximations
- **LDOS** Local Density of States
- **LSDA** Local Spin Density Approximations
- **MWNT** Multi Wall Nanotubes
- **m-SWNT** Metallic Single Wall Nanotube
- **s-SWNT** Semiconducting Single Wall Nanotube
- **SWNT** Single Wall Nanotube
- **TDOS** Total Density of States
- **TM** Transition Metal
- **US-PP** Ultrasoft Pseudopotential
- **VASP** Vienna Ab-initio Simulation Program
- **VdW** Van der Waals
- **XC** Exchange Correlations

List of Figures

List of Tables

Chapter 1

Introduction

Miniaturization is the act of making things on a greatly reduced scale. Nanotechnology is a giant step toward miniaturization. The smaller the wires and switches on silicon chips that run everything from toys to supercomputers, the more efficient and less expensive these things become. Since 1960s the number of switches and other elements on a finger-nail size chip has doubled every 18 months from dozens to tens of millions. The new field of science, nanotechnology, can now provide wires with diameters a scant few hundreds of millionths of an inch in diameter, a hundred or so atoms across. Why these state of the art wires are so important for nanoelectronics?

Scientists had in fact been looking for many years for a suitable molecule to use as a miniscule electrical wire. In a bottom-up strategy proposed to design ultra-small electronic circuits, individual atoms and molecules could be building blocks for the construction of devices. However, the fabrication of a single molecule device proved to be experimentally challenging because of the difficulty to achieve electrical contacts to molecules. In 1991, reported observation about this kind of molecules, **"Carbon Nanotubes"**, was done by Iijima[1]. In his first observation he found multi-wall nanotubes (Figure 1.1). It took, however, less than two years before single-wall carbon nanotubes (SWNTs) were discovered experimentally by also Iijima[2] at the NEC Research Laboratory in Japan and by Bethune[3] at the IBM Almaden Laboratory in California. These experimental discoveries and

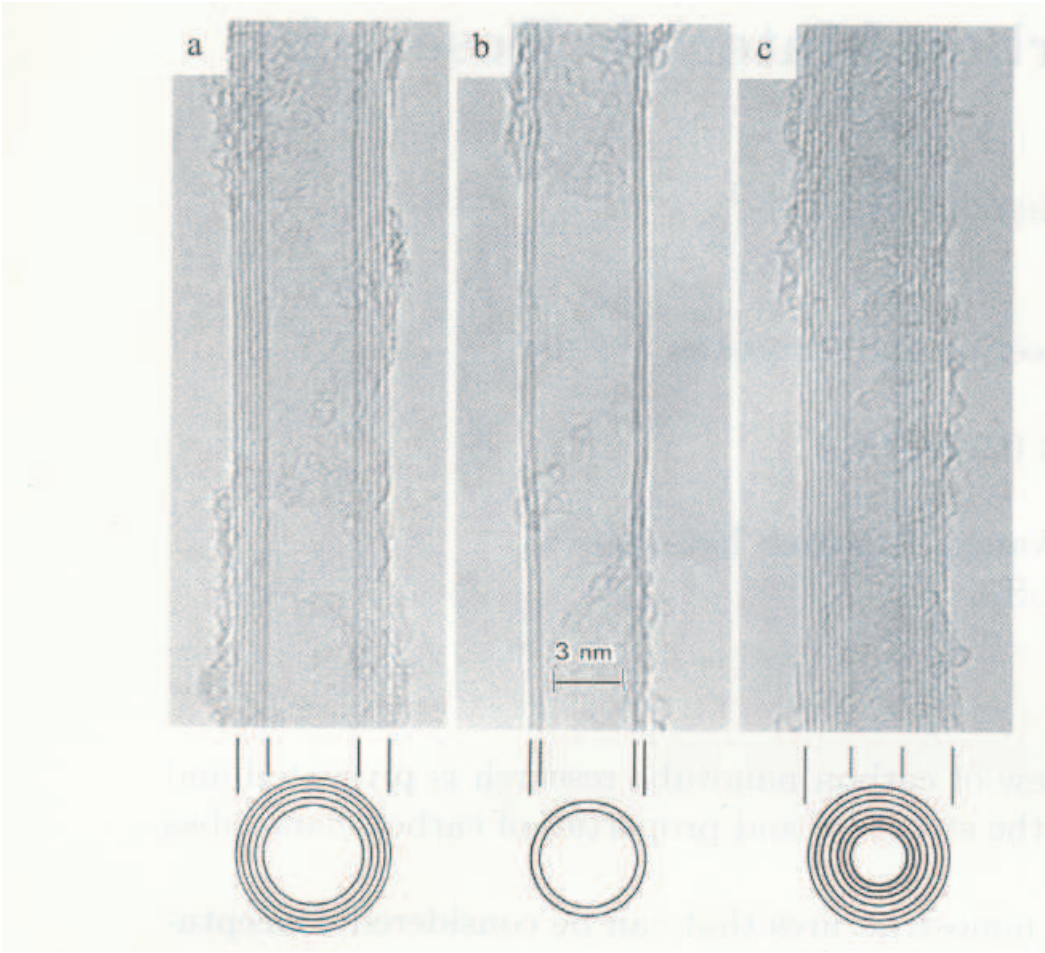

Figure 1.1: The observation by TEM of multi-wall coaxial nanotubes with various inner and outer diameters, d_i and d_0, and numbers of cylindrical shells N reported by *Iijima* in 1991: (a) $N = 5$, $d_0 = 67$Å; (b) $N = 2$, $d_0 = 55$Å; and (c) $N = 7$, $d_i = 23$Å, $d_0 = 65$Å. (Reproduced from Ref. [1])

the theoretical work, which predicted many remarkable properties of carbon nanotubes, launched this field and propelled it forward. The field has been advancing at a rapid pace ever since leading many interesting discoveries. Carbon nanotubes were soon recognized as ideal candidates for nanotechnology. They are robust, flexible and long enough to connect two microfabricated devices[4, 5]. Above all, they can be well-conducting. It took a few years however, until 1995, before it became possible to produce clean carbon nanotubes consisting of only one shell in large, practical quantities[6].

Carbon nanotubes are unique nanostructures (Figure 1.2)with remarkable

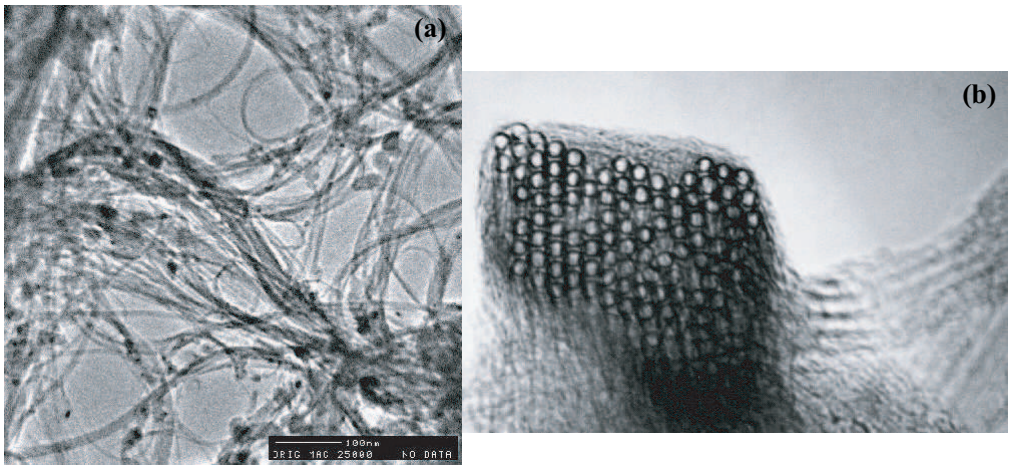

Figure 1.2: Images of carbon nanotubes, taken by a transmission electron microscope (TEM) (reproduced from Ref. [6]). (a) An entangled web of nanotube ropes. The scale bar is 100 nm. (b) A cross section of a rope with many parallel nanotubes, packed in an ordered lattice. Each circle within the rope, with a diameter of about 1.4 nm, is a nanotube. The scale bar is 10 nm.

electronic and mechanical properties[4, 5], so stemming from the close relation between carbon nanotubes and graphite, and some from their one-dimensional aspects. Initially, carbon nanotubes aroused great interest in the research community because of their exotic electronic structure. As other intriguing properties have been discovered, such as their remarkable electronic transport properties[7, 8, 9, 10, 11, 12, 13, 14], their unique Raman spectra[5] (figure 1.3), and their unusual mechanical properties, interest has grown in their potential use in nanometer-sized electronics and in a variety of other applications.

Carbon nanotubes can be semiconducting or metallic which depends on two parameters, the diameter and the chiral winding of the carbon network along the tube shell. Although this prediction was already made in 1992, it was confirmed experimentally only six years later by scanning tunnelling microscopy (STM) measurements[11, 15]. STM proved to be a useful technique to study nanotubes since it has the power to reveal both the atomic and electronic structure. It is possible to obtain beautiful images of atomically resolved nanotubes from which their chiralities can be obtained. An example is shown for example in Figure 1.4 together with a theoretical model of a nanotube with a comparable chirality. The tip of an STM can also be used as a spectroscopic probe by keeping the tip fixed

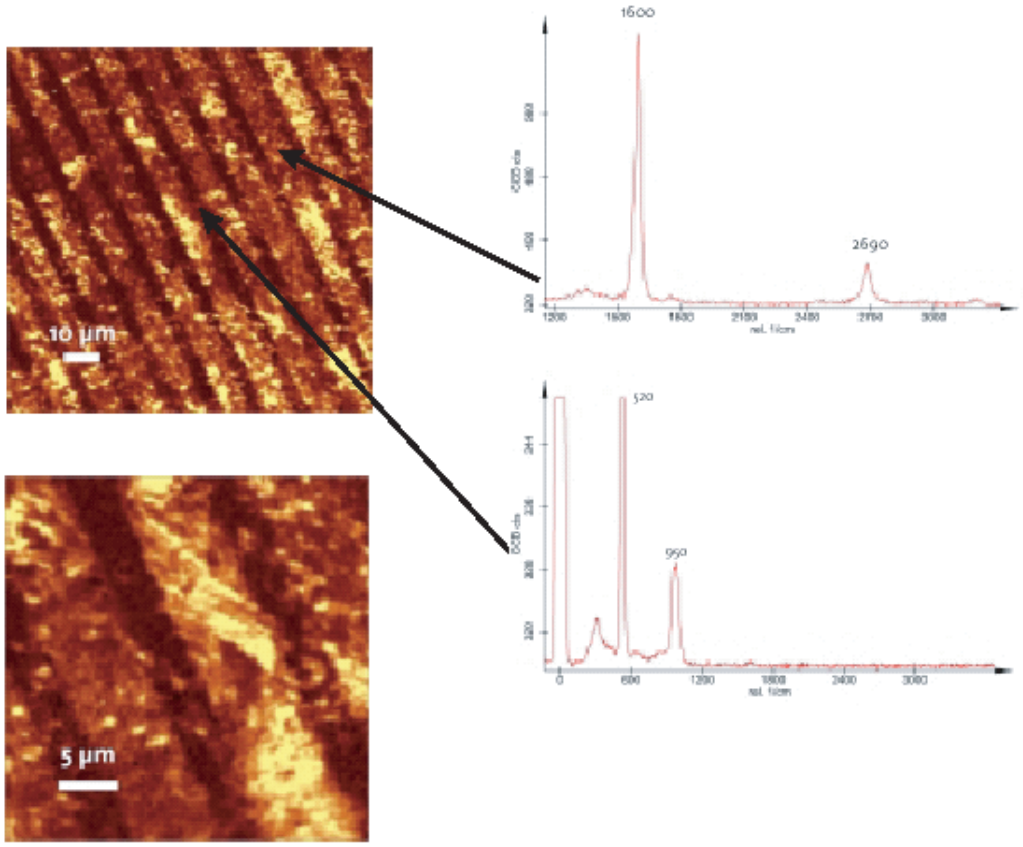

Figure 1.3: Image of the integral intensity of all Raman lines: Carbon nanotubes assembled in rows with corresponding Raman spectra Scan range: 100×100 μm.(Samples were obtained from Prof. Tsukruk, Iowa State University,USA)

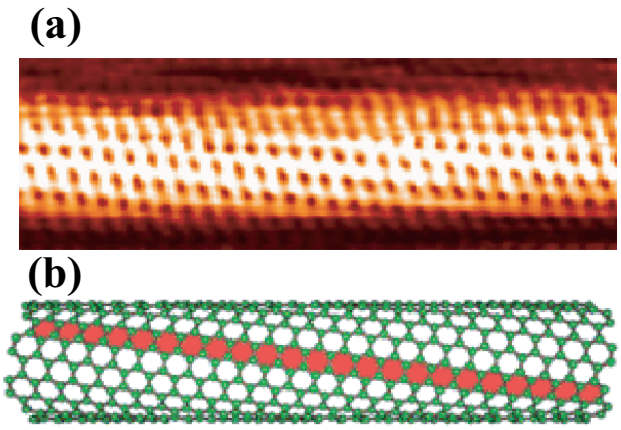

Figure 1.4: An atomically resolved STM image of a chiral carbon nanotube (a) compared to a theoretical model of a nanotube with a similar chirality (b) The diameter of the tube is 1.2 nm.(Reproduced from [11, 15])

above the sample and measure the tunnel current as a function of the bias voltage. By taking current-voltage spectra on a large number of nanotubes with various chiralities, two classes of nanotubes could be identified[16] (Figure 1.5). The STM spectra for these two classes corresponded remarkably well to the predicted electronic density of states (DOS) for the metallic and the semiconducting type, respectively. Due to the quantization of available energy modes in the circumferential direction the DOS for nanotubes does not consist of one smooth band but it splits up into several subbands with sharp singularities at the onsets. These subbands represent separate one-dimensional channels for conduction along the nanotube [16]. The subbands and their sharp onsets were indeed observed in the tunnelling DOS that was obtained from the STM spectroscopy measurements[16].

Both the semiconducting and metallic types of nanotubes may be of use for nanoscale electronic devices (Figure 1.6(a,b,c)). Junctions between two different nanotubes that have a different electronic character are interesting as well. Theoretical calculations have shown that two nanotubes with different chirality and similar diameter can connect to each other when defect pairs of five- and seven-rings of carbon are present in the hexagonal carbon lattice [18]. The connections appear as sharp kinks (Figure 1.6d) which have been also observed in real nanotube material. Figure 1.6e shows for example a sharply kinked nanotube

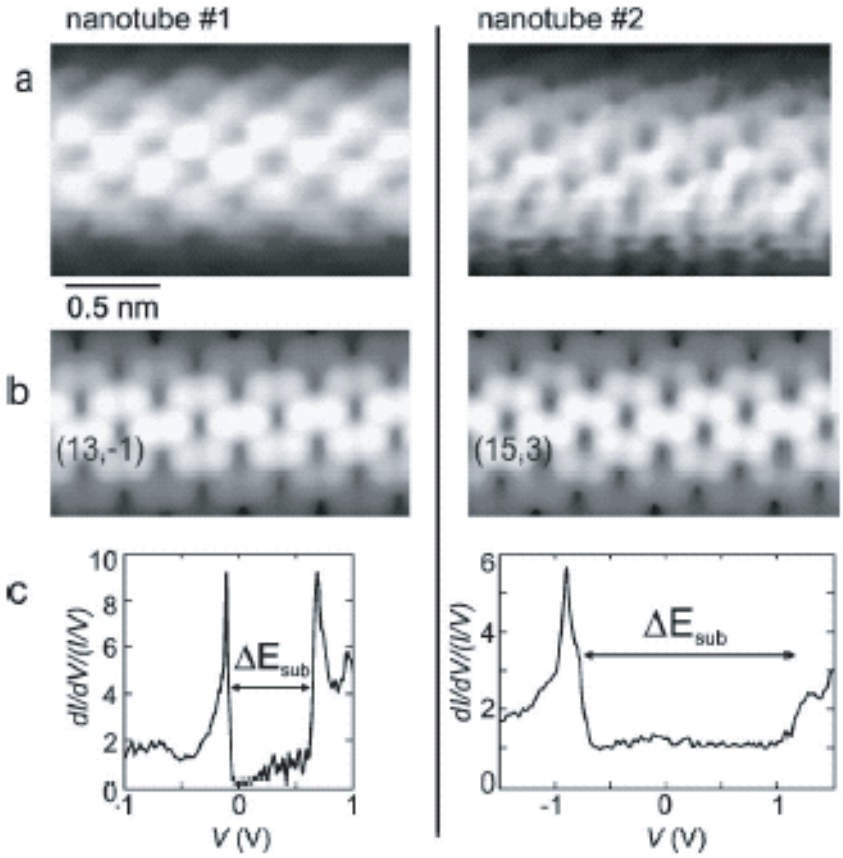

Figure 1.5: STM images and tunnel spectra for two different carbon nanotubes. The 0.5-nm bar indicates the scale for all four images in (a) and (b). (a) Atomically resolved STM images of two nanotubes 1 and 2. (b) Two calculated images based on the (n,m) indices that are found for the nanotubes shown in (a). (b) Normalized dI/dV spectra for these nanotubes. Nanotube 1 appears to be semiconducting whereas nanotube 2 is metallic. Band edge separations ΔE_{sub} are indicated for both curves. (Reproduced from Ref. [16])

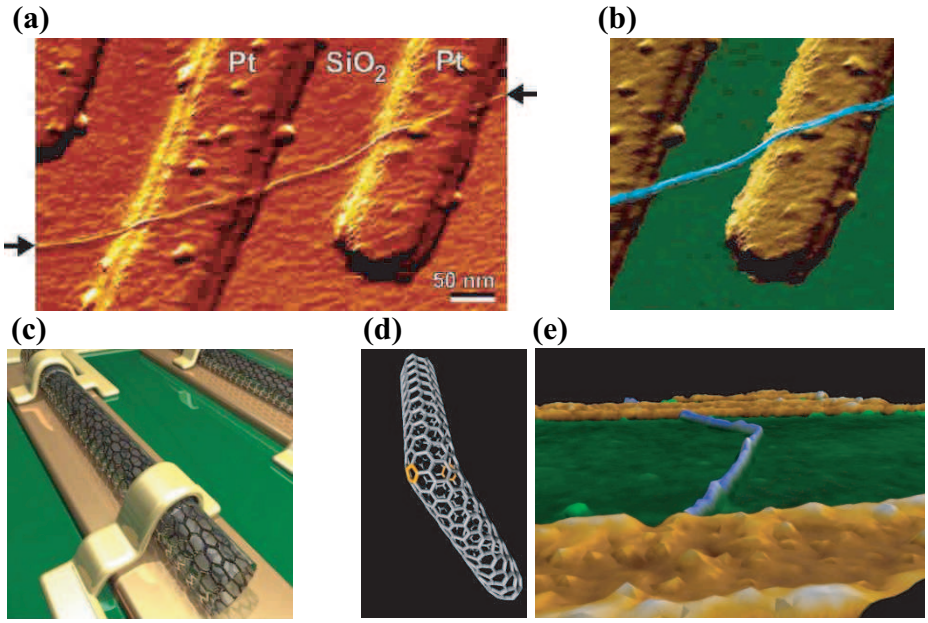

Figure 1.6: A nanotube as a molecular electronic wire on two microfabricated electrodes. By applying a bias voltage over the electrodes, a current can be measured through the molecule. (a)-(b) show nanotube device. Pt electrodes used in this device. The electrode in the upper-left corner acts as a gate and can modulate the conductance of the nanotube by applying an electric field. The scale bar is 50 nm. (c) Artistic figure of nanotube device used for transistor action. (c) Nanotube kinks. A theoretical model for a junction between two nanotubes with different chirality and similar diameter. Such a junction is possible when defect pairs of pentagons and heptagons are present in the hexagonal lattice. In this model the five-and seven-ring are opposite to each other in the kink. (b) A nanotube that contains a kink lying across electrodes. Such a sample layout allows to measure the electronic transport across a nanotube kink. The scale bar is 200 nm. (Reproduced from Ref. [17])

lying across electrodes. Recent electronic transport measurements on this type of sample indicate that these kinks can indeed be semiconductor-metal junctions [19]. The mechanical properties of carbon nanotubes are also of large interest to scientists. Nanotubes have extremely high Young modulus. When they are strongly bent, they do not break but buckle. When the bending strain is released, nanotubes come back to its original position.

1.0.1 Historical Introduction

Very small diameter (less then 10 nm) carbon filaments were prepared in the 1970's and 1980's through the synthesis of vapor grown carbon fibers by the decomposition of hydrocarbons at high temperatures in the presence of transition metal catalyst particles of < 10 nm diameter. However, no detailed systematic studies of such very thin filaments were reported in these early years. It was the Iijima's observation of the multiwall carbon nanotubes in Fig. 1.1 in 1991 that heralded the entry of many scientists into the field of carbon nanotubes, stimulated at first by the remarkable 1D quantum effects predicted for their electronic properties, and subsequently by the promise that the remarkable structure and properties of carbon nanotubes might give rise to some unique applications. The most striking of these theoretical developments was the prediction that carbon nanotubes could be either semiconducting or metallic depending on their geometrical characteristics, namely their diameter and the orientation of their hexagons with respect to the nanotube axis. Though predicted in 1992, it was not until 1998 that these predictions regarding their remarkable electronic properties were corroborated experimentally.

A major breakthrough occurred in 1996 when Smalley[6] and coworkers at Rice university successfully synthesized bundles of aligned single wall carbon nanotubes, with a small diameter distribution, thereby making it possible to carry out many sensitive experiments relevant to 1D quantum physics, which could not previously be undertaken. Of course, actual carbon nanotubes have finite length, contain defects, and interact with other nanotubes or with the substrate and these factors often complicate their behavior.

In 1997, Dekker[21] and his coworkers made first step to use nanotubes as a nanodevices. They made electrical contacts to carbon nanotubes so that a large array of electrodes have been fabricated with conventional electron beam lithography, metal-evaporation and lift-off. They investigated the quantum conductance of SWNT. Also in this year carbon nanotubes dealt with as a hydrogen storage device. Bethune et al.[22] proposed that SWNT can be used as a potential hydrogen storage. In 1998, aligned SWNT synthesized by using chemical vapor deposition technique[23]. At that year nanotube peapods synthesized[24]. In 2000, unusual high thermal conductivity observed in nanotubes[25]. The thermal conductivity of both SWNTs and MWNTs should reflect the on-tube phonon structure, regardless of tube-tube coupling. Measurements of the thermal conductivity of bulk samples show graphite-like behavior for MWNTs but quite different behavior for SWNTs, specifically a linear temperature dependence at low T which is consistent with one-dimensional phonons.

In 2001, integration of SWNT for logic circuits achieved[26]. Nanotubes circuits using electrical breakdown obtained by Collins et al.[26] At that time superconductivity observed in nanotubes[27].

1.1 Functionalization of carbon nanotubes

With their remarkable physical, electronic, and chemical properties, they are potential materials for their use in various applications ranging from reinforced fibers and nanocomposites to field-emission devices to capability of hydrogen storage. However, many of these applications require modifications to the pristine nanotube to render it functionally active for the various applications. The central problem in carbon nanotube functionalization remains a method of modifying while preserving the strength and conductivity of nanotubes. This process is usually named functionalization, and carries great potential in tailoring new nanostructures for engineering them according to a desired application. Functionalization can be handled with different cases. For example, side-wall functionalization, which occurs with interaction of nanotubes with different chemical

molecules. With this case we investigate the change of electronic properties with the circumference of wide spectrum of molecules or atoms. There are many reasons why one would want to form chemical attachments to the walls or ends of carbon nanotubes; these chemical bonds might be used to tailor the interaction of the nanotube with other entities, such as solvent, a polymer matrix, or other nanotubes. The challenge is to find a way to make carbon nanotubes reproducible, reliable and chemically active. Mechanical functionalization, which happens with mechanical deformation or other external physical effects applied to nanotube. With this external condition, it is possible to change the whole electronic structure of carbon nanotubes. Organic functionalization becomes an interesting application for biologists; many of the efforts in functionalization have so far been directed towards solubilization of nanotubes and nanotube bundles.

We followed a logical order that starts from fundamental aspects and ends with technological applications. We first established a background concerning the atomic and electronic structure of various SWNTs. We then examined various methods which are used to modify the properties of SWNTs to generate new nanostructures. We describe comprehensive study of functionalization through this thesis. The organization of the thesis is as follows. In Chapter II, we discuss the physics behind the theoretical calculations. Generally, in our calculations we use ab-initio first principles pseudopotential plane wave method within **Density Functional Theory** (DFT). Extensive information about DFT and the approximations used in theoretical calculations are also described in this chapter. Chapter III is devoted to the description of physical properties of carbon nanotubes. Chapter IV includes the chemical relation between atomic or molecular oxygen with carbon nanotube. Chapter V treats the individual adsorption of 24 different atoms (ranging from alkali and simple metal atoms to group IV atoms and most transition metal atoms), where their binding structures and binding energies, and the effect of their adsorption on the electronic structure, have been investigated. Since the ground state for most of the transition metal atoms adsorbed on the surface of SWNTs is magnetic, and hence has net spin, this section is important for the magnetic properties of functionalized nanotubes. Physical properties of full-metal covered of carbon nanotubes are treated in Chapter VI.

We discovered new interesting materials with the full-coverage of nanotubes with transition metal atoms. We also searched new materials for spintronic applications with the metal-coverage. Contact problem is in range of our thesis studies. Searching a good material and surface which can be candidate of contact with carbon nanotubes is also important research subject. This comes from importance of contact properties in the nanoscopic electronic devices. Enabling low resistance ohmic contacts to nanotubes are critical to elucidating their intrinsic electrical properties and obtaining functional electronic devices with useful characteristics. In nanoelectronics, people aimed at connecting two or more carbon nanotubes in device applications. We treat contact properties of two physically interacting nanotubes in Chapter VII. Physics of crossing nanotubes defines so that here we handled crossing nanotubes, nanotube grid and so on. In this chapter we also investigate transport properties of these structures. We will indicate the importance of contact region by looking transport properties of crossed tubes. In Chapter VIII, extensive study of hydrogen storage properties of nanotubes are studied.

Chapter 2

Theoretical Methods and Calculations

In this chapter, the theoretical approaches and approximations used in standard first principles calculations, in particular of Density Functional Theory (DFT), will be described. Here, I will present most essential features of the DFT for the sake of completeness. The details of the theory can be obtained from the review article by Kohanoff et.al.[28].

2.1 The problem of structure of matter

Here we handle a collection of interacting atoms, which may also affected by some external field. This ensemble of particles may be in the gas phase (molecules and clusters), or in a condensed phase (solids, surfaces, wires). However, in all cases we can describe the system by a number of nuclei and electrons interacting through Coulombic (electrostatic) forces. Formally, we can write the Hamiltonian of such a system in the following general form:

$$\begin{aligned}\hat{H} &= -\sum_{I=1}^{P}\frac{\hbar^2}{2M_I}\nabla_I^2 - \sum_{i=1}^{N}\frac{\hbar^2}{2m}\nabla_i^2 + \frac{e^2}{2}\sum_{I=1}^{P}\sum_{J\neq I}^{P}\frac{Z_I Z_J}{|\mathbf{R}_I-\mathbf{R}_J|} \\ &+\frac{e^2}{2}\sum_{i=1}^{N}\sum_{j\neq i}^{N}\frac{1}{|\mathbf{r}_i-\mathbf{r}_j|} - e^2\sum_{I=1}^{P}\sum_{i=1}^{N}\frac{Z_I}{|\mathbf{R}_I-\mathbf{r}_i|} \end{aligned} \quad (2.1)$$

where $\mathbf{R} = \mathbf{R}_I$, $I = 1...P$, is a set of P nuclear coordinates, and $\mathbf{r} = \mathbf{r}_i$, $i = 1...N$, is a sets of N electronic coordinates. Z_i and M_I are the P nuclear charges and masses, respectively. All the ingredients are perfectly known and, in principle, all the properties can be derived by solving the many body Schrödinger equation:

$$\hat{H}\Psi_i(\mathbf{r},\mathbf{R}) = E_i\Psi_i(\mathbf{r},\mathbf{R}) \quad (2.2)$$

In practice, this problem is almost impossible to treat in a full quantum mechanical framework. Only in a few cases a complete analytic solution is available, and numerical solutions are also limited to a very small number of particles. The problem is the full Schrödinger equation cannot be easily decoupled into a set of independent equations so that, in general, we have to deal with $(3P+3N)$ coupled degrees of freedom. The usual choice is to solve this problem is to resort to some sensible approximations. The large majority of the calculations presented in the literature are based on: (1) the adiabatic separation of nuclear and electronic degrees of freedom (adiabatic approximation), and (2) the classical treatment of nuclei.

2.2 Born-Oppenheimer Approximation

The possibility of treating separately the electrons and the ions of a real system, ab-initio calculations generally rely on, is the result of the adiabatic approximation of Born and Oppenheimer [29] which is a consequence of the large mass difference between the two families of particles. In other words, being much

lighter than the ions, the electrons can move in a solid much faster than the nuclei and the electronic configuration can be considered as completely relaxed in its ground state at each position the ions assume during their motion. This means that while studying the electronic degrees of freedom the ions can be considered at rest; thus the total wavefunction of the system can (approximately) be written as the product of a function describing the ions and another for the electrons depending only parametrically upon the ionic positions:

$$\Psi(\mathbf{R},\mathbf{r}) = \Phi(\mathbf{R})\psi_{\mathbf{R}}(\mathbf{r}) \tag{2.3}$$

where $\mathbf{R} = \mathbf{R}_I$ is the set of all the nuclear coordinates, and $\mathbf{r} = \mathbf{r}_i$ is the same quantity for all the electrons in the system (though not explicitly indicated, the many particle wavefunction $\psi_{\mathbf{R}}(r)$ also depends on the electronic spin degrees of freedom). Within this approximation, the ionic wavefunction $\Phi(\mathbf{R})$ is the solution of the Schrödinger equation:

$$\left(-\sum_I \frac{\hbar^2}{2M_I}\frac{\partial^2}{\partial R_I^2} + E(R)\right)\Phi(\mathbf{R}) = \varepsilon\Phi(\mathbf{R}) \tag{2.4}$$

where M_I is the mass of the I^{th} nucleus and $E(\mathbf{R})$ is the so called Born-Oppenheimer potential energy surface corresponding to the ground state energy of the electronic system when the nuclei are fixed in the configuration $\mathbf{R}$. More generally electronically excited potential energy surfaces can be defined which are important when electronic transitions driven by ionic motion, through the non adiabatic coupling terms (electron-phonon interaction), are considered. The potential energy surface can be computed solving the Schrodinger problem for the electrons:

$$\left(-\sum_I \frac{\hbar^2}{2m}\frac{\partial^2}{\partial \mathbf{r}_i^2} + \frac{e^2}{2}\sum_{i\neq j}\frac{1}{|\mathbf{r}_i - \mathbf{r}_j|} - \sum_{iI}\frac{Z_I e^2}{|\mathbf{r}_i - \mathbf{R}_I|} + \frac{e^2}{2}\sum_{I\neq J}\frac{Z_I Z_J}{\mathbf{R}_I - \mathbf{R}_J}\right)\psi^{\alpha}_{\mathbf{R}}(\mathbf{r}) = E_{\alpha}(\mathbf{R})\psi^{\alpha}_{\mathbf{R}}(\mathbf{r}) \tag{2.5}$$

where Z_I is the charge of the I^{th} nucleus, $-e$ and m are the electronic charge and mass, and α is an index for the electronic state.

The equations describing the electronic and the ionic problems are obtained from the equation for the total system assuming the wavefunction factorization of eq. 2.3 and neglecting the *non adiabatic* terms which come from the kinetic energy operator for the nuclei acting on the electronic wavefunction $\psi_{\mathbf{R}}(\mathbf{r})$. This is expected to be a good approximation for most real materials since the neglected terms are of the order of the ratio m_e/M between the (effective) electronic mass and the ionic one. The separation among electronic and ionic degrees of freedom is a very useful simplification of the problem and allows to treat the ions within a classical formalism as generally done in molecular dynamics calculations. However the electronic problem is a quantum many body problem; the total wavefunction of the system depends on the coordinates of all the electrons and cannot be decoupled in single particle contributions because of their mutual interaction, so that the problem is still far too complicated to be solved exactly in practical computations. Owing to this difficulty, further developments are required to perform ab-initio calculations for real materials. Density Functional Theory provides a framework for these developments.

2.3 Density Functional Theory

DFT is a general approach to the ab-initio description of quantum many-body systems, in which the original many-body problem is taken as single-particle problem. For the most simple case of (nondegenerate) stationary problems, DFT is based on the fact that any ground state observable is uniquely determined by the corresponding ground state density n, i.e. can be understood as a functional of n. This statement applies in particular to the ground state energy, which allows to represent the effects of the particle-particle interaction in an indirect form via a density-dependent single-particle potential. In addition to the Hartree (direct) contribution this potential contains an exchange-correlation (xc) component, which is obtained from the so called xc-energy functional. The exact

density functional representation of this crucial quantity of DFT is not known, the derivation of suitable approximations being the major task in DFT.

The total ground state energy of an inhomogeneous system composed by N interacting electrons is given by:

$$\begin{aligned} E &= <\Phi|\hat{T}+\hat{V}+\hat{U}_{ee}|\Phi> \\ &= <\Phi|\hat{T}|\Phi> + <\Phi|\hat{V}|\Phi> + <\Phi|\hat{U}_{ee}|\Phi> \end{aligned} \tag{2.6}$$

where $|\Phi>$ is the N-electron ground state wavefunction, which has neither the form given by the Hartree approximation nor the Hartree-Fock form. In fact, this wave function has to include correlations amongst electrons, and its general form is unknown. $\hat{T}$ is kinetic energy, $\hat{V}$ is the interaction with external fields, and $\hat{U}_{ee}$ is the electron-electron interaction. We are going to concentrate now on this latter, which is the one that introduces many-body effects.

$$\hat{U}_{ee} =<\Phi|\hat{U}_{ee}|\Phi>= \left\langle \Phi \left| \frac{1}{2}\sum_{i=1}^{N}\sum_{j\neq i}^{N}\frac{1}{|\mathbf{r}_i-\mathbf{r}_j|}\right|\Phi\right\rangle = \int \frac{\rho_2(\mathbf{r},\mathbf{r}')}{|\mathbf{r}-\mathbf{r}'|}d\mathbf{r}d\mathbf{r}' \tag{2.7}$$

with

$$\rho_2(\mathbf{r},\mathbf{r}') = \frac{1}{2}\sum_{\sigma,\sigma'} <\Phi|\Psi^{\dagger}_{\sigma}(\mathbf{r})\Psi^{\dagger}_{\sigma'}(\mathbf{r}')\Psi_{\sigma'}(\mathbf{r}')\Psi_{\sigma}(\mathbf{r})|\Phi> \tag{2.8}$$

the two-body density matrix expressed in real space, being Ψ and $\Psi^{\dagger}$ the annihilation and creation operators for electrons, which obey the anticommutation relations $\{\Psi_{\sigma}(\mathbf{r}),\Psi^{\dagger}_{\sigma'}(\mathbf{r}')\} = \delta_{\sigma,\sigma'}\delta(\mathbf{r}-\mathbf{r}')$. We define now the two-body direct correlation function $g(\mathbf{r},\mathbf{r}')$ in the following way:

$$\rho_2(\mathbf{r},\mathbf{r}') = \frac{1}{2}\rho(\mathbf{r},\mathbf{r})\rho(\mathbf{r}',\mathbf{r}')g(\mathbf{r},\mathbf{r}') \tag{2.9}$$

where $\rho(\mathbf{r},\mathbf{r}')$ is the one body density matrix (in real space), whose diagonal elements $\rho(\mathbf{r}) = \rho(\mathbf{r},\mathbf{r})$ correspond to the electronic density. The one-body density matrix is defined

$$\rho(\mathbf{r},\mathbf{r}') = \sum_{\sigma} \rho_{\sigma}(\mathbf{r},\mathbf{r}') \tag{2.10}$$

$$\rho_{\sigma}(\mathbf{r},\mathbf{r}') = < \Phi|\Psi^{\dagger}_{\sigma}(\mathbf{r})\Psi_{\sigma}(\mathbf{r}')|\Phi > \tag{2.11}$$

With this definition, the electron-electron interaction is written:

$$U_{ee} = \frac{1}{2}\int \frac{\rho(\mathbf{r})\rho(\mathbf{r}')}{|\mathbf{r}-\mathbf{r}'|} d\mathbf{r}d\mathbf{r}' + \frac{1}{2}\int \frac{\rho(\mathbf{r})\rho(\mathbf{r}')}{|\mathbf{r}-\mathbf{r}'|}[g(\mathbf{r},\mathbf{r}')-1]d\mathbf{r}d\mathbf{r}' \tag{2.12}$$

The first term is the classical electrostatic interaction energy corresponding to a charge distribution $\rho(\mathbf{r})$. The second term includes correlation effects of both, classical and quantum origin. Basically, $g(\mathbf{r},\mathbf{r}')$ takes into account the fact that the presence of an electron at $\mathbf{r}$ discourages a second electron to be located at a position $\mathbf{r}'$ very close to $\mathbf{r}$ because of the Coulomb repulsion. In other words, it says that the probability of finding two electrons in proximity (two particles with charges of the same sign, in the general case) is reduced with respect to the probability of finding them at infinite distance. This is true already at the classical level, and it is further modified at the quantum level. Exchange further diminishes this probability in the case of electrons having the same spin projection, due to the Pauli exclusion.

To understand the effect of exchange, let us imagine that we stand on an electron with spin $\uparrow$, and we look at the density of the other $(N-1)$ electrons. Pauli principle forbids the presence of electrons with spin $\uparrow$ at the origin, but it says nothing about electrons with spin $\downarrow$, which can perfectly be located at the origin. Therefore;

$$g_X(\mathbf{r},\mathbf{r}') \rightarrow \frac{1}{2}, \quad for\ \mathbf{r} \rightarrow \mathbf{r}' \tag{2.13}$$

In Hartree-Fock theory we can rewrite the electron-electron interaction as

$$U_{ee}^{HF} = \frac{1}{2}\int \frac{\rho^{HF}(\mathbf{r})\rho^{HF}(\mathbf{r}')}{|\mathbf{r}-\mathbf{r}'|}d\mathbf{r}d\mathbf{r}' + \frac{1}{2}\int \frac{\rho^{HF}(\mathbf{r})\rho^{HF}(\mathbf{r}')}{|\mathbf{r}-\mathbf{r}'|}\left[-\frac{\sum_\sigma |\rho_\sigma^{HF}(\mathbf{r},\mathbf{r}')|^2}{\rho^{HF}(\mathbf{r})\rho^{HF}(\mathbf{r}')}\right]d\mathbf{r}d\mathbf{r}' \tag{2.14}$$

meaning that the exact expression for the exchange depletion (also called *exchange hole* or *Fermi hole*) is:

$$g_X(\mathbf{r},\mathbf{r}') = 1 - \frac{\sum_\sigma |\rho_\sigma^{HF}(\mathbf{r},\mathbf{r}')|^2}{\rho^{HF}(\mathbf{r})\rho^{HF}(\mathbf{r}')} \tag{2.15}$$

The density and density matrix are calculated from HF ground state Slater determinant.

The calculation of the correlation hole $-g_C(\mathbf{r},\mathbf{r}')-$ is a major problem in many body theory and, up to the present, it is an open problem in the general case of an inhomogeneous electron gas. The exact solution for the homogeneous electron gas is known numerically[30], and also in a number of different analytical approximations. There are several approximations that go beyond the homogeneous limit by including slowly varying densities through its spatial gradients (gradient corrections), and also expressions for the exchange correlation energy that aims at taking into account very weak, nonlocal interactions of the Van der Waals type[31] (dispersion interactions). The energy of the many-body electronic system can, then, be written in the following way:

$$E = T + V + \frac{1}{2}\int \frac{\rho(\mathbf{r})\rho(\mathbf{r}')}{|\mathbf{r}-\mathbf{r}'|}d\mathbf{r}d\mathbf{r}' + E_{XC} \tag{2.16}$$

where

$$V = \sum_{I=1}^{P}\left\langle \Phi|\sum_{i=1}^{N} v(\mathbf{r}_i - \mathbf{R}_I)|\Phi\right\rangle = \sum_{I=1}^{P}\int \rho(\mathbf{r})v(\mathbf{r}-\mathbf{R}_I)d\mathbf{r} \tag{2.17}$$

$$T = \left\langle \Phi| - \frac{\hbar^2}{2m}\sum_{i=1}^{N}\nabla_i^2|\Phi\right\rangle = -\frac{\hbar^2}{2m}\int [\nabla_{\mathbf{r}}^2\rho_1(\mathbf{r},\mathbf{r}')]_{\mathbf{r}'=\mathbf{r}}d\mathbf{r} \tag{2.18}$$

and E_{XC} is the exchange and correlation energy

$$E_{XC} = \frac{1}{2}\int \frac{\rho(\mathbf{r})\rho(\mathbf{r}')}{|\mathbf{r}-\mathbf{r}'|}[g(\mathbf{r},\mathbf{r}')-1]d\mathbf{r}d\mathbf{r}' \tag{2.19}$$

2.3.1 Thomas-Fermi Theory

According to the Thomas-Fermi Theory (1927), the total energy can be constructed in terms only of the electronic density[32]. They used the expression for the kinetic, exchange and correlation energies of the homogeneous electron gas to construct the same quantities for the inhomogeneous system in the following way $E_\alpha = \int \varepsilon_\alpha[\rho(\mathbf{r})]d\mathbf{r}$, where $\varepsilon_\alpha[\rho(\mathbf{r})]$ is the energy density (corresponding to the state α), calculated locally for the value of the density at that point in space. This was the first time that the *local density approximation*, of LDA was used. For the homogeneous electron gas, the density is related to the Fermi energy (ϵ_F) by

$$\rho = \frac{1}{3\pi^2}(\frac{2m}{\hbar^2})^{3/2}\epsilon_F^{3/2} \tag{2.20}$$

The kinetic energy of the homogeneous gas is $T = 3\rho\epsilon_F/5$, so that the kinetic energy density is:

$$t[\rho] = \frac{3}{5}\frac{\hbar^2}{2m}(3\pi^2)^{2/3}\rho^{5/3} \tag{2.21}$$

Then, the kinetic energy is written $T_{TF} = C_k \int \rho(\mathbf{r})^{5/3}d\mathbf{r}$, with $C_k = 3(3\pi^2)^{2/3}/10 = 2.871$ atomic units. The inhomogeneous system is thought of as locally homogeneous. At variance with the usual approaches in modern density functional theory, here the LDA is applied also to the kinetic energy. Neglecting exchange and correlation in expression 2.16 we arrive to Thomas-Fermi theory:

$$E_{TF}[\rho] = C_k \int \rho(\mathbf{r})^{5/3}d\mathbf{r} + \int v(\mathbf{r})\rho(\mathbf{r})d\mathbf{r} + \frac{1}{2}\int\int \frac{\rho(\mathbf{r})\rho(\mathbf{r}')}{|\mathbf{r}-\mathbf{r}'|}d\mathbf{r}d\mathbf{r}' \tag{2.22}$$

It can be seen that E_{TF} depends only on the electronic density, it is a *functional* of the density. Assuming intuitively some variational principle, one can search for the density $\rho(\mathbf{r})$ which minimizes $E_{TF}[\rho]$, subjected to the constraint that the total integrated charge be equal to the number of electrons: $\int \rho(\mathbf{r})d\mathbf{r} = N$. This can be put in terms of functional derivatives:

$$\frac{\delta}{\delta\rho(\mathbf{r})}(E_{TF}[\rho] - \mu \int \rho(\mathbf{r})d\mathbf{r}) = 0 \tag{2.23}$$

i.e.

$$\mu = \frac{5}{3}C_k\rho(\mathbf{r})^{2/3} + v(\mathbf{r}) + \int \frac{\rho(\mathbf{r}')}{|\mathbf{r} - \mathbf{r}'|}d\mathbf{r} \tag{2.24}$$

with μ the chemical potential.

Exchange can be straightforwardly added to the expression above by considering Slater's expression for the homogeneous electron gas: $\varepsilon_X[\rho] = -C_X \int \rho^{4/3}(\mathbf{r})d\mathbf{r}$, with $C_X = 3(3/\pi)^{1/3}/4$. Expression 2.24 is modified by the addition of the term $-(4/3)C_X\rho(r)^{1/3}$. This level of approximation is called *Thomas-Fermi-Dirac* theory.

Correlation can also be easily added by using any approximation to the homogeneous electron gas, for instance the one proposed by Wigner: $\varepsilon_C[\rho] = -0.056\rho^{4/3}/[0.079 + \rho^{1/3}]$.

2.3.2 Hohenberg-Kohn theorem

In 1964, P. Hohenberg and W. Kohn[37] formulated and proved a theorem which put on solid mathematical grounds the former ideas, which were first proposed by Thomas and Fermi. The theorem is divided into two parts:

i) The external potential is univocally determined by the electronic density, except for a trivial additive constant.

We will suppose the opposite to hold, that the potential is not univocally determined by the density. Then one would be able to find two potentials v, v' such that their ground state density ρ is the same. Let Ψ and $E_0 =< \Psi|\hat{H}|\Psi >$ be the ground state and ground state energy of $\hat{H} = \hat{T} + \hat{U} + \hat{V}$, and Ψ' and $E'_0 =< \Psi'|\hat{H}'|\Psi' >$ the ground state and ground state energy of $\hat{H}' = \hat{T}' + \hat{U}' + \hat{V}'$. Due to the variational principle, we have:

$$E_0 < \left\langle \Psi'|\hat{H}|\Psi' \right\rangle = \left\langle \Psi'|\hat{H}'|\Psi' \right\rangle + \left\langle \Psi'|\hat{H} - \hat{H}'|\Psi' \right\rangle = E'_0 + \int \rho(\mathbf{r})(v(\mathbf{r}) - v'(\mathbf{r}))d\mathbf{r}, \tag{2.25}$$

where, we have also used that different Hamiltonians have necessarily different ground states $\Psi \neq \Psi'$. It is straightforward to show since the potential is a multiplicative operator. Now we can simply reverse the situation of Ψ and Ψ' (H and H'), and readily obtain:

$$E'_0 < \left\langle \Psi|\hat{H}'|\Psi \right\rangle = \left\langle \Psi|\hat{H}|\Psi \right\rangle + \left\langle \Psi'|\hat{H}' - \hat{H}|\Psi' \right\rangle = E_0 - \int \rho(\mathbf{r})(v(\mathbf{r}) - v(\mathbf{r}'))d\mathbf{r}. \tag{2.26}$$

Adding these two inequalities, it turns out that $E_0 + E'_0 < E'_0 + E_0$, which is strange. There are no $v(\mathbf{r}) \neq v'(\mathbf{r})$ that correspond to the same electronic density for the ground state.

Since $\rho(\mathbf{r})$ univocally determines $v(\mathbf{r})$, then is also determines the ground state wave function Ψ.

ii) Let $\tilde{\rho}(\mathbf{r})$ be a non-negative density normalized to N. Then: $E_0 < E_v[\tilde{\rho}]$, for

$$E_v[\tilde{\rho}] = F[\tilde{\rho}] + \int \tilde{\rho}(\mathbf{r})v(\mathbf{r})d\mathbf{r} \tag{2.27}$$

with

$$F[\tilde{\rho}] = \left\langle \Psi[\tilde{\rho}] | \hat{T} + \hat{U} | \Psi[\tilde{\rho}] \right\rangle \tag{2.28}$$

where $\Psi[\tilde{\rho}]$ is the ground state of a potential which has $\tilde{\rho}$ as its ground state density.

The knowledge of $F[\rho]$ implies that one has solved the full many-body Schrödinger equation. It has to be remarked that $F[\rho]$ is a *universal* functional which does not depend explicitly on the external potential. It depends only on the electronic density. In the Hohenberg-Kohn formulation, $F[\rho] = \left\langle \Psi \left| \hat{T} + \hat{U} \right| \Psi \right\rangle$, where Ψ is the ground state wave function. These two theorems form the basis of *density functional theory*, or DFT.

Using DFT one can determine the electronic ground state density and energy exactly provided that $F[\rho]$ is known. A common misleading statement is that DFT is a ground state theory, and that the question of excited states cannot be addressed within it. This is actually an incorrect statement, because the density determines univocally the potential, and this, in turn, determines univocally the many-body wavefunctions, *ground and excited states*, provided that the full many-body Schrödinger equation is solved. For the ground state such a scheme was devised by Kohn and Sham and will be discussed in the next subsection.

2.3.3 Kohn-Sham Equations

In 1965, W. Kohn and L. Sham[42] proposed the ideas of replacing the kinetic energy of the interacting electrons with that of an equivalent non-interacting system, because this latter can be easily calculated. The density matrix $\rho(\mathbf{r}, \mathbf{r}')$ that derives from the (interacting) ground state is the sum of the spin up and down density matrices, $\rho(\mathbf{r}, \mathbf{r}') = \sum_s \rho_s(\mathbf{r}, \mathbf{r}')$ $(s = 1, 2)$. The latter can be written :

$$\rho_s = \sum_{i=1}^{\infty} n_{i,s} \varphi_{i,s}(\mathbf{r}) \varphi_{i,s}^*(\mathbf{r}') \tag{2.29}$$

where $\{\varphi_{i,s}(\mathbf{r})\}$ are single-particle spin orbitals, and $\{n_{i,s}\}$ are the occupations numbers of these orbitals. In the atomic units ($\hbar^2 = m$) the kinetic energy can be written exactly as

$$T = \sum_{s=1}^{2} \sum_{i=1}^{\infty} n_{i,s} \left\langle \varphi_{i,s} \left| -\frac{\nabla^2}{2} \right| \varphi_{i,s} \right\rangle \tag{2.30}$$

In the following we shall assume the equivalent non-interacting system, *i.e.* a system of non-interacting fermions whose ground state density coincides with that of the interacting system, does exist. We shall call this the *non-interacting reference system* of density $\rho(r)$, which is described by the Hamiltonian

$$\hat{H}_R = \sum_{i=1}^{N} \left(-\frac{\nabla_i^2}{2} + v_R(\mathbf{r}_i) \right) \tag{2.31}$$

where the potential $v_R(\mathbf{r})$ is such that the ground state density of $\hat{H}_R$ equals ρ, and the ground state energy equals the energy of the interacting system. This Hamiltonian has no electron-electron interactions and, thus, its eigenstates can be expressed in the form of Slater determinants (SD)

$$\Psi_s(\mathbf{r}) = \frac{1}{\sqrt{N!}} SD[\varphi_{1,s}(\mathbf{r}_1)\varphi_{2,s}(\mathbf{r}_2)...\varphi_{N_s,s}(\mathbf{r}_{N_s})] \tag{2.32}$$

where we have chosen the occupation numbers to be $i \leq N_s$(s=1,2), and 0 for $i > N_s$. this means that the density is written as

$$\rho(r) = \sum_{s=1}^{2} \sum_{i=1}^{N_s} |\varphi_{i,s}(\mathbf{r})|^2 \tag{2.33}$$

while kinetic term is

$$T_R[\rho] = \sum_{s=1}^{2} \sum_{i=1}^{N_s} \left\langle \varphi_{i,s} \left| -\frac{\nabla^2}{2} \right| \varphi_{i,s} \right\rangle \tag{2.34}$$

The single-particle orbitals $\varphi_{i,s}(r)$ are the N_s lowest eigenfunctions of $\hat{h}_R = -\frac{\nabla^2}{2} + v_R(r)$, *i.e.*

$$\left\{-\frac{\nabla^2}{2} + v_R(\mathbf{r})\right\}\varphi_{i,s}(\mathbf{r}) = \varepsilon_{i,s}\varphi_{i,s}(\mathbf{r}) \tag{2.35}$$

Using $T_R[\rho]$, the universal density functional can be written in the following form:

$$F[\rho] = T_R[\rho] + \frac{1}{2}\int\int \frac{\rho(\mathbf{r})\rho(\mathbf{r}')}{|\mathbf{r}-\mathbf{r}'|}d\mathbf{r}d\mathbf{r}' + E_{XC}[\rho] \tag{2.36}$$

where this equation defines the exchange and correlation energy as a functional of the density.

The fact that $T_R[\rho]$ is the kinetic energy of the non-interacting reference system implies that the correlation piece of the true kinetic energy has been ignored, and has to be taken into account somewhere else. In practise this is done by redefining the correlation energy functional in such a way as to include kinetic correlations.

Upon substitution of this expression for F in the total energy functional $E_v[\rho] = F[\rho] + \int \rho(\mathbf{r})v(\mathbf{r})d\mathbf{r}$, the latter is usually is renamed the Kohn-Sham (KS) functional:

$$E_{KS}[\rho] = T_R[\rho] + \int \rho(\mathbf{r})v(\mathbf{r})d\mathbf{r} + \frac{1}{2}\int\int \frac{\rho(\mathbf{r})\rho(\mathbf{r}')}{|\mathbf{r}-\mathbf{r}'|}d\mathbf{r}d\mathbf{r}' + E_{XC}[\rho] \tag{2.37}$$

In this way we have expressed the density functional in terms of the $N = N_\uparrow + N_\downarrow$ orbitals (Kohn-Sham orbitals) which minimize the kinetic energy under the fixed density constraint.

The Kohn-Sham orbitals always satisfy Eqs. 2.35 and the problem is to determine the effective potential v_R or v_{eff} as it is also known. This can be done

by minimizing the KS functional over al densities which integrate to N particles. for the minimizing (i.e. correct) density ρ we have

$$\frac{\delta T_R[\rho]}{\delta\rho(\mathbf{r})} + v(\mathbf{r}) + \int \frac{\rho(\mathbf{r}')}{|\mathbf{r}-\mathbf{r}'|} + \frac{\delta E_{XC}[\rho]}{\delta\rho(\mathbf{r})} = \mu \tag{2.38}$$

The functional derivative $\delta T_R[\rho]/\delta\rho(\mathbf{r})$ can be quickly found by considering the noninteracting Hamiltonian $\hat{H}_R$ (2.31). Its ground state energy is E_0. We can construct the functional

$$E_{v_R}[\tilde{\rho}] = T_R[\rho] + \int \tilde{\rho}(\mathbf{r}) v_R(\mathbf{r}) d\mathbf{r} \tag{2.39}$$

Then, clearly $E_{v_R}[\tilde{\rho}] \geq E_0$ and only for the correct density ρ we will have $E_{v_R}[\rho] = E_0$. Hence the functional derivative of $E_{v_R}[\tilde{\rho}]$ must vanish for the correct density leading to

$$v_R(\mathbf{r}) = -\frac{\delta T_R[\rho]}{\delta\rho(\mathbf{r})} + \mu_R \tag{2.40}$$

where μ_R is the chemical potential for the non-interacting system.

To summarize, the KS orbitals satisfy the well-known self-consistent Kohn-Sham equations

$$\left\{-\frac{\nabla^2}{2} + v_{eff}(\mathbf{r})\right\} \varphi_{i,s}(\mathbf{r}) = \varepsilon_{i,s}\varphi_{i,s}(\mathbf{r}) \tag{2.41}$$

where the effective potential v_R or v_{eff} is given by:

$$v_{eff}(\mathbf{r}) = v(\mathbf{r}) + \int \frac{\rho(\mathbf{r}')}{|\mathbf{r}-\mathbf{r}'|} d\mathbf{r}' + \mu_{XC}[\rho(\mathbf{r})] \tag{2.42}$$

and the electronic density is constructed with Kohn-Sham orbitals

$$\rho(\mathbf{r}) = \sum_{i=1}^{N_s} \sum_{s=1}^{2} |\varphi_{i,s}(\mathbf{r})|^2 \tag{2.43}$$

The exchange-correlation potential $\mu_{XC}[\rho(\mathbf{r})]$ defined above is simply the functional derivative of the exchange-correlation energy $\delta E_{XC}[\rho]/\delta\rho$. Notice the similarities between the Kohn-Sham and Hartree equations.

The solution of the Kohn-Sham equations has to be obtained by iterative procedure, in the same way of Hartree and Hartree-Fock equations. As in these methods, the total energy cannot be written simply as the sum of the eigenvalues $\varepsilon_{i,s}$, but double counting terms have to be subtracted:

$$E_{KS}[\rho] = \sum_{i=1}^{N_s} \sum_{s=1} 2\varepsilon_{i,s} - \frac{1}{2} \int\int \frac{\rho(\mathbf{r})\rho(\mathbf{r}')}{|\mathbf{r}-\mathbf{r}'|} d\mathbf{r} d\mathbf{r}' + \left\{ E_{XC}[\rho] - \int \rho(\mathbf{r}) \mu_{XC}[\rho](\mathbf{r}) d\mathbf{r} \right\} \tag{2.44}$$

2.3.3.1 Summary

We have described a theory that is able to solve the complicated many-body electronic ground state problem by mapping the many-body Shrödinger equation into a set of N coupled single particle equations. Therefore, given an external potential, we are in a position to find the electronic density, the energy, and any desired ground state property (e.g. stress, phonons, etc.). The density of the non-interacting reference system is equal to that of the true interacting system. Up to now the theory is exact. We have not introduced any approximation into the electronic problem. All the ignorance about the many fermion problem has been displaced to the $E_C[\rho]$ term, while the remaining terms in the energy are well-known.

2.4 Exchange and correlation

Up to this point no approximation was introduced into the theory, but there still exists a term (the exchange-correlation energy) in principle, that has a very complicated expression which is not known explicitly. Some assumptions are thus needed in the definition of E_{XC} to convert the DFT to a *practical tool for ab-initio calculations*.

If the exact expression for the kinetic energy including correlation effects, $T[\rho] = \langle \Psi[\rho] | T | \Psi[\rho] \rangle$, (with $\Psi[\rho]$ is the interacting ground state of the external potential which has ρ as the ground state density), were known, then we could use the original definition of the exchange-correlation energy which does not contain kinetic energy contributions:

$$E^0_{XC}[\rho] = \frac{1}{2} \int \int \frac{\rho(\mathbf{r})\rho(\mathbf{r}')}{|\mathbf{r} - \mathbf{r}'|} [g(\mathbf{r}, \mathbf{r}') - 1] d\mathbf{r} d\mathbf{r}' \tag{2.45}$$

Since we are using non-interacting expression for the kinetic energy $T_R[\rho]$, we have to redefine it in the following way:

$$E_{XC}[\rho] = E^0_{XC} + T[\rho] - T_R[\rho] \tag{2.46}$$

It can be shown that the kinetic contribution to the correlation energy (the kinetic contribution to exchange is just Pauli's principle, which is already contained in $T_R[\rho]$ and in the density when adding up the contributions of the N lowest eigenstates) can be taken into account by averaging pair correlation function $g(\mathbf{r}, \mathbf{r}')$ over the strength of the electron-electron interaction, i.e.

$$E_{XC}[\rho] = \frac{1}{2} \int \int \frac{\rho(\mathbf{r})\rho(\mathbf{r}')}{|\mathbf{r} - \mathbf{r}'|} [\tilde{g}(\mathbf{r}, \mathbf{r}') - 1] d\mathbf{r} d\mathbf{r}' \tag{2.47}$$

where

$$\tilde{g}(\mathbf{r},\mathbf{r}') = \int_0^1 g_\lambda(\mathbf{r},\mathbf{r}')d\lambda \tag{2.48}$$

and $g_\lambda(\mathbf{r},\mathbf{r}')$ is the pair correlation function corresponding to the Hamiltonian $\hat{H} = \hat{T}+\hat{V}+\lambda\hat{U}_{ee}$[43]. If we separate the exchange and correlations contributions, we have:

$$\tilde{g}(\mathbf{r},\mathbf{r}') = 1 - \frac{\sum_\sigma |\rho_\sigma(\mathbf{r},\mathbf{r}')|^2}{\rho(\mathbf{r})\rho(\mathbf{r}')} + \tilde{g}_C(\mathbf{r},\mathbf{r}') \tag{2.49}$$

with $\rho_\sigma(\mathbf{r},\mathbf{r}')$ the spin up and down components of the one body density matrix, which in general is a non-diagonal operator. For the homogeneous electron gas the expression for the density matrix is well-known, so that the exchange contribution to $\tilde{g}(\mathbf{r},\mathbf{r}')$ assumes an analytic closed form

$$g_X(\mathbf{r},\mathbf{r}') = g_X(|\mathbf{r}-\mathbf{r}'|) = \frac{9}{2}\left(\frac{j_1(k_F|\mathbf{r}-\mathbf{r}'|)}{k_F|\mathbf{r}-\mathbf{r}'|}\right)^2 \tag{2.50}$$

where $j_1(x) = [\sin(x) - x\cos(x)]/x^2$ is the first order spherical Bessel function.

We are now going to define the exchange-correlation hole $\tilde{\rho}_{XC}(\mathbf{r},\mathbf{r}')$ in the following form:

$$E_{XC}[\rho] = \frac{1}{2}\int\int \frac{\rho(\mathbf{r})\tilde{\rho}_{XC}(\mathbf{r},\mathbf{r}')}{|\mathbf{r}-\mathbf{r}'|}d\mathbf{r}d\mathbf{r}' \tag{2.51}$$

or $\tilde{\rho}_{XC}(\mathbf{r},\mathbf{r}') = \rho(\mathbf{r}')[\tilde{g}(\mathbf{r},\mathbf{r}') - 1]$.

Then, $E_{XC}[\rho]$ can be written as the interaction between the electronic charge distribution and the charge distribution that has been displaced by the exchange and correlation effects. i.e. by the fact that the presence of an electron at $\mathbf{r}$ reduces the probability for a second electron to be at $\mathbf{r}'$, in the vicinity of $\mathbf{r}$. Actually, $\tilde{\rho}_{XC}(\mathbf{r},\mathbf{r}')$ is the exchange-correlation hole averaged over the strength of the interaction, which takes into account kinetic correlations. The properties of $\tilde{g}(\mathbf{r},\mathbf{r}')$ and $\tilde{\rho}_{XC}(\mathbf{r},\mathbf{r}')$ are very interesting and instructive:

- $\tilde{g}(\mathbf{r},\mathbf{r}') = \tilde{g}(\mathbf{r}',\mathbf{r})$ (symmetry)

- $\int \tilde{g}(\mathbf{r},\mathbf{r}')\rho(\mathbf{r}')d\mathbf{r}' = \int \tilde{g}(\mathbf{r},\mathbf{r}')\rho(\mathbf{r})d\mathbf{r} = N-1$ (normalization)

- $\int \tilde{\rho}_{XC}(\mathbf{r},\mathbf{r}')d\mathbf{r}' = \int \tilde{\rho}_{XC}(\mathbf{r},\mathbf{r}')d\mathbf{r} = -1$

This means that the exchange-correlation hole contains exactly *one* displaced electron.

2.4.1 The Local Density Approximation

The main idea of the Local Density Approximation (LDA) is to consider the general inhomogeneous electronic systems as locally homogeneous, and then to use the exchange-correlation hole corresponding to the homogeneous electron gas for which there are very good approximations. This means:

$$\tilde{\rho}_{XC}^{LDA}(\mathbf{r},\mathbf{r}') = \rho(\mathbf{r})\left(\tilde{g}^h[|\mathbf{r}-\mathbf{r}'|,\rho(\mathbf{r})]-1\right) \tag{2.52}$$

with $\tilde{g}^h[|\mathbf{r}-\mathbf{r}'|,\rho(\mathbf{r})]$ the pair correlation function of the homogeneous gas, which depends only on the distance between $\mathbf{r}$ and $\mathbf{r}'$ and is evaluated at the density ρ^h itself locally equals $\rho(\mathbf{r})$. Within this approximation, the exchange-correlation energy density is defined as:

$$\epsilon_{XC}^{LDA}[\rho] = \frac{1}{2}\int \frac{\tilde{\rho}_{XC}^{LDA}(\mathbf{r},\mathbf{r}')}{|\mathbf{r}-\mathbf{r}'|}d\mathbf{r}' \tag{2.53}$$

and the exchange correlation energy becomes

$$E_{XC}^{LDA} = \int \rho(\mathbf{r})\epsilon_{XC}^{LDA}[\rho]d\mathbf{r}. \tag{2.54}$$

In general, the exchange-correlation energy density is not a functional of ρ. From its very definition it is clear that it has to be a non-local object, because it reflects the fact that the probability of finding an electron at $\mathbf{r}$ depends on the presence of other electrons in the surroundings, through the exchange-correlation hole.

There are in fact two approximations embodied in the LDA:

1. The LDA exchange-correlation hole is centered at $\mathbf{r}$, and interacts with the electronic density at $\mathbf{r}$. The true XC hole is actually centered at $\mathbf{r}'$ instead of $\mathbf{r}$.

2. The pair correlation function (g) is approximated by that of the homogeneous electron gas of density $\rho(\mathbf{r})$ corrected by the density ratio $\rho(\mathbf{r})/\rho(\mathbf{r}')$ to compensate the fact that the LDA XC hole is centered at $\mathbf{r}$ instead of $\mathbf{r}'$.

2.4.2 The Local Spin Density Approximation

In magnetic systems or, in general, in systems where open electronic shells are involved, better approximations to the exchange-correlation functional can be obtained by introducing the two spin densities, $\rho_\uparrow(\mathbf{r})$ and $\rho_\downarrow(\mathbf{r})$ such that $\rho(\mathbf{r}) = \rho_\uparrow(\mathbf{r}) + \rho_\downarrow(\mathbf{r})$, and the magnetization density is $\zeta(\mathbf{r}) = (\rho_\uparrow(\mathbf{r}) - \rho_\downarrow(\mathbf{r}))/\rho(\mathbf{r})$. The non-interacting kinetic energy (2.34) splits trivially into *spin-up* and *spin-down* contributions, and the external and Hartree potential depend on the full electron density $\rho(\mathbf{r})$, but the approximate XC functional- even if the exact functional should depend only on $\rho(\mathbf{r})$- will depend on both spin densities independently, $E_{XC} = E_{XC}[\rho_\uparrow(\mathbf{r}), \rho_\downarrow(\mathbf{r})]$. Kohn-Sham equations then read exactly as in (2.41), but the effective potential $v_{eff}(\mathbf{r})$ now acquires a spin index:

$$\begin{aligned} v_{eff}^{\uparrow} &= v(\mathbf{r}) + \int \frac{\rho(\mathbf{r}')}{|\mathbf{r}-\mathbf{r}'|} d\mathbf{r}' + \frac{\delta E_{XC}[\rho_\uparrow(\mathbf{r}), \rho_\downarrow(\mathbf{r})]}{\delta \rho_\uparrow(\mathbf{r})} \\ v_{eff}^{\downarrow} &= v(\mathbf{r}) + \int \frac{\rho(\mathbf{r}')}{|\mathbf{r}-\mathbf{r}'|} d\mathbf{r}' + \frac{\delta E_{XC}[\rho_\uparrow(\mathbf{r}), \rho_\downarrow(\mathbf{r})]}{\delta \rho_\downarrow(\mathbf{r})} \end{aligned} \tag{2.55}$$

The density given by the expression (2.43) contains a double summation, over the spin states and over the number of electrons in each spin state N_s. These latter have to be determined according to the single particle eigenvalues, by asking for the lowest $N = N_\uparrow + N_\downarrow$ to be occupied. This defines a Fermi energy ε_F such that the occupied eigenstates have $\varepsilon_{i,s} < \varepsilon_F$.

In the case of non-magnetic systems $\rho_\uparrow(\mathbf{r}) = \rho_\downarrow(\mathbf{r})$, and everything reduces to the simple case of double occupancy of the single-particle orbitals.

The equivalent of the LDA in the spin-polarized systems is the *local spin density approximation* (LSDA), which basically consists of replacing the XC energy density with a spin-polarized expression:

$$E_{XC}^{LSDA}[\rho_\uparrow(\mathbf{r}), \rho_\downarrow(\mathbf{r})] = \int [\rho_\uparrow(\mathbf{r}) + \rho_\downarrow(\mathbf{r})] \varepsilon_{XC}^h[\rho_\uparrow(\mathbf{r}), \rho_\downarrow(\mathbf{r})] d\mathbf{r} \tag{2.56}$$

2.4.2.1 Why does the LDA work so well in many cases ?

1. It satisfies the sum rule that the XC hole contains exactly one displaced electron:

$$\int \tilde{\rho}_{XC}^{LDA}(\mathbf{r}, \mathbf{r}') d\mathbf{r}' = \int \rho(\mathbf{r}) \tilde{g}^h[|\mathbf{r} - \mathbf{r}'|, \rho(\mathbf{r})] d\mathbf{r}' = -1 \tag{2.57}$$

because for each $\mathbf{r}$, $\tilde{g}_h[|\mathbf{r}\text{-}\mathbf{r}'|, \rho(\mathbf{r})]$ is the pair correlation function of an existing system, i.e. the homogeneous gas at density $\rho(\mathbf{r})$. Therefore, the middle expression is just the integral of the XC hole of the homogeneous gas. For this latter, both, approximations and numerical results carefully take into account that the integral has to be -1.

2. Even if the exact $\tilde{\rho}_{XC}$ has no spherical symmetry, in the expression for the XC energy what really matters is the spherical average of the hole:

$$E_{XC}[\rho] = -\frac{1}{2} \int \rho(\mathbf{r}) \left(\frac{1}{R(\mathbf{r})} \right) d\mathbf{r} \tag{2.58}$$

with

$$\frac{1}{R(\mathbf{r})} = \int \frac{\tilde{\rho}_{XC}(\mathbf{r},\mathbf{r}')}{|\mathbf{r}-\mathbf{r}'|} d\mathbf{r}' = 4\pi \int_0^\infty s\tilde{\rho}_{XC}^{SA}(\mathbf{r},s)ds \tag{2.59}$$

and

$$\tilde{\rho}_{XC}^{SA}(\mathbf{r},s) = \frac{1}{4\pi}\int_\Omega \tilde{\rho}_{XC}(\mathbf{r},\mathbf{r}')d\Omega \tag{2.60}$$

The spherical average $\tilde{\rho}_{XC}^{SA}(\mathbf{r},s)$ is reproduced to a good extent by the LDA, whose $\tilde{\rho}_{XC}$ is already spherical.

2.4.2.2 LDA properties

The features of the LDA is written as:

1. It favors more homogeneous systems.

2. It over-binds molecules and solids.

3. Chemical trends are usually correct.

4. For "good" systems (covalent, ionic, and metallic bonds): geometries are good, bond lengths, bond angles and phonon frequencies are within a few percent, while dielectric properties are overestimated by about a 10%.

5. In finite systems the XC potential does not decay as $-e^2/r$ in the vacuum region, thus affecting the dissociation limit and ionization energies. This is a consequence of the fact that both the LDA and LSDA fail at cancelling the self-interaction included in the Hartree term of the energy. This is one of the most severe limitations of these approximations.

2.4.2.3 When does the LDA fail ?

The LDA is very successful an approximation for many systems of interest, especially those where the electronic density is quite uniform such as bulk metals, but also for less uniform systems as semiconductors and ionic crystals. There are, however, a number of known features that the LDA fails to reproduce:

1. In atomic systems, where the density has large variations, and also the self-interaction is important.

2. In weak molecular bonds, e.g. hydrogen-bonds, because in the bonding region the density is very small and the bonding is dominated by inhomogeneities.

3. In van der Waals –closed shell– systems, because there the binding is due to dynamical charge-charge correlations between two separated fragments, and this is an inherently non-local interaction.

4. In metallic surfaces, because the XC potential decays exponentially while it should follow a power law (image potential).

5. In negatively charged ions, because the LDA fails to cancel exactly the electronic self-interaction, due to approximative character of the exchange. Self-interaction corrected functionals have been proposed[48], although they are not satisfactory from the theoretical point of view because the potential depends on the electronic state, while it should be the same for all states. The solution to this problem is the exact treatment of exchange.

6. The energy band gap in semiconductors turns out to be very small. The reason is that when one electron is removed from the ground state, the exchange hole becomes screened, and this is absent in the LDA. On the other hand, also Hartree-Fock has the same limitation, but the band gap turns out to be too large.

2.4.3 Generalized Gradient Approximations

The exchange-correlation energy has a gradient expansion of the type

$$E_{XC}[\rho] = \int A_{XC}[\rho]\rho(\mathbf{r})^{4/3}d\mathbf{r} + \int C_{XC}[\rho]|\nabla\rho(\mathbf{r})|^2/\rho(\mathbf{r})^{4/3}d\mathbf{r} + ... \quad (2.61)$$

which is asymptotically valid for densities that vary slowly in space. The LDA retains only the leading term of Eq. 2.61 It is well-known that a straightforward evaluation of this expansion is ill-behaved, in the sense that it is not monotonically convergent, and it exhibits singularities that cancel out only when an infinite number of terms is re-summed, like in the random phase approximation (RPA). In fact, the first order correction worsens the results, and the second order correction is plagued with divergences[58]. The largest error of this approximation actually arises from the gradient contribution to the correlation term. Provided that the problem of the correlation term can be cured in some way, as the real space cutoff method proposed by Langreth and Mehl[59], the biggest problem remains with the exchange energy.

One of the main lessons learnt from these works is that the gradient expansion has to be carried out carefully in order to retain all the relevant contributions to the desired order. The other important lesson is that these expansions easily violate one or more of the *exact* conditions required for the exchange and the correlation holes. For instance, the normalization condition, the negativity of the exchange density, and the self interaction cancellation (the diagonal of the exchange density has to be minus a half of the density). Perdew has shown that imposing these conditions to functionals that originally do not verify them, results in a remarkable improvement of the quality of exchange energies[61]. On the basis of this type of reasoning, a number of modified gradient expansions have been proposed along the years, mainly between 1986 and 1996. These have received the name of generalized gradient approximations (GGA).

The basic idea of GGAs is to express the exchange-correlation energy in the following form:

$$E_{XC}[\rho] = \int \rho(\mathbf{r})\varepsilon_{XC}[\rho(\mathbf{r})]d\mathbf{r} + \int F_{XC}[\rho(\mathbf{r}), \nabla\rho(\mathbf{r})]d\mathbf{r} \tag{2.62}$$

where the function F_{XC} is asked to satisfy a number of formal conditions for the exchange-correlation hole, like sum rules, long-range decay, etc. This can not be done by considering directly the bare gradient expansion (2.61). What is needed from the functional is a form that mimics a re-submission to finite order, and this is the main idea of the GGA, for which there is not a unique scheme. Naturally, not all the formal properties can be enforced at the same time, and this differentiates one functional from another. A thorough comparison of different GGA can be found in Ref.[63] In the following we quote a number of them:

1. Langreth-Mehl (LM) exchange-correlation functional[59].

$$\varepsilon_X = \varepsilon_X^{LDA} - a\frac{|\nabla\rho(\mathbf{r})|^2}{\rho(\mathbf{r})^{4/3}}(\frac{7}{9} + 18f^2) \tag{2.63}$$

$$\varepsilon_C = \varepsilon_C^{RPA} + a\frac{|\nabla\rho(\mathbf{r})|^2}{\rho(\mathbf{r})^{4/3}}(2e^{-F} + 18f^2) \tag{2.64}$$

where $F = b|\nabla\rho(\mathbf{r})|/\rho(\mathbf{r})^{7/6}$, $b = (9\pi)^{1/6}f$, $a = \pi/(16(3\pi^2)^{4/3})$, and $f = 0.15$.

2. Perdew-Wang'86 (PW86) exchange functional[64].

$$\varepsilon_X = \varepsilon_X^{LDA}(1 + 0.0864\frac{s^2}{m} + bs^4 + cs^6)^m \tag{2.65}$$

with $m = 1/15$, $b = 14$, $c = 0.2$, and $s = |\nabla\rho(\mathbf{r})|/(2k_F\rho)$ for $k_F = (3\pi^2\rho)^{1/3}$.

3. Perdew-Wang'86 (PW86) correlation functional[65].

$$\varepsilon_C = \varepsilon_C^{LDA} + e^{-\Phi}C_c(\rho)\frac{|\nabla\rho(\mathbf{r})|^2}{\rho(\mathbf{r})^{4/3}} \tag{2.66}$$

where

$$\Phi = 1.745\tilde{f}\frac{C_c(\infty)}{C_c(\rho)}\frac{|\nabla\rho(\mathbf{r})|}{\rho(\mathbf{r})^{7/6}} \tag{2.67}$$

$$C_c(\rho) = C_1 + \frac{C_2 + C_3 r_s + C_4 r_s^2}{1 + C_5 r_s + C_6 r_s^2 + C_7 r_s^3} \tag{2.68}$$

being $\tilde{f} = 0.11$, $C_1 = 0.001667$, $C_2 = 0.002568$, $C_3 = 0.023266$, $C_4 = 7.389 \times 10^{-6}$, $C_5 = 8.723$, $C_6 = 0.472$, $C_7 = 7.389 \times 10^{-2}$.

4. Perdew-Wang'91 (PW91) exchange functional[66].

$$\varepsilon_X = \varepsilon_X^{LDA}\left(\frac{1 + a_1 s \sinh^{-1}(a_2 s) + (a_3 + a_4 e^{-100s^2})s^2}{1 + a_1 s \sinh^{-1}(a_2 s) + a_5 s^4}\right) \tag{2.69}$$

where $a_1 = 0.19645$, $a_2 = 7.7956$, $a_3 = 0.2743$, $a_4 = -0.1508$, and $a_5 = 0.004$.

5. Perdew-Wang'91 (PW91) correlation functional[66].

$$\varepsilon_C = \varepsilon_C^{LDA} + \rho H[\rho, s, t] \tag{2.70}$$

with

$$H[\rho, s, t] = \frac{\beta}{2\alpha}\ln\left(1 + \frac{2\alpha}{\beta}\frac{t^2 + At^4}{1 + At^2 + A^2t^4}\right) + C_{c0}[C_c(\rho) - C_{c1}]t^2 e^{-100s^2} \tag{2.71}$$

and

$$A = \frac{2\alpha}{\beta}[e^{-2\alpha\varepsilon_C[\rho]/\beta^2} - 1]^{-1} \tag{2.72}$$

where $\alpha = 0.09$, $\beta = 0.0667263212$, $C_{c0} = 15.7559$, $C_{c1} = 0.003521$, $t = \frac{|\nabla\rho(\mathbf{r})|}{(2k_s\rho)}$ for $k_s = (4k_F/\pi)^{1/2}$, and $\rho\varepsilon_C[\rho] = \varepsilon_C^{LDA}[\rho]$.

6. Becke'88 (B88) exchange functional[67].

$$\varepsilon_X = \varepsilon_X^{LDA}(1 - \frac{\beta}{2^{1/3}A_x}\frac{x^2}{1+6\beta x\sinh^{-1}(x)}) \tag{2.73}$$

for $x = 2(6\pi^2)^{1/3}s = 2^{1/3}|\nabla\rho(\mathbf{r})|/\rho(\mathbf{r})^{4/3}$, $A_x = (3/4)(3/\pi)^{1/3}$, and $\beta = 0.0042$.

7. Closed-shell Lee-Yang-Parr (LYP) correlation functional[281].

$$\varepsilon_C = -a\frac{1}{1+d\rho^{-1/3}}\left\{\rho + b\rho^{-2/3}\left[C_F\rho^{5/3} - 2t_W + \frac{1}{9}\left(t_W + \frac{1}{2}\nabla^2\rho\right)\right]e^{-c\rho^{-1/3}}\right\} \tag{2.74}$$

where

$$t_W = \frac{1}{8}\left(\frac{|\nabla\rho|^2}{\rho} - \nabla^2\rho\right) \tag{2.75}$$

and $C_F = 3/10(3\pi^2)^{2/3}$, $a = 0.04918$, $b = 0.132$, $c = 0.2533$, and, $d = 0.349$. This correlation functional is nor based on the LDA as the others, but it has been derived as an extension of the Colle-Salvetti expression for the electronic correlation in Helium, to other closed-shell systems.

8. Perdew-Burke-Ernzerhof (PBE) exchange-correlation functional[69].

First the enhancement factor F_{XC} over the local exchange, is defined:

$$E_{XC}[\rho] = \int \rho(\mathbf{r})\varepsilon_X^{LDA}[\rho(\mathbf{r})]F_{XC}(\rho,\zeta,s)d\mathbf{r} \tag{2.76}$$

where ρ is the local density, ζ is the relative spin polarization, and $s = |\nabla\rho(\mathbf{r})|/(2k_F\rho)$ is the dimensionless density gradient, as in Perdew-Wang'86:

$$F_X(s) = 1 + \kappa - \frac{\kappa}{1+\mu s^2/\kappa}, \tag{2.77}$$

where $\mu = \beta(\pi^2/3) = 0.21951$ and $\beta = 0.066725$ is related to the second order gradient expansion[66]. This form: a) satisfies the uniform scaling condition, b)

recovers the correct electron gas limit because $F_x(0) = 1$, c) obeys the spin scaling relationship, d) recovers the LSDA linear response limit for $s \to 0$ ($F_X(s) \to 1 + \mu s^2$), and e) satisfies the *local* Lieb-Oxford bound[70], $\varepsilon_X(\mathbf{r}) \geq -1.679\rho(\mathbf{r})^{4/3}$, i.e. $F_X(s) \leq 1.804$, for all $\mathbf{r}$, provided that $\kappa \leq 0.804$. PBE choose the largest allowed value $\kappa = 0.804$. Other authors have proposed the same form, but with values of κ and μ fitted empirically to a database of atomization energies[71, 72]. The proposed values of κ violate Lieb-Oxford inequality.

The correlation energy is written in a form similar to PW91[66], i.e.

$$E_C^{GGA} = \int \rho(\mathbf{r})[\varepsilon_C^{LDA}(\rho, \zeta) + H[\rho, \zeta, t]]d\mathbf{r} \tag{2.78}$$

with

$$H[\rho, \zeta, t] = (e^2/a_0)\gamma\phi^3 \ln\left\{1 + \frac{\beta\gamma^2}{t}[\frac{1 + At^2}{1 + At^2 + A^2t^4}]\right\}. \tag{2.79}$$

Here, $t = |\nabla\rho(\mathbf{r})|/(2\phi k_s\rho)$ is a dimensionless density gradient, $k_s = (4k_F/\pi a_0)^{1/2}$ is the Thomas-Fermi screening wave number, and $\phi(\zeta) = [(1 + \zeta)^{2/3} + (1 - \zeta)^{2/3}]/2$ is a spin-scaling factor. The quantity β is the same as for the exchange term $\beta = 0.066725$, and $\gamma = (1 - \ln 2)/\pi^2 = 0.031091$. The function A has the following form:

$$A = \frac{\beta}{\gamma}[e^{-\varepsilon_C^{LDA}[\rho]/(\gamma\phi^3 e^2/a_0)} - 1]^{-1} \tag{2.80}$$

So defined, the correlation-correlation term H satisfies the following properties: a) it tends to the correct second-order gradient expansion in the slowly-varying (high density) limit ($t \to 0$), b) it approaches minus the uniform electron gas correlation $-\varepsilon_C^{LDA}$ for rapidly varying densities ($t \to \infty$), thus making the correlation energy to vanish (this results from the correlation hole sum rule), c) it cancels the logarithmic singularity of ε_C^{LDA} in the high density limit, thus forcing the correlation energy to scale to a constant under uniform scaling of the density.

This GGA retains the correct features of LDA (LSDA), and combines them with the inhomogeneity features which are supposed to be the most energetically important. It sacrifices a few correct, but less important features, like the correct nonuniform scaling of the exchange energy in the rapidly varying density region.

In the beginning of the age of GGAs, the most popular scheme (methods) was to use Becke'88 exchange complemented with Perdew'86 correlations corrections (BP). Becke'88 for exchange remained preferred, while Lee-Yang-Parr correlation proved to be more accurate than Perdew'86, particularly for hydrogen bonded systems (BLYP). The most recent GGA in the market is the PBE due to Perdew, Burke and Ernzerhof[69]. This is very satisfactory from the theoretical point of view, because it verifies many of the exact conditions for the XC hole, and it does not contain any fitting parameters. In addition, its quality is equivalent or even better then BLYP[73].

The different recipes for GGAs verify only some of the mathematical properties known for the exact exchange-correlation hole. A compilation and comparison of different approximations can be found in the work of Levy and Perdew[74].

We carried out comparative studies between LDA and some functionals of GGAs to understand their capacity in predicting experimental properties such as lattice constant, cohesive energy and band gap. We used Si crystal as a prototype. Table 2.1 compares physical properties by using different functionals with each other and experimental values.

2.4.3.1 Trends of the GGAs

The general trends of GGAs concerning improvements over the LDA are the following:

1. They improve binding energies and also atomic energies.

2. They improve bond lengths and angles.

3. They improve energetics, geometries and dynamical properties of water, ice

Table 2.1: Calculated and experimental values of cohesive energies, E_c, lattice constants, c and energy gaps, E_g for Si crystal by using LDA, functionals of GGA; Langreth-Mehl (LM), Perdew-Wang 86 (PW86), Perdew-Wang 91 (PW91), Perdew-Becke (B88), Perdew-Burke-Ernzerhof (PBE).

XC	E_c (eV)	c (Å)	E_g (eV)
Experiment[75]	-4.63	5.43	1.17
LDA	-5.98	5.39	0.47
LM	-5.97	5.39	0.47
PW86	-5.13	5.49	0.88
PW91	-5.43	5.46	0.66
B88	-5.27	5.44	0.72
PBE	-5.98	5.39	0.47

and water clusters. BLYP and PBE show the best agreement with experiment. In general, they improve the description of hydrogen-bonded systems, although this is not very clear for the case of $F...H$ bond.

4. Semiconductors are marginally better described within the LDA then in GGA, except for the binding energies.

5. For 4d-5d transition metals the improvement of the GGA over the LDA is not clear, and will depend on how well the LDA does in the particular case.

6. Lattice constants of noble metals (Ag, Au, Pt) are overestimated. The LDA values are very close the experiment, and thus any modification can only worsen them.

7. There is some improvement for the gap problem (and consequently for the dielectric constant), but it is not substantial because this feature is related to the description of the screening of he exchange hole when one electron is removed, and this feature is usually not fully taken into account by GGA.

8. They do not satisfy the known asymptotic behavior, e.g. for isolated atoms:

(a)$v_{XC}(\mathbf{r}) \sim -e^2/r$ for $r \to \infty$ while $v_{XC}^{LDA,GGA}(\mathbf{r})$ vanish exponentially.

(b) $v_{XC}(\mathbf{r}) \to const$ for $r \to 0$ while $v_{XC}^{LDA}(\mathbf{r}) \to const$, but $v_{XC}^{GGA}(\mathbf{r}) \to -\infty$.

2.5 Periodic Systems: the Bloch Theorem

The description of real (bulk) materials within ab-initio calculations is based on the assumption that the atoms which compose them are at rest in their equilibrium positions and these form an infinite, periodically repeated structure. In mathematical terms, if we call V the external potential acting on the electrons, we have:

$$V(\mathbf{r}+\mathbf{R}) = V(\mathbf{r}) \tag{2.81}$$

where $\mathbf{R}$ is a direct lattice vector corresponding to an integer linear combination of three fundamental vectors determining the periodicity of the lattice in three independent directions. The whole electronic Hamiltonian and all the physical quantities describing the periodical system also share the translational invariance of the lattice and this allows to use the Bloch theorem which states that the single particle electronic wave function can be expressed in the form

$$\psi_{n,\mathbf{k}}(\mathbf{r}) = e^{\mathbf{k}.\mathbf{r}} u_{n,\mathbf{k}}(\mathbf{r}) \tag{2.82}$$

where $\mathbf{k}$ is the crystal momentum of the electrons (it actually describes the translational properties of the wavefunction), n is a discrete index (called the band index) classifying states corresponding to the same $\mathbf{k}$-vector and $u_{n,\mathbf{k}}(\mathbf{r})$ is a function with the same periodicity of the crystal:

$$u_{n,\mathbf{k}}(\mathbf{r}+\mathbf{R}) = u_{n,\mathbf{k}}(\mathbf{r}) : \tag{2.83}$$

Due to the translational invariance of the system different $\mathbf{k}$-points can be treated independently. In fact, the Hamiltonian commutes with the operators which generate translations through the points of the lattice and is thus block diagonal on the basis set of the eigenvectors of these latter operators which corresponds to Bloch wavefunction of the form given in 2.82 and are classified by

k. In this context the band index n numbers the eigenvalues of the hamiltonian belonging to the same **k**-block.

The **k**-vectors are defined within the so called first Brillouin Zone (BZ) of the reciprocal space which has a periodic structure whose fundamental lattice vectors $\mathbf{G}_i$ are related to the ones of the real (direct) space $\mathbf{R}_i$ as follows:

$$\mathbf{G}_i.\mathbf{R}_j = 2\pi\delta_{ij} \qquad i,j = 1,2,3. \tag{2.84}$$

The sums over the electronic states which define many physical quantities as, for instance, E_{band} and $\rho(\mathbf{r})$, actually correspond to integrals over the BZ (and sums over the band index n). Using the symmetry of the crystal, the integration can be conveniently confined in a smaller region of the BZ, the so called irreducible wedge of the Brillouin zone (IBZ). This result can be further improved by the use of the special point integration technique which allows to perform reciprocal space integration (needed for example when calculating the charge density or the sum of the eigenvalues) using generally a small set of **k**-vectors in the IBZ. These points can be chosen according to different techniques [76](in this thesis we use the Monkhorst and Pack scheme) and in general the accuracy of the (approximate) method can be checked by the convergence properties of the physical properties of interest upon increasing their number. As an example, the reciprocal space integration for the charge density is performed as a sum over a discrete set of vectors:

$$\tilde{\rho}(\mathbf{r}) = \sum_{\mathbf{k}\epsilon\ IBZ} \omega_{\mathbf{k}} \sum_n f_{n,\mathbf{k}} |\psi_{n,\mathbf{k}}(\mathbf{r})|^2 \tag{2.85}$$

from which the electronic charge density results through a symmetrization procedure:

$$\rho(r) = \frac{1}{N_S} \sum_S \tilde{\rho}(S^{-1}\mathbf{r} - f) \tag{2.86}$$

where N_S is the number of symmetry operations S in the space group of the

crystal and f a possible fractional translation. In Eq. 2.85 the $\omega_{\mathbf{k}}$ coefficient is the **k**-point weight calculated within the special point technique.

The special points technique is very efficient in the description of semiconductors or insulators but gives poor results when directly applied to metals. This happens because the region around the Fermi level (which is crossed by some electronic states) needs to be sampled quite accurately and in general a larger number of vectors is required. If the used **k**-point grid is not fine enough, there could also be problems of instability during the self-consistent run because even small shifts in the Fermi energy could include or exclude in the reciprocal space sums (like the one in Eq. 2.85) a finite number of electronic states thus producing considerable fluctuations in the corresponding quantities. A possible solution to this problem can be achieved using the tetrahedron method which consists in decomposing the BZ into symmetry breaking elemental volumes and connecting the energy bands between neighboring **k**-points by linear interpolation. However this method presents some important drawbacks [77] so that we choose to use another approach to the problem of describing metallic systems. This technique consists in introducing a finite smearing of the Fermi distribution (actually corresponding to consider a finite effective temperature) which smoothes the weight of the states around this level and avoids large fluctuations in the calculated quantities. The convoluting function used to introduce the smearing can be chosen in many ways: finite temperature Fermi distribution, Lorentzian, Gaussian [78], cold smearing factors [79], and so on. In this thesis the Methfessel and Paxton smearing technique [80] is used which adopts a combination of Gaussians and polynomials as spreading functions. This approximation works quite well for metals (even if a larger number of k-points is usually required than for semiconductors) and the accuracy of the reciprocal space integrations at finite smearing can be checked by their convergence properties upon increasing the number of the special **k**-vectors in the IBZ and reducing the broadening width σ. The main drawback introduced by the smearing technique is the dependence of the ground state total energy on the chosen σ. The Methfessel and Paxton methods allows to considerably reduce this dependence by accurately choosing the convoluting function to smear the Fermi distribution.

2.5.1 Brillouin Zone Sampling

Electronic states are allowed only at a set of **k**-points determined by the boundary conditions that apply to the bulk solid. The infinite number of electrons in the periodic solid are accounted for by an infinite number of **k**-points. The Bloch theorem changes the problem of calculating an infinite number of electronic wavefucntions to one of calculating a finite number of wavefunctions at an infinite number of **k**-points. The occupied states at each **k**-point contribute to the electronic potential, so that in principle an infinite number of calculations are needed. However, the electronic wavefunctions at **k**-points that are very close together will be almost identical. This suggests that the DFT expressions that contain a sum over **k**-points (or, equivalently, an integral over the Brillouin zone) can be efficiently evaluated using a numerical scheme that performs summation over a small number of special points in the Brillouin zone. In addition, symmetry considerations suggest that only **k**-points within the irreducible segment of the Brillouin zone should be taken into account. A number of prescriptions exist for generating such points and corresponding weights to be used in the summation (see Payne et al.[81], 1992 and Srivastava and Weaire[82], 1987 for reviews). Using these methods, one can obtain an accurate approximation of the electronic potential and the total energy of an insulator by calculating electronic states at a very small number of **k**-points. The calculations for metallic systems require a more dense set of **k**-points to determine the Fermi level accurately.

The magnitude of any error in the total energy due to limited **k**-point sampling can always be reduced by using a denser set of **k**-points, in much the same way as the convergence with respect to the number of basis set functions is achieved. It is important to achieve high convergence with respect to the **k**-point sampling when the energies of two systems with different symmetries are compared, for example if you are looking at the relative stabilities of a FCC and an HCP structure. There is no cancellation of errors in this case and both energies have to be absolutely converged.

2.5.1.1 Monkhorst-Pack Special Points

One of the most popular schemes for generating **k**-points was proposed by Monkhorst and Pack[83] (1976). This scheme, which was later modified to include hexagonal systems (Monkhorst and Pack[83], 1977), produces a uniform grid of **k**-points along the three axes in reciprocal space. The Monkhorst-Pack grid is defined by three integers, q_i where $i = 1, 2, 3$, which specify the number of divisions along each of the axes. These integers generate a sequence of numbers according to the following:

$$u_r = (2r - q_i - 1)/2q_i \tag{2.87}$$

where r varies from 1 to q_i. The Monkhorst-Pack grid is obtained from these sequences by:

$$k_{prs} = u_p b_1 + u_r b_2 + u_s b_3 \tag{2.88}$$

This set of $q_1 q_2 q_3$ distinct points is further symmetrized and weights are assigned according to the number of symmetry images of a given point in the symmetrized set.

It is possible to add a constant shift to all of the points in the set before symmetrization. This operation, when applied to hexagonal symmetry systems, results in a slightly modified recipe for the points along the a and b axes:

$$u_p = (p - 1)/q_i \tag{2.89}$$

where p varies from 1 to q_i.

2.6 The Planewave Basis Set

In order to solve the KS equations by practical calculations we need to transform the original integro-differential problem into a more tractable algebraic one. This can be achieved by expanding the electronic wavefunctions on a basis set and using this representation in all operators in the hamiltonian. The one chosen in this work (and one of the most used in ab-initio calculations) is the Plane Wave (PW) basis set [84] which takes advantage from efficient algorithms, like the Fast Fourier Transform (FFT), to move back and forth from real to reciprocal space. The Bloch electronic wave function in Eq. 2.82 can thus be represented in the form:

$$\psi_{\mathbf{k}_v}(\mathbf{r}) = \frac{1}{(N\Omega)^{1/2}} \sum_{\mathbf{G}} e^{i(\mathbf{k}+\mathbf{G}).\mathbf{r}} c_v(\mathbf{k}+\mathbf{G}) \tag{2.90}$$

where is the volume of the unit cell, the $\mathbf{G}$ vectors are the reciprocal lattice vectors, and the $c_v(\mathbf{k}+\mathbf{G})$ coefficients are normalized in such a way that:

$$\sum_{\mathbf{G}} |c_v(\mathbf{k}+\mathbf{G})|^2 = 1 \tag{2.91}$$

Using this expansion, the KS equations can be written in reciprocal space as:

$$\sum_{\mathbf{G}'} [\frac{\hbar^2}{2m} + v_h(\mathbf{G}-\mathbf{G}') + v_{xc}(\mathbf{G}-\mathbf{G}') + v_{ext}(\mathbf{G},\mathbf{G}')] c_v(\mathbf{k}+\mathbf{G}') = \epsilon_{\mathbf{k}_v} c_v(\mathbf{k}+\mathbf{G}) \tag{2.92}$$

It is evident from this expression that the Hamiltonian has block diagonal form with respect to the $\mathbf{k}$ vectors and the diagonalization can thus be performed within each of these block separately. As we are studying the ground state properties of the system, for each $\mathbf{k}$-point only a finite number of the lowest-energy electronic states on which all the electrons of the system can be accommodated, need to be computed to obtain the charge density. This quantity is then used to construct

a new guess of the potential to be reintroduced in the Kohn-Sham equations for the successive step of the iterative diagonalization. Of course the PW expansion is exact in the limit of infinite number of **G**-vectors. In practical calculations one can deal only with a finite number of plane waves and usually chooses those contained in a sphere of maximum kinetic energy E_{cut} (the energy cut-off):

$$\frac{\hbar^2}{2m}|\mathbf{k}+\mathbf{G}|^2 \leq E_{cut} \tag{2.93}$$

The accuracy we obtain in resolving the KS equation under the condition in Eq. 2.93 has to be checked each time by increasing the value of the energy cut-off and studying the convergence of the properties we are interested in. The big advantage of using the PW expansion mainly consists in the fact that E_{cut} is the only parameter in the theory which controls the accuracy of the description of the system under consideration. This means that, once E_{cut} is fixed, all the wavefunctions of the system whose variation takes place over distances larger than (and up to) $2\pi\hbar/\sqrt{2mE_{cut}}$ can be well described.

2.7 Pseudopotentials

Unfortunately, the PW expansion uses the same resolution in each region of space so that, to describe the ionic cores and the electronic states partially localized around them, we would need an intractably large number of **G**-vectors. One possible way around this difficulty is the Pseudopotential (PP) technique, which is based on the assumption that the most relevant physical properties of a system, as far as bonding and chemical reactivity are concerned, are brought about by its valence electrons only, while the ionic cores (the nuclei dressed by the most internal electronic cloud) can be considered as frozen in their atomic configurations. The valence electrons thus move in the effective external field produced by these inert ionic cores and the pseudopotential tries to reproduce the interaction of the true atomic potential on the most external (valence) states

without explicitly including the core states in the calculations. There exist different procedures to build a pseudopotential but the general ideas they rely on are similar. Once a full potential calculation is performed for the isolated atom, the electronic states are divided into two categories: the internal states and the valence ones. The internal electrons remain frozen in their ground state atomic configuration whereas for the external ones a pseudowavefunction is built (which matches the corresponding full potential one in the region external to a fixed core radius) which is chosen to be smooth and nodeless inside the core, while conserving the total valence charge in this region (norm conserving condition). Given a choice for both the core radius and the shape of the pseudowavefunction, a pseudopotential is built (inverting the Schrödinger-like equation for the considered electronic state) which reproduces the scattering properties of the "real" valence states of the reference atomic configuration in a region of energies which has to be as large as possible in order to give good transferability of the pseudopotential when used in different chemical environments. Owing to the smoothness of the pseudowavefunction, the calculations can be performed with a reasonable number of plane waves. However in order to reproduce the scattering properties of the all-electrons (AE) wavefunctions of several angular momenta, it is usually necessary to split the pseudopotential in a local part (matching the real full potential outside the core) and a non local one (vanishing outside the core) which acts in different ways on each different angular momentum channel. The first expression for this non local contribution was given in a semi-local form [85, 86, 87] where the non-locality is built just on the angular coordinates:

$$V(\mathbf{r},\mathbf{r}') = V_{loc}(\mathbf{r})\delta(\mathbf{r}-\mathbf{r}') + \sum_{l=0}^{l_{max}} V_l \delta(\mathbf{r}-\mathbf{r}') P_l(\mathbf{r},\mathbf{r}') \tag{2.94}$$

where P_l is the projector operator onto the l^{th} angular momentum subspace. However, in order to make the PW calculation more efficient, Kleinman and Bylander (KB) [88] replaced the above semilocal expression with a fully separable form:

$$V(\mathbf{r},\mathbf{r}') = V_{loc}(\mathbf{r})\delta(\mathbf{r}-\mathbf{r}') + \sum_i |i> V_i < i| \tag{2.95}$$

where the wavefunctions $|i>$ are (modified) atomic pseudo-states such that the KB potential reproduces the action of the original semilocal one on the reference atomic pseudowavefunctions.

The most complete generalization (and improvement) of this scheme was introduced by Vanderbilt [89, 90] who found a method to increase the transferability of the PPs while reducing the workload necessary to describe the pseudowavefunctions inside the cores. The region of energy corresponding to occupied states in the crystals is sampled with more than one projector so that the index i in eq. 2.95 runs not just on the atomic reference states but also, for each angular momentum, on a set of (usually two) energy values around them used to reproduce the correct scattering properties of the ion. This requires a generalization of the expression 2.95 whose non local part becomes:

$$V_{nl} = \sum_{i,j} B_{ij}|\beta_i >< \beta_j| \tag{2.96}$$

where the functions $|\beta_i>$ are built from the chosen pseudowavefunctions (corresponding to the chosen energy ε_i) and local pseudopotential and are localized in the core region (they vanish at a chosen core radius of the atom on that site), while the matrix B_{ij} is an Hermitian operator built using the same quantities. This is already a very useful improvement as it allows to increase the PP transferability, but the most important reduction of the computational load introduced by the ultrasoft (US) PPs comes from the relaxation of the norm conserving condition on the pseudowavefunctions and the possibility of choosing them as smooth as possible inside the core regions. This is possible by introducing a generalized overlap operator:

$$S = 1 + \sum_{i,j} q_{i,j}|\beta_i >< \beta_j| \tag{2.97}$$

so that the orthonormality condition to be satisfied in the solution of the KS equations is:

$$< \psi_i|S|\psi_j >= \delta_{ij} \tag{2.98}$$

In these expressions $q_{i,j}$ is the integral of the augmentation charge density,

$$q_{i,j} = \int Q_{i,j}(r)dr \tag{2.99}$$

$$Q_{i,j}(r) = \psi_i^{AE*}(r)\psi_j^{AE}(r) - \psi_i^{PS*}(r)\psi_j^{PS}(r) \tag{2.100}$$

where the wavefunctions appearing in eq. 2.100 are the atomic (all-electrons and pseudo) states used to build the crystal electronic ones. Owing to this generalization of the overlap, the charge density has to be completed with the augmentation part on the ionic cores:

$$n(r) = \sum_{k,v} f_{kv}[|\psi_{kv}(r)|^2 + \sum_{l,i,j} Q_{ij}^l(r - R_l) < \psi_{kv}|\beta_i^l >< \beta_j^l|\psi_{kv} >] \tag{2.101}$$

In this expression an index, I, counting the different ions, in position R_I has been added to the augmentation charges Q_{Iij} and to the f functions. This modification in n(r) also involves the expression of the potential in the KS equations. If we describe the external potential in the form:

$$V(r, r') = V_{loc}(r)\delta(\mathbf{r} - \mathbf{r}') + \sum_{l,i,j} D_{ij}^{lion}|\beta_i^l >< \beta_j^l| \tag{2.102}$$

the coefficient $D_{i,j}^{Iion}$ have to be calculated as:

$$D_{ij}^{lion} = B_{ij}^l + \epsilon_j q_{ij}^l \tag{2.103}$$

and the KS equations (which have to be solved with the generalized orthonormality condition 2.98) finally read:

$$[-\frac{\hbar^2\nabla^2}{2m} + \sum_{l,i,j} D_{ij}^l |\beta_i^l >< \beta_j^l| + V_{eff}]|\psi_{kv} >= \epsilon_{kv} S|\psi_{kv} > \tag{2.104}$$

where

$$V_{eff} = V_{loc} + V_{Hxc} \quad and \quad D_{ij}^{lion} + \int V_{eff}(r) Q_{ij}^l (r - R) dr \tag{2.105}$$

As evident from the last expression, the pseudopotential needs to be updated at each iteration (the effective potential V_{eff} is built with the electronic charge density) and this makes it participate to the screening process, further increasing its transferability. The prize to be paid to obtain the advantages introduced by US PPs (beside updating the D_{ij}^I coefficients each time) consists in the fact that we need a very large cut-off energy to describe the augmentation contribution to the charge density. However this term is important just in the calculation of $n(r)$ and does not enter the diagonalization problem which has the dimension fixed by the (smaller) wave function energy cut-off.

2.7.1 The non-linear core correction

The PW PPs method is based on the assumption that the electronic charge density can be separated into a valence term $n_v(r)$ and a frozen core contribution $n_c(r)$. In its original form H and xc potentials in the solid are calculated using $n_v(r)$ only. This is not an approximation for the Hartree potential because it's linear in the charge density and the contribution coming from the core term can be easily separated from the other (and included in the local part of the pseudo potential). The problem exists instead for the xc potential which is not linear in the density. Thus separating the xc energy density as

$$\epsilon_{xc}(n_v(r) + n_c(r)) \sim \epsilon_{xc}(n_v(r)) + \epsilon_{xc}(n_c(r)) \tag{2.106}$$

introduces a systematic error which is more serious when the two contributions to the charge density considerably overlap with each other. It follows that the systems having valence electrons strongly penetrating in the core regions (they usually are very localized external states like d bands for transition metals or f states in rare earths compounds)

may be affected by this problem. The exact solution would be to include the core states with strong overlap with the valence ones in the valence manifold, but this would become very expensive from a computational point of view, also requiring a larger space for the wavefunctions to be stored. The non linear core correction (NLCC) approximately overcomes this difficulty including the core contribution in the charge density when computing the xc energy and potential. The xc energy thus results:

$$E_{xc}[n_v + n_c] = \int (n_v(r) + n_c(r))\epsilon_{xc}(n_v(r) + n_c(r))dr \tag{2.107}$$

where the core contribution is still fixed in its frozen atomic configuration (it is not updated during iteration). The need of introducing the NLCC formalism is particularly evident when dealing with magnetic crystals: without including the core contribution (which is spin unpolarized), into the charge density, the magnetic polarization ξ,

$$\xi(r) = \frac{n^{\uparrow} - n^{\downarrow}}{n^{\uparrow} + n^{\downarrow}} \tag{2.108}$$

could be significantly overestimated thus spuriously enhancing the tendency of the system to acquire a finite magnetization.

2.8 Numerical calculations

We performed our numerical calculations by using Vienna *Ab-initio* Simulation Program (VASP) program. VASP is a program package which includes *ab-initio* first principles calculations using pseudopotentials and a plane wave basis set. The approach implemented in VASP is based on the (finite temperature) local-density approximation with the free energy as variational quantity and an exact evaluation of the electronic ground state. Most of the algorithms implemented in VASP use an iterative matrix-diagonalization scheme: we used algorithms based on the conjugate gradient scheme [91]. For the mixing of the charge density an efficient Broyden/Pulay mixing scheme[92] is used. Fig. 2.1 shows a typical flow-chart of VASP. Input charge density and wavefunctions are independent quantities. Within each selfconsistency loop the charge density is used to set up Hamiltonian, then the wavefunctions are optimized iteratively so that they get closer to the exact wavefunctions of this Hamiltonian. From the optimized wavefunctions a new charge density is calculated, which is then mixed with the old input-charge density. The interaction between ions and electrons is described by ultra-soft Vanderbilt pseudopotentials (US-PP). US-PP. Forces and the full stress tensor can be calculated with VASP and used to relax atoms into their instantaneous ground-state. If forces are smaller than a force convergent value, program reaches required accuracy then we get point on the Born-Oppenheimer surface. In order to check the stability of this point we also treat phonon ananlysis and finite temperature Molecular Dynamics simulations. So that after these tests we will obtain local minima for a given system.

2.9 Charge Density

In order plot total or band-decomposed charge density of a system, we wrote charge density program which uses fast-fourier-transform (FFT) routine. Program reads wavefunctions which are obtained with VASP program and it creates charge density values in reciprocal space. At the same time **G**-vectors are also

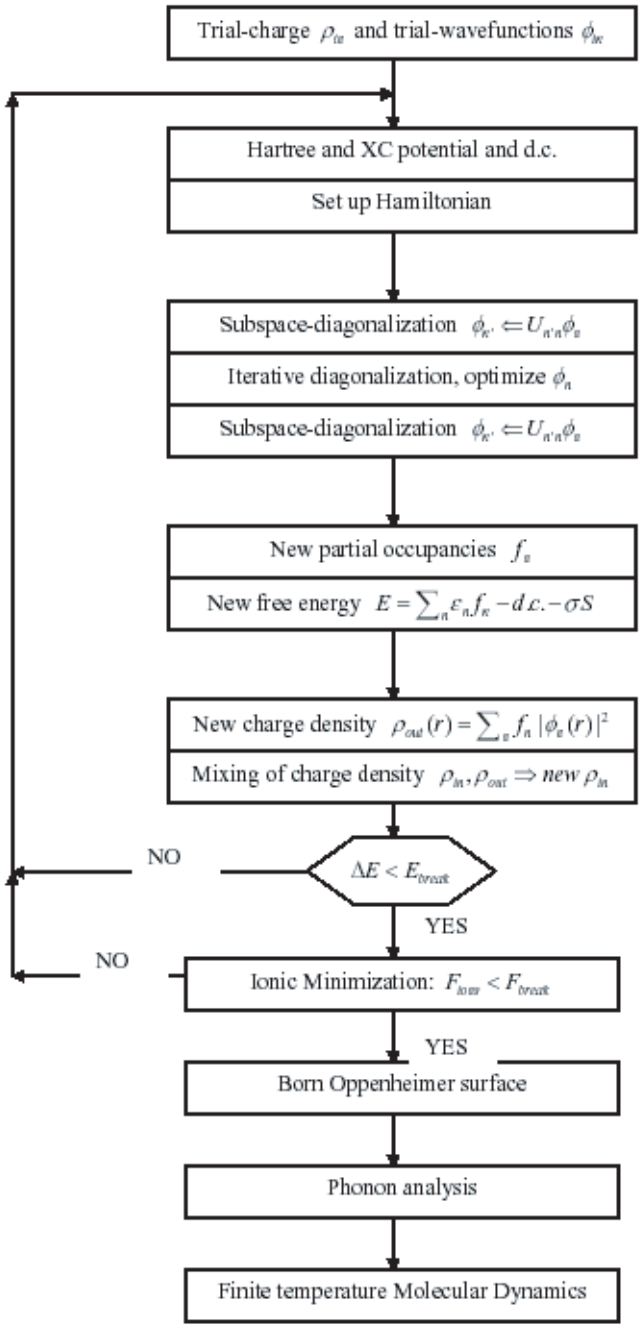

Figure 2.1: Flow chart of VASP program.

created. By applying FFT routine charge densities are obtained in real space. In this manner, we can obtain total charge density on a given plane with a dense mesh points or partial (band decomposed) charge densities for a desired band.

Chapter 3

Carbon Nanotubes

3.1 Introduction

Carbon is the lightest atom in column IV of the periodic table and is an element with unique properties. Carbon differs in many ways from Si, Ge, and Sn, the other column elements, which all have sp^3-bonding in their cubic solid ground states, while carbon in the condensed phase has a hexagonal ground state graphite with sp^2 bonding and is highly anisotropic, nearly two-dimensional (2D) semimetal; lying close in energy to diamond, a three-dimensional (3D) material with nearly isotropic properties. The recent discoveries of fullerenes (a zero-dimensional form of carbon) and carbon nanotubes (a 1D form) have stimulated great interest in carbon materials overall.

In first subsection, I will present a brief description of growth techniques of nanotubes. After that I will outline the relations governing the geometry of nanotubes. Finally, I discuss some of the basic electronic and structural properties of these nanotubes extracted from theoretical studies.

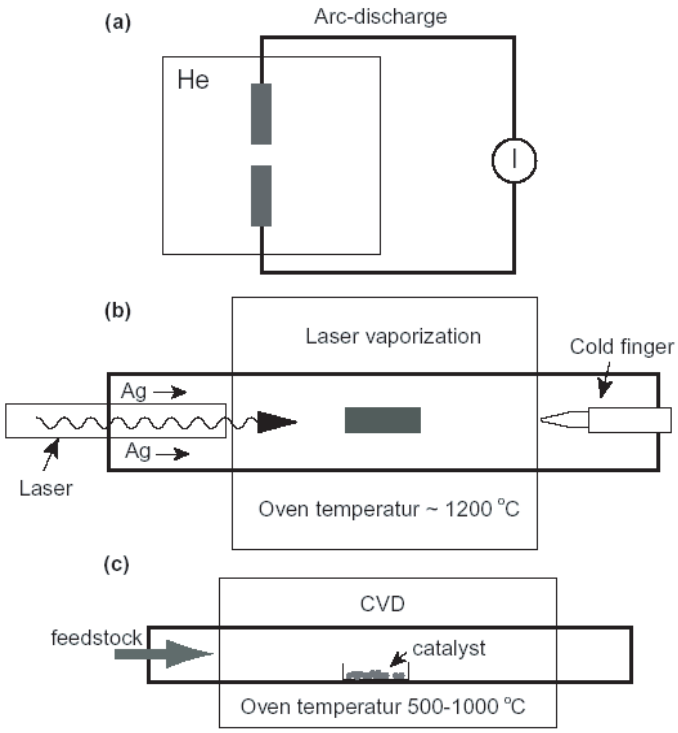

Figure 3.1: Schematic experimental setup for the three common carbon nanotube growth methods, (a) arc-discharge, (b) laser ablation (vaporization) and (c) chemical vapor deposition (CVD).

3.2 Carbon Nanotube Growth

There are three common methods for growing carbon nanotubes: Arc-discharge, laser vaporization and chemical vapor deposition (CVD). The arc-discharge and laser vaporization methods are similar while the CVD method differs. An illustration of the three methods is shown in Figure 3.1.

3.2.1 Laser Vaporization

In laser vaporization, also called laser ablation, one uses laser pulses to vaporize a target consisting of graphite mixed with transition metals. The vaporized material is swept down through the pipe to the cold finger by a flow of inert gas. A schematic view of the setup is seen in Figure 3.1 (b). The water cooled

cold finger lies just outside the oven, which is heating the pipe to a temperature around 1200 C^o. On the cold finger the material condenses as SWNTs and carbon-catalyst soot. The growth mechanism has not been exactly determined yet but some explanation have been proposed [93]: The laser-pulses heat the target surface made of carbon and catalyst transition metals and the result is a fume of vaporized molecules and atoms that cools as the fume expand. As the carbon atoms and molecules cools they condense into larger molecules, before these molecules can close into a smaller fullerene as for example a C_{60}, a catalyst particle attaches to the carbon molecule and prevent the closing. The catalyst might even open already closed smaller fullerenes when they attach to them. The carbon molecules rolls up into fullerenes to avoid dangling bonds at the edges. From these carbon-catalyst molecules the tubes grow. The feedstock is carbon atoms or molecules that either hit the catalyst or the tube/rope (A rope is a bundle of carbon nanotubes lying together like the fibers in a rope.). In the last case the atoms diffuses along the rope until they reach the catalyst-carbon interface and then participates in the building of a nanotube. This mechanism also explains why the tubes in a rope almost always have nearly identical lengths[93]:

If one tube is shorter than the other then there is an enhanced chance that a carbon atom diffusing along the rope will hit the shorter tubes interface before it hits the carbon catalyst interface at the end of the rope and this process is speeding up the growth of the shorter tube until it catches up with the rest of the tubes in the rope [6]. This process happens until the catalyst particle gets too big or the fume gets to cold for diffusion of the carbon through or along the catalyst and rope to happen. It has also been proposed that the process can be terminated by a saturation or covering of so much of the catalyst particle by carbon atoms, that the diffusion is impossible.

3.2.2 Arc-discharge

In an arc-discharge method the graphite rods, doped with a transition metal for single-wall growth, are heated by an electric arc. The two carbon electrodes are separated by $\sim$1 nm and a voltage difference of 20-25 V is applied resulting in a

current between 50-120 A. The heating takes place in an inert gas and the tubes grows in the fume around the negative electrode. For the production of single-wall tubes with the arc-discharge method the growth mechanism is presumably the same as in the laser-ablation method.

3.2.3 Chemical vapor deposition

Although the laser-ablation method can give a relative high yield of nanotubes both this and the arc-discharge method need very high temperatures to work. Graphite vaporizes at temperatures over 3000 C^o so these two methods demand a lot of energy and are therefore not adequate for scale up production. Besides this there is also the problem of placing the tubes where you want them. In CVD growth you have some control of the positioning.

In a CVD system the growth is taking place on a chip that has been prepared with catalyst material. The chip is placed in a oven heated to 500-1000 C^o. The carbon is applied by a feedstock gas that could be methane CH_4. The reason for this choice is that it is the most stable of the hydrocarbons. A schematic setup for the growth method is seen in Figure 3.1(c). The nanotube is growing on the catalyst particles, so by placing these in predefined islands one can have tubes growing from these exact spots. There have been different proposals of how to control the growth direction of the nanotube. It have been shown that to some extent the growth direction can be controlled by an electrical field and that this method might even be able to distinguishing between semiconducting and metallic tubes [94, 95].

Another advantage of the CVD method is that the tubes are grown directly on the chip and therefore there is no need for purification and one also avoids the deposition process. Both the purification and the deposition processes tend to introduce defects and it is therefore advantageous to avoid them. Unfortunately this was not a possible approach, in our case, since we wanted the tubes lying on a GaAs substrate and at CVD growth temperature the amorphous As and the GaAs decomposes.

3.3 Physics of Carbon nanotubes

For 1D systems on a cylindrical surface, translational symmetry with a screw axis could affect the electronic structure and related properties. The interesting electronic properties of 1D multilayer carbon nanotubes are seen to arise predominately from intralayer interactions, rather than from interlayer interactions between multilayers within a single wall carbon nanotube or between two different nanotubes. Since the symmetry of a single nanotube is essential for understanding the basic physics of carbon nanotubes, we focuses on the symmetry properties of single layer nanotubes.

3.3.1 Fundamental parameters and relations from carbon nanotubes

It is convenient to specify a general carbon nanotubule in terms of the tubule diameter d_t and the chiral angle θ, which are shown in figure 3.2. The chiral vector $\mathbf{C}_\mathrm{h}$ is defined in table 3.1 in terms of the integers (n, m) and the basis vectors a_1 and a_2 of the honeycomb lattice, which are also given in the table in terms of rectangular coordinates. the integers (n, m) uniquely determine d_t and θ. The length L of the chiral vector $\mathbf{C}_\mathrm{h}$ is directly related to the tubule diameter d_t. The chiral angle θ between the $\mathbf{C}_\mathrm{h}$ direction and the zigzag direction of the honeycomb lattice $(n, 0)$ is related in table 3.1 to the integers (n, m).

We can specify a single-wall C_{60}-derived carbon nanotube by bisecting a C_{60} molecule at the equator and joining the two resulting hemispheres with a cylindrical tube having the same diameter as the C_{60} molecule, and consisting of the honeycomb structure of a single layer of graphite. If the C_{60} molecule is bisected normal to a five-fold axis, the armchair tubule is formed. It is specified with (n, n) integers (Fig. 3.3(a)). If the C_{60} molecule is bisected normal to a 3-fold axis, the zigzag tubule is formed which is defined with $(n, 0)$ (Fig. 3.3(b)). Armchair and zigzag nanotubes of larger diameter, and having correspondingly larger caps, can likewise be defined, and these nanotubules have a general appearance shown in

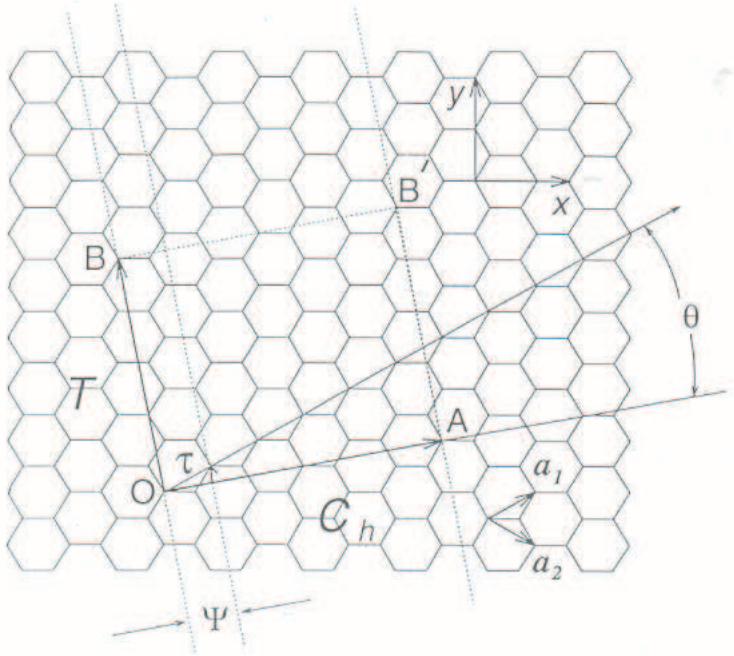

Figure 3.2: The 2D graphine sheet is shown along with the vector which specifies the chiral nanotube. The chiral vector **OA** or $\mathbf{C}_{\rm h} = {\rm n}\mathbf{a}_1 + {\rm m}\mathbf{a}_2$ is defined on the honeycomb lattice by unit vectors $\mathbf{a}_1$ and $\mathbf{a}_2$ and the chiral angle θ is defined with respect to the zigzag axis. Along the zigzag axis $\theta = 0^o$. Also shown are the lattice vector **OB**=**T** of the 1D tubule unitcell, and the rotation angle ψ and the translation τ which constitute the basic symmetry operation $R =< \psi|\tau >$. The diagram is constructed for (n, m)=$(4, 2)$. Ref. [96]

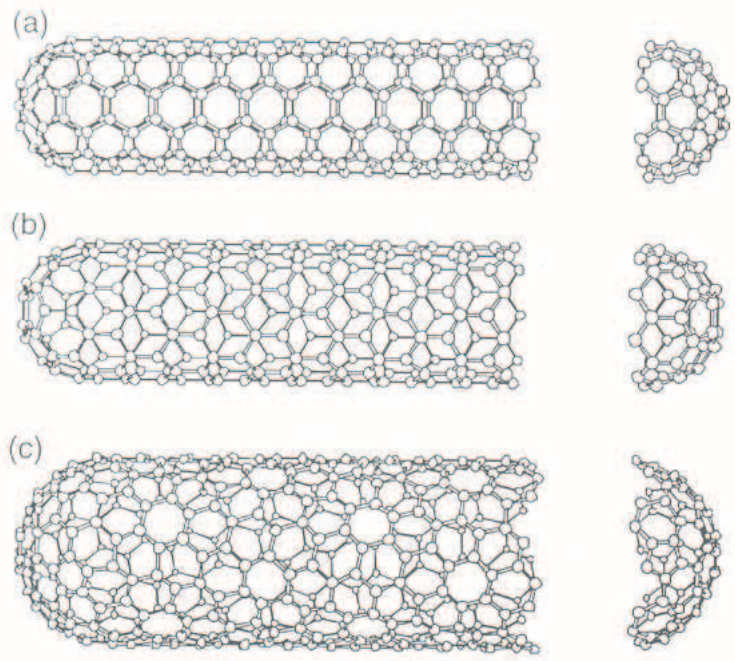

Figure 3.3: By rolling up a graphene sheet (a single layer of carbon atoms from a 3D graphite crystal) as a cylinder and capping each end of the cylinder with half of a fullerene molecule, a "fullerene-derived tubule," one layer in thickness, is formed. Shown here is a schematic theoretical model for a single-wall carbon tubule with the tubule axis **OB** (see. Fig. 3.2) normal to: (a) the $\theta = 30^o$ direction (an "armchair" tubule), (b) $\theta = 0^o$ (a "zigzag" tubule), and (c) a general direction **B** with $0 < |\theta| < 30^o$ (a "chiral" tubule). The actual tubules shown in the figure correspond to (n, m) values of (a)(5,5), (b)(9,0), and (c) (10,5). Ref. [96]

Fig. 3.3. In addition, a large number of chiral carbon nanotubes can be formed for $0 < |\theta| < 30^o$, with a screw axis along the axis of tubule. It is described with (n, m), which is $n \neq m$. A representative chiral nanotube is shown in Fig. 3.3(c)

The unit cell of the carbon nanotube is shown in Fig. 3.2 as the rectangle bounded by the vectors $\mathbf{C}_\mathrm{h}$ and $\mathbf{T}$, where $\mathbf{T}$ is the 1D translation vector of the nanotube. The vector $\mathbf{T}$ is normal to $\mathbf{C}_\mathrm{h}$ and extends from the origin to the first lattice point **B** in the honeycomb lattice. It is convenient to express $\mathbf{T}$ in terms of the integers (t_1, t_2) given in table 3.1, where it is seen that the length of $\mathbf{T}$ is $\sqrt{3}L/d_R$ and d_R is either equal to the highest common divisor of (n, m), denoted by d, or to $3d$, depending on whether $n - m = 3dr$, r being an integer, or not. The number of carbon atoms per unit cell n_c of the 1D tubule is 2N (N is defined

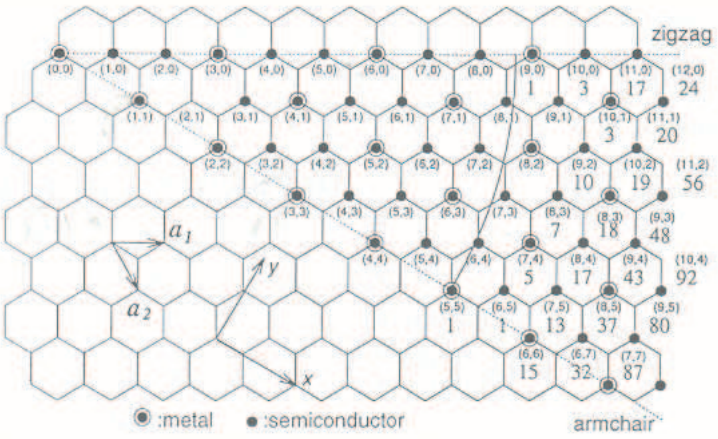

Figure 3.4: The 2D graphine sheet is shown along with the vector which specifies the chiral nanotube. The pairs of integers (n, m) in the figure specify chiral vectors $\mathbf{C}_h$ (see table 3.1) for carbon nanotubes, including zigzag, armchair, and chiral tubules. Below each pair of integers (n, m) is listed the number of distinct caps that can be joined continuously to the cylindrical carbon tubule denoted by (n, m). The circled dots denote metallic tubules and the small dots are for semiconducting tubules. Ref. [96]

as the number of hexagon in the unit cell), as given in table 3.1, each hexagon (or unit cell) of the honeycomb lattice containing two carbon atoms.

Figure 3.4 shows the number of distinct chiral vectors which are specified with the pairs of integers (n, m). By wrapping the graphene sheet along the direction of chiral vector, we obtain zigzag, armchair and chiral nanotubes. The circled dots in the figure denote metallic tubules and the small dots describe semiconducting tubules. The reason of different electrical properties of nanotubes described with (n, m) pairs will be explained in section 3.4.

Corresponding to selected and representative (n, m) pairs, listed values in Table 3.3.1 for various parameters enumerated in Table 3.1, including the tubule diameter d_t, the highest common divisors d and d_R, the length L of the chiral vector $\mathbf{C}_h$ in units of a (where a is the length of the 2D lattice vector), the length of the 1D translation vector $\mathbf{T}$ of the tubule in units of a, and the number of carbon hexagons per 1D tubule unit N.

Table 3.1: Parameters of carbon nanotubes Ref. [96]

Symbol	Name	Formula	Value
a_{C-C}	carbon-carbon distance		1.421Å graphite
a	length of unit vector	$\sqrt{3}a_{C-C}$	2.46 Å
$\mathbf{a}_1$,$\mathbf{a}_2$	unit vectors	$\left(\frac{\sqrt{3}}{2}, \frac{1}{2}\right) a, \left(\frac{\sqrt{3}}{2}, -\frac{1}{2}\right) a$	in (x, y) coordinates
$\mathbf{b}_1$,$\mathbf{b}_2$	reciprocal lattice vectors	$\left(\frac{1}{\sqrt{3}}, 1\right) \frac{2\pi}{a}, \left(\frac{1}{\sqrt{3}}, -1\right) \frac{2\pi}{a}$	in (x, y) coordinates
$\mathbf{C}_h$	chiral vector	$\mathbf{C}_\mathrm{h} = \mathrm{n}\mathbf{a}_1 + \mathrm{m}\mathbf{a}_2 \equiv (\mathrm{n}, \mathrm{m})$	n, m : integers
L	circumference of nanotube	$L = \lvert\mathbf{C}_\mathrm{h}\rvert = \mathrm{a}\sqrt{\mathrm{n}^2 + \mathrm{m}^2 + \mathrm{nm}}$	$0 \leq \lvert m\rvert \leq n$
d_t	diameter of nanotube	$d_t = \frac{L}{\pi} = \frac{\sqrt{n^2+m^2+nm}}{\pi} a$	
θ	chiral angle	$\sin\theta = \frac{\sqrt{3}m}{2\sqrt{n^2+m^2+nm}}$ $\cos\theta = \frac{2n+m}{2\sqrt{n^2+m^2+nm}}$ $\tan\theta = \frac{\sqrt{3}m}{2n+m}$	$0 \leq \lvert\theta\rvert \leq 30^o$
d	the highest common divisor of (n, m)		
d_R	the highest common divisor of $(2n + m, 2m + n)$	$d_R = \begin{cases} d, & \text{if } n-m \text{ not a multiple of } 3d \\ 3d, & \text{if } n-m \text{ a multiple of } 3d. \end{cases}$	
$\mathbf{T}$	translational vector of 1D unit cell	$\mathbf{T} = \mathrm{t}_1\mathbf{a}_1 + \mathrm{t}_2\mathbf{a}_2 \equiv (\mathrm{t}_1, \mathrm{t}_2)$ $t_1 = \frac{2m+n}{d_R}$ $t_2 = -\frac{2n+m}{d_R}$	t_1, t_2: integers
T	length of $\mathbf{T}$	$T = \frac{\sqrt{3}L}{d_R}$	
N	number of hexagons per 1D unit cell	$N = \frac{2(n^2+m^2+nm)}{d_R}$	$2N \equiv n_C/unit-cell$
$\mathbf{R}$	symmetry vector	$\mathbf{R} = \mathrm{p}\mathbf{a}_1 + \mathrm{q}\mathbf{a}_2 \equiv (\mathrm{p}, \mathrm{q})$ $d = mp - nq$, $0 \leq p \leq n/d$, $0 \leq q \leq m/d$	p, q: integers
M	number of 2π revolutions	$M = [(2n + m)p + (2m + n)q]R$ $N\mathbf{R} = \mathrm{M}\mathbf{C}_\mathrm{h} + \mathrm{d}\mathbf{T}$	M: integer
R	basic symmetry operation	$R =< \psi\lvert\tau >$	
ψ	rotation operation	$\psi = 2\pi\frac{M}{N}, \left(\chi = \frac{\psi L}{2\pi}\right)$	ψ: radians
τ	translation operation	$\tau = \frac{d\mathbf{T}}{N}$	τ, χ: length

Table 3.2: Values for characterization parameters for selected carbon nanotubes labelled by (n, m) Ref. [96]

(n,m)	d	d_R	d_t(Å)	L/a	T/a	N	$\psi/2\pi$	τ/a	M
(5,5)	5	15	6.78	$\sqrt{75}$	1	10	1/10	1/2	1
(9,0)	9	9	7.05	9	$\sqrt{3}$	18	1/18	$\sqrt{3}/2$	1
(6,5)	1	1	7.47	$\sqrt{91}$	$\sqrt{273}$	182	149/182	$\sqrt{3/364}$	149
(7,4)	1	3	7.55	$\sqrt{93}$	$\sqrt{31}$	62	17/62	$1/\sqrt{124}$	17
(8,3)	1	1	7.72	$\sqrt{97}$	$\sqrt{291}$	194	71/194	$\sqrt{3/388}$	71
(10,0)	10	10	7.83	10	$\sqrt{3}$	20	1/20	$\sqrt{3}/2$	1
(6,6)	6	18	8.14	$\sqrt{108}$	1	12	1/12	1/2	1
(10,5)	5	5	10.36	$\sqrt{175}$	$\sqrt{21}$	70	1/14	$\sqrt{3/28}$	5
(20,5)	5	15	17.95	$\sqrt{525}$	$\sqrt{7}$	70	3/70	$1/\sqrt{28}$	3
(30,15)	15	15	31.09	$\sqrt{1575}$	$\sqrt{21}$	210	1/42	$\sqrt{3/28}$	5
.	.	.	.	.	.	.	.	.	.
.	.	.	.	.	.	.	.	.	.
.	.	.	.	.	.	.	.	.	.
(n,n)	n	$3n$	$\sqrt{3}na/\pi$	$\sqrt{3}n$	1	$2n$	$1/2n$	1/2	1
(n,0)	n	n	na/π	n	$\sqrt{3}$	$2n$	$1/2n$	$\sqrt{3}/2$	1

3.3.1.1 Symmetry of Carbon Nanotubes

The symmetry groups for carbon nanotubes can be either symmorphic [such as armchair (n, n) and zigzag $(n, 0)$ tubules], where the translational and rotational symmetry operations can each be executed independently, or the symmetry group can be non-symmorphic (for a general nanotube), where the basic symmetry operations require both a rotation ψ and translation τ and is written as $R =< \psi|\tau >$[97]. Here the symmorphic case in some detail and refer the reader to the paper by Euklund *et. al.* [98]

The symmetry operations of the infinitely long armchair tubule ($n = m$), or zigzag tubule ($m = 0$), are described by the symmetry groups D_{nh} or D_{nd} for even or odd n[99]. Character tables for the D_n groups are given in figure 3.3 (for odd $n = 2j + 1$) and in figure 3.4 (for even $n = 2j$), where j is n integer.

Table 3.3: Character table for group $D_{(2j+1)}$. Ref. [96]

$\Re$	E	$2C_{\phi_j{}^1}$	$2C_{\phi_j{}^2}$	...	$2C_{\phi_j{}^j}$	$(2j+1)C_2'$
A_1	1	1	1	...	1	1
A_2	1	1	1	...	1	-1
E_1	2	$2cos\phi_j$	$2cos2\phi_j$	...	$2cosj\phi_j$	0
E_2	2	$2cos2\phi_j$	$2cos4\phi_j$	...	$2cos2j\phi_j$	0
.	.	.	.	.	.	.
.	.	.	.	.	.	.
.	.	.	.	.	.	.
E_j	2	$2cosj\phi_j$	$2cos2j\phi_j$	...	$2cosj^2\phi_j$	0

Useful basis functions are listed in figure 3.5 for both symmorphic groups (D_{2j} and D_{2j+1}) and non-symmorphic groups $C_{N/\Omega}$[98].

Table 3.4: Character table for group $D_{(2j+1)}$. Ref. [96]

$\Re$	E	C_2	$2C_{\phi_j{}^1}$	$2C_{\phi_j{}^2}$	...	$2C_{\phi_j{}^{j-1}}$	$(2j)C_2'$	$(2j)C_2''$
A_1	1	1	1	1	...	1	1	1
A_2	1	1	1	1	...	1	-1	-1
B_1	1	-1	1	1	...	1	1	-1
B_2	1	-1	1	1	...	1	-1	1
E_1	2	-2	$2cos\phi_j$	$2cos2\phi_j$	...	$2cos(j-1)\phi_j$	0	0
E_2	2	2	$2cos2\phi_j$	$2cos4\phi_j$	...	$2cos2(j-1)\phi_j$	0	0
.	.	.	.	.	.	.	.	.
.	.	.	.	.	.	.	.	.
.	.	.	.	.	.	.	.	.
E_{j-1}	2	$(-1)^{j-1}2$	$2cos(j-1)\phi_j$	$2cos2(j-1)\phi_j$	...	$2cos(j-1)^2\phi_j$	0	0

The symmetry group for the chiral tubules are Abelian groups. The corresponding space groups are non-symmorphic and the basis symmetry operations $R =< \psi|\tau >$ require translations τ in addition to the rotations ψ. The irreducible representations for all Abelian groups have phase factor ϵ, consistent with the requirement that all h symmetry elements of the symmetry group commute.

To find the symmetry operations for the Abelian group for a carbon nanotube specified by the (n, m) integer pair, we introduce the basic symmetry vector $\mathbf{R} = \mathrm{p}\mathbf{a}_1 + \mathrm{q}\mathbf{a}_2$, shown in Figure 3.5, which has a very important physical meaning. The projection of $\mathbf{R}$ on the $\mathbf{C}_h$ axis specifies by the angle of rotation ψ in the basic symmetry operation $R =< \psi|\tau >$, while the projection of $\mathbf{R}$ and $\mathbf{T}$ axis specifies the translation τ. In Figure 3.5 the rotation angle ψ is shown as $\chi = \psi L/2\pi$. If we translate $\mathbf{R}$ by (N/d) times, we reach a lattice point B'' (see Figure 3.5). This leads to the relation $N\mathbf{R} = \mathrm{M}\mathbf{C}_\mathrm{h} + \mathrm{d}\mathbf{T}$ where the integer M

Table 3.5: Basis functions for groups $D_{(2j)}$ and $D_{(2j+1)}$. Ref. [96]

Basis function		D_{2j}	D_{2j+1}	$C_{N/\Omega}$
(x^2+y^2, z^2)		A_1	A_1	A
	z	A_2	A_1	A
	R_z	A_2	A_2	A
(xz, yz)	(x, y)	E_1	E_1	E_1
(xz, yz)	(R_x, R_y)	E_1	E_1	E_1
(x^2-y^2, xy)		E_2	E_2	E_2
		.	.	.
		.	.	.
		.	.	.

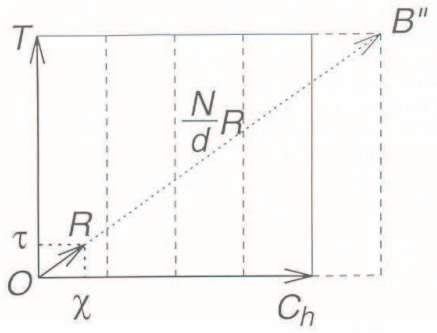

Figure 3.5: The relation between the fundamental symmetry vector $\mathbf{R} = \mathrm{p}\mathbf{a}_1 + \mathrm{q}\mathbf{a}_2$ and the two vectors of the tubule unit cell for a carbon nanotube specified by (n, m) which, in turn, determine the chiral vector $\mathbf{C}_h$ and the translation vector $\mathbf{T}$. The projection of $\mathbf{R}$ on the $\mathbf{C}_h$ and $\mathbf{T}$ axes, respectively, yield ψ (or χ) and τ. After (N/d) translations, $\mathbf{R}$ reaches a lattice point B''. The dashed vertical lines denote normals to the vector $\mathbf{C}_h$ at distances of $L/d, 2L/d, 3L/d, ..., L$ from the origin. Ref. [96]

is interpreted as the integral number of 2π cycles of rotation which occur after N rotations of ψ. Explicit relations for $\mathbf{R}$, ψ, and τ are contained in Table 3.1. If d is the largest common divisor of (n, m) is an integer greater than 1, than (N/d) translations of $\mathbf{R}$ will translate the origin O to a lattice point B'', and the projection $(N/d)\mathbf{R}.\mathbf{T} = \mathrm{T}^2$. The total rotation angle ψ then becomes $2\pi(M/d)$ when $(N/d)\mathbf{R}$ reaches a lattice point B''. Listed in Table 3.3.1 are values for several representative carbon nanotubes for the rotation angle ψ in units of 2π, and the translation length τ in units of lattice constant a for the graphene layer, as well as values for M.

3.4 Electronic Structures of Carbon Nanotubes

The electronic structure of carbon nanotubes can be deduced by mapping the band structure of graphene in a 2D hexagonal lattice onto a cylinder. Basically, one takes the dispersion relation for graphene and imposes it with periodic boundary conditions in one direction. Out of this grows a band structure that is semiconducting or metallic depending on the direction and size of the boundary condition. Thus to find the band structure of carbon nanotubes the first step is to find the band structure of graphene.

Carbon atom has six electrons around it which occupy the $1s^2$, $2s^2$ and $2p^2$ orbitals respectively. The $1s^2$ core electrons are tightly bound to the atom while the four $2s^2$ and $2p^2$ valence electrons are more weakly bound. In the crystalline phase these valence electrons give rise to the $2s$, $2p_x$, $2p_y$ and $2p_z$ orbitals. Because of the little energy difference between the $2s$ and the $2p$ orbitals a mixing of these will take place, this mixing is called hybridization. When one $2s$ and two $2p$ electrons participate in the mixing it is called an sp^2 hybridization.

In graphene it is the electrons participating in the sp^2 hybridization which are responsible for the bindings to the three nearest neighbor atoms in the plane. This kind of bond is called a σ-bond. The last p_z electron then makes a π-orbital perpendicular to the plane. It is the electron in this orbital, that is responsible for the weak binding between the planes in graphite, and which is able to move around, both in and perpendicular to the graphite plane, making graphite a semimetal or a zero gap semiconductor. Now, I will focus on a single graphene sheet, thus ignoring movement perpendicular to the plane.

The hexagonal lattice of graphene is shown in Figure 3.6 where one notices that there are two atoms in every unit cell. The distance between two nearest neighbor (n.n.) atoms is $a_C = 1.42$ Å. The unit cell that is seen in the figure is defined by the unit vectors $\mathbf{a}_1$ and $\mathbf{a}_2$. In x-y-coordinates these vectors are given by

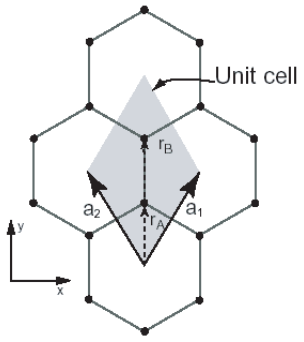

Figure 3.6: A hexagonal lattice with the lattice vectors $\mathbf{a}_1$ and $\mathbf{a}_2$, the grey area corresponds to one choice of unit cell, $\mathbf{r}_A$ and $\mathbf{r}_B$ points to the two atoms in the unit cell.

$$\mathbf{a}_1 = (\frac{a}{2}, \frac{\sqrt{3}}{2}a), \qquad \mathbf{a}_2 = (-\frac{a}{2}, \frac{\sqrt{3}}{2}a) \tag{3.1}$$

where $a = |a_1| = |a_2| = 1.42$ Å$\times\sqrt{3} = 2.46$ Å is the lattice constant.

Lets we calculate the electronic structure using the tight binding or LCAO approximation scheme. Since there is only one orbital on each atom, participating in the band structure, but two atoms in every unit cell we have that the Bloch function $\Phi_\alpha(k, r)$ can be written

$$\Phi_\alpha(k, r) = \frac{1}{\sqrt{N}} \sum_{R\epsilon G} e^{ik.R} \phi_\alpha(r - R) \tag{3.2}$$

Here $\alpha = A, B$ corresponding the A and B atoms in the unit cell (see Figure 3.6), ϕ_α is the wave function for the p_z orbitals which by the approximation is localized at the position of the α-atom, N is the number of lattice points and G is a set of vectors pointing to every lattice point in the graphene. The eigenfunctions of the electron in the solid can now be written as a linear combination of the Bloch function for the A and B atoms. So

$$\Psi_j(k, r) = \sum_{\alpha=1} 2C_{j\alpha}(k)\Phi_\alpha(k, r). \tag{3.3}$$

Putting this into the Schrödinger equation minimizing the energy by varying the coefficients and doing some algebra we get to a secular equation which is defined by

$$det[\hat{H} - E_i S] = 0 \tag{3.4}$$

Here $\hat{H}$ and S are matrices called the transfer and the integral matrix with $\hat{H}_{jj'}$ and $S_{jj'}$ as the entries. These are given by

$$\hat{H}_{jj'}(k) =< \Phi_j|H|\Phi_{j'} > \quad and \quad S_{jj'}(k) =< \Phi_j|\Phi_{j'} > \tag{3.5}$$

Eq 3.4 is of degree n and its solution gives the n different eigenvalues for $E(k)$ resulting in the dispersion relation for the n bands, where n is the number of electronic orbitals participating in the band structure in each unit cell. In graphite this number is 2 due to the two atoms participating each with one orbital. From eq 3.5 we have that

$$\begin{aligned}
\hat{H}_{AA} = \hat{H}_{BB} &= < \Phi_A|H|\Phi_A >= \frac{1}{N}\sum_{R,R'} e^{ik.(R-R')} < \phi_A(r-R')|H|\phi_A(r-R) > \\
&= \frac{1}{N}\sum_{R=R'} < \phi_A(r-R')|H|\phi_A(r-R) > \\
&+ \frac{1}{N}\sum_{R\neq R'} e^{ik.(R-R')} < \phi_A(r-R')|H|\phi_A(r-R) > \\
&= \frac{1}{N}\sum_{R=R'} \epsilon_{2p} + (terms \;\; more \;\; distant \;\; than \;\; n.n.) \approx \epsilon_{2p}
\end{aligned} \tag{3.6}$$

To deduce the last line we have used the tight binding approximation. That is the assumption that ϕ_α is localized to such a degree that the only contributions from overlapping wave functions we need to calculate is between n.n. The other matrix elements are assumed to be vanishingly small. ϵ_{2p} is the orbital energy from the $2p$ level which is not simply the energy value for the free atom since the Hamiltonian contains a crystal potential. $\hat{H}_{AA}$ is the diagonal element in the transfer matrix. The off-diagonal terms are given by

$$\begin{aligned}
\hat{H}_{AB} &= \hat{H}^*_{BA} = \frac{1}{N}\sum_{R,R'} < \phi_A(r-R')|H|\phi_B(r-R) > \\
&= \frac{1}{N}\sum_{R=R'} < \phi_A(r-R')|H|\phi_B(r-R) > \\
&+ \frac{1}{N}\sum_{R'=R+a_1} e^{-ik.a_1} < \phi_A(r-R')|H|\phi_B(r-R) > \\
&+ \frac{1}{N}\sum_{R'=R+a_2} e^{-ik.a_2} < \phi_A(r-R')|H|\phi_B(r-R) > \\
&+ (terms\ \ more\ \ distant\ \ than\ \ n.n.) \qquad (3.7)
\end{aligned}$$

Due to symmetry it is seen that $< \phi_A(r-R)|H|\phi_B(r-R) >=< \phi_A(r-(R+a_1))|H|\phi_B(r-R) >=< \phi_A(r-(R+a_2))|H|\phi_B(r-R) >$ and this will from now on be denoted γ_1. It should be noted that due to symmetry i.e., $< \phi_A(r-R)|H|\phi_B(r-R) >=< \phi_B(r-R)|H|\phi_A(r-R) > \gamma_1$ is a real number. The last term in eq 3.7 is small and with the tight binding approximation we neglect it. Using this and γ_1 we now get

$$\hat{H}_{AB} = \hat{H}^*_{BA} = \gamma_1(1 + e^{-ik.a_1} + e^{-ik.a_2}) = \gamma_1 g(k) \qquad (3.8)$$

With the use of the unit vectors a_1 and a_2 we find that

$$g(k) = 1 + e^{-i(k_x\frac{a}{2}+k_y\frac{\sqrt{3}}{2}a)} + e^{-i(-k_x\frac{a}{2}+k_y\frac{\sqrt{3}}{2}a)} = 1 + e^{-ik_y\frac{\sqrt{3}}{2}a}2\cos(\frac{k_x a}{2}) \qquad (3.9)$$

To get to the secular equation we now need to find the integral matrix S. $S_{AA} = S_{BB} = 1$ under the assumption that the wave function is normalized. The off diagonal terms in the integral matrix are calculated similar to the off diagonal terms in the transfer matrix and we get

$$S_{AB} = S^*_{BA} = \frac{1}{N}\sum_{R,R'} e^{ik.(R-R')} < \phi_A(r-R')|\phi_B(r-R) >$$

$$
\begin{aligned}
&= \frac{1}{N}\sum_{R'=R+a_1} e^{-ik.a_1} < \phi_A(r-R')|\phi_B(r-R) > \\
&+ \frac{1}{N}\sum_{R'=R+a_2} e^{-ik.a_2} < \phi_A(r-R')|\phi_B(r-R) > \\
&+ \ (terms \ \ more \ \ distant \ \ than \ \ n.n.) \qquad (3.10)
\end{aligned}
$$

Again we have that $< \phi_A(r-R)|\phi_B(r-R) >=< \phi_A(r-(R+a_1))|\phi_B(r-R) >=< \phi_A(r-(R+a_2))|\phi_B(r-R) >$. These quantities will from now on be denoted by γ_0. By neglecting the last term in eq 3.10 we get

$$S_{AB} = S^*_{BA} = \gamma_0 f(k) \qquad (3.11)$$

Having calculated all the matrix elements we can now write the transfer and integral matrix as

$$
\begin{aligned}
\hat{H} &= \begin{pmatrix} \epsilon_{2p} & \gamma_1 g(k) \\ \gamma_1 g^*(k) & \epsilon_{2p} \end{pmatrix} \qquad (3.12) \\
S &= \begin{pmatrix} 1 & \gamma_0 g(k) \\ \gamma_0 g^*(k) & 1 \end{pmatrix}
\end{aligned}
$$

This gives us the secular equation for graphite which is

$$\det[\hat{H} - E_i S] = \det \begin{bmatrix} \epsilon_{2p} - E_i & (\gamma_1 - E_i\gamma_0)g(k) \\ (\gamma_1 - E_i\gamma_0)g^*(k) & \epsilon_{2p} - E_i \end{bmatrix} = 0 \qquad (3.13)$$

To find the dispersion relation is now a matter of doing a simple calculation where we get

$$E_i(k) = \frac{\epsilon_{2p} \pm |g(k)|\gamma_1}{1 \pm |g(k)|\gamma_0} \qquad (3.14)$$

Here $|g(k)|$ is given by

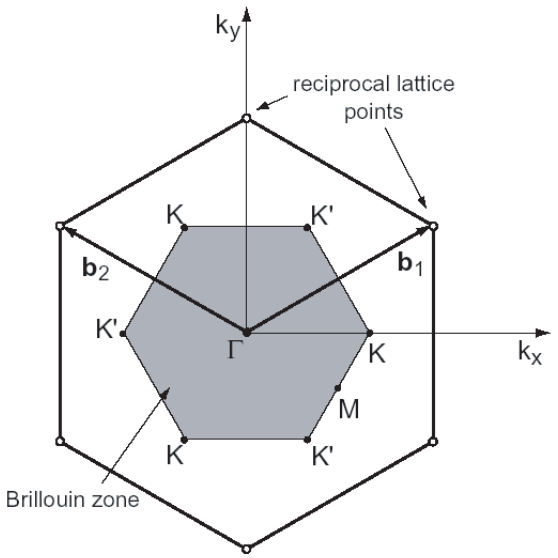

Figure 3.7: The figure shows the reciprocal lattice point and the Brillouin zone for graphene, with its high symmetry points. K and K' are the points where the π and π^* dispersion bands is touching each other. The three K points are equivalent since they are connected by the reciprocal lattice vectors $\mathbf{b}_1$ and $\mathbf{b}_2$. Since the points K and K' cannot be connected by the reciprocal lattice vectors these point are not equivalent.

$$|g(k)| = \sqrt{1 + 4\cos(\frac{\sqrt{3}k_y a}{2})\cos(\frac{k_x a}{2}) + 4\cos^2(\frac{k_x a}{2})} \tag{3.15}$$

The Brillouin zone of two-dimensional graphite is shown as the shaded area in Figure 3.7 where Γ, K, K', and M represent points of high symmetry. The reciprocal unit vectors are given by

$$b_1 = (\frac{2\pi}{a}, \frac{2\pi}{\sqrt{3}a}), b_2 = (-\frac{2\pi}{a}, \frac{2\pi}{\sqrt{3}a}). \tag{3.16}$$

In Figure 3.8, the energy dispersion relation of a graphene sheet is drawn with the help of eq 3.14 where we have chosen our energy level such that $\epsilon_{2p} = 0$ and the parameters used for γ_0 and γ_1 are given by $\gamma_0 = 0.129$ eV and $\gamma_1 = -3.033$ eV [100]. The curve in Figure 3.8(b) is a slice of Figure 3.8(a) between the symmetry point. The upper half of the energy dispersion relation curves is called π^* or the

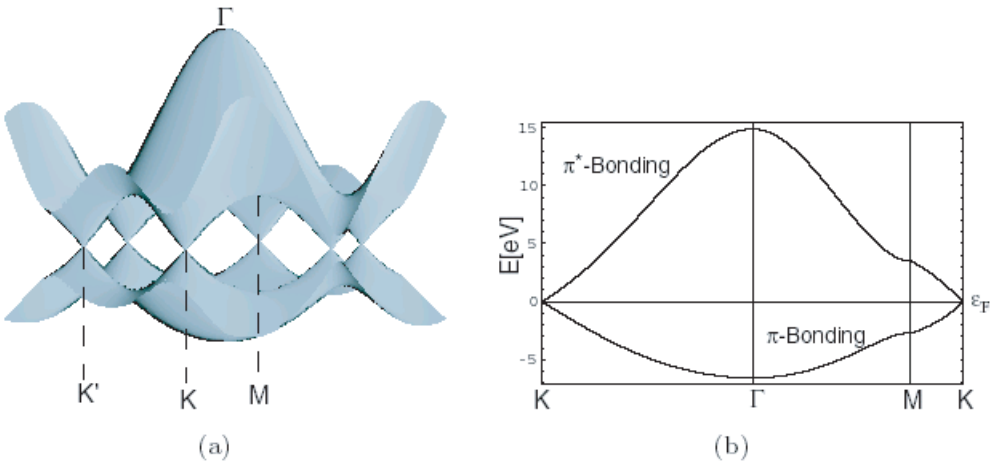

Figure 3.8: (a) Shows the dispersion relation for graphene, called the tent dispersion. The points Γ, K, K', M is high symmetry points and their placement in the Brillouin zone can be seen in Figure 3.7, (b) is appeared by cutting (a) in straight lines between the points $K \rightarrow \Gamma \rightarrow M \rightarrow K$

anti bonding band and π is then the bonding band. It is seen that the two bands are degenerated at the K and K_0 points where they attain the same value. This is also the energy of the Fermi energy ε_F. We have two atoms per unit cell and therefore two π electrons per unit cell so the electrons fully occupy the lower π band leaving the π^* anti-bonding band empty. A density of states calculation shows that the density of states at the Fermi surface is zero making graphite a zero-gap semiconductor or a semi-metal. When the overlapping integral γ_0 becomes zero the dispersion relation eq 3.14 simplifies to

$$E_i(k) = \pm\gamma_1|g(k)| = \pm\gamma_1\sqrt{1 + 4\cos(\frac{\sqrt{3}k_y a}{2})\cos(\frac{k_x a}{2}) + 4\cos^2(\frac{k_x a}{2})} \qquad (3.17)$$

This approximation is called the Slater-Koster scheme and is used as a simple approximation for the electronic structure of graphene.

3.4.1 Band structure of carbon nanotubes

From the electronic structure of graphene the electronic structure of a carbon nanotube can be found by imposing the geometrical constrains from the nanotube on the band structure of graphene. It will be shown that armchair tubes are always metallic while zigzag and chiral tubes can be either metallic or semiconducting depending on the geometry.

3.4.1.1 Dispersion Relation of carbon nanotubes

From the translation and chiral vectors we can find the reciprocal lattice vectors. Since there are 2N atoms in the unit cell this should lead to N pairs of π-bonding and π^*-antibonding bands. The reciprocal lattice vectors K_1 and K_2 for a carbon nanotube are defined by the following relations

$$\begin{aligned} \mathbf{C}_\mathrm{h}.\mathbf{K}_1 &= 2\pi \qquad \mathbf{C}_\mathrm{h}.\mathbf{K}_2 = 0 \\ \mathbf{T}.\mathbf{K}_1 &= 0 \qquad \mathbf{T}.\mathbf{K}_2 = 2\pi \end{aligned} \tag{3.18}$$

With the use of this equation,

$$\mathbf{K}_1 = \frac{1}{N}(-t_2\mathbf{b}_1 + t_1\mathbf{b}_2), \quad \mathbf{K}_2 = \frac{1}{N}(m\mathbf{b}_1 - n\mathbf{b}_2) \tag{3.19}$$

where $\mathbf{b}_1$ and $\mathbf{b}_2$ are the reciprocal lattice vector for graphite and $t_1 = \frac{2m+n}{d_R}$ and $t_2 = -\frac{2n+m}{d_R}$. Under the periodic boundary conditions the only allowed wavevector components in the circumferential direction are those that obey $\mathbf{k}.\mathbf{C}_h = l2\pi$, where l is an integer. The vectors that fulfill this requirement are those whose circumferential component is a multiple of $\mathbf{K}_1$. The number of allowed wave vectors in the circumferential direction ends up being N since $N.\mathbf{K}_1 = -\mathrm{t}_2\mathbf{b}_1 + \mathrm{t}_1\mathbf{b}_2$ is a reciprocal lattice vector for graphene. Under the assumption of an infinite long nanotube there are no boundary for the wave vectors along the tube and all states in this direction are allowed. Although we still have

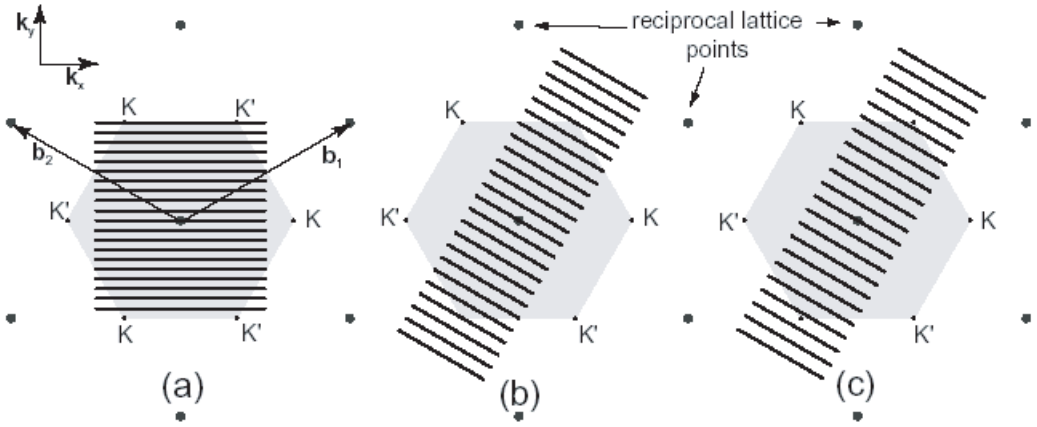

Figure 3.9: An illustration of three Brillouin zones of graphene (gray areas) mutual displaced for clearance. The black lines shows allowed wave vectors for three different kinds of tubes (in all the cases some of the lines have been translated with reciprocal lattice vectors making them as close to symmetrical around Γ as possible). (a) shows the allowed states for a (10,10) tube. It can be seen that it is metallic since one of the lines go through the K and K' points. (b) shows the allowed states for a (12,0) tube which is also metallic. (c) is the same figure for a (11,0) tube and it can be seen that it is semiconducting since none of the lines go through the K and K' points.

that the nanotube is invariant under a translation of T and so we must have that $\frac{2\pi}{|T|}$ is the length of the Brillouin zone along the tube. In the circumferential direction the diameter is $\mathbf{C}_\mathrm{h}$ giving the Brillouin zone in this direction a length of $\frac{2\pi}{|\mathbf{C}_\mathrm{h}|}$ but since the lattice in this direction is only repeated once, i.e., once around the tube, there is only one state in this direction, making the nanotubes Brillouin zone essentially one dimensional. In Figure 3.9 the allowed states for an electron in a nanotube are indicated by the black lines on a background of the reciprocal lattice of graphene where the light-grey hexagon indicate the first Brillouin zone of a graphene sheets.

The dispersion relation can now be found by slicing the dispersion relation for graphene (Figure 3.8) along the lines with allowed wave vectors that are seen as black lines in Figure 3.9. These black lines indicating the allowed states are defined by

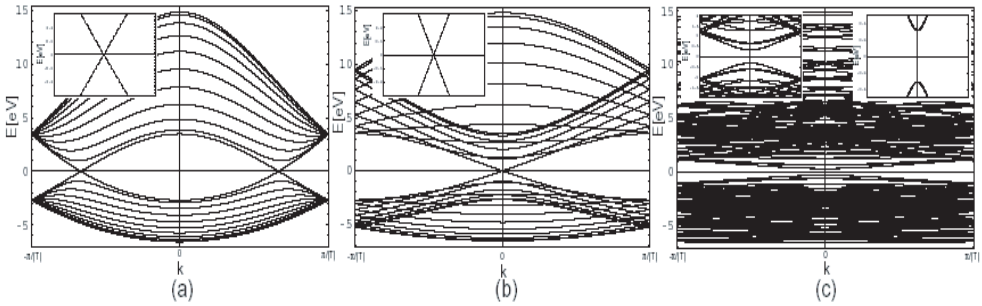

Figure 3.10: Band diagram of dispersion relation for three different tubes (a) is a metallic (10,10) tube, the inset is zoom-in of the bands touching the Fermi surfaces $-0.95 < k < 0.75$. (b) is a metallic (15,0) tube the inset is again a zoom-in around $k = 0$. (c) is semiconducting (12,8) tube. Due to the huge unit cell there are a lot of bands. Left inset is energy zoom-in where k is in the same range as in the big plot. The right inset is a zoom-in energy and around k=0 showing the band gap.(Reproduced from Ref. [101])

$$\mathbf{k} = \mathrm{l}_1\mathbf{K}_1 + \mathrm{l}_2\frac{\mathbf{K}_2}{|\mathbf{K}_2|} \quad \text{where} \quad -\frac{\pi}{|\mathbf{T}|} \leq \mathrm{l}_2 \leq \frac{\pi}{|\mathbf{T}|}, \quad \mathrm{l}_1 = 0, 1, ..., \mathrm{N} - 1. \tag{3.20}$$

If one of these slices happens to cut through the K point the nanotube will be metallic and if the slice does not cut through a K point it will be semiconducting.

It can be seen that $K = \frac{1}{3}(b_1 - b_2)$. A necessary condition for a metallic tube is then that there exists a pair l_1, l_2 such that $k = K$. With a little algebra this turns out to be equivalent to

$$\frac{n-m}{3} = l_1 \tag{3.21}$$

Since l_1 is an integer the condition for a metallic nanotube is that $n - m$ is a multiple of 3. The condition for $k = K_0$ turns out to be precisely the same. In the case of a metallic tube we therefore have two bands touching each other at two points as seen on the dispersion relation in Figure 3.10(a) (in Figure 3.10(b) the band touching the Fermi surface($\varepsilon_F = 0$) is degenerated)[101]. This results in two conduction channels giving the nanotube a conductance of $4e^2/h$ where

$2e^2/h$ is the quantum of conductance. For all other choices of (n, m) the tube will be semiconducting with a band gap and it can be shown that this band gap is inversely proportional to the diameter. This is due to the fact that the band gap is determined by the distance between the allowed states indicated by the black lines in Figure 3.9 and the K, K' points. As the diameter is increased the distance between the black lines are diminished and this implies that the distance between these states and the K points must also be smaller.

Band calculations of SWNTs were initially performed by using a one–band π–orbital tight binding model.[114] Subsequently, experimental data [11, 15, 115, 116] on the band gaps were extrapolated to confirm the inverse proportionality with the radius of the nanotube.[117] Later, first principles calculation [118] within Local Density Approximation (LDA) showed that the σ^*–π^* hybridization becomes significant at small R (or at high curvature). Recent analytical studies[119, 120, 121] showed the importance of curvature effects in carbon nanotubes. Nonetheless, band calculations performed by using different methods have been at variance on the values of the band gap. Extensive theoretical analysis of the band structure of SWNTs together with the curvature effects on geometric and electronic structure has been carried out recently [105] by using first-principles pseudopotential planewave method[81] calculations within the Generalized Gradient Approximation[122] (GGA).

The inset to Fig. 3.11 shows a schematic side view of a zigzag SWNT which indicates two types of C–C bonds (d_1 and d_2) and C–C–C bond angles (Θ_1 and Θ_2). The variations of the normalized bond lengths (*i.e.* d_1/d_0 and d_2/d_0 where d_0 is the optimized C–C bond length in graphene) and the bond angles with tube radius R (or n) are shown in Fig. 3.11a and 3.11b, respectively. Both the bond lengths and the bond angles display a monotonic variation and approach the graphene values as the radius increases. As pointed out earlier for the armchair SWNTs [123], the curvature effects, however, become significant at small radii. The zigzag bond angle (θ_1) decreases with decreasing radius. It is about 12^o less than 120^o for the $(4, 0)$ SWNT, while the length of the corresponding zigzag bonds (d_2) increases with decreasing R and the length of the parallel bond (d_1) decreases to a lesser extent with decreasing R. The angle involving this latter

bond (θ_2) is almost constant.

An internal strain is implemented upon the formation of tubular structure from the graphene sheet. The associated strain energy, which is specified as the curvature energy, E_{cur}, is calculated (Ref. [105]) as the difference of total energy per carbon atom between the bare SWNT and the graphene (*i.e.* $E_{cur} = E_{T,SWNT} - E_{T,graphene}$) for $4 \leq n \leq 15$. The calculated curvature energies are shown in Fig. 3.11c. As expected E_{cur} is positive and increases with increasing curvature. The cohesive energy of SWNTs are also curvature dependent, and are calculated from the expression $E_{coh} = E_T[C] - E_T[SWNT]$ in terms of the total energy of free carbon atom, and total energy of SWNT per carbon atom. For a zigzag tube, it is small for small n and increases with n, and eventually saturates to the cohesive energy of graphene. Similar trends also exist for the armchair tubes. In classical theory of elasticity the curvature energy is given by the following expression [124, 125, 126] $E_{cur} = \alpha/R^2$, where $\alpha = Yt^3\Omega/24$. Here Y is the Young's modulus, t is the thickness of the tube, and Ω is the atomic volume. Interestingly, curvature energies obtained from first-principles calculations yield a perfect fit to the relation α/R^2 as seen in Fig. 3.11c. In this fit α is found to be 2.14 eV Å^2/atom, using the value of Y and an appropriate choice of t.[105]

According to the zone folding scheme a (n, m) SWNT has been predicted to be metallic when $n - m = 3 \times integer$, since the double degenerate π and π^* states, which overlap at the K–point of the hexagonal Brillouin zone (BZ) of graphene folds to the Γ point of the tube [114, 129]. Thus, to the first order all (n, n) armchair tubes are metallic, but $(n, 0)$ zigzag tubes becomes metallic when n is multiples of 3. In Fig. 3.4, a map of chiral vector specified by (n, m) indices indicate whether a SWNT is a semiconductor or metal. This simple picture provides a qualitative understanding, but fails to describe some important features, in particular for small radius or *metallic* nanotubes. SWNTs specified by "C" in Fig. 3.4 form a subgroup of semiconducting tubes, which have a small band gap induced by the curvature. This situation is clearly shown in Table 3.6, where the band gaps E_g of $(n, 0)$ SWNTs calculated by different methods are compared.

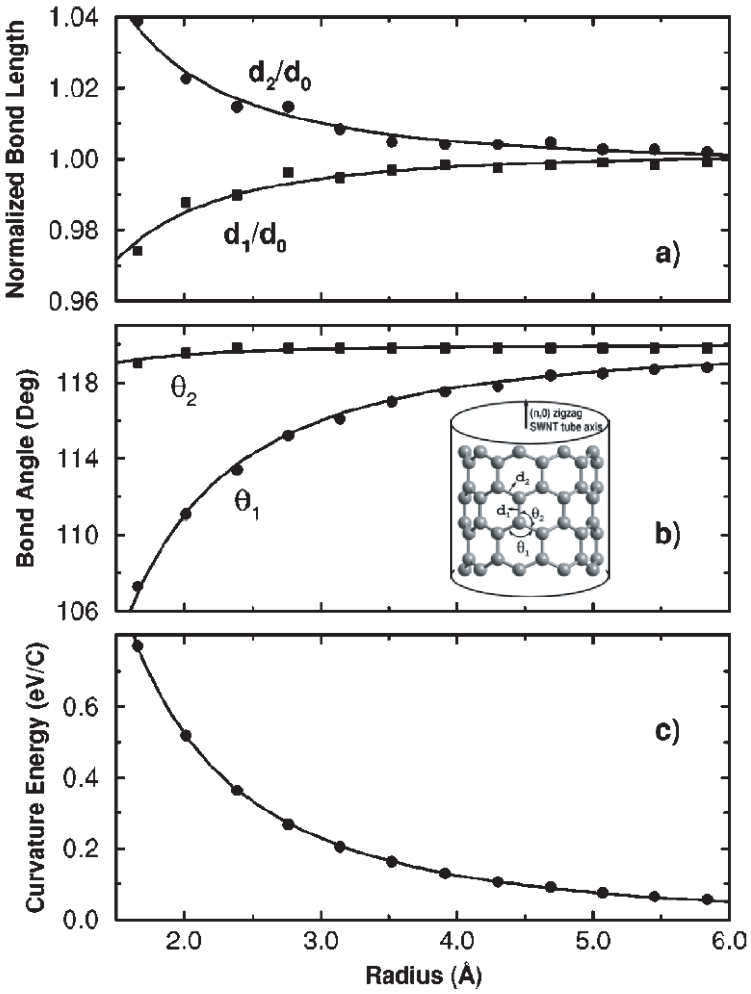

Figure 3.11: Inset: A schematic side view of a zigzag SWNT, indicating two types of C–C bonds and C–C–C bond angles. These are labelled as d_1, d_2, θ_1 and θ_2. (a) Normalized bond lengths (d_1/d_0 and d_2/d_0) versus the tube radius R. ($d_0 = 1.41$ Å). (b) The bond angles (θ_1 and θ_2) versus R. (c) The curvature energy, E_{cur} per carbon atom with respect to graphene as a function of tube radius. The solid lines are the fit to the data as α/R^2. (Reproduced from Ref. [105])

Table 3.6: Band gap, E_g, as a function of radius R of (n,0) zigzag nanotubes. M denotes the metallic state. First row values were obtained within GGA in Ref. [105] Second and third rows from Ref. [118] are LDA results, while all the rest are tight-binding (TB) results. Two rows of Ref. [128] are for two different TB parametrizations.

n	4	5	6	7	8	9	10	11	12	13	14	15
R (Å)	1.66	2.02	2.39	2.76	3.14	3.52	3.91	4.30	4.69	5.07	5.45	5.84
Ref. [105]	M	M	M	0.243	0.643	0.093	0.764	0.939	0.078	0.625	0.736	0.028
Ref. [118]			M	0.09	0.62	0.17						
Ref. [118]			0.05	1.04	1.19	0.07						
Ref. [114]			0.21	1.0	1.22	0.045	0.86	0.89	0.008	0.697	0.7	0.0
Ref. [128]				0.79	1.12		0.65	0.80				
Ref. [128]				1.11	1.33		0.87	0.96				

First-principles GGA calculations[105] resulted in small, but non-zero energy band gaps of 93, 78 and 28 meV for $(9,0)$, $(12,0)$ and $(15,0)$ SWNTs, respectively. These gaps are measured by Scanning Tunnelling Spectroscopy (STS) experiments [104] as 80, 42 and 29 meV, in the same order. Recently, Kim *et al.*[127] synthesized ultralong and high percentage of semiconducting SWNTs where another experimental evidence for the small band gap tubes has been provided. The biggest discrepancy noted in Table 3.6 is between the tight-binding and the first-principles values of the gaps for small radius tubes such as $(7,0)$. These results indicate that curvature effects are important and the simple zone folding picture has to be improved. Moreover, the analysis of the LDA bands of the $(6,0)$ SWNT calculated by Blase *et al.* [118] brought another important effect of the curvature. The antibonding singlet π^*- and σ^*- states mix and repel each other in curved graphene. As a result, the purely π^*-state of planar graphene is lowered with increasing curvature. For zigzag SWNTs, the energy of this singlet π^*–state is shifted downward with increasing curvature.

In Fig. 3.12a, the double degenerate π–states (which are the valence band edge at the Γ–point), the double degenerate π^*–states (which become the conduction band edge at Γ for large R), and the singlet π^*–state (which is in the conduction band for large R) are shown. As seen, the shift of the singlet π^*–state is curvature dependent, and below a certain radius determines the band gap. For tubes with radius greater than 3.3 Å (*i.e.* $n > 8$), the energy of the singlet π^*–state at the Γ–point of the BZ is above the doubly degenerate π^*–states (*i.e.* bottom of the conduction band), while it falls between the valence and conduction band

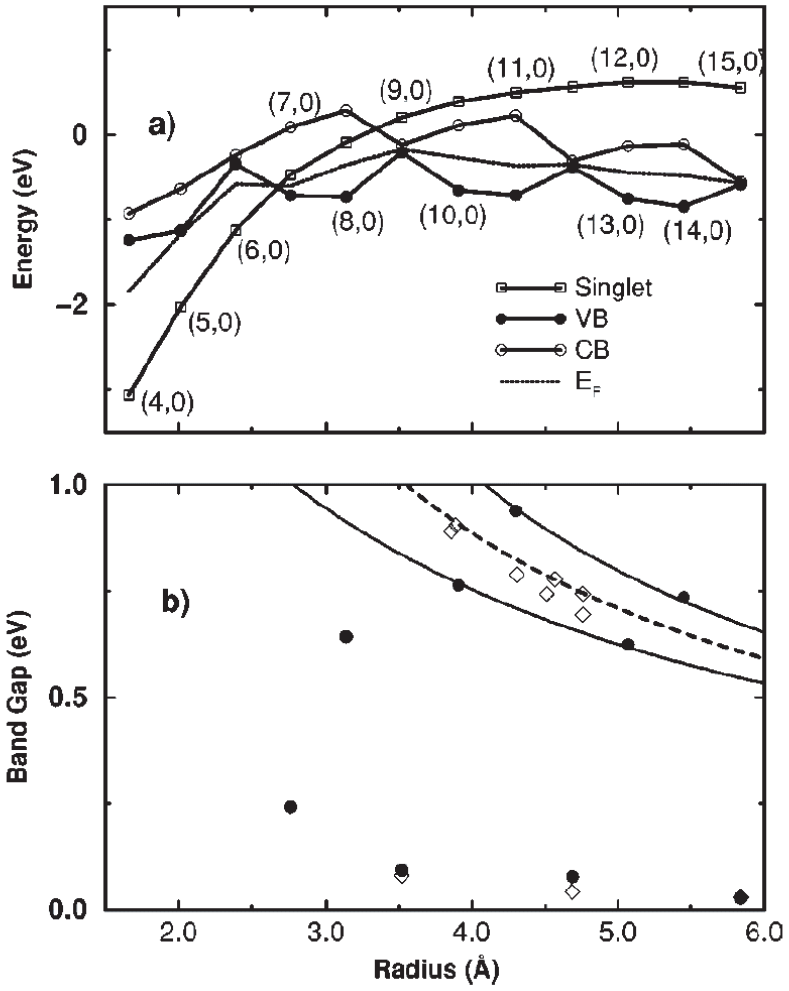

Figure 3.12: (a) Energies of the double degenerate π–states (VB), the double degenerate π^*–states (CB) and the singlet π^*–state as a function of nanotube radius. Each data point corresponds to n ranging from 4 to 15 consecutively. (b) The calculated band gaps of Ref. [105] are shown by filled symbols. Solid (dashed) lines are the plots of Eq. 3.23 (Eq. 3.22). The experimental data taken from [15, 104, 116] are shown by open diamonds. (Reproduced from Ref. [105])

edges for $n = 7, 8$, and eventually dips even below the double degenerate valence band π–states for the zigzag SWNT with radius less than 2.7 Å (*i.e.* $n < 7$). Therefore, all the zigzag tubes with radius less than 2.7 Å are metallic. For $n = 7, 8$, the edge of the conduction band is set by the singlet π^*–state, but not by the double degenerate π^*–state. The band gap derived from the zone folding scheme is reduced by the shift of this singlet π^*–state as a result of curvature induced $\sigma^* - \pi^*$ mixing. This explains why the tight-binding calculations predict band gaps around 1 eV for $n = 7, 8$ tubes, while the self-consistent calculations predict much smaller value. Based on π–orbital tight binding model, it was proposed [117] that E_g behaves as

$$E_g = \gamma_0 \frac{d_0}{R}, \tag{3.22}$$

which is independent from helicity. Within the simple π–orbital tight-binding model, γ_o is taken to be equal to the hopping matrix element $V_{pp\pi}$. d_0 is the bond length in graphene. However, as seen in Fig. 3.12b, the band gap displays a rather oscillatory behavior. The relation given in Eq. 3.22 was obtained by a second order Taylor expansion of one-electron eigenvalues of π-orbital tight-binding model [117] around the K–point of the BZ, and hence it fails to represent the effect of the helicity. By extending the Taylor expansion to the next higher order, Yorikawa and Muramatsu [128, 130] included another term in the empirical expression of the band gap variation,

$$E_g = V_{pp\pi} \frac{d_0}{R} \left[1 + (-1)^p \gamma cos(3\theta) \frac{d_0}{R} \right], \tag{3.23}$$

which depends on the chiral angle, θ, as well as an index p. Here γ is a constant and the index p is defined as the integer from $k = n - 2m = 3q + p$. The factor $(-1)^p$ comes from the fact that the allowed $\mathbf{k}$ is nearest to either the K- or $K^{'}$-point of the hexagonal Brillouin zone. For zigzag nanotubes $\theta = 0$, and hence the solid lines in Fig. 3.12b are fits to the empirical expression, $E_g = V_{pp\pi} d_0/R \pm V_{pp\pi} \gamma d_0^2/R^2$, obtained from Eq. 3.23 by using the parameters $V_{pp\pi} = 2.53$ eV and $\gamma = 0.43$. The agreement between the first-principles calculations[105] and the STS data [15, 116] is very good considering the fact that there might be some uncertainties in identifying the nanotube in the experiment.

The situation displayed in Fig. 3.12 indicates that the variation of the band gap with the radius is not simply $1/R$, but additional terms incorporating the chirality dependence are required. Most importantly, the mixing of the singlet π^*–state with the singlet σ^*–state due to the curvature, and its shift towards the valence band with increasing curvature is not included in neither the π–orbital tight binding model, nor the empirical relations expressed by Eq. 3.22 and 3.23. This behavior of the singlet π^*–states is of particular importance for the applied radial deformation that modifies the curvature and in turn induces metallization [111, 131, 132] as discussed in section 6.2 and 7.2.

3.4.2 Density of States

The right figure of Fig. 3.13 schematically shows the density of states (DOS) that can be derived from the energy dispersion diagrams shown in the left figure. The linear crossing bands near the Fermi level yield a small constant DOS for the armchair nanotube. At energies away from the Fermi energy, the next subbands lead to Van Hove singularities at the onset due to the one-dimensional nature of the subbands. The energy separation between the first singularities above and below the Fermi level is here defined as ΔE_{sub}. The DOS for a semiconducting nanotube also consists of a series of sharp van Hove singularities. In this case however, there is an energy gap ΔE_{gap}.

For chiral nanotubes, the unit cell $T \times C$ is typically an order of magnitude larger than for nonchiral nanotubes. It has been argued that a large number of subbands and therefore also many singularities in the DOS may be expected [133]. However, it has been found that near the Fermi level a universal DOS exists that scales with diameter and depends, to first order, only on the metallic or semiconducting character of a nanotube [134, 135, 136]. The DOS for a chiral nanotube with the same diameter is therefore similar to that of a zigzag or an armchair nanotube. This is illustrated in Fig. 3.9. Near the Fermi point **K**, the energy dispersion is approximately radially symmetric within the k_x,k_y-plane (see Fig. 3.7). The point of closest approach from **K** to any allowed k-line (**K**1)

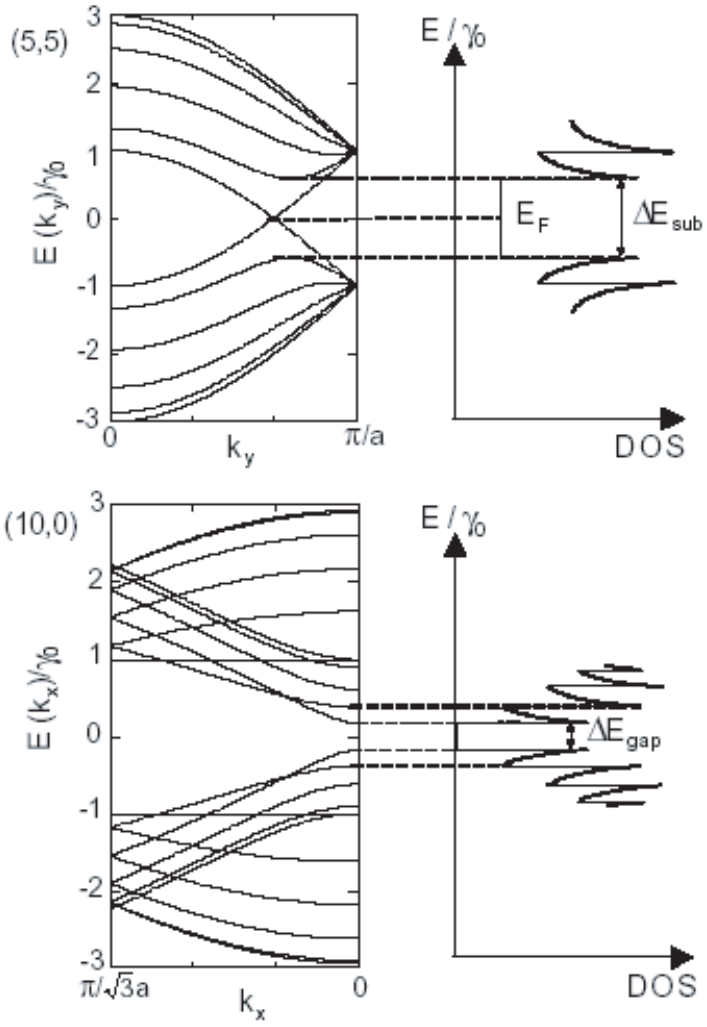

Figure 3.13: The energy band diagram (left) and density of states (right) for a metallic (top) and a semiconducting (bottom) nanotube. The energy dispersion diagrams are calculated with Eqs. (2.4) and (2.5) for a (5,5) and (10,0) nanotube respectively. The energy is divided by the energy overlap integral $\gamma_0 = 2.9$ eV. In the density of states (DOS) diagrams a series of sharp peaks appear which are the subband onsets. The energy differences between the first two singularities near the Fermi level are indicated for the metallic and the semiconducting case by ΔE_{sub} and ΔE_{gap} respectively.

yields therefore the first Van Hove singularity. The second point of closest approach (**K**2) yields the next singularity etc. A different chirality means that the allowed k-lines are rotated and oriented differently around **K**. However, due to the discreteness of the hexagonal lattice it can be found that for semiconducting nanotubes the discrete

3.5 Transport Properties of Carbon Nanotubes

I will focus on the transport properties of metallic tubes and not go into the area of semiconducting tubes.

The insets in Figure 3.10 (a) and (b) show the dispersion relation for a zigzag and an armchair metallic nanotube around the Fermi energy[101]. It can be seen that the dispersion relation for energies right around the Fermi energy is highly linear.

To find this linear dispersion we expand the function $g(k)$ defined in eq 3.9 around **K** by writing $k = \mathbf{K} + \kappa$ using the expansion in eq 3.14, setting $E_i(k) = E_i(\mathbf{K}) + \epsilon(\kappa) = \epsilon(\kappa)$ since $E_i(\mathbf{K}) = 0$, $\gamma_0 = 0$ and as before $\epsilon_{2p} = 0$ we get

$$\epsilon(\kappa) = \pm\frac{\gamma_1 a\sqrt{3}}{2}|\kappa| \tag{3.24}$$

The signs are for the left and right moving branch of the two crossing lines seen in the insets in Figure 3.10 (a) and (b). From this we can find the Fermi velocity

$$v_F = \frac{1}{\hbar}\frac{\partial\epsilon(\kappa)}{\partial\kappa} = \frac{\gamma_1 a\sqrt{3}}{2\hbar} = 9.81 \times 10^5 \tag{3.25}$$

It is seen that this value does not depend upon the indices (n;m) so this is the value of the Fermi velocity for all metallic carbon nanotubes.

3.5.1 Definition of the Ballistic Transport

In this section I will define what I mean by ballistic transport, since it seems that people are using it in different meanings depending on which system they are actually measuring upon. Before going into this discussion I will define the relevant lengths with the help of Datta[137].

Mean Free Path l_m

We begin by defining a collision time τ_c which is the time between two collisions changing the state of the electron. The momentum relaxation time τ_m then has a relation to the collision time τ_c with a constant α_m describing the efficiency by which each collision changes the momentum of the electron. So we have the relation

$$\frac{1}{\tau_c} \rightarrow \frac{1}{\tau_m}\alpha_m \tag{3.26}$$

By the Fermi velocity the corresponding length of the mean free path can easily be found to be $l_m = v_F\tau_m$.

Phase Relaxation Length l_ϕ

In the same way as τ_m is related to τ_c we can relate a phase relaxation time τ_ϕ to τ_c with a constant α_ϕ describing the efficiency at which each collision destroys the phase. So

$$\frac{1}{\tau_c} \rightarrow \frac{1}{\tau_\phi}\alpha_\phi \tag{3.27}$$

This scattering time can also be converted to a length that for $\tau_m \sim \tau_\phi$ is given by $l_\phi = v_F\tau_\phi$.

The effectiveness at which different collision process changes the momentum and phase is very different. Electron-electron interaction does not change the momentum of the system, since any momentum loss by one electron is picked up

by the other electron so $\alpha_m = 0$ but $\alpha \neq 0$ in this process. It can also be seen that elastic collisions with any static impurities have $\alpha_m \neq 0$ but $\alpha_\phi = 0$. So even though τ_m and τ_ϕ both have a relation to τ_c the efficiency with which a collision couples to them can be very different.

A sample of length L can be in different regimes depending on its relation to l_m and l_ϕ. Normally one defines three regimes; ballistic, diffusive and ohmic. Ohmic is where $L \gg l_m$, l_ϕ basically normal classic conductors, diffusive is where $L > l_m$ and $l_m < l_\phi$. The problem about ballistic transport is that it is in some cases used in the meaning $L < l_m$, l_ϕ and sometimes it is just $L < l_m$ with no reference to l_ϕ so we could have either $l_\phi > L$ or $l_\phi > L$ or $l_\phi > L$. I will in this thesis in most cases understand ballistic transport as the regime where $L < l_m$, l_ϕ at the times where this is not the case it will be clearly stated.

3.5.2 Phase Coherence Length

Normally a way to obtain information about the coherence length l_ϕ of a material is to evaluate the magnetoresistance in a transport experiment. But SWNTs are not expected to show any magnetic field dependence except in extremely high fields so this method cannot be used for tubes. Still some groups have managed to extract some information. Liang et. al.[138] have seen Fabry-Perot interference in a nanotube with a length of 530 nm measured at 4 K, since the electron wave is interfering with it self the coherence length must be much longer than the length of the nanotube. Actually the coherence length has to be at least three times as long as the nanotube to get any kind of interference. Liang et al. also show that the mean free path $l_m \geq 530$nm i.e., transport must be ballistic. Avouris et al.[139] have measured the phase coherence length in ropes of carbon nanotubes to be on the order of microns at temperatures around 1 K.

As long as an electron is keeping its phase it will not make spin-flips. It can, however still process around an external magnetic field, thereby changing its spin direction, but it will happen in a coherent way i.e., the polarization of the electron gas is kept. On the other hand the electrons can keep their spin even though they

are not phase coherent. It is expected that electrons in nanotubes will keep their spins over long distances since the g-factor is around 2 and there is nearly no spin-orbit coupling due to the low mass of the carbon atoms.

3.5.3 Ballistic Transport

Due to the one-dimensionality of SWNTs the branch of allowed states can be described as straight lines crossing the Fermi energy. Since a scattering electron needs to have an empty state to scatter to and there are less available states in a carbon nanotube than in a ordinary metal the amount of scattering in a carbon nanotube must be anticipated to be severely decreased. Furthermore carbon nanotubes are nearly perfect molecules so the number of impurities and lattice defects are very limited, this also helps to diminish the scattering. Theoretical calculations show that metallic tubes are unaffected by long potential scatters [13].

Experimentally there have also been a lot of groups showing evidence of long mean free paths in SWNTs. McEuen et al.[13] found that a tube with a length of 8 μm measured at low temperatures, did not contain any significant back-scatterers, the length was estimated from the charging energy in the Coulomb blockade regime.

Bachtold et al.[140] and Pablo et al.[141] have made scanned gate measurement of the intrinsic resistance in SWNTs. Batholds group measured the potential a function of length and the result is seen in Figure 3.14. The figure shows the electrostatic potential in a metallic tube. It can be seen that the potential is nearly constant which is a sign of very low intrinsic resistance, they set an upper bound on the intrinsic resistance per nanotube on $R_i = 3$ kΩ. If we imagine diffusive transport then by measuring the length of the tube we can find the resistivity and from the Drude formula thereby the momentum relaxation time τ_m.

$$\tau_m = \frac{m}{\rho n_{1D} e^2}, \rho = \frac{R_i}{L} \tag{3.28}$$

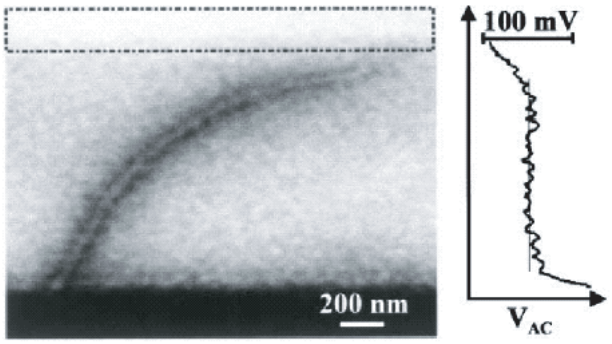

Figure 3.14: Shows the electrostatic potential through a metallic carbon nanotube measured with Electrostatic Force Microscopy (EFM). It can be seen that the potential is constant corresponding to very low intrinsic resistance indicating that the tube is ballistic. From [140].

Here m is the electron mass, e is the electron charge, L is the length of the tube and n_{1D} is the number of electron per unit length participating in the transport. To estimate this number we take the density of states at the Fermi surface which in a metallic nanotube is given by $D(\epsilon_F) = \frac{a}{2\pi^2\gamma_1 d_t}$ the units of this density is per energy per carbon atom to get a number per length out we multiply with $\frac{number\ of\ carbon\ atom}{length} = \frac{2N}{|T|}$ and make an estimate which says it is the electrons from the Fermi energy and 1 eV down that participate in the transport. This is a rough estimate and without a doubt to far down in energy but it still can give us an upper bound for the number of electrons participating. From this we get

$$\tau_m > \frac{m}{\rho e^2}\frac{|T|\pi^2\gamma_1 d_t}{aN} = 6.4 \times 10^{-12} s \tag{3.29}$$

From this a lower bound for the mean free path l_m is $l_m > v_F\tau_m = 6.3$ μm. This is longer than the nanotube which indicates that we are in the ballistic regime which at the same time invalidates the use of the Drude formula. Still the conclusion from these arguments are that the transport is ballistical which is also the conclusion Batholds group reaches with some other arguments. Both groups have made their measurement at room temperature and Bachtold et al.[140] find ballistic transport over a length > 1 μm while Pablo et al.[141] find that there is ballistic transport over a length that is at least 1.5

So metallic nanotubes are ballistic conductors with a mean free path of more than one micron. The precise length of the mean free path is very depending on surroundings, perfection of the tube and geometry such as if the tube has any kinks.

3.5.4 Spin-Flip

From the two previous sections it is clear that the amount of scatters in a carbon nanotube is really small. At low temperatures we have ballistic transport for many microns. At higher temperatures the mean free path is still very long but there has not been any evidence of room temperature coherent transport over microns in carbon nanotubes. Still it is reasonable to assume that the spin flip length is pretty long. This is because the normal scattering mechanism causing spin- ip is inelastic scattering on impurities and spin orbit coupling. In carbon nanotubes we have a very pure system so the amount of impurity is normally really low. At the same time is the carbon nuclear very light giving a small spin-orbit coupling. For the Zeeman splitting to have a significant size the applied external field has to be pretty big since carbon nanotubes have a g-factor of 2 making this spin splitting in most cases negligible.

3.5.5 Landauer-Büttiker Formalism

In a system made of two leads contacting a nanotube we must have that the total resistance is given by $R = h/4e^2 + R_i + R_{c1} + R_{c2}$ where $h/4e^2$ is the contact resistance that comes from the current going from a continuum of modes in the contacts to the four quantized modes in the tube. This resistance cannot be avoided, R_i is the intrinsic resistance of the tube and $R_{c1,c2}$ are the resistances stemming from the metal tube junction. As just mentioned many metallic nanotubes show ballistic transport meaning that $R_i = 0$ or at least very low, so most of the electrons are passing through the tube without being scattered. In these systems at low temperatures we have $L < l_m$, l_ϕ.

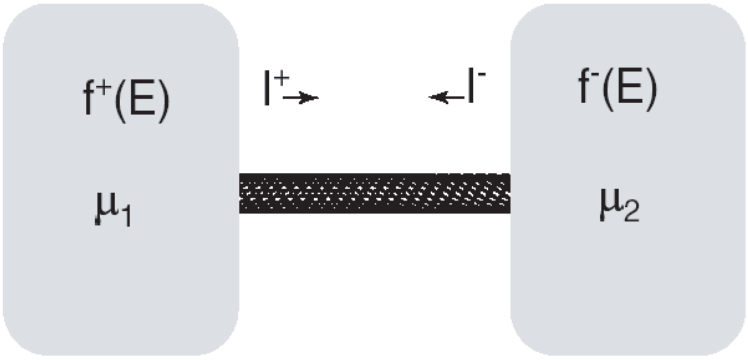

Figure 3.15: Illustrates a simple model for the system that we are looking at

Landauer-Büttiker formalism[142] can be used to describe transport in ballistic systems at low temperatures, where the conductance is taking place in a limited number of modes, such as the case is for carbon nanotubes.

So we imagine coherent electron waves moving through a system that schematically looks like the one seen in Figure 3.15. The current I in such a system must be

$$I = I^+ - I^- = 2e\frac{1}{L}\sum_{j,k}[f^+(E) - f^-(E)]v_F = \frac{4e}{2\pi}\int \frac{1}{\hbar}\frac{\partial E}{\partial k}[f^+(E) - f^-(E)] \quad (3.30)$$

Here $I^+(I^-)$ is the current from left to right (right to left), $\frac{1}{L}$ is the density of states, e the charge, 2 is for the two spin degenerated modes conducting the current in a nanotube, f^+, f^- are the occupation functions in the left and right contact respectively and the $\sum$ is over spin j and k-states. In the last equation the sum has been changed to integral $\sum_k \rightarrow \frac{L}{2\pi}\int$. Since the measurement is taking place at low temperatures we approximate the occupation functions with the step-function $\Theta^+(E - \mu_1)$ and $\Theta^-(E - \mu_2)$ and get

$$I = \frac{4e}{h}[\mu_1 - \mu_2] = \frac{4e^2}{h}\frac{\mu_1 - \mu_2}{e} = G_0\frac{\mu_1 - \mu_2}{e} \quad (3.31)$$

Here $G_0 = \frac{4e^2}{h}$ is the conductance for a lead with two modes such as a nanotube. Quantized conductance have been observed in carbon nanotubes with conductance changes of $2e^2 = h$ by de Heer et al.[103].

3.6 Modification of electronic structure with radial deformation

Modification of electronic properties of condensed systems by an applied external pressure or strain in the elastic range has been subject of active study. However, in most of the cases, the changes one can induce by the elastic deformation are minute even negligible due to the rigidity of the crystals. On the other hand, the situation is rather different for SWNTs owing to their tubular geometry.[120] Carbon nanotubes display very interesting mechanical properties. While the MWNTs show the greatest values for the Young's modulus as high as 2 TPa, SWNTs appear to be very soft in the radial direction.[143] SWNTs are highly flexible: they can sustain remarkable elastic deformations. The softness of carbon nanotubes in the radial directions has been observed experimentally by the fact that the contact area is flattened when two nanotubes are brought close to each other.[144] If R is large, a nanotube takes a flattened structure.[145] It has been argued that SWNTs show linear elasticity under hydrostatic pressure up to 1.5 GPa at room temperature.

It has been shown that the structure and the electronic properties of SWNTs undergo dramatic changes by these deformations.[110, 131, 146, 147, 280, 149, 150, 151, 152, 153, 154, 155, 156] Significant radial deformation of SWNTs can be realized in the elastic range, whereby the curvature is locally changed. This way, zones with higher and lower curvatures relative to the undeformed SWNT can be attained on the same circumference[111, 112, 157, 158, 159, 160]. Tight-binding calculations have indicated that a SWNT may undergo an insulator-metal transition under a uniaxial or torsional strain [111, 155, 156]. Multiprobe transport experiments [110] on individual SWNTs showed that the electronic structure can be modified by bending the tube, or by applying a circumferential deformation.

Empirical extended Hückel calculations [146] predicted that the conductance of an armchair SWNT can be affected by the circumferential deformations and a band gap can develop in a metallic armchair SWNT upon twisting.

A systematic analysis of the effect of the radial deformation on the electrical properties has been carried out by Gülseren *et al.*[131] using first-principles total energy and electronic structure calculations. In their study the radial deformation is generated by applying uniaxial compressive stress σ_{yy} on a narrow strip on the surface of a SWNT. In practice such a deformation can be realized by pressing the tube between two rigid and flat surfaces. As a result, the radius is squeezed in the y–direction, while it is elongated along the x–direction, and hence the circular cross section is distorted to an elliptical form with major and minor axes, a and b, respectively. A natural variable to describe the radial deformation is the magnitude of the applied strain along the two axes,

$$\epsilon_{yy} = \frac{R_0 - b}{R_0}, \tag{3.32}$$

and

$$\epsilon_{xx} = \frac{R_0 - a}{R_0} \tag{3.33}$$

where R_0 is the radius of the undeformed (zero strain) nanotube. The point group of the undeformed nanotubes is D_{nh} or D_{nd} for n even or odd, respectively. Under radial deformation described above, the point group becomes C_{2h} or D_{2h}. However, depending on the nanotube orientation around the tube axes, the in-plane mirror symmetry can be broken. For the $(6, 6)$ tube, there are several different orientations to investigate the effect of mirror symmetry on the band crossing at the Fermi level. The first-principles calculations predict that elastic radial deformation does not have a noticeable effect on the first and second nearest neighbor C–C distances but it induces significant changes in the bond angles[131]. This observation is therefore important and has to be taken into account in tight binding studies of SWNTs with radial deformation.

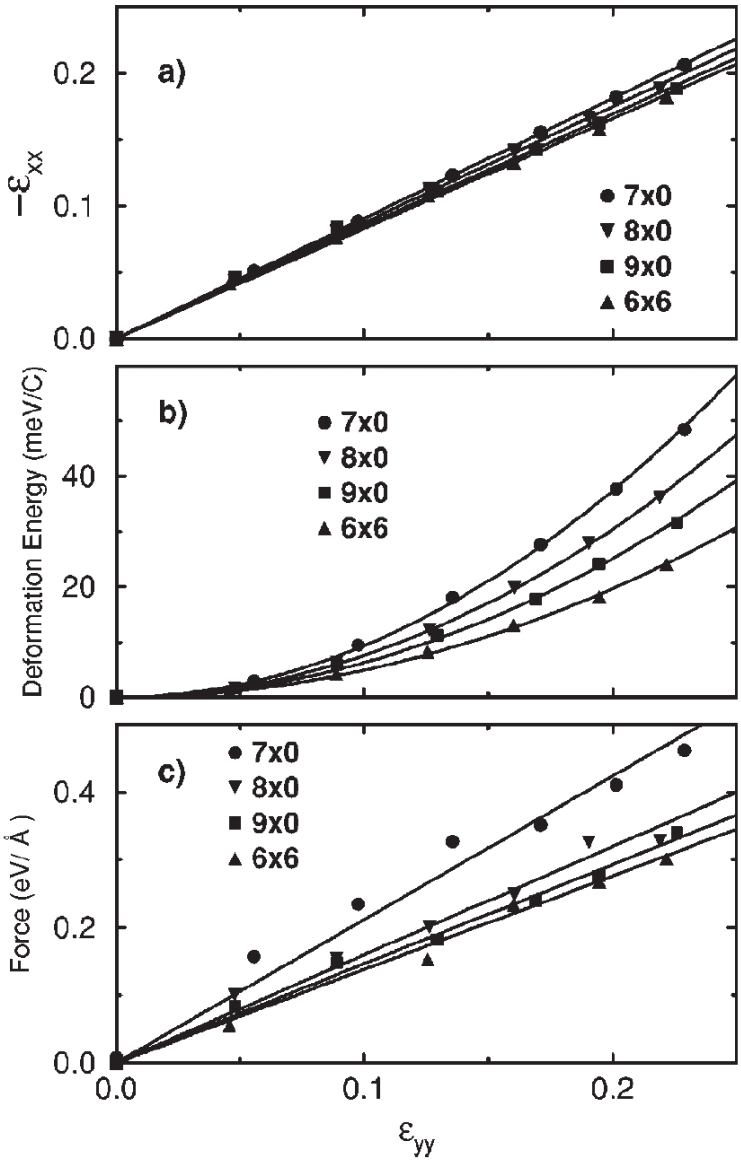

Figure 3.16: (a) The strain component $\epsilon_{xx} = (R_0 - a)/R_0$ along the major axis as a function of applied strain $\epsilon_{yy} = (R_0 - b)/R_0$ along the minor axis. The slope is the in-plane Poisson ratio, $\nu_{\|}$. (b) Variation of the elastic deformation energy per carbon atom, (c) The restoring force on fixed carbon atoms. For $(8, 0)$ SWNT, the force is scaled by 0.5 since it is only on one carbon atom, while for the other tubes it is on two carbon atoms. (Reproduced from Ref. [131]).

3.6.1 Elasticity

For the radial deformation, the relation between stress and strain is given by the generalized Hooke's law,

$$\sigma_{xx} = 0 = C_{11}\epsilon_{xx} + C_{12}\epsilon_{yy} \tag{3.34}$$

and

$$\sigma_{yy} = \frac{F_y}{A} = C_{12}\epsilon_{xx} + C_{11}\epsilon_{yy} \tag{3.35}$$

Here F_y is the restoring force applied on the surface area A, C_{11} and C_{12} are the in-plane elastic stiffness constants. Assuming the validity of the Hooke's law, the elastic deformation energy E_D (*i.e.* the difference between total energies of radially deformed and undeformed SWNT) as

$$E_D = \Omega \left[\frac{1}{2}(1+\nu_{\|}^2)C_{11} - \nu_{\|}C_{12}\right]\epsilon_{yy}^2 \tag{3.36}$$

in terms of the in-plane Poisson's ratio, $\nu_{\|}$[131]

$$\nu_{\|} = -\frac{\epsilon_{xx}}{\epsilon_{yy}} = \frac{C_{12}}{C_{11}}. \tag{3.37}$$

Deformation energies obtained from classical elasticity in Eq. 3.36 are compared with those calculated from first-principles in Fig. 3.16. Interestingly, the quadratic form obtained from classical theory fits very well to the elastic deformation energy calculated from the first-principles. Hooke's relation, and hence elastic character of the deformations, persists up to $\epsilon_{yy} = 0.25$. It is also noted that the SWNT becomes stiffer as R decreases. The variation of the restoring forces is expected to be linear in the elastic range. The restoring forces in Fig. 3.16c are in overall agreement with this argument, except the deviations at certain data points due to uncertainties in the first-principles calculations, which are amplified because the force is a derivative quantity. Elastic constants calculated from the first-principles are listed in Table 3.7.

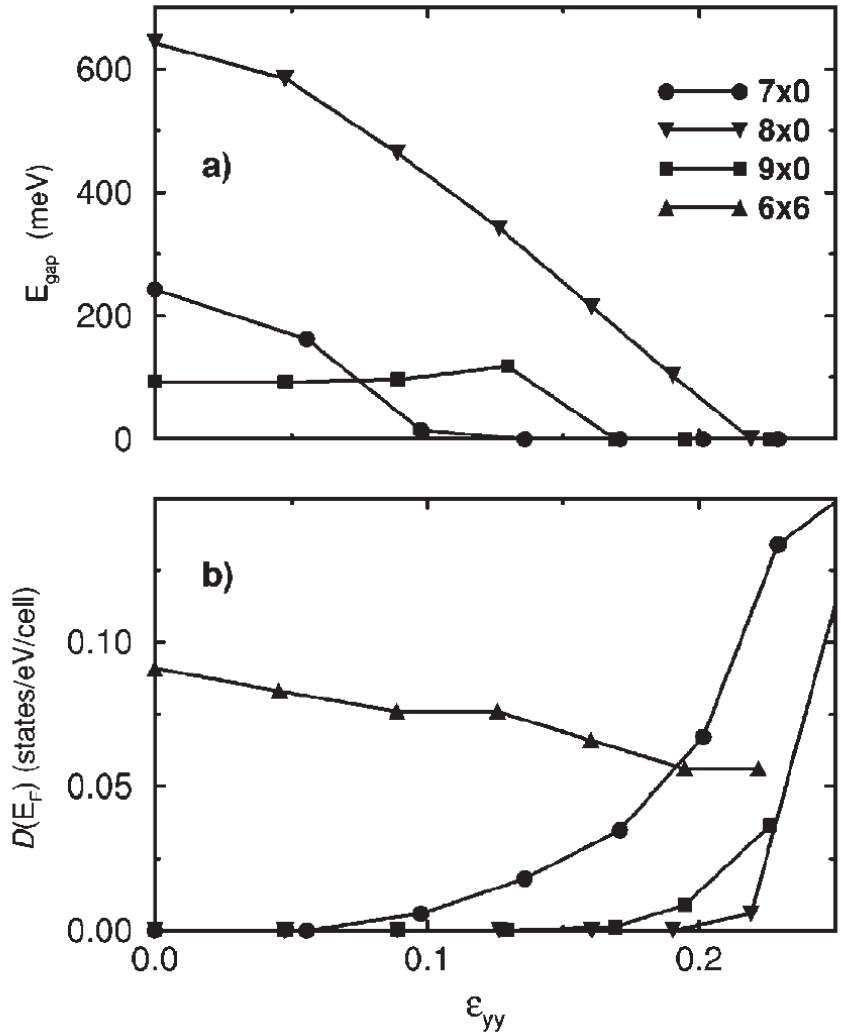

Figure 3.17: (a) The variation of the band gap, E_g. (b) Density of states at the Fermi level $\mathcal{D}(E_F)$ as a function of applied strain ϵ_{yy}. (Reproduced from Ref. [131]).

Table 3.7: In–plane elastic constants of SWNTs. All elastic constants are in GPa except for $\nu_{\|}$ which is unitless. $C_{eff} = C_{11}(1 - \nu_{\|}^2)$.(Reproduced from Ref.[131])

	Radius (Å)	$\nu_{\|}$	C_{eff}	C_{11}	C_{12}
(7,0)	2.76	0.904	129.88	713.36	645.15
(8,0)	3.14	0.874	98.70	416.88	364.20
(9,0)	3.52	0.864	91.02	319.67	270.36
(6,6)	4.06	0.828	86.12	273.46	226.34

3.6.2 Effect of radial deformation on the electronic structure

First-principles calculations confirm that the band gaps of zigzag tubes reduce with applied strain, and eventually vanish leading to metallization. Figure 3.17 summarizes the variation of band gap and density of states at the Fermi level, $\mathcal{D}(E_F)$, as a function of the applied strain. For $(7,0)$ and $(8,0)$ SWNTs the band gaps decrease monotonically and the onset of an insulator-metal transition follows with the band closures occurring at different values of strain. Upon metallization $\mathcal{D}(E_F)$ increases with increasing strain. However, the behavior of the $(9,0)$ tube is different. Initially, the band gap increases with increasing strain, but then decreases with strain exceeding a certain threshold value and eventually diminishes. For all these zigzag SWNTs the band gap strongly depends on the magnitude of the deformation, and E_g is closed at 13%, 22% and 17% strain for (7,0), (8,0) and (9,0) nanotubes, respectively. Whereas, the armchair $(6,6)$ SWNT, which is normally metallic, remained metallic with a slowly decreasing $\mathcal{D}(E_F)$ even for significant radial deformation. Earlier Delaney *et al.* [161] showed that the π^*-conduction and π-valence bands of a $(10,10)$ tube which normally cross at the Fermi level with quasi linear dispersion, open a pseudogap in the range of ~ 0.1 eV at certain directions of the BZ perpendicular to the axis of the tube owing to tube-tube interactions in a rope. The opening of the gap is caused by the broken mirror symmetry. Lammert *et al.* [151] pointed out the gapping by squashing $(20,20)$ and $(36,0)$ metallic tubes, since circumferential regions are brought into close proximity. Uniaxial stress of a few kilobars can reversibly collapse a small radius tube inducing a 0.1 eV gap, while the collapsed large radius tubes are

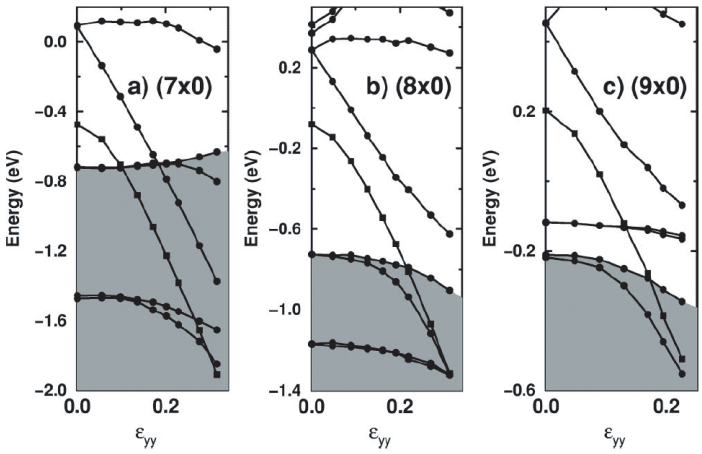

Figure 3.18: The variation of energy eigenvalues of states near the band gap at the Γ–point of the BZ as a function of the applied strain. The shaded region is the valance band. The singlet state originating in the conduction band is indicated by squares. (Reproduced from Ref. [131]).

stable. In the study of Park *et al.* [132], the bandgap of the $(5, 5)$ tube was monotonically increasing probably due to bilayer interactions, since the separation of the two nearest wall of the tube became comparable to the interlayer distance of graphite.

In order to explain the band gap variation of $(n, 0)$ tubes, the energies of a few bands near the band gap are plotted as a function of strain in Fig. 3.18. The singlet π^*–state in the conduction band shifts downwards in energy much faster than the other states do with increasing strain. This is due to the increasing curvature with increasing radial deformation. Since the singlet π^*–state lies below the double degenerate π^*–states for both $(7, 0)$ and $(8, 0)$ SWNTs, their band gaps are closed monotonically with increasing ϵ_{yy}. On the other hand, for the $(9, 0)$ SWNT this singlet π^*–state is above the double degenerate π^*–states. The increase of the band gap at the initial stages of radial deformation is connected with relatively higher rate of downward shift of the double degenerate π–valence band relative to the π^*–conduction band under low strains. Once the singlet π^*–band, which shows faster decrease with strain, crosses the doublet conduction band and enters into the gap, the band gap begins to decrease with increasing strain. Applying

a radial strain through the tip of an Atomic Force Microscope and by simultaneously measuring the conductance, Minot *et al.*[152] confirmed that the band structure of carbon nanotubes can be altered as predicted in Refs.[111, 131, 132] earlier.

3.6.3 Effect of radial deformation on the chemical reactivity

Srivastava *et al.*[162] examined the effect of conformational strain on the chemical reactivity of a SWNT. A $(10, 10)$ SWNT, which was either bent or subjected to torsional strain had kinks or ribbon structure on its surface. Actually those deformed places have sites with higher curvature as compared to the curvature of the bare $(10, 10)$ SWNT. Using a many-body, bond-order potential, they performed the classical trajectory simulations on the interaction between hydrogen atom and strained nanotube. These predicted that the chemisorption of hydrogen atoms is enhanced by as much as 1.6 eV at regions of high conformational strain. Analysis of atomic cohesive energies, local density of states obtained from empirical tight binding method showed that the sites with enhanced binding energies of hydrogen atom correspond to destabilized cohesive energies and electronic states near the Fermi level. The heightened chemical reactivity of deformed sites was attributed to the introduction of radical p-orbital character.

First-principles pseudopotential calculations have shown that indeed adsorption of foreign atoms on SWNTs can be modified continuously and reversibly.[113] The effect of radial deformation becomes noticeable through the binding properties of foreign atoms on undeformed SWNTs. This situation is described in Fig. 3.19, where the calculated binding energies E_b of H and Al adsorbed on the zigzag tubes are plotted as a function of the radius R for n =7,8,9,10,12. As described in the previous sections, H is adsorbed at the top site, directly above the C atom of the tube; Al favors H-site. It is seen that E_b decreases with increasing radius (or decreasing curvature), and eventually saturates at a value corresponding to that on graphene. The variation of binding energies of H and Al with the

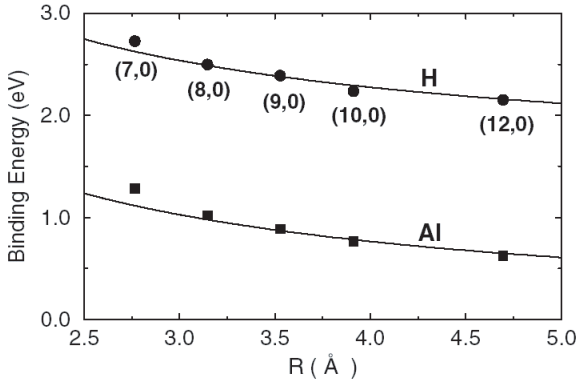

Figure 3.19: Binding energies E_b of single hydrogen and aluminum atom adsorbed on the zigzag SWNTs versus the radius of the tube R. The solid line is the fit to the $E_{b,A}(R) = E_{o,A} + C_A/R$ explained in the text. (Reproduced from Ref. [113]).

radius of the zigzag tube fits to the curve given by the expression,

$$E_{b,A}(R) = E_{o,A} + \frac{C_A}{R}. \tag{3.38}$$

where $E_{o,A}$ is the binding energy of the adatom A (here H or Al) on the graphene plane, and calculated to be 1.49 eV and -0.02 eV for H and Al, respectively [113]. The fitting parameter, C_A is calculated to be $\sim$3.14 eV/Å for both H and Al. Calculated data for $n < 7$ slightly deviate from the above simple $E_b(R)$ relation perhaps due to the fact that the singlet π^*-band, which is normally in the conduction band falls into the band gap as a result of increased curvature. Note that, while the band gap shows significant change with n [for example by going from $(8,0)$ to $(9,0)$ E_g changes from 0.65 eV to 0.09 eV], the binding energies vary smoothly with R^{-1}. Increase of E_b with decreasing R (or with decreasing n) shows that for small R the character of the surface deviates from that of the graphene. This result has been exploited to create different zones with different curvatures on the surface of a single SWNT by radial deformation and hence to attain different chemical reactivity.

The radial deformation can be created by applying a uniaxial compressive stress on a narrow strip on the surface of the SWNT.[113, 131] where the circular cross section of the bare tube is distorted to an elliptical one with major and

minor axes a and b, respectively. In Fig. 3.20(a) the variation of the binding energies of a single hydrogen atom adsorbed on the $(8,0)$ surface shows that E_b at the sharp site, *i.e.* near one of the ends of the major axis increases with increasing ϵ_{yy} (defined in Eq. 4), and traces the upper curve. The lower curve is associated with the adsorption on the flat site, *i.e.* near one of the ends of the minor axis. According to the predictions of this study, at the high curvature site E_b has increased by 0.85 eV for ϵ_{yy}=0.3. On the other hand, E_b for the adsorption on the low curvature (flat) site first decreases with increasing strain, and than saturates at an energy 0.25 eV less than that corresponding to $\epsilon_{yy} = 0$. The difference of binding energies of the sharp and flat sites is substantial and is equal to ∼1.1 eV for $\epsilon_{yy} = 0$. This is 44% of the binding energy of H on the undeformed SWNT. As a result of H adsorption, the sp^2 character of the bonding of the tube has changed locally and become more like sp^3. In Fig. 3.20b the binding energy of Al exhibits a behavior similar to that of H, despite H and Al favoring different sites on the (8,0) tube; E_b at the sharp site of the deformed SWNT increases with increasing ϵ_{yy}. For example E_b increases by ∼0.80 eV for ϵ_{yy} =0.3 which is 80% of the binding energy on the undeformed tube. For Al is adsorbed on the flat site, E_b first decreases with increasing ϵ_{yy}, then gradually increases. Adsorption of Al induces local changes in the atomic and electronic structures. For example, the surface of the tube where Al adsorbed expands.

We see that according to the first-principles calculations the chemical reactivity of a zigzag SWNT can be modified reversibly and variably by radial deformation. The effect of deformation is significantly different for the zigzag and armchair SWNTs. It is remarkable that Al, which does not bind to the graphite surface, can be adsorbed at high curvature site of a zigzag tube under radial deformation with a significant binding energy. Similarly, it has been shown that the H_2 molecule which is bound to the surface of $(8,0)$, becomes physisorbed at the high-curvature site with a significant binding energy [289]. If the physisorbed H_2 can approach to the surface as close as 1.5 Å, it dissociates into two H atom, each becomes bound to adjacent C atoms of SWNT at the surface. We believe that the tunable adsorption can have important implications for metal coverage and selective adsorption of foreign atoms and molecules on the carbon nanotubes,

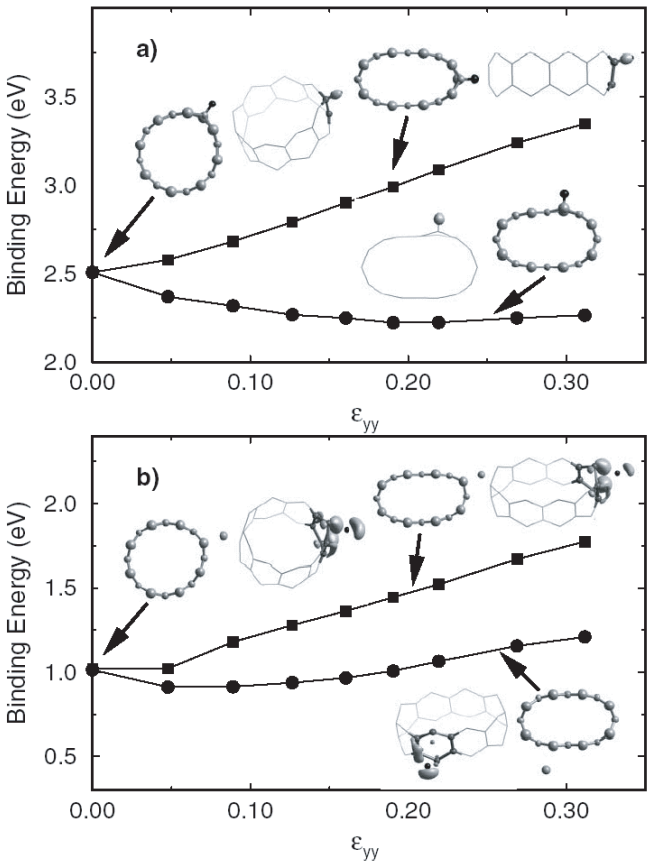

Figure 3.20: (a) Variation of the binding energies E_b of single hydrogen atom adsorbed on a (8,0) zigzag SWNT as a function of the radial deformation ϵ_{yy} defined in the text. The upper curve corresponds to H adsorbed on the high curvature site of the deformed tube. The lower curve is for the adsorption on the low curvature site. (b) Same as (a) for a single Al atom. (Reproduced from Ref. [113]).

and can lead to a wide variety of applications, ranging from hydrogen storage to chemical sensors and new nanomaterials.

3.6.4 Effect of pressure on nanoropes

It is anticipated that physical properties can also be altered by intertube interactions between nanotubes packed in hexagonal lattice, as so called nanoropes. Intertube interactions in nanoropes can be probed by applying external pressure to vary the intertube distance. For fullerenes, such high-pressure studies have yielded many interesting results[164] including new compounds such as the pressure-induced polymeric phases of C_{60}. Similar covalent bonding can occur between the nanotubes in a rope. Such a property could have important consequences for nanoscale device applications and composite materials that require strong mechanical properties since nanoropes consisting of interlinked SWNT will be significantly stronger than nanoropes composed of VdW packed nanoropes.[153]

Raman studies on SWNT ropes have been carried out up to 25.9 GPa, and have indicated that the mode intensities and energies are not completely reversible upon pressure cycling.[165] Those results have been interpreted as irreversible pressure induced changes in the atomic structure. Furthermore, observation of very large volume reduction and high compressibility[150] has suggested that a microscopic volume reducing deformation other than VdW compression can occur under high pressure. Some of these effects are tentatively attributed to crushing or flattening of nanotube surfaces in the rope deforming the circular cross section to elliptical or hexagonal ones.[150]. Peters *et al.*[166] reported that a structural phase transition occurred at 1.7 GPa. Furthermore they performed empirical uniform force field calculations, and obtained equilibrium lattice constants of the $(10, 10)$ nanotube rope as a function of applied pressure P. These calculations have indicated a sudden transition of structure at 1.75 GPa.[166] Their interpretation on the structural transition has been objected by Tang *et al.*[167] on the ground that their experiments were reversible up to $P = 4$ GPa.

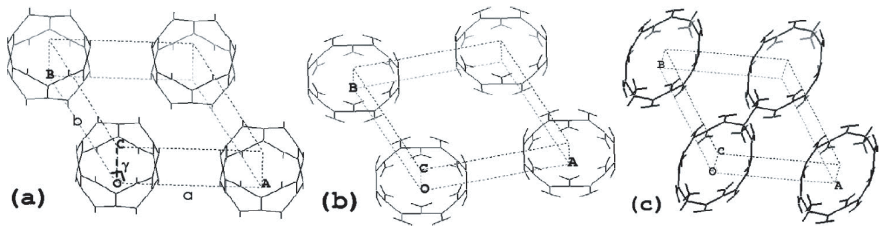

Figure 3.21: Optimized structures of SWNT ropes.(a) $(6,0)$, (b) $(7,0)$ nanotubes are packed by VdW interaction under zero pressure, and (c) $(7,0)$ one-dimensional interlinked under pressure. The interlinked structure in (c) has lower total energy than VdW packed structure in (b). Lattice parameters of the ropes, a, b, and c, and γ angle are shown. (Reproduced from Ref. [154]).

Yildirim *et.al*[154] were first to investigate the effects of pressure on the ropes based on the first-principles calculations. The zigzag tubes $(5,0)$, $(6,0)$, $(7,0)$, $(9,0)$ and armchair tube $(6,6)$ were included in that study. The pressure dependence was determined by minimizing the total energy as a function of nanotube separation, *i.e.* $E_T(a,b)$ while the other parameters, including atom positions, c, and $\gamma = 2\pi/n$ were optimized. At critical pressure, a structural phase transformation from VdW lattice to a new orthorhombic (space group C_mC_m) lattice was observed in which the nanotubes are interlinked along the [110] direction. The covalent bonding between nanotubes occurred at the high-curvature sites as a result of rehybridization of the carbon orbitals. Figure 3.21 compares the structure of VdW packed $(7,0)$ nanorope with that of 1D interlinked one. The same structural transformation was observed for the $(5,0)$, $(6,0)$, $(9,0)$ zigzag tubes.

The bonds interlinking two adjacent tubes have bond lengths comparable to those in diamond. This indicates that the rehybridization occurs from sp^2 to sp^3-type. However, the bond angles differ from exact value of tetrahedral angle and vary between 100^o and 120^o indicating some strain. For some $(n,0)$ tubes the energy difference between the 1D interlinked structure and VdW packed structure is small. Regardless of that, the 1D interlinked structure is stable once it is formed, since one has to overcome an energy barrier of 0.7 eV in order to break the links as illustrated in Fig. 3.22.

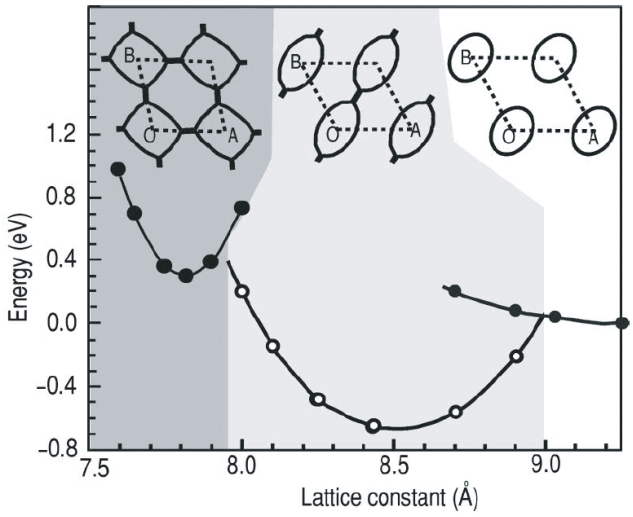

Figure 3.22: Total energy versus 2D lattice constant of $(7,0)$ nanotube ropes in different phases. The top view along the axis of the rope of the different phases are shown by inset. The zero of energy is set to the total energy calculated for the optimized structure of VdW packed rope at zero pressure. (Reproduced from Ref. [154]).

The total energies of the VdW and 1D interlinked phases cross each other at $a \sim 9$ Å with a small energy barrier of 46 meV/unitcell (552 K) from the VdW side. The pressure to attain this lattice constant is only about 0.3 GPa for the VdW phase, indicating that polymerization of VdW $(7,0)$ nanoropes could occur at modest pressures and temperatures. Conversely, 0.7 eV/unitcell (or 25 meV/atom) is required to go from 1D interlinked phase to the VdW packed structure. This energy is comparable to the 1D polymerization energy of C_{60}. Interestingly, at about $a \sim$8 Å there occurs another interlinked phase of $(7,0)$ nanorope, where nanotubes are interlinked along both a and b axes. This 2D interlinked phase is not favored energetically. Its minimum lies $\sim$ 1 eV/unitcell above the minimum of the 1D linked phase. However, once it is formed, it is stable and sixteen times stiffer (d^2E/da^2=13.7 eV/Å^2) than the VdW packed rope. The structures transform to even more complex structures at higher pressure. The rope of the $(6,6)$ armchair tubes do not form interlinking upto 60 GPa. They are rather hexagonally distorted such that local structure of nanotube faces is reminiscent of graphite sheet. Upon releasing the pressure the hexagonally

distorted (or polygonalized) structure returns to original one, indicating that the deformation of the $(6, 6)$ nanorope is elastic (See Fig. 3.23). The above structural transformations induced by the applied pressure lead to significant changes in the electronic structure[154]. In spite of the fact that an individual $(7, 0)$ tube is a semiconductor with E_g =0.65 eV, the dispersion of the bands near Fermi level in the direction perpendicular to the tube axis makes the VdW rope metallic. At high pressure (30 GPa), the (2D interlinked) high-density phase becomes a wide band-gap insulator with $E_g \sim 2$ eV.

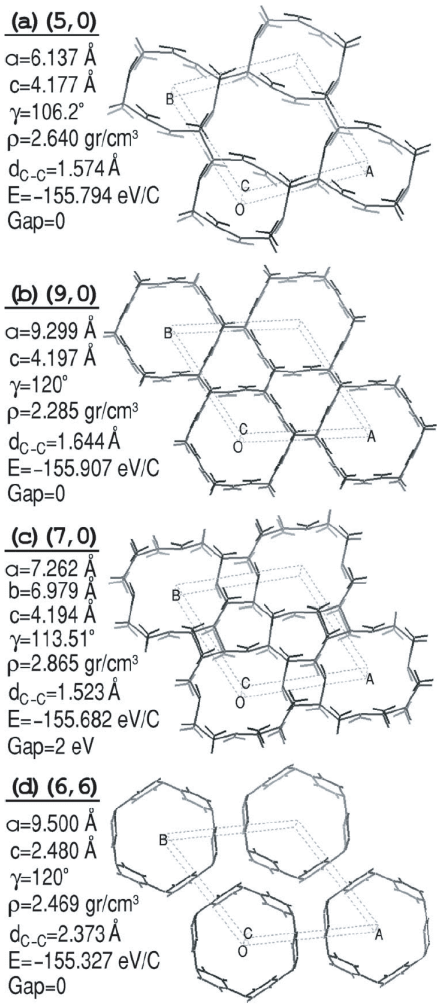

Figure 3.23: Two-dimensional crystal structure and relevant physical parameters for various high-density phases of carbon nanotubes. (a)2D interlinked structure of $(5,0)$ nanotubes. (b) A hexagonal network of $(9,0)$ nanotubes, in which $(9,0)$ tubes are interlinked along a, b, and [110] directions. (c) A very dense structure of $(7,0)$ nanotubes obtained under 30 GPa. (d) The optimized structure of $(6,6)$ armchair tubes under 53 GPa. Nanotubes are distorted in such a fashion that the local nearest-neighbor structure is reminiscent of the graphite. d_{C-C} indicates the smallest distance between two carbon atoms of nearest-neighbor tubes in the rope. (Reproduced from Ref. [154]).

Chapter 4

Oxygenation of SWNTs

This study presents an extensive and systematic analysis of the oxygenation of semiconducting and metallic SWNTs by using first principles pseudopotential plane wave method. Our study involves the physisorption of oxygen molecules, chemisorption of oxygen atoms and formation of oxide, and deals with the equilibrium binding geometry and corresponding electronic energy structure. The binding energies of oxygen molecule physisorbed at different sites are determined by calculating short and long range interaction.

The modification of electronic properties of carbon nanotubes by the adsorption of foreign atoms or molecules has been actively studied.[113, 168, 169, 170] Hydrogen chemisorption can give rise to modifications on the electronic and atomic structure.[168] It has been predicted that, depending on the hydrogen decoration, the tube can undergo changes between a wide band gap insulator and a metal with high density of states at the Fermi level.[171] A well-defined pattern of hydrogen adsorption can change the circular cross section to a square one.[171] Remarkable effects on the electrical resistance of a semiconducting single wall carbon nanotube (s-SWNT) upon exposure to gaseous molecules such as NO_2 and NH_3, have been reported.[169] Collins *et al.*[170] found similar effects for oxygen. Exposure to air or oxygen dramatically influences electrical resistance and the thermoelectric power of a SWNTs. A s-SWNT, which can be converted to a good metal and hence its electronic properties can be reversibly modified by

surprisingly small concentration of adsorbed oxygen has been proposed as a candidate for chemical sensor devices. Also the metallic connects to a device made from a SWNT could easily be realized by physisorption of O_2. Experimental studies on carbon nanotube field emitters have shown that the adsorption of ambient gases, in particular O_2 instantaneously induces a significant increase in the emission current.[172] In addition to functionalization, oxygenation involves other applications. For example, carbon nanotubes synthesized by using arc-discharge are purified from other undesired, carbon based nanoparticles through oxidation. At elevated temperatures, oxygen undergoes chemical reaction preferably with the strained C–C bonds and eliminates carbonaceous nanoparticles as well as the caps of nanotubes.[173, 174, 175]

Observed effects on the electronic structure of SWNTs due to O_2 physisorption have been subject to recent theoretical investigations based on first-principles calculations.[176, 177, 178, 179, 180, 181, 182, 183] Spin-unpolarized band structure calculations based on the local density approximation (LDA) predicted that the semiconducting $(8, 0)$ tube becomes metallic, since the valence band is hole doped by the Fermi level touching the top of the valence band as a result of O_2 physisorption.[176] The analysis based on the local spin density approximation (LSDA) has indicated that the physisorbed O_2 favors the triplet state. While the spin-up states are fully occupied, the spin-down states are nearly empty and hence give rise to finite density of states at the Fermi level.[176] The binding geometry and the corresponding electronic energy structure of O_2+SWNT system based on the first principles and fully relaxed, spin polarized calculations including the long range interactions have not been thoroughly investigated yet. Therefore, the previous, spin unpolarized calculations of the electronic structure may not show the real effect of O_2 physisorption on the electronic structure of s-SWNT. The energetics of oxygen adsorption on the surface of graphite [177] and on $(8, 0)$ SWNT were calculated for selected sites.[178] Adsorption and desorption of an oxygen molecule and various precursor states at the edges of finite size armchair $(5, 5)$ and zigzag $(9, 0)$ SWNTs were studied to provide an understanding of oxidative etching process.[179] Similarly, the mechanism of the oxidative etching of the caps and walls of the small radius $(5, 5)$ armchair SWNT was investigated.[180] The

effects of oxygen adsorption on the field emission from carbon nanotubes were treated by using an *ab-initio* approach.[181] Dynamics of thermal collision of O atom with $(6,0)$ SWNT is simulated by *ab-initio* calculations.[182]

In this study we presented a detailed, first-principles analysis of the oxygen adsorption on the SWNTs. Our prime motivation has been reveal how the adsorption of O_2 and O modify the electronic properties. The zigzag $(8,0)$ and armchair $(6,6)$ tubes are taken as prototype tubes for semiconducting (s-SWNT) and metallic (m-SWNT) single-wall carbon nanotubes, respectively. We expect similar trends in other tubes with curvature effects being emphasized at small radii.[131] In Section 4.1, we summarized the methods used in the calculations. In Section 4.2 we investigated the character of bonding and energetics in the adsorption of O_2. We calculated binding energy for O_2 adsorbed at different sites and coverage for both magnetic (spin-polarized) and non-magnetic (spin-unpolarized) states within the DFT.[291] We found that the O_2 + SWNT system in the triplet state becomes energetically more favorable, but the weak binding of O_2 on a SWNT is further weakened in the magnetic state. Moreover, in the magnetic state a small band gap opens between the top of the valence band of s-SWNT and the spin-up states of O_2. Previous first-principles calculations dealing with the physisorption of O_2 have omitted the van der Waals (VdW) interaction. Here, in addition to the short range (chemical) interaction, we calculated the long range VdW interaction for different adsorption sites of the O_2. In Section 4.3, we studied the chemisorption of atomic O at different sites and found that at certain conditions strained zigzag C–C bond is replaced by a strong C–O–C bridge bond upon the chemisorption of O atom. Results of electronic structure calculations for O_2+SWNT systems with different pattern and coverage are given in Section 4.4. Discussion of results and conclusions are presented in Section 4.6.

4.1 Method

Further to the extensive discussion about DFT method presented in Chapter II, we now give detailed parameters of our calculation. The first principles total energy and electronic structure calculations have been performed using the pseudopotential plane wave method [81] within the generalized gradient approximation (GGA).[122] We carried out both spin-unpolarized and spin-polarized calculations using a periodically repeating tetragonal supercell with lattice constants, a_{sc}, b_{sc} and c_{sc}. The lattice constants, a_{sc} and b_{sc}, are chosen such that the interaction between nearest neighbor tubes is negligible (the minimum C–C distance between two nearest neighbor tubes is taken as $\sim$10 Å). The lattice constant along the axis of the tube, c_{sc}, is taken to be equal to the one-dimensional (1D) lattice parameter, c, of the tube (which is specified as single supercell). To minimize the adsorbate-adsorbate interaction, some calculations are performed in longer supercells by taking $c_{sc} = 2c$ (double supercell). We used ultra soft pseudopotentials for carbon and oxygen atoms [89] and plane waves up to an energy cutoff of 400 eV. Owing to the very large lattice constants of the supercell, a_{sc} and b_{sc}, **k**–point sampling is done only along the tube axis. The Monkhorst-Pack special **k**–point scheme[83] is used with 12 and 6 **k**-points for single and double supercells, respectively. For all systems we studied all atomic positions of adsorbate and SWNT, as well as c are fully optimized by using the conjugate gradient (CG) method.

Relative to GGA, the LDA predicts a smaller lattice constant (or bond distance) and larger bulk modulus.[122, 185] In particular,for graphite we found that LDA cohesive energy was larger than both GGA and experiment, but interlayer distance calculated by GGA was much larger than experiment, as well as LDA. The ratio of lattice parameters of graphite, c_g/a_g, have been found to be 2.73 and 3.73 for LDA and GGA respectively. The corresponding experimental value [186] at zero temperature is 2.72. Upon including the long range interactions described below while GGA value improves to 2.73, LDA value is lowered to 2.47. This clearly shows that LDA overbinds. These trends are in agreement with those found by Janotti *et. al.*[187] and Furthmüller *et. al.*[188]. It is well

known that both GGA and LDA takes into account only short range (chemical) interactions, but excludes weak, long range van der Waals (VdW) interaction. However neither of these approximation describe correctly the asymptotic bonding behavior of neutral systems. The contribution of weak VdW interaction to the binding energy is usually omitted in the chemisorption of atoms or molecules resulting in strong bonding. The situation is, however, different in the case of the physisorption where the contribution of short range and long range interactions are comparable. Therefore, in treating the binding energy of the physisorbed O_2 we include the attractive VdW interaction, and calculate the corresponding energy, $E_{VdW} = \sum_{ij} C_{6ij}/r_{ij}^6$, using the asymptotic form of the Lifshitz's formula.[189, 190, 191] We assign a positive sign to E_{VdW} since stable binding is specified by positive energies in the present study. Here r_{ij} is the distance between ith O atom and jth C atom, and the constant C_{6ij} is calculated within the Slater-Kirkwood approximation[192] to be 10.604 eV(Å)^6. We note, however, that this standard calculation of VdW energy may involve ambiguities due to relatively small distance between the physisorbed molecule and SWNT. Nevertheless, the VdW interaction is attractive and strengthens the chemical bond.

4.2 Physisorption of O_2 molecules

We studied the bonding of O_2 by placing the molecule at different sites on the SWNT, and by calculating the binding energy corresponding to the optimized structure. Different physisorption positions described in Fig 4.1, *i.e.* on top of the axial C–C bond (A-site), above the center of the hexagonal carbon rings (H-site), on top of the zigzag C–C bond (Z-site), and perpendicular to the axis of the tube and above two adjacent zigzag bond (T-site) were considered.

The binding energy involves short and long range interaction, *i.e.* $E_b = E_s + E_{VdW}$. The contribution of the short range interaction (*i.e.* chemical bonding energy) is calculated by using the expression,

$$E_s = E_T[SWNT] + E_T[O_2] - E_T[O_2 + SWNT] \tag{4.1}$$

in terms of the GGA total energies of the fully optimized bare SWNT

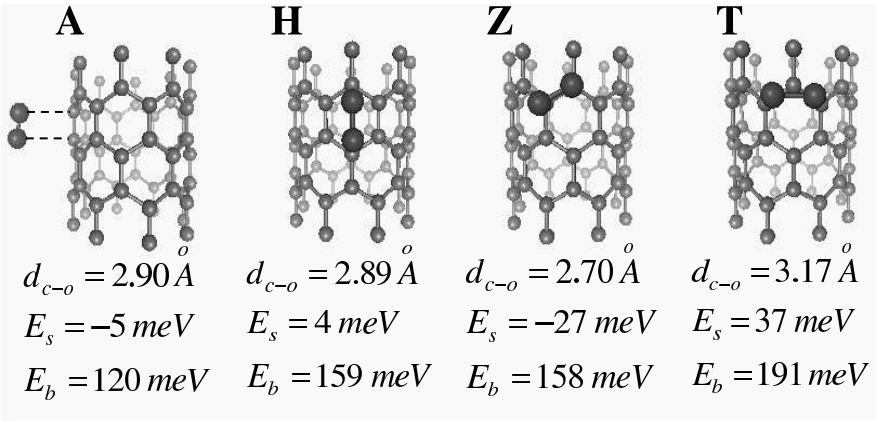

Figure 4.1: Schematic description of the physisorption sites of O_2 molecule on the $(8,0)$ SWNT. Geometrical data and binding energies corresponding to these sites are given in Table 4.1. The GGA optimized distance from one O atom of the molecule to the nearest C atom of SWNT is denoted by d_{C-O}. E_s is the GGA chemical bonding energy for spin-polarized triplet state. E_b is the binding energy including the van der Waals interaction.

($E_T[SWNT]$), the molecule ($E_T[O_2]$), and O_2 physisorbed on the SWNT ($E_T[O_2 + SWNT]$), which are calculated by using the same (single or double) supercell and calculational parameters. By definition, $E_s > 0$ in Eq. 4.1 corresponds to a stable and exothermic chemical bonding. In some cases, $E_s < 0$ is endothermic, but it corresponds to a local minimum where the desorption of O_2 from SWNT is prevented by a barrier. Note that the calculation of the bare molecules in the same supercell excludes the contribution of the nearest neighbor O_2–O_2 coupling in E_s. Our results for the bond dissociation energies of O_2 obtained from the double supercell is 8.60 eV and 5.86 eV for spin-unpolarized and spin-polarized triplet state calculations, respectively. The triplet state is the ground state of O_2. The experimental bond energy of O_2 in the triplet state, 5.2 eV,[193] is in fair agreement with the calculated value of 5.86 eV found in this study.

The VdW energies are calculated for a single O_2 physisorbed on a $(8,0)$ SWNT with a cutoff distance of 1000 unit cells. Using the binding geometries determined from the minimization of GGA total energies, $E_T[O_2 + SWNT]$, we calculated E_{VdW}'s to be 125, 155, 185 and 155 meV for A-, H-, Z-, and T-site, respectively. When we repeat the same calculations for a s-SWNT of 100 unit cell

long, these VdW energies changed only by 10^{-4} meV. We believe that this is a reasonable convergence for a tube having finite length. By adding these E_{VdW} values to those corresponding GGA chemical bonding energies, E_s we obtain binding energies E_b of physisorbed O_2 for different sites. Calculated binding energies of the physisorbed O_2 by using single and double supercells at various sites for spin-unpolarized and spin-polarized states are listed in Table 4.1. Our calculations of the binding energy as a function of the distance between O_2 and SWNT, $E_b(d) = E_s(d) + E_{VdW}(d)$ indicates that under the VdW interaction the equilibrium distance moves towards the surface of SWNT. Since $E_s(d)$ decreases much faster than $E_{VdW}(d)$ increases with decreasing d, the equilibrium distance occurs ~ 0.2 Å less than the GGA optimized distance. Note that in these calculations GGA and VdW interaction treated in different level of approximation; while the first one is calculated from the first-principles, the latter is empirical and is derived from the Lifshitz's asymptotic formula which is valid for large d. Similar arguments are also valid for the equilibrium distance calculated within LDA+VdW. The latter approximation is expected to yield relatively smaller equilibrium distance than the GGA+VdW.

The small binding energies in Table 4.1 are characteristics of physisorption. Although the spin unpolarized state of the O_2+SWNT system is energetically unfavorable, we first discuss it for comparison with previous calculations. Strongest binding for spin unpolarized calculations (u) occurs at Z-site with E_s=187 meV, where O_2 is placed on top of (and parallel to) a zigzag C–C bond. The stability of the Z-site physisorption is tested by starting from a configuration, where O_2 molecule is rotated from the equilibrium position by 90°, and hence becomes perpendicular to the underlying zigzag bond. Upon relaxing, the molecule rotated towards its original equilibrium, Z-site position. The GGA chemical bonding energy of the A-site physisorption is calculated to be 122 meV from single supercell. However, this energy increases to 221 meV when the O_2–O_2 coupling energy in the single cell is not subtracted from E_s. This can be achieved by taking $E_T[O_2]$ in Eq. 4.1 calculated from the double cell as the energy of the isolated O_2 molecule energy. The GGA spin-unpolarized chemical bonding energy of O_2 at A-site is calculated in the double cell and is found to be 141 meV, i.e. ∼20 meV larger than

Table 4.1: Calculated binding energies, E_b, of O_2 molecule at different sites of the $(8,0)$ SWNT. Different sites of physisorption, A-, H-, Z-, and T-sites, are described in Fig 4.1. Calculation of GGA chemical bonding energies, E_s are performed by using single (*i.e.* $c_{sc} = c$) and double (*i.e.* $c_{sc} = 2c$) supercells. In the third column u, s, and t indicate spin-unpolarized, spin-polarized singlet state and triplet calculations, respectively. The GGA optimized distance from one O atom of the molecule to the nearest C atom of SWNT is denoted by d_{C-O}. The average bond length of O_2 is 1.24 Å. The GGA chemical bonding energies E_s exclude the O_2–O_2 coupling energy except one given in the parenthesis. The binding energies, E_b in the sixth column includes the van der Waals interactions.

site	supercell	state	d_{C-O}(Å)	E_s(meV)	E_b(meV)
A	single	u	2.87	122 (221)	
	single	t	2.87	-32	
	single	s	2.87	-0.5	
	double	u	2.90	141	
	double	t	2.90	-5	120
H	double	u	2.89	155	
	double	t	2.89	4	159
Z	double	u	2.70	187	
	double	t	2.70	-27	158
T	double	u	3.17	172	
	double	t	3.17	37	191

that of the single supercell value. This suggests that the bonding between O_2 and SWNT becomes relatively stronger in the absence of O_2–O_2 coupling, since the charge rearrangement is affected in the presence of the latter interaction. Using a similar first-principles method within the local density approximation (LDA), Jhi *et al.*[176] found E_s =250 meV for the A-site physisorption. We repeated our calculations by using LDA, and found E_s=204 meV. Our LDA results are in fair agreement with that of Jhi *et al.* [176] and also confirm that LDA yields overbinding as compared to GGA. Surprisingly, Moon *et al.*[180] did not report a physisorbed state of O_2 on the $(5,5)$ armchair SWNT. For higher coverage, we considered that all A-sites in a unit cell of a s-SWNT are filled by physisorbed O_2 molecules. The energy E_s relative to the spin-unpolarized energy of an individual O_2 molecule is found to be larger than 400 meV per molecule from the single supercell. In compliance with the above arguments, the increased value of E_s with respect to the single A-site physisorption is due to the increased O_2–O_2 coupling, which is not subtracted from the chemical bonding energy.

Spin polarized calculations yield relatively lower (stronger) total energies, $E_T[O_2 + SWNT]$ and hence sets the triplet state as the ground state with a net magnetic moment of $\sim 2\mu_B$ per unitcell. In this case, GGA chemical bonding energies are generally weakened and at A- and Z-site they become even negative with E_s^t =-5 and -27 meV, respectively. The spin-polarized calculations yield that T-site is energetically most favorable site with E_s^t=37 meV. Then the binding energy E_b is found to be 191 meV by adding E_{VdW}=154 meV to E_s. This binding energy is in agreement with the recent measurement by Ulbricht *et. al.*[194] We note that these binding energies are small, and becomes exothermic mainly owing to the long range VdW interaction.

We also studied the physisorption of O_2 on the $(6,6)$ armchair SWNT to reveal the effect of metallicity of the tube on physisorption of O_2. We consider two possible physisorption sites; *i.e.* above the center of the hexagon (H-site), and on top of the C-C bond and perpendicular to the axis of the tube (B-site). B-site of a $(6,6)$ tube is similar to A-site of a $(8,0)$ tube, but in the former case the C–C bonds under the adsorbed O_2 is highly strained, since it lies on the circumference. The binding structure and binding energies calculated with spin

Table 4.2: Calculated C–O distance d_{C-O}, chemical bonding energy E_s, van der Waals energy E_{VdW}, and binding energy E_b for O_2 physisorbed on the H-, and B-site of $(6,6)$ armchair m-SWNT.

site	d_{C-O}(Å)	E_s(meV)	E_{VdW}(meV)	E_b(meV)
H	3.04	-19	151	132
B	2.92	-32	138	106

Table 4.3: Calculated chemical bonding energies of chemisorbed O atom at **a**-site and **z**-site. For E_s^{st} and E_s^{ss} the ground state for the oxygen chemisorbed SWNT is the singlet state, but isolated O atom (reference state) is in the triplet state and the singlet state, respectively. E_s^{tt} corresponds to the both isolated O and O chemisorbed SWNT in the triplet state. E_s^u stands for spin-unpolarized calculation. Energy unit is eV.

	a-site	z-site
E_s^{st}	3.16	3.18
E_s^{ss}	4.09	4.11
E_s^u	5.04	5.07
E_s^{tt}	1.88	

polarized GGA are given in Table 4.2.

4.3 Chemisorption of oxygen atoms

Atomic oxygen is reactive and highly electronegative. The ground state of the atomic oxygen is the triplet state, and its energy is found 0.93 eV lower than the singlet state. It forms strong bonds with the substrate atoms and eventually oxidizes the surface. For example, atomic O may break the Si–Si bond, and forms Si–O–Si on the surface of Si. In this respect, the effect of the adsorbed oxygen on the structural and electronic properties of a SWNT is important. The breaking of the O–O bond of a physisorbed O_2 molecule is unlikely owing to the weak interaction with the SWNT. However, it was shown that near the defect sites of the graphite surface O_2 molecule can dissociate.[177] A carbon nanotube, that can be visualized as a graphene rolled into a cylinder, is normally more reactive than the surface of graphite. As a result, O_2 physisorbed near the defect sites of a SWNT is expected to dissociate into atomic oxygens.[195] In fact, it was shown

that there is no activation barrier for dissociation of O_2 when it is adsorbed at the zigzag edge of a SWNT.[179] Owing to the concerted motion of the atoms at the proximity of the molecule and energy gained by the individual oxygen atoms engaging in the bonding with the SWNT concomitant with the dissociation, the activation energy for dissociation is expected to be low. In this section, we study the interaction between atomic O and SWNT, and reveal the nature of the chemical bonding. We consider only the short range interaction and hence resulting chemisorption energies, E_s for the following reasons. First, the chemisorption energies are rather high (in the range of 5 eV), and hence much larger than the VdW energies. Secondly, the Lifshitz's asymptotic formula may not be appropriate for relatively smaller inter atomic distances, r_{ij}, such as $d_{C-O} \sim 1.5$ Å, and yields energies which may give rise to misleading conclusions.[191] For example, we calculated E_{VdW} of O atom chemisorbed at the **a**-site to be 2.39 eV.

Various adsorption sites and summary of our results are shown in Fig 4.2. Spin-polarized calculations yield the singlet state with a net zero magnetic moment as the ground state. Since free oxygen atom has different energies for its different states (*i.e* $E_T^t[O]$ triplet state, $E_T^s[O]$ singlet state, and $E_T^u[O]$ spin-unpolarized state), E_s of chemisorbed O calculated from Eq. 4.1 depends on which reference state is taken. For example, for the **a**-site chemisorption one can give, $E_s^{tt} = 1.88$ eV, $E_s^{st} = 3.16$ eV, $E_s^{ss} = 4.09$ eV, $E_s^u = 5.04$ eV. Chemisorption energies calculated with respect to different reference states are listed in Table 4.3. In Fig 4.2, the chemisorption energies E_s obtained from the spin-unpolarized calculations are shown. Interestingly, spin-unpolarized calculations are resulted with approximately the same total energy as the singlet state. On the other hand, the total energy of the triplet state for **a**-site is found to be 1.28 eV higher (energetically less favorable) than that of the singlet state.

Among all sites considered in this study the single O adsorbed on top of the zigzag C–C bond (*i.e.* **z**-site) is energetically most favorable with $E_s = E_s^u$ =5.07 eV. The hollow (**c**-) site, *i.e.* the center of the hexagons on the surface of SWNT, appears to be a local minimum with relatively smaller E_s. Whereas the adsorption on top of carbon atoms does not correspond to a local minimum; O atom moves towards the center of neighboring C–C bonds. Apparently, atomic oxygen favors

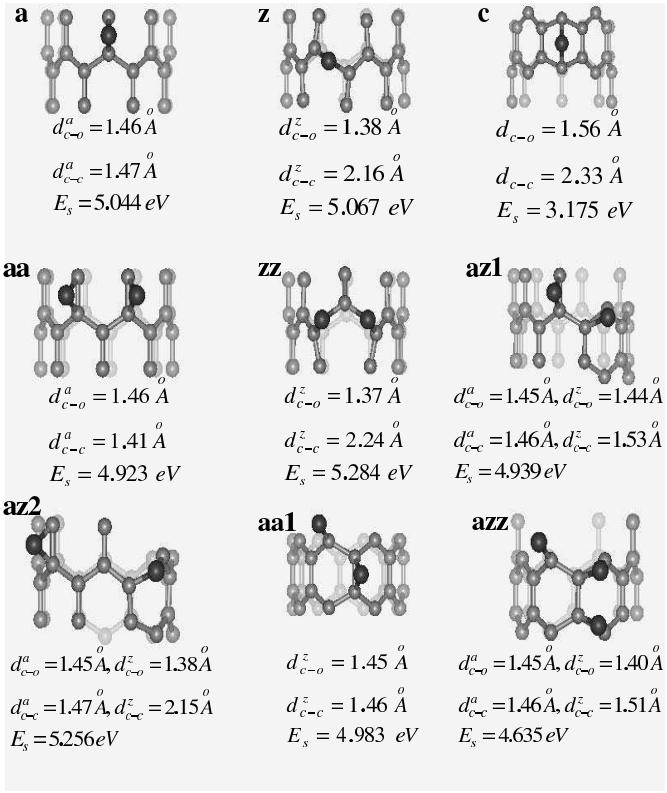

Figure 4.2: Schematic description of the various adsorption sites of atomic O on the $(8,0)$ SWNT. Some relevant geometrical data and GGA chemical bond (chemisorption) energies, corresponding to these sites are also given. E_s: chemisorption energy; d_{C-O}: length of the C–O bond; d_{C-C}: length of the C–C bond under adsorbed O atom. E_s is obtained from the spin-unpolarized calculations of the total energies in Eq. 4.1.

the bonding on top of a C–C bond, where strong C–O bonds can form. The binding energies as large as ~ 5 eV suggest that atomic O is, actually chemisorbed with a significant charge transfer from C to O. Moreover, the energy gained from the chemisorption of two atomic oxygen is more than the bond energy of O_2 in either magnetic or non-magnetic state. This implies the dissociation of O_2 followed by the chemisorption of individual O atoms is an exothermic process similar to other oxidation processes.

The binding energy of O at **a**-, and **z**-site are comparable, but the length of the C–C bond under adsorbed O is different for these different sites. The zigzag bond is elongated to 2.16 Å upon O chemisorption at **z**-site, while the length of the axial C–C bond is practically unaltered after O chemisorption at **a**-site. The elongation of the zigzag bond followed by the contraction of the C–O bonds indicates that the C–C bond of the bare SWNT is either broken or weakened after the chemisorption of O. One can argue that at the **a**-site the C–C bond could have not broken, if it is constrained by the periodic boundary condition. Binding energies (E_s=4.72, 4.99, 5.03 and 4.84 eV) and stress (σ=-45.9, -19.2, 9.2 and 37.8 kB) calculated for different values of lattice parameter (c=4.35,4.30,4.25, and 4.20 Å) invalidate this argument and confirms the fact that c changes slightly upon the chemisorption of a single O atom. Then the question as to why the C–C bond at **z**-site is broken upon the chemisorption of O, but not at **a**-site can be answered by the fact that the zigzag bonds are highly strained and hence their sp^2 character are modified.[113, 131] This is an important manifestation of the curvature effect.[118] Experimentally, it was shown that oxygen exposure first oxidizes, eventually etches away the nanotube with smaller radius.[196] Earlier, we showed that the binding energy of Al and H increases at the high curvature site of a SWNT under a circumferential elliptic deformation.[113] It is, therefore, expected that the reactivity of SWNT for oxygen chemisorption, even the dissociation of O_2 molecule can be enhanced at the high curvature sites which is realized by the applied radial deformation. The charge density contour plots on the planes passing through the O atom chemisorbed at either **a**- or **z**-sites and the underlying C–C bond are compared in Fig 4.3. In the case of **a**-site chemisorption we see that the C–C bond survives with characteristic bonding charge, but

new C–O bonds are formed. On the other hand, while the C–C bond of **z**-site is weakened, even is broken, the C–O bonds become stronger as compared to the similar bonds at **a**-site chemisorption.

Other relevant sites and configurations in O chemisorption are also included in Fig 4.2. The binding energies do not change significantly in the case of more O atoms are chemisorbed at neighboring sites. Notably, the total binding energy of two O atoms chemisorbed on top of adjacent zigzag bonds (*i.e.* **zz**-site chemisorption) is $\sim$ 10.4 eV; 4.5 eV higher than the bond dissociation energy of the bare O_2 molecule in the triplet state. Therefore the chemisorption of two O atoms following the dissociation of physisorbed O_2 molecule in the triplet state is exothermic. The comparison of the **az1**-, and **az2**-site chemisorption reveals that the zigzag C–C bond is stabilized by an adjacent **a**-site chemisorption. However, this bond is broken when **a**- and **z**-site chemisorption are farther apart. In the **azz** configuration the average binding energy of three O atoms is lowered, but is still close to the binding energy of a single O. This implies that higher coverage of O atom on the SWNT can be stable. We examined two different high oxygen coverage corresponding to the oxidation of the nanotube. These are half coverage, (where oxygen atoms are adsorbed to all the **a**-sites) and full coverage, (where oxygens are adsorbed to all **a**- and **z**-sites of SWNT). The half coverage was stable with an average binding energy of 4.96 eV. In the case of full coverage, O_2 molecules reformed due to the increased interaction between closely lying adsorbed O atoms.

4.4 Electronic structure

In the previous sections we studied the atomic structure and energetics of O_2 and O adsorption on s-SWNT and m-SWNT, and revealed various stable adsorption sites (and patterns) at different coverage. In this section, we will examine the electronic structure corresponding to these adsorption patterns. Because of supercell method used in the present study we obtain energy bands and density of states corresponding to a periodically repeating adsorption pattern. For the

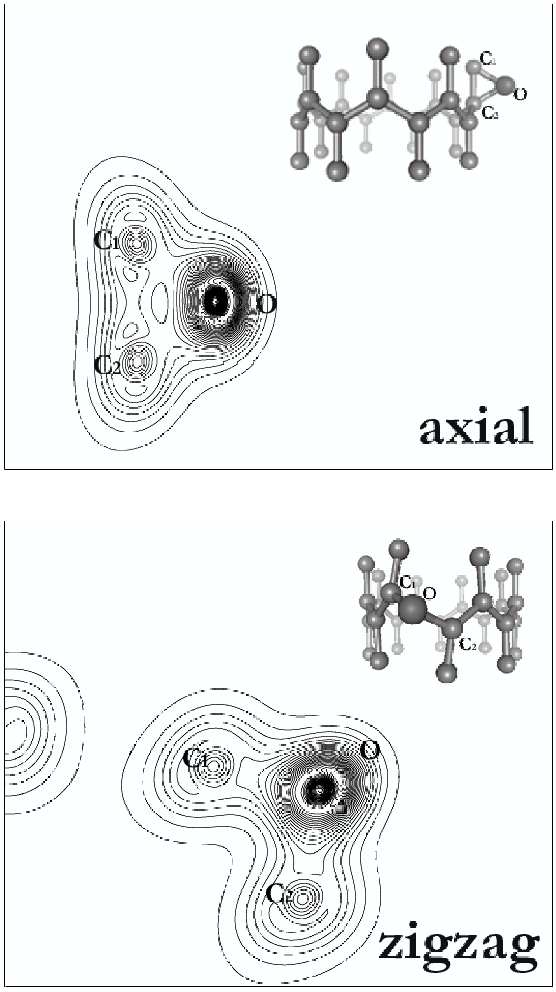

Figure 4.3: Charge density contour plots on a plane containing O atom and nearest C–C bond in the case of **a**-site chemisorption (a) and **z**-site chemisorption (b). These chemisorption sites and their atomic configuration are described as insets.

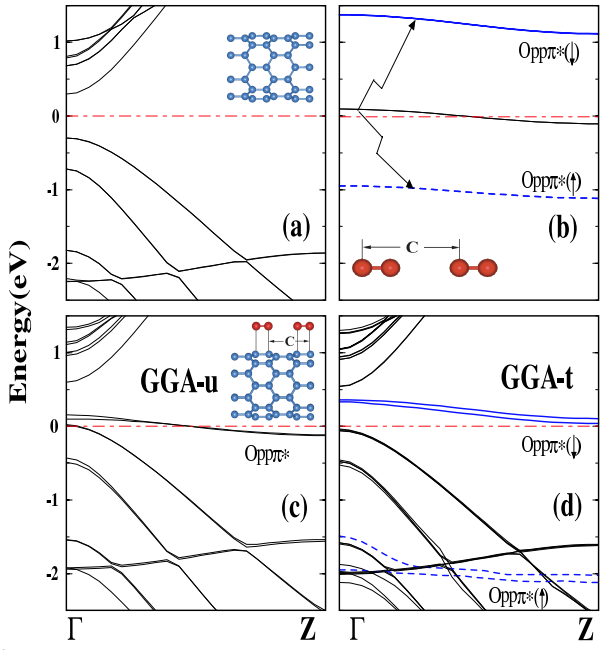

Figure 4.4: (a) Spin unpolarized energy bands of the $(8,0)$ bare s-SWNT; (b) spin polarized (dashed lines) and spin unpolarized (solid lines) energy bands of the linear O_2 chain with the same lattice parameter c; (c) spin unpolarized energy bands of the O_2 physisorbed on the $(8,0)$ tube with $O_{pp\pi^*}$ state pinning the Fermi level. (d) Spin-polarized bands corresponding to (c). Zero of energy is taken at the Fermi level shown by dash-dotted line. Up-spin and down-spin bands are indicated by corresponding arrows. Here $c_{sc} = c$.

energy level structure of a single adsorbate, the adsorbate-adsorbate interaction indigenous to the supercell method can be reduced by taking relatively longer cell sizes allowing longer nearest neighbor distances. Under these circumstances the bands are flatten and represent the energy level of the dopant.

First we studied the electronic energy structure of an oxygen molecule physisorbed on A-site of $(8,0)$ SWNT. Although A-site is not energetically most favorable site we consider it in order to compare our results with those of Jhi *et. al.*,[176] who performed first-principle LDA and LSDA calculations for a single O_2 physisorbed per unit cell.

In Fig 4.4(a) we present the band structure of the bare $(8,0)$ SWNT, which is a semiconductor with a band gap $E_g \sim 0.7$ eV at Γ-point between the bottom of the conduction band E_C and the top of the valence band E_V. The $\pi^* - \sigma^*$

hybridized singlet state is in the conduction band.[118, 131] The free linear chain of O_2 molecules, in principle, has a weak bonding state with an equilibrium lattice parameters slightly larger than c. In Fig 4.4(b), the free linear chain of O_2 in registry with the $(8, 0)$ tube has half filled doubly degenerate $pp\pi^*$ bands. For the triplet state, (which is energetically more favorable than the spin unpolarized state as well as singlet state) these bands split into two doubly degenerate bands [$pp\pi^*(\uparrow)$ and $pp\pi^*(\downarrow)$]. The $pp\pi^*(\uparrow)$ bands are filled and separated from the empty $pp\pi^*(\downarrow)$ bands by an energy gap of $\sim$2 eV. In Fig 4.4(c) spin unpolarized GGA calculations with $c_{sc} = c$ yield doubly degenerate, half filled $pp\pi^*$ bands in the band gap for the physisorption of O_2 at A-site. The Fermi level touching the top of the valence band E_V makes the system metallic.

The above situation is, however, changed in the spin polarized calculations, which yields the triplet state as the ground state. Under these circumstances two O$pp\pi^*$ bands split into four bands, two of them occur $\sim$2eV below the valence band of s-SWNT. Remaining two empty bands rise 350 meV above E_V at the Γ-point and make a band gap of 90 meV [see Fig 4.4(d)]. Therefore, the hole doping picture developed from the LDA and LSDA calculations[176] does not appear in the present spin polarized GGA calculation, since the bands of triplet ground state open a band gap. To reveal the source of disagreement between the present GGA results and the LSDA results of Jhi *et. al*[176], we carried out LDA and LSDA calculations (with the binding geometry used by Jhi *et. al*[176] and also with fully relaxed atomic structure, and using different type of pseudopotentials and cut-off energies). We found that all our LDA (spin-unpolarized) calculations are in agreement with our spin-unpolarized GGA calculations yielding O$pp\pi^*$ band overlapping with the top of the s-SWNT valence band, and hence are confirming the results of Jhi *et. al*[176]. However, all our LSDA calculations (corresponding to the triplet ground state) have resulted in a significant band gap (of 140-90 meV) agreeing with the present spin-polarized GGA results.

Note that the bands here are only the artifact of the supercell method, and hence in the absence of band dispersion the energy level due to the single physisorbed O_2 and the top of the s-SWNT valence band, E_V shall be relatively larger than the calculated band gap. Our arguments are better explained by

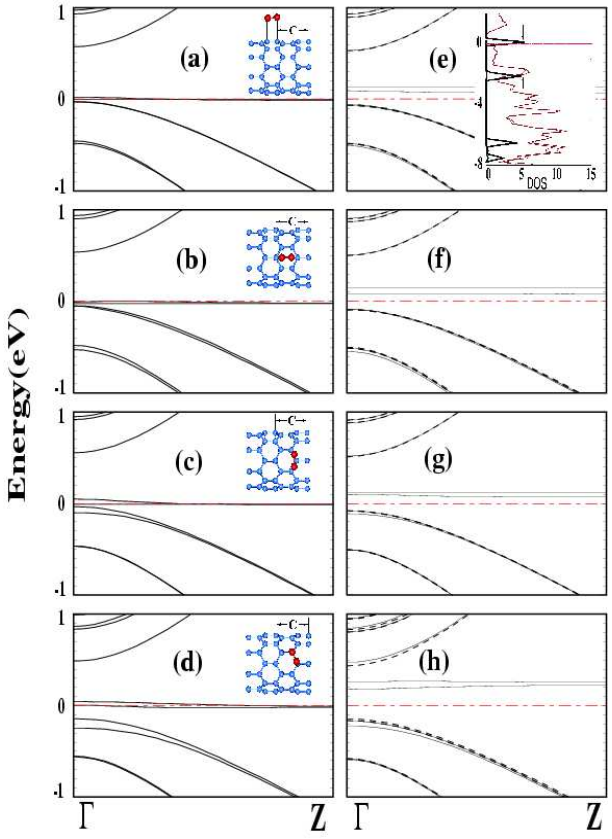

Figure 4.5: Spin unpolarized and spin polarized bands of O_2 physisorbed on different sites of $(8, 0)$. calculations are performed by using double cells. The adsorption sites are shown by insets. (a) Spin-unpolarized and (e) triplet state bands for A-site physisorption. The total density of states with thin and dashed lines, and partial density of states of adsorbed O_2 with thick lines are presented in panel (e). The zero of energy is taken at the Fermi level indicated by dash-dotted lines. (b) spin-unpolarized and (f) triplet state bands for H-site. (c) and (g) are same for T-site; (d) and (h) for Z-site. For the triplet state in left panels, the spin-up and spin-down bands are shown by dashed and thin lines

double cell calculations in which the O_2-O_2 coupling is reduced due to the large distance ($\sim$7 Å) between nearest molecules. In Fig 4.5 we summarize our results for spin unpolarized and triplet ground state bands obtained from double cell calculations. Owing to relatively large O_2-O_2 distance, the bands related with the physisorbed molecule can be taken as if the energy levels of the single adsorbate. We see that spin-paired bands in Fig 4.5(a),(b),(c),(d) (which are in fact energetically unfavorable) comply with the hole doping picture[176] for all sites except Z-site. For the latter, half filled O_2 states are 0.2 eV above E_V. On the other hand, the situation is rather different for triplet ground state bands illustrated in Fig 4.5(e),(f),(g),(h). A sizable energy band gap of 0.2-0.4 eV occurs between E_V and the unoccupied spin-down bands [O$pp\pi^*(\downarrow)$ states] of oxygen molecule. This situation eliminates the hole doping picture. The dispersionless O$pp\pi^*(\downarrow)$ bands indicate that the coupling between O_2 molecules are negligible.

The effects of band formation are examined by studying the electronic energy structure corresponding to various patterns of physisorbed O_2. In Fig 4.6 we show the band structures and density of states calculated for the zigzag chain and row of O_2 physisorbed on $(8,0)$ s-SWNT in the triplet ground state. In the zigzag chain, O_2 molecules are placed initially above the adjacent axial C-C bonds (*i.e.* A-sites), but upon relaxation they are tilted by 40^o and inclined side ways to increase O-O separation of nearest molecules. We calculated the chemical bonding energy E_s =56 meV/molecule. Since the number of O_2 molecules per single cell is doubled, the O$pp\pi^*(\uparrow)$ and O$pp\pi^*(\downarrow)$ bands are doubled as compared to those illustrated in Fig 4.4(d). The system is a semiconductor with a direct band gap E_g $\sim$0.4 eV. As clearly seen from the total and partial density of states the O$pp\pi^*$ bands are split by $\sim$ 2.5 eV upon spin polarization. The band structure of the O_2 row in Fig 4.6(b) display slightly different situation. Here the gap between the lowest O$pp\pi^*(\downarrow)$ band and E_V reduced to 25 meV at the Z-point; it is so far the smallest band gap we obtained from spin polarized calculations. While this band complies with the hole doping picture since its is in the range of thermal excitation at room temperature, the metallization of s-SWNT is still too far.

Electronic energy structure of higher O_2 coverage was further analyzed by a system where initially O_2 molecules are physisorbed to all A-sites of $(8,0)$

tube. Upon relaxation of the system, the distance between O_2 molecule and SWNT surface has increased continuously. This indicates that under increased O_2–O_2 coupling the chemical bonding is weakened and eventually molecules start to escape from the surface of s-SWNT. The VdW interactions was needed to keep the molecules attached to s-SWNT. At each step of ionic relaxation, the bands derived from the bare s-SWNT and molecular oxygen are clearly identified. This situation suggests a negligible mixing between O_2 and s-SWNT states. In fact, the bands of bare s-SWNT remain practically unchanged, and the states of O_2 are broadened into bands owing to the intermolecular coupling. Several bands derived from O$pp\pi^*(\uparrow)$ states form a sharp peak at $\sim$2 eV below E_V. Empty bands derived from O$pp\pi^*(\downarrow)$ states occur always above E_V, and appear as another peak. Even in full coverage we see that empty O_2 states and highest filled s-SWNT states are separated by a gap of $\sim$100 meV, so that the electron transfer from SWNT to empty O_2 states and hence the metallization of the tube is prohibited. Under these circumstances, the s-SWNT+O_2 system can be viewed by two semiconductors forming a two-liquid system. The first one is due to O_2; the second one is a due to s-SWNT. The excitation of the electrons from s-SWNT bands to O_2 states may mediate intermixing of these two liquids.

The physisorption of O_2 on the (6,6) armchair SWNT has been investigated for the bridge (B-) and hollow (H-) sites described as inset in Fig. 4.7. Similar to the (8,0) tube, O_2 adsorbed on the (6,6) SWNT has magnetic ground state ($\mu \sim 1.9\mu_B$) for both sites. The spin-polarized electronic energy band structures are presented in Fig. 4.7. Because of relatively weak O_2-SWNT interaction, the overall features of the bands associated with O_2 are similar. The π^*-conduction and π-valence bands of the bare (6,6) SWNT, which normally cross at E_F, split upon O_2 physisorption. While the spin-up bands continue to cross, spin-down bands open a gap. At the middle of the gap two O$pp\pi^*(\downarrow)$ bands are located. Accordingly, the metallic (6,6) SWNT continues to be metallic with a constant density of states at E_F only for spin-up electrons. Such a situation may occur due to symmetry breaking [161] and is certainly important for spintronics.

Electronic states of oxygen atom chemisorbed on a SWNT depends on the

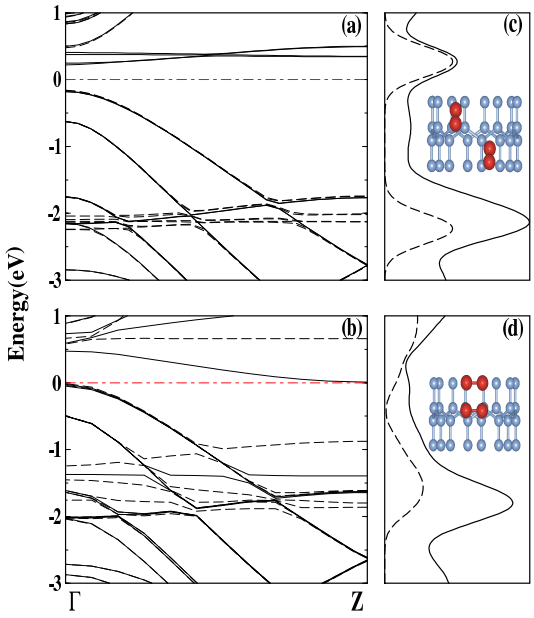

Figure 4.6: (a) Spin polarized electronic energy band structure of the zigzag chain of O_2 adsorbed above the adjacent axial C-C bonds along the axis of a $(8, 0)$ s-SWNT as shown by inset. Solid and dashed lines are the spin-down and spin-up bands. The zero of energy is taken at the Fermi level E_F indicated by dash-dotted line. (b) Corresponding total density of states of s-SWNT+O_2 and partial density of states on the oxygen atoms are shown by solid and dashed lines. (c) Band structure of the row of O_2 physisorbed at T-sites as shown by inset. (d) Same as (b).

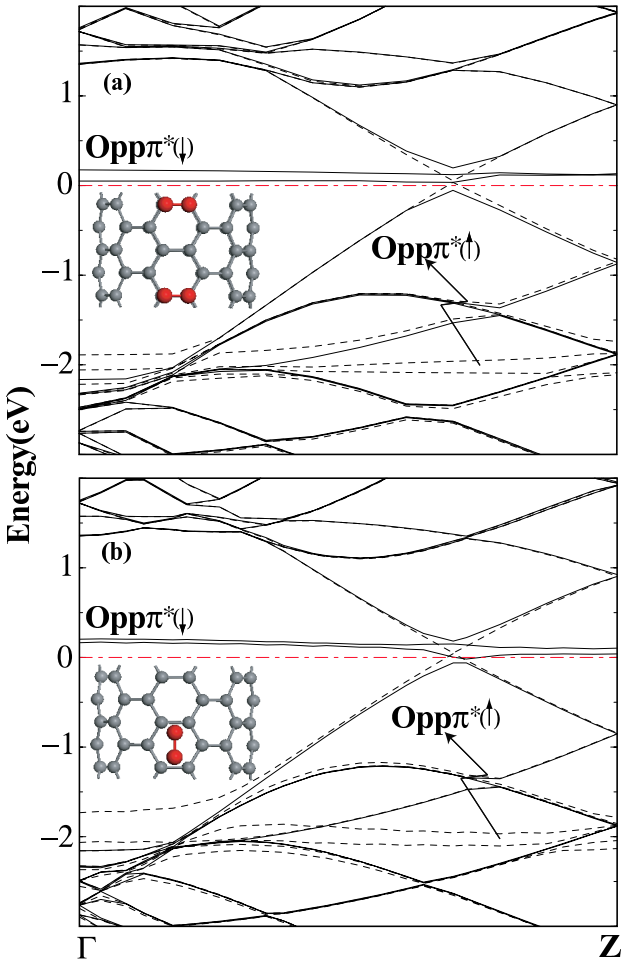

Figure 4.7: Energy band structures of O_2 physisorbed on the (6,6) armchair SWNT. (a) B-site, (b) H-site. Spin-up and spin-down bands are shown by broken and continuous lines.

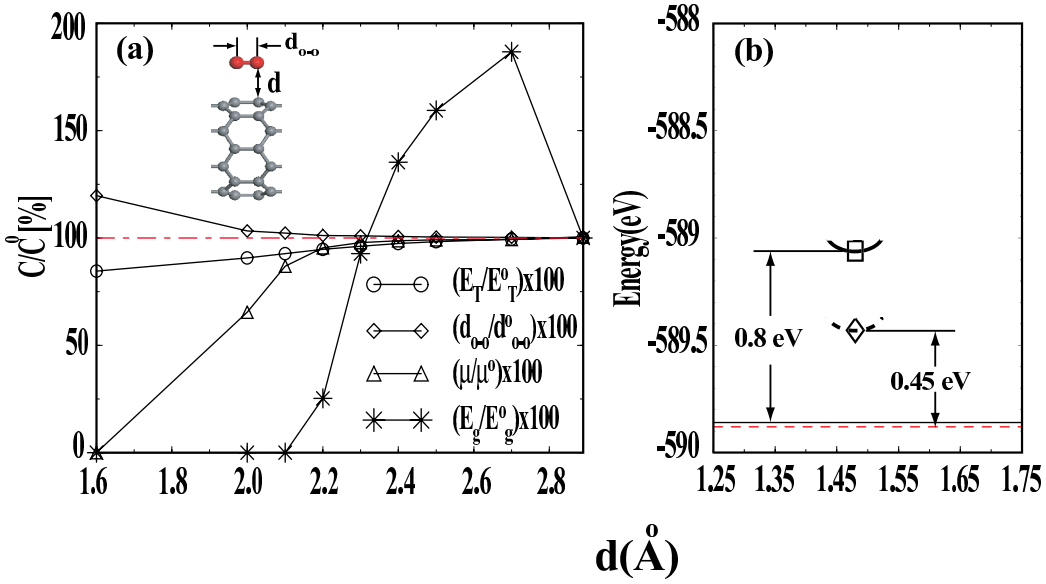

Figure 4.8: (a)Variation of the percentage values of $\mathbf{C/C^o}$ (E_T/E^o_T; d_{O-O}/d^o_{O-O}; μ/μ^o; and E_g/E^o_g) with the O_2-SWNT separation d. E^o_T, d^o_{O-O}, μ^o and E^o_g corresponds to the stable physisorption state with $d^o = 2.89$ Å at the A-site. (b) The total energies of the singlet bound states found at small d at Z-site (square) and at the A-site (diamond). The total energy of the triplet ground state corresponding to the physisorption state for the Z- and A- sites at $d \sim 2.9$Å are shown by continuous and broken lines.

coverage and pattern of adsorption. For example, since single oxygen (per unit-cell) chemisorbed at **a**-site gives rise to flat bands below E_V, the band gap of $(8,0)$ SWNT remains unaffected. However, as a well-known and usual effect of oxygen, the band gap of $(8,0)$ tube opens up to 3.64 eV when all **a**-sites are filled by the chemisorbed oxygen atom.

4.5 Singlet Bound State

The interaction of O_2 with SWNT as a function of O_2-SWNT distance d has been examined by calculating the total energy E_T, bond distance of O_2 d_{O-O}, magnetic moment μ, and energy gap E_g of the O_2 physisorbed (8,0) SWNT. In these calculations, d has been constrained, but d_{O-O} has been relaxed.

Figure 4.8(a) shows the variation of the ratio of E_T, d_{O-O}, μ, E_g to their corresponding equilibrium value at $d^o = 2.89$Å. We see that $|E_T|$ decreases in the range 1.6Å$< d <$2.9Å. For a wide range of O_2-SWNT separation, E_g continues to exist, and the total energy difference between the spin-polarized and spin-unpolarized O_2+SWNT, (i.e. $\Delta E_T = 0.86$ eV) induces the gap E_g and prevents it from closing. For $\sim$ 1.6Å$< d < d^o$ a strong perpendicular force $F_\perp$ is generated on the O_2 molecule to push it away from SWNT. The magnetic moment of O_2+SWNT diminish at a distance $d <$ 2Å. Moreover, the singlet state of adsorbed O_2 leads to a bound state at the Z-site at $d = 1.48$Å and 0.8 eV above the corresponding physisorption state. (i.e. $E_T - {E^o}_T = 0.8$ eV). Similar singlet bound state occurs also at the A-site at $d = 1.47$Å and 0.45 eV above the physisorption state of the A-site at $d = 2.89$Å. These singlet bound states in Fig 4.8(b) correspond to local minima on the Born-Oppenheimer surface and are separated from the more energetic physisorption states by an energy barrier. We note that these states [197, 295] are neither easily accessible from the physisorption state, nor supporting the hole-doping picture because the band gap of ~ 0.5 eV. However, O_2 adsorbed at the H- site of the (6,6) SWNT behave differently. In Fig 4.9, we show the variation of $E_T(d)$, $F_\perp(d)$, $\mu(d)$ and $d_{O-O}(d)$ in the range of 1.3Å$< d <$3Å. As d decreases from the physisorption distance, $\mu(d)$ decreases rapidly and vanishes at $d = 2$Å. The variation of E_T, $F_\perp$ and d_{O-O} indicates that, at $d \sim 1.25$Å, d_{O-O} is increased to 2.5Å and hence the bond is broken, i.e. O_2 molecule dissociates into two O atoms. Passing over a barrier, $|E_T|$ increases and $|F_\perp(d)|$ decreases. In contrast to this site, the O_2 molecule has a bound singlet state at the B-site with $d_{O-O} = 1.51$Å.

4.6 Discussions

The physisorption of O_2 molecules and chemisorption of O atoms are investigated for different coverage and adsorption patterns. Binding is stabilized by the Van der Waals interaction. Our results obtained from spin polarized calculations reveal that: (i) An O_2 molecule can be adsorbed at different sites on a SWNT with comparable binding energies. Adsorption at T-site of a $(8, 0)$ tube is found to be

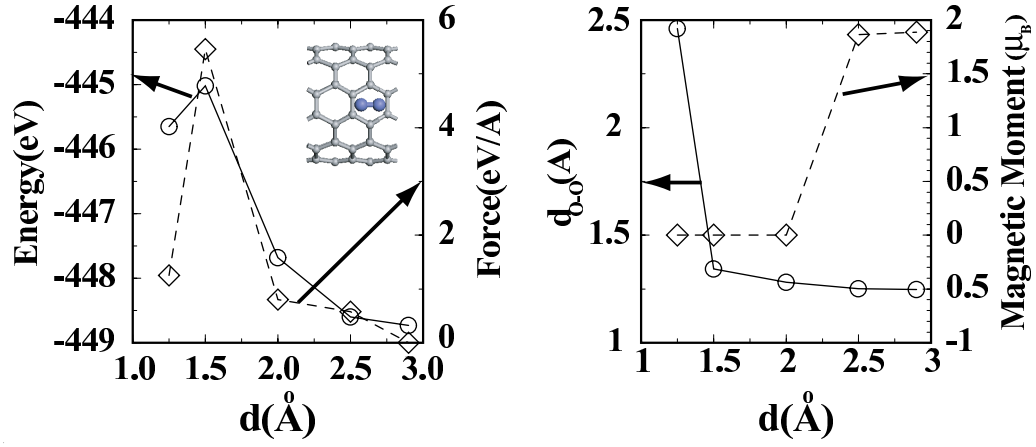

Figure 4.9: Variation of the total energy, E_T; force acting on the O_2 molecule, $F_\perp$; bond distance of O_2, d_{O-O}; and magnetic moment, μ with O_2-(6,6) SWNT distance d for O_2 adsorbed on the H-site of the (6,6) SWNT. Calculations have been performed in the double-cell.

energetically most favorable. The ground state of the adsorbed O_2 molecule is the triplet state with a net magnetic moment of $2\mu_B$ Bohr magneton. The binding energies calculated by including short and long range interactions are small and characteristics of physisorption. (*ii*) Stable chain formation and also uniform coverage of O_2 molecules in the triplet ground state on a s-SWNT are also possible. Since physisorbed O_2 has net magnetic moment in the ground state, new magnetic molecules (or nanomagnets) can be constructed as a result of O_2 decoration. (*iii*) GGA electronic structure calculations performed for optimized atomic geometry corresponding to the triplet ground state indicate that the unoccupied O$pp\pi^*(\downarrow)$ bands (states) of O_2 occur 0.2–0.4 eV above the top of the valence band of the s-SWNT. Only the row of O_2 among different patterns studied here yields a band gap as small as 25 meV. No matter how the coverage and pattern of adsorbed O_2 be, Fermi level always occurred above but close to E_V. The energy position of O$pp\pi^*(\downarrow)$ bands are robust and are not affected by small shift of GGA optimized equilibrium position of O_2 under van der Waals attraction. According to these results the hole doping of s-SWNT by the physisorption of O_2 is not valid. This conclusion is also corroborated by Derycke *et. al.*[199] who showed that the main effect of oxygen physisorption is not to dope the bulk of the tubes, but to modify the barriers of the metal-semiconductor contact. It should be noted that the metallization of the tube can occur only by the lowering of O$pp\pi^*(\downarrow)$ states and

dipping into the valence band of the s-SWNT. As a result, charge is transferred from s-SWNT to the molecule, whereby the physisorption state changes into a chemisorption state. This argument is corroborated by the fact that the same $pp\pi^*(\downarrow)$ level of single O_2^- molecule is lowered significantly. It appears that the lowering of O$pp\pi^*(\downarrow)$ state and hence electron transfer from C atoms to O_2 does not occur by itself; it may be prevented by a kinetic barrier.[194] Perhaps adsorption at a different environment, such as a defect site and impurity, or other factors help to overcome the kinetic barrier. (iv) The metallic (6,6) tube continues to be metallic for spin-up bands of SWNT which cross at E_F. Spin-down bands of SWNT open a gap, and empty $Opp\pi^*(\downarrow)$ states are located in this gap.

(v) Character of binding and range of the binding energy of O_2 adsorbed on the metallic $(6,6)$ armchair tube are similar to those on the semiconducting $(8,0)$ tube. (vi) Dissociation of O_2 molecule and then chemisorption of individual O atoms is an exothermic process. However, an O_2 molecule physisorbed on a perfect $(8,0)$ tube cannot dissociate by itself at low temperature owing to a finite activation energy. Our calculations predict that individual O atoms are adsorbed preferably on top of the C–C bonds and bind with C atoms by forming directional O–C bonds. On the other hand, a metal atom like Al favors the H-site leading to non-directional bonds between metal atom and SWNT.[113, 200] The axial C–C bond survives after an oxygen atom is chemisorbed on top of this bond. In contrast, upon O chemisorption the zigzag C–C bond is broken while C–O bond is strengthen. The oxidation of the nanotube in the conventional sense starts with the breaking of the strained zigzag C–C bonds upon the chemisorption of O. The band gap of the $(8,0)$ tube is further opened at high O coverage.

We obtained different behavior for different tubes as d decreases. While O_2 physisorbed at the H-site of the (6,6) SWNT is dissociated at $d \sim 1.25$Å. Singlet bound states of O_2 occur at $d \sim 1.47$Å for the A- and Z- sites of the (8,0) SWNT, and for the B- site of the (6,6) SWNT. These conclusions are expected to be valid for similar tubes with different radii, except that the binding energies are modified due to the curvature effect. [113, 171]

Chapter 5

Adsorption of individual atoms on SWNT

As we have shown through adsorption of O_2 and on the surface of SWNTs[1, 201, 202] can be functionalized by adsorption of atoms or molecules, which can induce dramatic changes in the physical and chemical properties of the bare tube. Functionalization of SWNTs has been attracting our interest for two possible, insofar technologically important applications; namely fabrication of metallic nanowires and nanomagnets. As nanoelectronics are promising rapid miniaturization providing higher and higher device density and operation speeds, the fabrication of interconnects with high conductance and low energy dissipation appear to be real technological problems.

Theoretical studies [200] have indicated that stable rings and tubes of Al atoms can form around a semiconducting SWNT. It is argued that either persistent currents through these conducting nanorings, or conversely very high magnetic fields can be induced at their center.[200] Such a set-up has been also proposed as possible qubits in quantum computation.[216]It has been shown experimentally that the implementation of iron atoms inside the tube can give rise to magnetization.[217] Such a system may be specified as nanomagnet, and can be used in several applications ranging from various research tools to high density

storage devices.

It is expected that novel molecular nanomagnets and electromagnetic devices can be generated from these metallic nanostructures formed by the adsorption of specific atoms on the surface of SWNTs. Thus, the study of adsorption of atoms on nanotube surfaces is essential to achieve low resistance ohmic contacts to nanotubes, to produce nanowires with controllable size, and to fabricate nanomagnets and functional nanodevices.

This chapter presents our study of the adsorption of individual transition metal atoms on the surface of a semiconducting (8,0) and also a metallic (6,6) SWNT. The binding geometry and binding energy and resulting electronic structure of various (most of the transition metal atoms) have been investigated. The prime objective is to reveal the character and geometry of the bonding, and to understand why transition metal atoms form strong bonds while others are only weakly bound. The effect of the adsorption on the physical properties, such as electronic, magnetic, is another issue, which we deal in detail in this work. Specifically, we addressed the question whether the ground state of a SWNT with an adsorbed atom has a net spin. We have explored the situation whether the magnetic ground state gives rise to the bands with one type of spin. We believe that our results are important for a number of applied and theoretical research, such as coating of carbon nanotubes, design and fabrication of functionalized nanodevices and nanomagnets, spintronics, gluing and solding SWNTs, and forming metal-SWNT junctions and contacts.

5.1 Method of calculations

Spin-unpolarized and spin-polarized (relaxed) DFT calculations within GGA have been carried out for single atom, bare SWNT, and single atom absorbed SWNT. Ultra soft pseudopotentials [89] and plane waves up to an energy cutoff of 300 eV are used. The Brillouin zone of the supercell is sampled by (1,1,11) **k**-points within the Monkhorst-Pack special **k**—point scheme.[83] Calculations have been

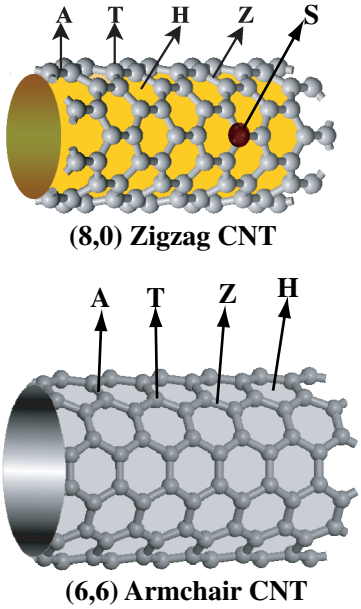

Figure 5.1: A schematic description of different binding sites of individual atoms adsorbed on a zigzag (8,0) tube. H: hollow; A: axial; Z: zigzag; T: top; S: substitution sites.

performed in momentum space by using periodically repeating tetragonal super-cell with lattice constants, $a_s = b_s \sim 15$ Å and c_s. To minimize the adsorbate-adsorbate interaction, the lattice constant along the axis of the tube, c_s, is taken to be twice the 1D lattice parameter of the bare tube, *i.e.* $c_s \sim 2c$ for the zigzag SWNT and $c_s \sim 4c$ for the armchair SWNT.

For the adsorption of individual atoms we considered four possible sites (*i.e.* H-site, above the hexagon; Z-, and A-sites above the zigzag and axial C-C bonds; and T-site above the carbon atom) as described in Fig. 6.1.

The binding energies $E_b^{u(p)}$ are obtained from the total energies corresponding to either non-magnetic (spin-unpolarized) state with zero net spin or magnetic (spin-relaxed) state with net spin. A bare nanotube has a non-magnetic ground state with zero net spin. $E_b^{u(p)} > 0$ corresponds to a CG optimized stable structure and indicates the bonding (a local or global minimum on the Born-Oppenheimer surface). Only the short range (chemical) interactions are included in the binding

energy, $E_b^{u(p)}$. Long range Van der Waals interaction, E_{VdW} is expected to be much smaller than the chemisorption binding energy and is omitted. However, for specific elements the binding energy is small and the character of the bond is between chemisorption and physisorption. In this case, the weak and attractive Van der Waals interaction energy is comparable with the physisorption energy. It can be calculated from the asymptotic form of the Lifshitz's formula.[189]

5.2 Binding geometry and binding energy

The cohesive energies of C atoms in the (8,0) and (6,6) tube, *i.e.* $E_c = (NE_T^u[C] - E_T^u[SWNT])/N$, (N being the number of C atoms in the unit cell of SWNT) are calculated to be $E_c^{(8,0)}$ =9.06 eV and $E_c^{(6,6)}$ =9.14 eV, respectively. The zigzag (8,0) SWNT is an insulator with a calculated band gap, E_g =0.64 eV. The (6,6) armchair SWNT is a metal, since π^*-conduction and π-valence bands cross at the Fermi level. As far as the electronic properties are concerned, our study has sampled two extreme cases in the class of SWNTs. The binding geometries and binding energies E_b^u, calculated from spin-unpolarized total energies are given in Table 5.1 for the (8,0) SWNT and in Table 5.2 for the (6,6) SWNT.

We note that specific adsorbate-SWNT (A+SWNT) systems are found to be in a magnetic ground state, hence $E_T^p[A+SWNT] < E_T^u[A+SWNT]$. No matter what the value of the binding energy is, a stable binding of a particular A+SWNT geometry is meaningful if it belongs to a ground state. In Table 5.3 and Table 5.4 we present the differences between the spin-unpolarized and spin-polarized total energies, *i.e.* $\Delta E_T = E_T^u[A+SWCT] - E_T^p[A+SWNT]$. Here $\Delta E_T > 0$ indicates that magnetic ground state with a net spin is favored.

We can extract following useful information from the results of calculations listed in these Tables. In general, the binding energies calculated for non-magnetic state are higher than those corresponding to the magnetic ground state. Most of the transition metal atoms adsorbed on the (8,0) and (6,6) SWNT have magnetic ground state with $\Delta E_T > 0$, and hence they give rise to the net magnetic

Table 5.1: Calculated binding energies and average carbon-adatom bond distances, $\bar{d}_{C-A}$ of individual atoms adsorbed at H-, Z-, A-, and T-sites of the (8,0) SWNT as described in Fig. 6.1. Binding energies, E_b^u are obtained from spin-unpolarized total energies calculated for fully relaxed atomic structure. . →H implies that the adatom at the given site is not stable and eventually it moves to the H-site.

Atom	H (eV)	A (eV)	Z (eV)	T (eV)	$\bar{d}_{C-A}$ (A^o)
Ti	2.9	2.1	2.7	2.1	2.2
V	3.2	2.2	→ H	→ H	2.1
Cr	3.7	2.5	→ H	→ H	2.0
Mn	3.4	2.5	→ H	→ H	2.1
Fe	3.0	2.5	→ H	1.6	2.1
Co	2.8	2.5	→ H	→ H	2.1
Ni	2.2	2.4	2.3	→ A	1.9
Cu	0.5	0.8	0.6	→ A	2.1
Zn	0.05	0.05	0.03	0.04	3.7
Mo	4.6	3.0	→ H	→ H	2.2

Table 5.2: Calculated binding energies and average carbon-adatom bond distances, $\bar{d}_{C-A}$ of individual atoms adsorbed at H-, Z-, A-, and T-sites of the (6,6) SWNT as described in Fig. 6.1. Binding energies, E_b^u are obtained from spin-unpolarized total energies calculated for fully relaxed atomic structure.

Atom	H (eV)	A (eV)	Z (eV)	T (eV)	$\bar{d}_{C-A}$ (A^o)
Ti	2.62	1.66	1.79	1.74	2.2
Mn	3.25	→ H	→ H	→ H	2.1
Mo	4.34	→ H	→ H	→ H	2.2
Au	0.23	0.27	→ T	0.41	2.3

Table 5.3: Strongest binding site (as described in Fig. 6.1); adsorbate-C distance $\bar{d}_{C-A}$; the difference between spin-unpolarized and spin-polarized total energies ΔE_T; binding energy E_b^u obtained from spin-unpolarized calculations; binding energy E_b^p obtained from spin-polarized calculations; magnetic moment (μ_B per supercell) of the magnetic ground state corresponding to the adsorption of various individual atoms on the (8,0) SWNT.

Atom	Site	$\bar{d}_{C-A}(A^o)$	$\triangle E_T(eV)$	$E_b^{su}(eV)$	$E_b^{sp}(eV)$	$\mu(\mu_B)$
Ti	H	2.2	0.58	2.9	2.2	2.21
V	H	2.2	1.20	3.2	1.4	3.67
Cr	H	2.3	2.25	3.7	0.4	5.17
Mn	H	2.4	2.42	3.4	0.4	5.49
Fe	H	2.3	1.14	3.1	0.8	2.27
Co	H	2.0	0.41	2.8	1.7	1.05
Ni	A	1.9	0.02	2.4	1.7	0.04
Cu	A	2.1	0.03	0.8	0.7	0.53
Zn	H	3.7	0	0.05	0.04	0
Mo	H	2.2	0.32	4.6	0.4	4

Table 5.4: Strongest binding site (as described in Fig. 6.1); adsorbate-C distance $\bar{d}_{C-A}$; the difference between spin-unpolarized and spin-polarized total energies ΔE_T; binding energy E_b^u obtained from spin-unpolarized calculations; binding energy E_b^p obtained from spin-polarized calculations; magnetic moment μ per supercell corresponding to the magnetic ground state corresponding to the adsorption of individual Ti, Mn, Mo, Au atoms on a (6,6) SWNT.

Atom	Site	$\bar{d}_{C-A}(A^o)$	$\triangle E_T$(eV)	E_b^{su}(eV)	E_b^{sp}(eV)	$\mu(\mu_B)$
Ti	H	2.2	0.48	2.62	1.81	1.68
Mn	H	2.5	2.23	3.25	0.1	5.60
Mo	H	2.3	0.2	4.34	0.1	3.61
Au	T	2.3	0.02	0.41	0.28	0.79

moment ranging from $5.49\mu_B$ (for Mn) to zero magnetic moment. Ni adsorbed SWNT has very low magnetic moment ($0.04\mu_B$). Our spin-polarized and spin-unpolarized calculations show that these transition metal atoms in Table 5.3 have also magnetic ground state when they are free. Since a bare SWNT having a non-magnetic ground state, the net spin of the A+SWNT system originates from the magnetic moment of the adsorbed atom. The calculated magnetic moments of these free atoms are in good agreement with the values given by Moore.[222] The magnetic moment generated upon the adsorption of individual transition atoms has important implications, and points to an issue, whether molecular magnets (or nanomagnets) can be produced from carbon nanotubes. Addressing this issue may open an active field of study of transition metal atom covered according to a well-defined pattern or substitutional transition atom doped SWNTs. Implementation of transition metal atoms inside the tube might be another interesting subject of study. Whether a permanent magnetic moment by the exchange interaction can be generated on these transition metal coated SWNTs would be an interesting question to answer. Recently, the magnetization and hysteresis loops of iron nanoparticles partially encapsulated at the tips and inside of aligned carbon nanotubes have been demonstrated by recent experimental works.[217]

Figure. 5.2 presents the variation of the ground state properties[223] (such as the cohesive energy E_c and bulk modulus B), binding energies E_b^u and E_b^p of the first row transition metal elements with respect to the number of d-electrons N_d. $E_c(N_d)$ and $B(N_d)$ curves show a minimum (at $N_d = 5$ for the $3d^5 4s^2$ configuration of Mn atom) between two maxima of equal strength; first maximum occurs at $N_d = 3$ or 4, the second one at $N_d = 7$. This behavior of bulk properties were explained by the Friedel model.[224] Although the overall shape of the variation of the binding energies of first row transition metal atoms with N_d, $E_b^p(N_d)$ is reminiscent of the $B(N_d)$ and $E_c(N_d)$, there are some differences. The binding energy of Ti($N_d = 2$) is highest, and hence the first maximum is higher than the second one $E_b^p(N_d = 7)$ and $E_b^p(N_d = 8)$ corresponding to the binding energies of Co and Ni. While the binding energy of Sc(N_d=1) is close to that of Ti at the first maximum, the binding energy of Cu($N_d = 10$) is small, and it eventually decreases to almost zero for Zn, which has a filled valence shells (i.e $3d^{10}4s^2$).

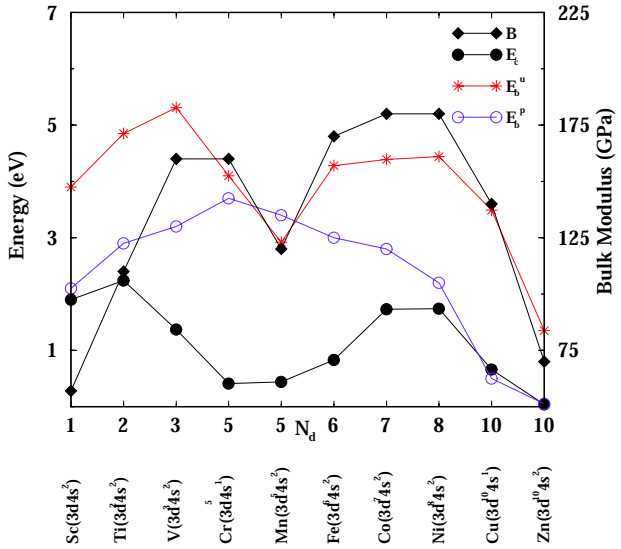

Figure 5.2: Variation of the calculated spin-unpolarized E_b^u and spin-polarized E_b^p binding energy of transition metal atoms with respect to the number of d-electrons N_d. The bulk cohesive energy E_c and the bulk modulus B from Ref. [75] is included for the comparison of the trends.

Interestingly, Cr and Mn atoms which have the same $3d^5 4s^2$ configuration, have similar binding energies forming the minimum between double maximum, but different E_c and B. The variation of E_b^u and E_b^p with N_d, however, shows dramatic differences. While $E_b^p(N_d)$ mimics $E_c(N_d)$ and has a minimum for N_d =5, as E_c and B do, E_b^u passes through a maximum. This situation confirms that magnetic states correspond to ground state.

Binding energies listed in Table 5.3 are of particular interest for coating of SWNTs by metal atoms, and hence for the fabrication of nanowires. We also note that in forming a good coverage not only adatom-SWNT interaction, but also other factors, possibly adatom-adatom interaction play a crucial role. Here we point out an interesting trend between Table 5.1 and Table 5.2, and also between Table 5.3 and Table 5.4. The binding energies E_b^u, as well as E_b^p and magnetic moments of the adatom adsorbed on the (8,0) SWNT came out to be consistently lower for the adatom adsorbed on the (6,6) tube. Perhaps, this trend can also be explained by the curvature effect.[113, 118]

The transition metal atoms with a few d-electrons, such as Sc, Ti, Nb, Ta

form strong bonds with a binding energy ranging from 2.4 eV to 1.8 eV, and hence can be suitable for metal coating of SWNT. These metals can also be used as a buffer layer to form uniform coating of good conductors such as Au, Ag, Cu. Most of the adatoms we studied yield strongest binding at the H-site.

5.3 Electronic structure of adatom-SWNT system

Modification of electronic structure induced by the adsorbed foreign atoms is the prime interest of this study. We analyze the induced modifications by energy band structure and local and total density of states obtained for fully relaxed structures. An individual atom adsorbed on an SWNT may give rise to resonance states in the valence and conduction bands, and also localized states in the band gaps. Owing to the supercell method used in this study the energy states associated with an single adsorbate form energy bands, however. Actually these bands correspond to a linear chain of adsorbates with a 1D lattice constant c_s. The dispersion or width of the bands is a measure of the adsorbate-adsorbate coupling.

5.3.1 Semiconducting (8,0) SWNT

The localized states are relevant for the doping of a semiconducting SWNT. Depending on their position relative to the band edges they are specified as donor states (if they are close to the edge of the conduction band E_C) or as acceptor states (if they can occur close to the edge of the valence band, E_V). The latter case is also known as hole doping. Whether the associated localized state is a donor or acceptor state can be inferred from the energy position of the band in the gap.

In Fig. 5.4 the spin-polarized band structure and TDOS of adsorbed transition metal atoms (*i.e.* Au, Mn, Mo, and Ti) display a different situation due to magnetic ground state. Au yield two bands in the band gap of bare SWNT;

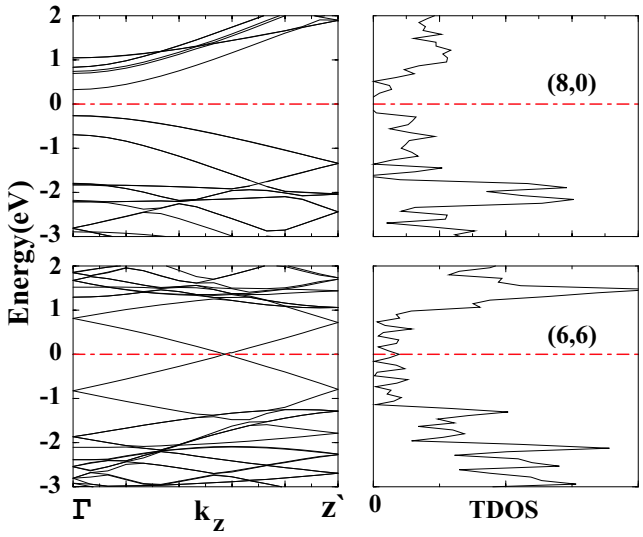

Figure 5.3: Energy band structures and total density of states (TDOS) of bare tubes with fully relaxed atomic structure. (a) Electronic structure of the semiconducting (8,0) zigzag SWNT calculated for the double primitive unit cells consisting of 64 C atoms. (b) same for the metallic (6,6) armchair SWNT calculated for the quadruple primitive unit cells including 96 C atoms. Zero of energy is set at the Fermi level E_F.

these are filled Au spin-up and empty spin-down bands. This is in compliance with the calculated magnetic moment of 1.02 μ_B per adsorbed Au atom. There is a small band gap of $\sim$0.2 eV between these Au bands. Comparing these bands with those of bare (8,0) SWNT in Fig. 5.3(a), we see that the adsorbtion of Au did not induce significant modification in the bands of (8,0), except the Au $6s(\uparrow)$ and Au $6s(\downarrow)$ bands in the gap, give rise to two sharp peaks below and above E_F, respectively in TDOS. That the contribution of SWNT states to these peaks is minute and the band gap between the conduction and valence bands of SWNT is practically unchanged confirms the weak interaction between Au and SWNT. Filled Au $5d(\uparrow)$ and $5d(\downarrow)$ bands occur in the valence band of SWNT 2 eV below E_F. Free Mn atom has normally $(3d^5)(4s^2)$ configuration and has magnetic moment of $5\mu_B$. The flat spin-up and spin-down bands of Mn occur in the band gap and near the edge of valence band. The band gap between the highest occupied spin-up and lowest empty spin-down band is very small (< 0.1 eV). The d-bands of adsorbed Mo occur in the band gap and near the top of

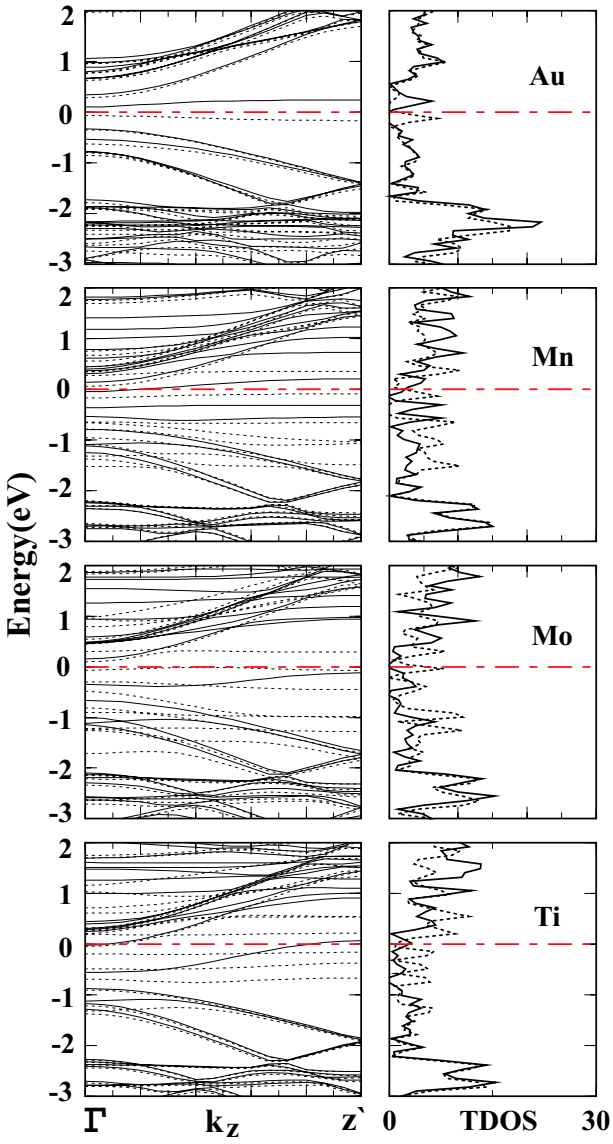

Figure 5.4: Energy band structures and total density of states (TDOS) of single Au, Mn, Mo, and Ti adsorbed on a zigzag (8,0) tube. Zero of energy is set at the Fermi level. Bands and state density of spin-up and spin-down states are shown by dotted and continuous lines, respectively. Mn, Mo, Ti are adsorbed at the H-site; and Au is adsorbed at the T-site.

the valence band of SWNT. The band gap between the highest occupied spin-up band and the lowest spin-down band is ∼0.2 eV. Thus, the highest occupied state due to Mo occurs near the edge of conduction band. The number of $4d(\uparrow)$ bands confirm that the net magnetic moment of Mo adsorbed SWNT is $4\mu_B$ per cell. Three bands formed from Ti $3d(\uparrow)$ are fully occupied and accommodate 3 electrons of adsorbed Ti atom. Other Ti $3d(\uparrow)$ bands occur above E_F, but they overlap with the conduction band of SWNT. The dispersive and almost fully occupied spin-down band is formed from the states of carbon and hence derived from the conduction band of the bare SWNT. The SWNT is metallized upon Ti adsorbtion, since this band cross the Fermi level and also overlap with the other conduction bands. This situation is in accordance with the Mulliken analysis, which predicts electrons are transferred from Ti to SWNT.

5.4 Discussions

We have shown that interesting physical properties can be generated by the adsorption of single atom on a SWNT. Changes in the physical properties depend on the valency of the adsorbate. Na having $3s$-valence state with small ionization potential donates this valence electron to the empty conduction band of semiconducting SWNT. Therefore, adsorption of Na results in the metallization of the (8,0) tube. Similar effects occur upon the adsorption of Al. However, adsorption of individual transition metal atoms gives rise to dramatically different results. Because of their occupied d-states, the transition metal adsorbed SWNT has a magnetic ground state. In most of the cases, adsorbed individual transition atom gives rise to a band gap between spin-up and spin-down bands within the supercell geometry. Ti , that leads to a metal, appears to be an exception. Another important property that is specific for Ti is its continuous coating of SWNT. This should be related to both Ti-Ti and Ti-SWNT interaction. Whether the Ti covered SWNT leads to regular atomic structure, and the nanowire produced from Ti covered SWNT allows ballistic quantum transport are important issues requiring further investigations. The adsorption of transition metal atoms on the (6,6) tube exhibits similar trends as the (8,0) tube, except that the binding

energies in the former are consistently smaller. We attribute this behavior to the relatively smaller curvature of the (6,6) tube.

Higher coverage and decoration of adsorbed foreign atoms can produce nanostructures (such as nanomagnets, nanometer size magnetic domains, 1D conductors and thin metallic connects, and electronic devices) which may find interesting technological application, such as spintronics and high density data storage, and interconnects between devices. The d-orbitals of the transition metal atoms are responsible for relatively higher binding energies, which display an interesting variation with the number of filled d-states.

Chapter 6

Metal-atom coverage of SWNTs

Motivated by the experimental work of Zhang *et al.* [72] showing the continuous coating of SWNT by Ti, we investigated the coverage of (8,0) tube by specific transition element atoms, such as Ti, Fe, Co, Cr, *etc.*, and metal-atom coverage such as Ga element.

6.1 Magnetic nanowires obtained from uniform transition-metal-atom coverage of carbon nanotubes.

The fabrication of interconnects with high conductance and low energy dissipation has been a real challenge in rapidly developing field of nanoelectronics. Very thin metal wires and atomic chains have been produced by retracting the STM tip from an indentation and then by thinning the neck of the materials that wets the tip.[204, 205, 226] While those nanowires produced so far played a crucial role in understanding the quantum effects in electronic and thermal conductance,[102, 191, 207, 208] they were neither stable nor reproducible to offer any relevant application. It has been shown that SWNTs can serve as templates to produce reproducible, very thin metallic wires with controllable sizes.[210] Continuous Ti

coating of varying thickness, and quasi continuous coating of Ni and Pd were obtained by using electron beam evaporation techniques.[211] Good conductors, such as Au, Al, were able to form only isolated discrete particles or clusters instead of a continuous coating of SWNT. Low resistance ohmic contacts to metallic and semiconducting SWNTs have been achieved also by Ti and Ni atoms.[212] In spite of the impact made by these experimental works[210, 211, 212] there has been very little effort so far to present an atomic scale understanding of uniform Ti coverage.

In this study we show that a semiconducting s-SWNT is transformed to a good conductor as a result of Ti coverage. Moreover, Ti covered tubes have magnetic ground state with a net magnetic moment. These results have important implications in nanoscience and nanotechnology. We carried out first-principles, spin-unpolarized (SU) and spin-relaxed (SR) calculations within the generalized gradient approximation[122]. Calculations have been performed in momentum space by using periodically repeating tetragonal supercell with lattice constants, $a_s = b_s \sim 20$ Å and $c_s = c$ (c being the 1D lattice constant of SWNT). The Brillouin zone of the supercell is sampled by using special **k**-point scheme. All atomic positions (*i.e.* all adsorbed Ti atoms and carbon atoms of SWNT), as well as c_s(hence c) have been optimized. Using same parameters of calculations we achieved to reproduce structural parameters of bulk Ti, as well as Ti_2 and Ti_3 molecules.

An individual Ti atom is adsorbed at specific sites on the external and internal surface of SWNT. The H-site, *i.e.* above the center of hexagon formed by C-C bonds, is found to be energetically most favorable site with a binding energy of $E_b = 2.2$ eV for the magnetic ground state. The average C-Ti distance, $\overline{d}_{C-Ti}$ has been found to be 2.2 Å. At the internal H-site, the bonding is stronger and the binding energy is $E_b = 2.5$ eV, the average bond distance $\overline{d}_{C-Ti} = 2.3$Å[220]. The magnetic moment of the individual Ti absorbed (8,0) SWNT is calculated to be $\mu = 2.2\mu_B$ (Bohr magneton). Ti $3d$-orbitals play a crucial role in the bonding and electrons are transferred from Ti to SWNT.[220, 227]

6.1.1 Geometrical Analysis

A strong Ti-SWNT chemical interaction is responsible from the continuous coating. Here, the Ti coverage of (8,0) SWNT has been analyzed first by attaching Ti atoms at all H-sites in the unit cell, and subsequently by optimizing the atomic structure and the lattice constant c. The relaxation of the SWNT lattice was crucial in obtaining stable structures; frozen lattice constant has led to instabilities. The average binding energy, $\bar{E}_b = (16E_T[Ti] + E_T[SWNT] - E_T[16Ti + SWNT])/16$, has been found (in terms of the total energies of individual Ti atom, optimized bare SWNT and Ti covered SWNT) to be 4.3 eV. Apparently, owing to the Ti-Ti coupling, $\bar{E}_b$ comes out much higher than the binding energy of the adsorbed single Ti atom. For the same reason the charge transfer from Ti to C has decreased to $\sim$0.3 electrons, and $\bar{d}_{C-Ti}$ increased to $\sim$ 2.5Å.

The optimized atomic structure shown in Fig. 6.1 depicts an interesting feature of the Ti covered SWNT. Atoms have rearranged in a quasi 1D "crystalline" structure and formed a square-like cross section. We distinguish three specific C atoms (identified as C1, C2, and C3) and three Ti atoms (Ti1, Ti2 and Ti3) depending on their different bonding geometry. The C1 and Ti1 atoms located at the corner of square are at the high curvature site, while C3 and Ti3 are at the flat region. In spite of the periodic arrangement of adsorbed Ti and underlying C atoms, the Ti-Ti, Ti-C, and C-C bond-distances show some dispersion depending on their location. The histogram in Fig. 6.1 identifies different types of bonds at different places.

6.1.2 Electronic Transport

The energy band structure and the TDOS of the Ti covered (8,0) SWNT are presented in Fig. 6.7. The band structure of the bare semiconducting (8,0) SWNT has changed dramatically having several bands crossing the Fermi level. Accordingly, the Ti covered SWNT becomes a good conductor with high density of states at the Fermi level, $\mathcal{D}(E_F)$. The current associated with the electron transport can be given by a Landauer type expression,[228]

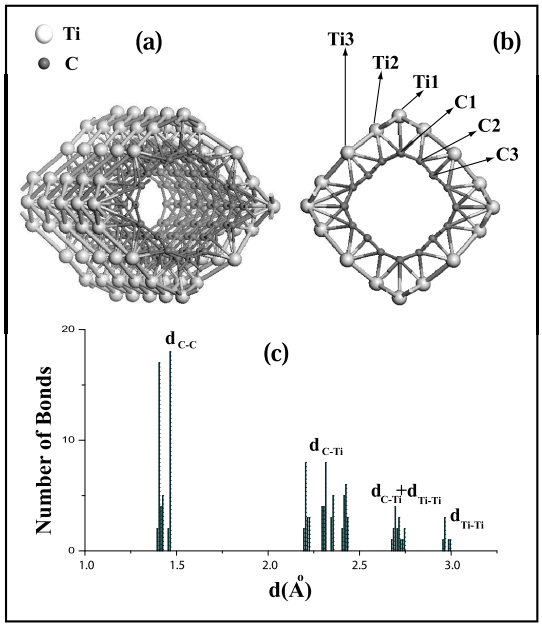

Figure 6.1: (a) Fully optimized atomic structure of Ti covered (8,0) SWNT. (b) The cross section with different types of C atoms (identified as C1, C2, and C3) and adsorbed Ti atoms (Ti1, Ti2 and Ti3). Dark-small and light-large circles indicate C and Ti atoms, respectively. (c) Histograms show the variation of bond-lengths of different carbon-carbon ($\overline{d}_{C-C}$), carbon-Ti ($\overline{d}_{C-Ti}$) and Ti-Ti ($\overline{d}_{Ti-Ti}$) bonds.

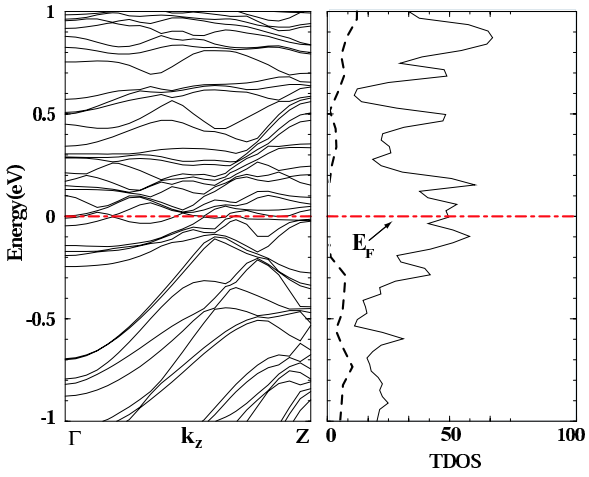

Figure 6.2: (a) Electronic energy band structure of a Ti covered (8,0) SWNT. (b) The total density of states (TDOS). TDOS of bare (8,0) tube is shown by dashed lines. Zero of energy is taken at the Fermi level.

$$I(V_b) = \frac{2e^2}{h} \int_{\mu_R}^{\mu_L} dE(f_L - f_R)\mathcal{T}(E, V_b)dE \tag{6.1}$$

in terms of the bias voltage V_b; the Fermi distribution function of left and right electrodes f_L and f_R, and their chemical potentials μ_L and μ_R. $\mathcal{T}(E, V_b)$ is the transmission function for the total electrons calculated using the Green's function approach. Electron scattering in the contacts is crucial for the calculation of conductance. Therefore, the calculation of quantum conductance **G** of an interconnect between two electrodes requires detailed description of the contacts and phonon spectrum at the operation temperature. Here, since we are concerned only with the nanowire, we infer **G** from an ideal Ti covered SWNT. Under these circumstances, the mean free path of electrons l_m becomes infinite at T=0, and the electronic transport occurs ballistically and coherently. This situation has been treated as an ideal 1D constriction, where the electrons are confined in the transversal direction, but propagate freely along the axis.[102] The current is expressed as $I = \sum_i 2\eta_i e v_i[\mathcal{D}_i(E_F + eV_b) - \mathcal{D}_i(E_F)]$ where degeneracy, group velocity and density of states of each subband crossing E_F are given by η_i, v_i, $\mathcal{D}_i$, respectively. Since $\mathcal{D}_i(E_F + eV_b) - \mathcal{D}_i(E_F) \sim (eV_b)d\mathcal{D}_i(E)/dE \mid_{E_F}$ and $v_i = (h^{-1})\partial\mathcal{D}_i/\partial E \mid_{E_F}$, then $G = I/V_b = \sum_i 2\eta_i e^2/h$. Accordingly each subband crossing the Fermi level is counted as η_i current-carrying state for two spins with channel transmission $\mathcal{T} = 1$. Then the maximum "ideal" conductance of defect-free Ti covered ideal tube becomes $G = 2e^2 N_b/h$, where $N_b = \sum \eta_i$. Calculated conductance is four times higher than that of bare metallic armchair tube. High $\mathcal{D}(E_F)$ in Fig. 6.7 justifies this result.

In reality, $\mathcal{T}(E)$ in Eq. 6.1 is reduced due to scattering of carriers from the abrupt change of cross sections and irregularities at the contacts to electrodes and from the imperfections, impurities, and electron-phonon scattering in the tube by itself. In a self-consistent treatment the contact potential also causes $\mathcal{T}$ to decrease. Therefore, a rigorous treatment of the conductance of a finite-size Ti coated SWNT (device) requires a detailed description of electrodes and the contact structure. We note that the regular structure shown in Fig. 6.1 may occur under idealized conditions; normally irregularities are unavoidable, in particular for a thick Ti coating. While the channel transmission is decreased in the thick

but inhomogeneous Ti coating, **G** is expected to be still high owing to the new conductance channels opened at E_F. Based on these arguments and in view of the high $\mathcal{D}(E_F)$ in Fig. 6.7, the conductance of a Ti coated tube can be several $2e^2/h$.

Any defect in 1D system gives rise to the localization of current transporting states which is characterized by the localization length ξ. While $\xi \sim l_m$ for a strictly 1D wire, $\xi \sim l_m d/\lambda_F$ for a 1D stripe and $\xi \sim l_m d^2/\lambda_F^2$ for a wire with width or diameter d and Fermi wavelength, $\lambda_F = h/mv_F$.[229] We expect that for the present Ti covered SWNT $\xi \sim l_m(d/\lambda_F)^\alpha$ with $1 < \alpha < 2$. Then the net resistance of (Ti+SWNT) wire having length L between two contact and including contact resistance R_c and localization effect can be given by $R = R_c + he^{L/\xi}/2e^2$. A very crude estimation yields $\xi \geq 200$Å, which is much larger than a typical L for interconnects in nanoelectronics.

The origin of metallicity is the next question we will address. First, let us consider the nanotube having the same atomic configuration, hence the same square-like cross section as in Fig. 6.1, but depleted from all adsorbed Ti atoms. The local densities of states (LDOS) at C1, C2, and C3 carbon atoms in Fig. 6.3(a) clarify whether such a deformed SWNT continues to be semiconducting. For the atom C3, which is located at the center of the edge of square, *i.e.* at the flat region of the tube the state density vanishes at E_F. In contrast, as one approaches the corner, LDOS at E_F increases, and eventually at C1 (*i.e.* the atom at the corner of the square) has the highest density. This situation implies that the square nanotube by itself (without Ti) can be viewed as if four metal strips passing through its four corners, and four semiconductors at the flat edges. The metallization is induced by the singlet conduction band that crossed the Fermi level due to enhanced $\pi^* - \sigma^*$ hybridization at the corner region in Fig. 6.3(a) and 6.3(b) [113, 118, 230]. In Fig. 6.3(c), the LDOS and orbital projected LDOS calculated at Ti atoms have high state density at E_F due to the states derived mainly from Ti $3d$-orbitals. Accordingly, the main contribution to the high $\mathcal{D}(E_F)$ in Fig. 6.7 is due to adsorbed Ti atoms, but the underlying carbon tube itself has some contribution.

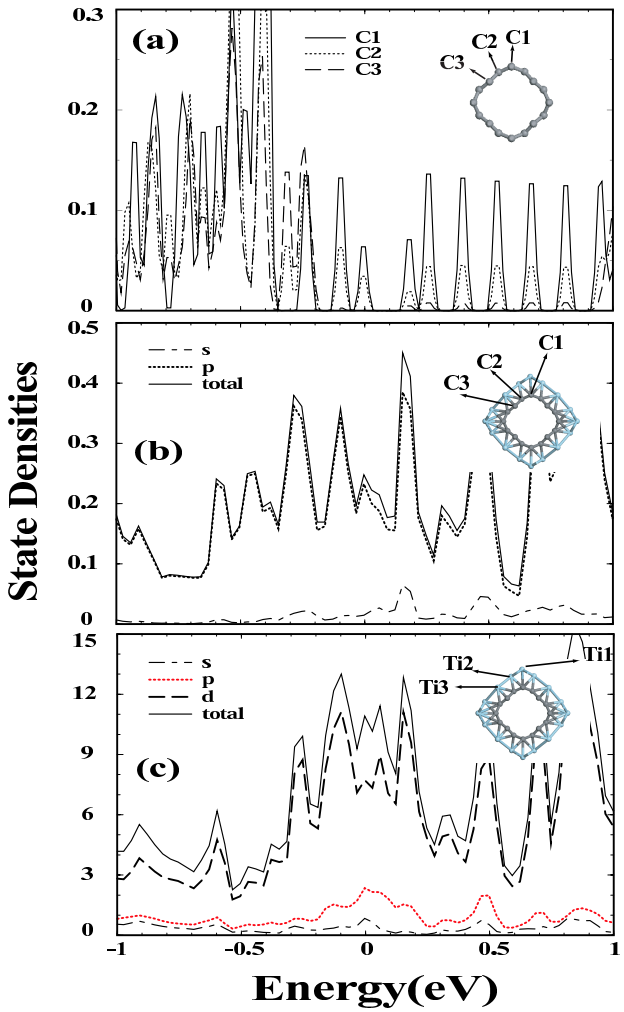

Figure 6.3: Calculated state densities.(a) Local density of states (LDOS) on C1, C2, C3 atoms of carbon nanotube which has the same atomic configuration and square-like cross section as the carbon nanotube covered by Ti as shown in Fig. 6.1. See inset. (b) LDOS on the carbon atoms of the Ti covered SWNT (*i.e.* C1+C2+C3). (c) LDOS calculated on the Ti atoms of the Ti covered SWNT (*i.e.* Ti1+Ti2+Ti3). Partial density of states of *s*-, *p*-, and *d*-orbitals are also shown.

Uniform coverage of Ti on the SWNT is crucial for the future technological applications. Ti can be used as a buffer layer to form uniform coating of good conductors, such as Au, Cu, on the SWNT,[220] since these atoms have low binding energy (0.5 and 0.7 eV, respectively). Strong Ti-SWNT interaction can be utilized to bond or to connect individual SWNTs in order to form T, Y and cross junctions or grids. It appears that fabrication of photonic band gap materials or nanowave guides based on SWNT may not be a mere speculation. Earlier, it has been shown that quantum structures can be realized on a single s-SWNT through band gap modulation either by modulating radial deformation or by modulating adsorption of hydrogen atoms.[230, 231] These quantum structures can be connected to the electrodes through their both ends which are metallized by Ti coverage. This way one can fabricate an electronic nanodevice on a single SWNT, such as a Schottky barrier diode or a resonant tunnelling device.

The uniform Ti coverage of SWNT may be of interest in a completely different field of research. Individual Fe atom is weakly bound on a SWNT, but it has a magnetic ground state. The binding energy and the magnetic moment have been calculated to be $E_b = 0.8$ eV, $\mu \approx 2\mu_B$, respectively. However, our calculations have revealed that Fe, Co, Mn, Cr, Mo, and Ga atoms cannot form a uniform and continuous coverage (shown in Fig. 6.4); rather they are accumulated into small clusters attached to the surface of SWNT. Alternatively, uniform coating of Fe can be realized over the Ti covered SWNT and hence nanomagnets can be generated. The exchange interaction and the ferromagnetism of these quasi 1D nanomagnets would be an important subject of study. The individual Cr and Mn adsorbed on the (8,0) tube have also low binding energy ($E_b \sim 0.4$ eV), but high magnetic moment ($\mu = 5.17$ and 5.49 μ_B, respectively) [220]. Similar to the case of Fe, magnetic nanostructures can be obtained when these atoms cover or decorate the Ti covered SWNT. This way, the band structures of these magnetic nanostructures can be engineered for desired spin-dependent electron transport. Interestingly, the SR total energy of Ti covered (8,0) tube is found to be $\sim$ 0.6eV/cell lower than SU total energy. Hence Ti covered (8,0) tube shown in Fig. 6.1 has magnetic ground state with calculated magnetic moment

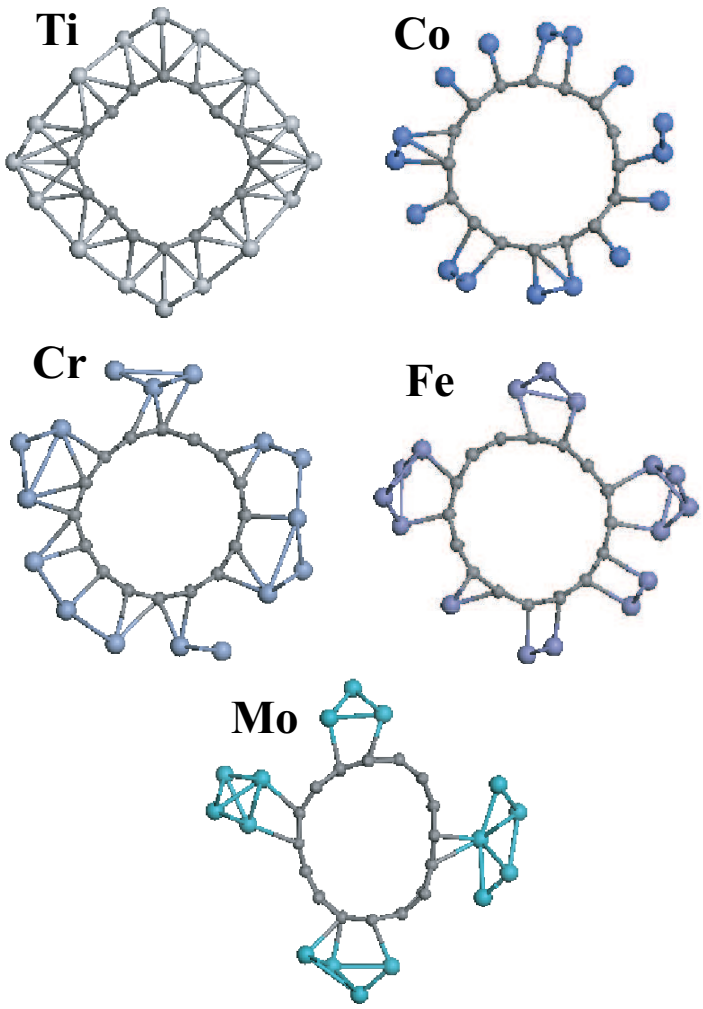

Figure 6.4: Fully optimized atomic structures of Ti, Co, Cr, Fe, Mo covered (8,0) SWNT.

of $\sim 15.3\mu_B$. The magnetization and hysteresis loops of iron nanoparticles partially encapsulated at the tips and inside of aligned carbon nanotubes have been demonstrated by recent experimental works.[217] Through *ab-initio* calculations it has been shown that SWNTs filled or coated with transition metal elements can exhibit substantial spin-polarization [232].

Finally, we demonstrated that the uniform coverage of Ti resulting in a regular atomic structure occurs also for SWNTs with different radius and chirality. Fig. 6.5 shows the optimized atomic structure of Ti covered (9,0) zigzag and (6,6) armchair tubes. The former bare tube has a very small band gap of 0.09eV, radius of 3.6Å and odd number of C atoms on the circumference. The latter tube is a metal and has radius of 4.1Å and chiral angle of 30^o when it is free of Ti. However, both tubes become metal with high $\mathcal{D}(E_F)$ and have magnetic ground state upon coverage with Ti shown in Figure 6.6. The calculated magnetic moments are $13.7\mu_B$ and 9.5 μ_B for (9,0) and (6,6) SWNTs, respectively. Sharp corners of the square-like cross section in Fig 6.1 start to be flattened and change to polygonal form for the Ti covered (6,6) SWNT.

6.1.3 Coverage and strain dependent magnetization of titanium coated SWNTs

Spintronics aims to increase the information transport capacity and versatility of electronic devices by using the spin-degrees of freedom of conduction electrons[233, 234, 235, 236, 237]. Owing to the broken spin-degeneracy in a magnetic ground state, energy bands $E_n(\mathbf{k}\uparrow)$ and $E_n(\mathbf{k}\downarrow)$ split, and may lead to different density of states for different spin orientation. Here, we elucidate our findings reported earlier as a short communication [238] by placing emphasis on the electronic structure of Ti coated SWNT corresponding to its ferromagnetic ground state and by further investigating its spin-dependent properties. We, in particular, are concerned with the spin-polarization at E_F,

$$P(E_F) = \frac{|D^{\uparrow}(E_F) - D^{\downarrow}(E_F)|}{D^{\uparrow}(E_F) + D^{\downarrow}(E_F)} \tag{6.2}$$

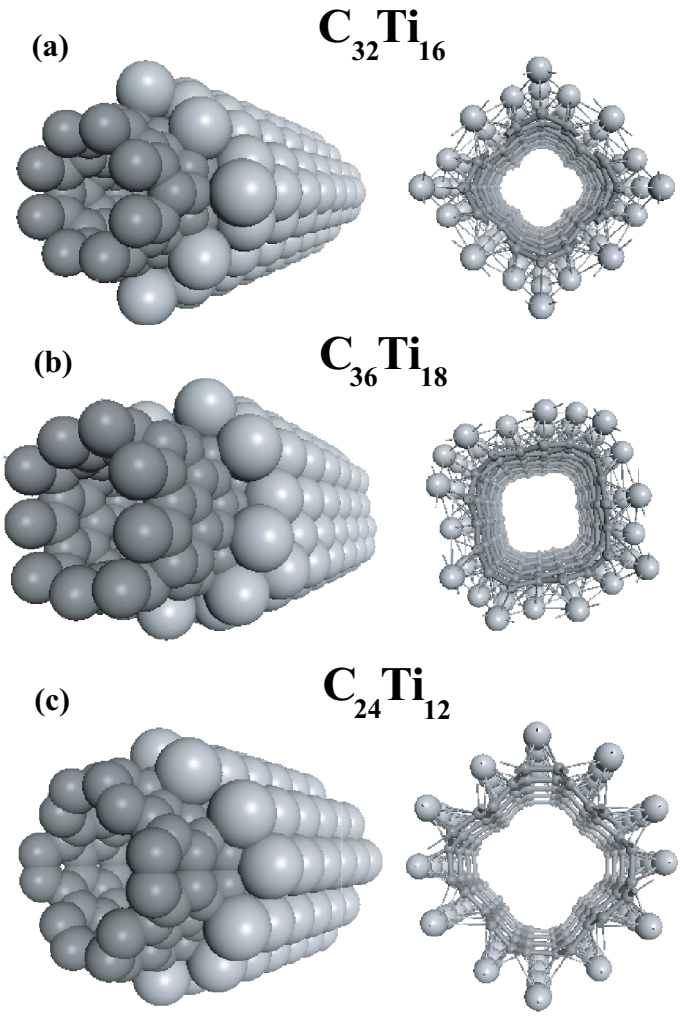

Figure 6.5: Optimized atomic structures of Ti covered: (a) (8,0) SWNT ($C_{32}Ti_{16}$); (b) (9,0) SWNT ($C_{36}Ti_{18}$); (c) (6,6) SWNT ($C_{24}Ti_{12}$).

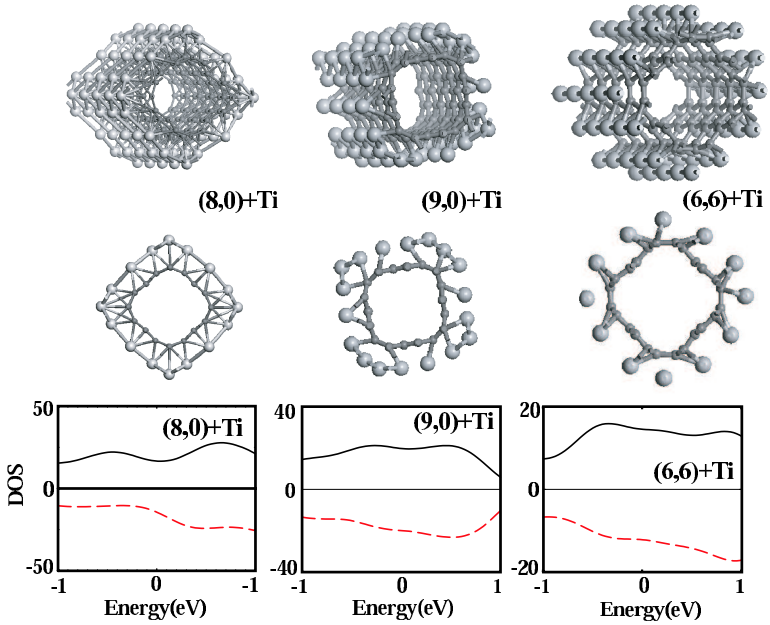

Figure 6.6: Optimized atomic structure of (8,0) and (9,0) zigzag, and (6,6) armchair SWNT which are uniform covered with Ti. Corresponding density of states for spin-up and spin-down electrons are shown.

in terms of majority (minority) spin density of states $D^{\uparrow}(E_F)$ ($D^{\downarrow}(E_F)$). We investigate how the magnetic moment μ, and $P(E_F)$ can be modified with the applied strain and amount of Ti coverage. We found that μ, as well as $P(E_F)$ depend strongly on the applied strain and on the Ti coverage. While a strain of $\epsilon_{zz} = 0.1$ along the axis of the tube induces 25% increase of μ, the adsorption of four additional Ti atoms on the Ti coated (8,0) SWNT, causes to 44% reduction of the magnetic moment. The radial strain leading to the elliptical deformation of the circular cross section modifies the spin-dependent electronic structure near E_F. The manipulation of spin-dependent properties of Ti coated SWNT with applied strain and with Ti coverage suggest interesting technological applications such as spin filter, spin-resonant-tunnelling diode, unipolar spin transistor and nanoscale magnetism, *etc.*.

Now we investigate the effect of the adsorption of additional Ti atoms on $C_{32}Ti_{16}$ surface. Whether regular atomic structure and the electronic properties of $C_{32}Ti_{16}$ are affected will be the issue we shall clarify. To this end, we consider

four additional Ti atoms are attached at the corners of the square-like cross section of $C_{32}Ti_{16}$ to make $C_{32}Ti_{20}$. The fully optimized, stable atomic structure of $C_{32}Ti_{20}$ is shown in Fig. 6.7(d). The adsorption of four additional Ti atoms corresponds to the initial stage of second Ti atomic layer to cover SWNT surface. The average binding energy of these additional Ti atoms was found to be ∼4.6 eV/atom. It is larger than that of $C_{32}Ti_{16}$ owing to the onset of Ti-Ti coupling in 3D. The effect of these four Ti atoms on the structure of $C_{32}Ti_{16}$ is minute. However, the calculated magnetic moment undergoes a dramatic change upon the chemisorption; μ of $C_{32}Ti_{16}$ decreases from 15.3 $\mu_B/cell$ to 6.8 $\mu_B/cell$ in $C_{32}Ti_{20}$. This important result implies that the net magnetic moment of Ti covered SWNT is strongly dependent on the amount, as well as geometry of Ti coverage. The magnetization of the nanostructure $C_{4n}Ti_N$ can be engineered by varying the number N, and the decoration of adsorbed Ti atoms.

Next, we examine the effect of Ti coverage on the spin-dependent electronic properties. Spin-polarized energy band structure and densities of states for majority and minority spin states of the Ti coated (8,0) SWNT are presented in Fig. 6.7. The band structure of the bare (8,0) sSWNT has changed dramatically; the band gap between conduction and valence band diminished because of several bands crossing the Fermi level. Since up-spin and down-spin state are separated, we can define corresponding $I^{\uparrow}$ and $I^{\downarrow}$. The total current in magnetic systems can be obtained as $I = I^{\uparrow} + I^{\downarrow}$ where $I^{\uparrow}$ ($I^{\downarrow}$) is the contribution to the current from majority (minority) spin current-carrying states. The current for a given spin orientation is obtained using same type of the Landauer formula[102, 137, 239],

$$I^{\uparrow(\downarrow)}(V_b) = \frac{e^2}{h}\int_{\mu_R}^{\mu_L} dE(f_L - f_R)\mathcal{T}^{\uparrow(\downarrow)}(E, V_b) \tag{6.3}$$

Here $\mathcal{T}^{\uparrow(\downarrow)}(E, V_b)$ is written for the majority or spin-up (spin-down) electrons calculated using the Green's function approach. We note that this expression differs from Eq. 6.1 since the spin of electrons are distinguished. In the above expression the mixing of spin-channels, namely the spin-flip from one orientation to the other is not allowed. In reality, owing to the coupling with phonons the spin-flip can take place. Here, since we are concerned with transport properties of

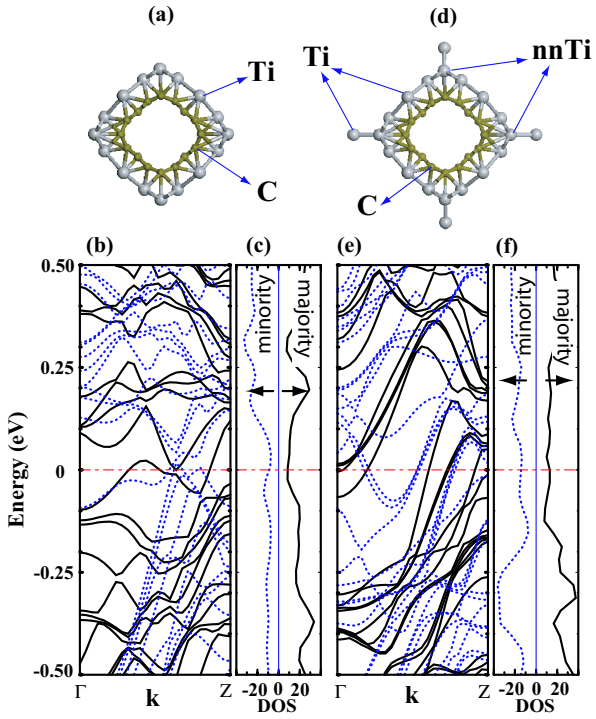

Figure 6.7: (a) Fully optimized atomic structure and square-like cross section of Ti coated (8,0) zigzag SWNT including 16 Ti atoms per unit cell ($C_{32}Ti_{16}$). Ti and C atoms are indicated by large-light and small-dark circles. (b) Spin-polarized band structure of $C_{32}Ti_{16}$ at $\epsilon_{zz} = 0$ with the Fermi level set to zero of energy. Majority spin, $E_n(\mathbf{k}\uparrow)$ and minority spin, $E_n(\mathbf{k}\downarrow)$ bands are shown by continuous and dotted lines, respectively. Spin polarized density of states for majority $D^{\uparrow}(E)$ and minority $D^{\downarrow}(E)$ spin states. (d) Fully optimized atomic structure of Ti covered (8,0) SWNT including four additional Ti atoms adsorbed at the corners of the square-like tube (*i.e.* $C_{32}Ti_{24}$). (e) and (d) show corresponding spin-polarized band structure and DOS, respectively. Nearest Ti atoms to the four additional adsorbed Ti atoms are indicated by nnTi.

nanowire rather than with a particular device, we infer G from an ideal Ti covered SWNT. Now the current, for example, for majority spin states can be expressed as $I^{\uparrow} = \sum_i \eta_i^{\uparrow} e v_i^{\uparrow} D_i^{\uparrow}(E_F + eV_b) - D_i^{\uparrow}(E_F)]$ where degeneracy, group velocity and density of states of each subband crossing E_F for spin-up electrons are given by $\eta_i^{\uparrow}$, $v_i^{\uparrow}$, $D_i^{\uparrow}$, respectively. Since $D_i^{\uparrow}(E_F + eV_b) - D_i^{\uparrow}(E_F) \sim (eV_b)\partial D_i^{\uparrow}(E)/\partial E \mid_{E_F}$ and $1/v_i^{\uparrow} = h\partial D_i^{\uparrow}/\partial E \mid_{E_F}$, then $G^{\uparrow} = I^{\uparrow}/V_b = \sum_i \eta_i^{\uparrow} e^2/h$. Accordingly each subband crossing the Fermi level is counted as $\eta_i^{\uparrow(\downarrow)}$ current-carrying state for a given spin direction with channel transmission $\mathcal{T}^{\uparrow(\downarrow)} = 1$. Then the maximum "ideal" conductance of defect-free Ti covered ideal tube becomes $G^{\uparrow(\downarrow)} = e^2 N_b^{\uparrow(\downarrow)}/h$, where $N_b^{\uparrow(\downarrow)} = \sum \eta_i^{\uparrow(\downarrow)}$. We found $G^{\uparrow} = 4e^2/h$, $G^{\downarrow} = 5e^2/h$ for $C_{32}Ti_{16}$ and $G^{\uparrow} = 6e^2/h$, $G^{\downarrow} = 8e^2/h$ for $C_{32}Ti_{20}$. Apparently, more bands which cross the Fermi level increase $D^{\uparrow}(E_F)$ and $D^{\downarrow}(E_F)$ upon the adsorption of additional four Ti atoms.

We note that the regular structure shown in Fig. 6.7 may occur under idealized conditions; normally irregularities are unavoidable, in particular for a thick Ti coating. While the transmission coefficient can decrease in the thick but inhomogeneous Ti coating, G is expected to be still high owing to the new conductance channels opened at E_F.

Densities of states corresponding to majority and minority spin states in Fig. 6.7 indicate that $P(E_F)$ is low and hence $C_{32}Ti_{16}$ and $C_{32}Ti_{20}$ structures apart being high-conducting may not be of interest for spintronics applications. Present results indicate that the spin-dependent electronic structure and the magnetic moment of these nanostructures can be modified also by applied axial and radial strain, ϵ_{zz}. In Fig. 6.8(a) the magnetization of a Ti covered (8,0) SWNT is plotted as a function of c. Each theoretical data point corresponds to the magnetic moment of $C_{32}Ti_{16}$ system relaxed under the constraint of a fixed c, hence under a given axial strain ϵ_{zz}. Figure 6.8(b) and 6.8(c) also show the change of stress and total energy as a function of c. The equilibrium lattice parameter occurs at $c_0 = 4.17$ Å. The axial strain is defined as $\epsilon_{zz} = (c - c_0)/c$. Starting from a compressive range with $\epsilon_{zz} < 0$, the net magnetic moment μ of $C_{32}Ti_{16}$ increases with increasing c, and continues to increase by stretching the system along the tube axis in the expansive range with $\epsilon_{zz} > 0$.

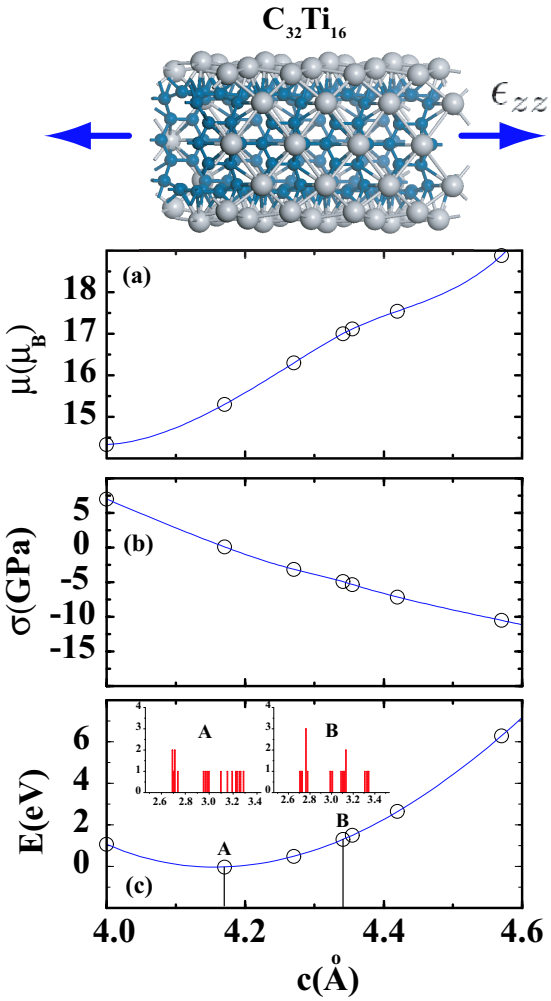

Figure 6.8: Top Inset: side view of the Ti covered (8,0) SWNT (*i.e.* $C_{32}Ti_{16}$) strained along its axis. $\epsilon_{zz} > 0$ corresponds to the stretched structure with $c > c_0$. (a) Variation of the magnetic moment μ per unit cell of $C_{32}Ti_{16}$ as a function of the lattice parameter c or strain. (b) Calculated axial stress in the system as a function of c. (c) Variation of the total energy E with c. The minimum of E occurs at $c_0 = 4.17$ Å. Insets in (c) show the distribution of Ti-Ti bond-lengths corresponding to $c_0 = 4.17$ Å and $c = 4.34$ Å.

Ferromagnetism in magnetic structures is generally explained in terms of Heisenberg model which considers spin-spin coupling between magnetic atoms at different lattice sites through exchange interaction. First-principles calculations based on DFT, which treat the magnetism of metallic structures from the viewpoint of itinerant electrons reveal that a ferromagnetic state is energetically favorable. In fact, when c increases, average Ti-Ti distance will increase (see inset in Fig. 6.8). Here parallel spin alignment is promoted by a $p-d$ hybridization, hence by electron transfer between the localized d orbitals of Ti atoms and extended $2p$ orbitals of C atoms. The important role of C atoms is also pointed out in recent DFT calculations[220], where p-orbitals of C are found to interact strongly with the d-orbitals of adsorbed Ti. The stronger the $p-d$ hybridization, the lower the $d-d$ exchange interaction and consequently resulting magnetic moment. Here increasing Ti-Ti distance decreases the $d-d$ coupling between Ti-Ti atoms, but increases the $p-d$ hybridization. The fact that in the absence of Ti-Ti coupling the magnetic moment of $C_{32}Ti_{16}$ could be sixteen times the magnetic moment of $C_{32}Ti$, *i.e* 16×2.2 μ_B instead of 15.3 μ_B, corroborates our arguments.

The decrease of magnetic moment of $C_{32}Ti_{16}$ from 15.3 μ_B to 6.8 μ_B owing to the adsorption of four additional Ti atoms can be explained also by using similar arguments. In Fig. 6.7(d), additional Ti atoms adsorbed at the high curvature sites of square-like cross section of $C_{32}Ti_{16}$ affect the interaction between existing Ti atoms at their close proximity with nearest C atoms of SWNT. These Ti atoms are specified as nnTi atoms in Fig. 6.7(d). Increasing coupling among Ti atoms by forming 3D-like Ti particles at the corners causes electronic charge which was donated to nearby C atoms to be back donated to nnTi atoms and hence to decrease the $p-d$ hybridization. A detailed charge density analysis show that the excess charge of ~ 0.3 electrons at each carbon atom interacting with nnTi atoms of $C_{32}Ti_{20}$ decreases to ~ 0.2 electrons upon the adsorption of four additional Ti atoms. At the end, nnTi atoms which initially carry majority spin as others, have their spin flipped upon the adsorption of additional Ti atom. This situation implies that the magnetic moment of Ti coated SWNT will decrease further as Ti coverage increases.

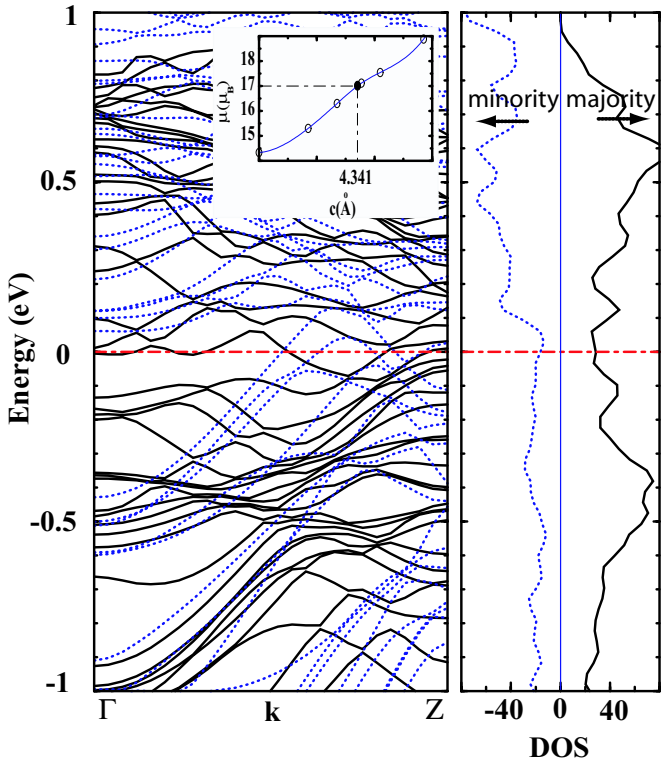

Figure 6.9: Calculated spin-polarized band structure of $C_{32}Ti_{16}$ under $\epsilon_{zz} = 0.04$ at $c = 4.34$ Å. $E_n(\mathbf{k} \uparrow)$ and $E_n(\mathbf{k} \downarrow)$ are shown by continuous and dotted lines, respectively. Corresponding densities of majority and minority spin states are shown in the panel on the right hand side.

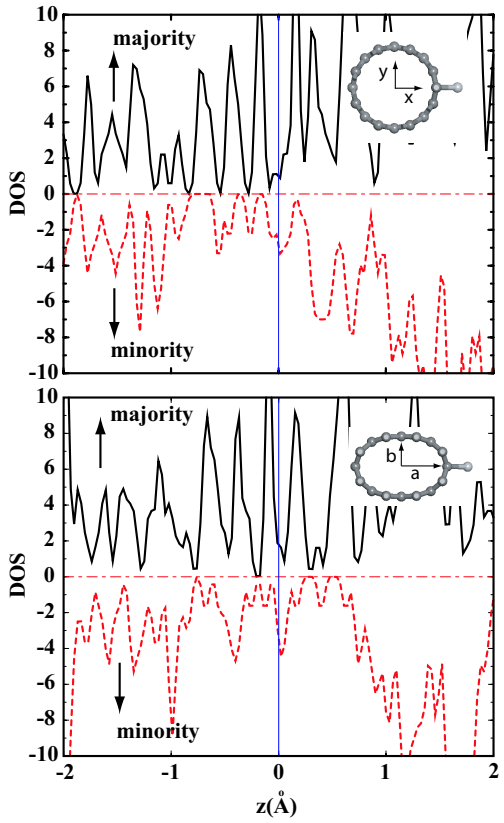

Figure 6.10: Densities of majority and minority spin states of $C_{32}Ti$ showing curvature effect on $P(E)$. (a) Density of spin states for a single Ti atom adsorbed on a bare (8,0) SWNT. (b) Density of states for a single Ti atom adsorbed on the high curvature site of (8,0) SWNT under radial deformation $\epsilon_{yy} = 0.3$, which transforms the circular cross section to an elliptical one as shown by insets.

Half-metals[235, 236, 237] are another class of materials, which exhibit spin-dependent electronic properties relevant for spintronics. Half-metals, where the bands exhibit metallic behavior for one spin direction, but become semiconducting for the opposite spin-direction provide ultimate spin polarization of $P = 1$ at E_F. Accordingly, the difference between the majority and minority spin electrons per unit cell should be an integer number. Interestingly, as seen in Fig. 6.8(a) the magnetic moment of $C_{32}Ti_{16}$ becomes equal to 17 μ_B under the strain $\epsilon_{zz} \sim 0.04$ corresponding to $c = 4.34$ Å. An integer μ per unit cell reminds the possibility of a half-metallic behavior. In Fig. 6.9 the band structure and DOS of $C_{32}Ti_{16}$ corresponding to $\epsilon_{zz} \sim 0.04$ are illustrated. Here, since both $E_n(\mathbf{k} \uparrow)$ and $E_n(\mathbf{k} \downarrow)$ cross the Fermi level, the system is a ferromagnetic metal, but $P(E_F)$ is significantly increased as compared to the case of $\epsilon_{zz} = 0$ shown in Fig. 6.7(b). Hence, whereas the half-metallic behavior did not occurred, the spin-polarization has been enhanced significantly and becomes suitable for spintronic applications. The analysis of spin-polarized bands of $C_{32}Ti_{16}$ for c_0 =4.17 Å and c =4.34 Å shows that in the later 64% (36%) of the current is carried by majority (minority) spin states. Whereas, in the case of c_0 =4.17 Å (*i.e.* $\epsilon_{zz} = 0$) the shares of majority and minority spins are almost equal. This is clearly another interesting effect of applied strain.

Finally, we explore the effect of radial strain $\epsilon_{yy} = (b - R)/R$, which is defined in terms of the minor, b and major, a axis of the elliptically deformed cross section and the radius R of the bare tube. Earlier studies have revealed important effects of the radial deformation of SWNTs on their electronic and chemical properties[111, 240]. For example a sSWNT has become metallic and electronic charge distribution on its surface has undergone a significant change. It has been also found that the chemical activity of SWNT at the high curvature site has increased to lead to a stronger bonding with foreign atoms such as H, Al[171]. Here we expect that the spin-dependent electronic structure of Ti adsorbed on SWNT is affected by radial deformation. In Fig. 6.10, we show the calculated $D^{\uparrow}(E)$ and $D^{\downarrow}(E)$ of the $C_{32}Ti$, where Ti is adsorbed on the bare, as well as at the high curvature site of a radially deformed ($\epsilon_{yy} \sim 0.3$) (8,0) SWNT. Radial deformation had minute effect to the value of net magnetic moment. However,

the dispersion of bands and $P(E)$ near E_F have been affected by radial deformation. The forms of $D^{\uparrow}(E)$ and $D^{\downarrow}(E)$ near E_F suggest that the spin-dependent transport under bias voltage V_b can be monitored by ϵ_{yy}.

6.1.4 Discussion

We showed that Ti atoms can form a uniform coverage on SWNTs. Upon Ti coverage the Ti+SWNT nanowire undergoes three major changes: (*i*) Depending on the radius and the chirality the circular cross section changes to either square like or polygonal form. (*ii*) It becomes a quasi 1D metal with high state density at E_F. Owing to the uniform and periodic atomic structure, the several states at E_F contribute to quantum ballistic transport with high transmission probability and hence high conductance. (*iii*) Ti covered SWNT have a magnetic ground state with net magnetic moment.

Spin-relaxed calculations predict interesting spin-dependent electronic and magnetic properties. The magnetic moment of the (8,0) SWNT can increase with increasing number of adsorbed Ti atoms to a value as large as 15.3 μ_B; it, however, decreases if additional Ti atoms are adsorbed on the Ti coating covering on SWNT surface. On the other hand, electronic conduction channels for each spin direction undergo a change; while $G^{\uparrow} = 4e^2/h$ ($G^{\downarrow} = 5e^2/h$) for $C_{32}Ti_{16}$, it changes to $G^{\uparrow} = 6e^2/h$ ($G^{\downarrow} = 8e^2/h$) for $C_{32}Ti_{20}$. We showed that the magnetic properties of the Ti covered SWNT can be modified also by applied axial strain; the magnetic moment increases with increasing ϵ_{zz} (namely by stretching the tube). Not only net magnetic moment, but also the spin-polarization at the Fermi level can be increased by increasing axial strain. Finally, we studied the effect of the radial strain on the spin-dependent electronic and magnetic properties. We found the dispersion of the spin-dependent bands and resulting density of states near the Fermi level of a single Ti-atom-adsorbed (8,0) SWNT is modified upon radial deformation. We expect that these coverage and strain dependent electronic and magnetic properties of Ti coated SWNTs can lead to interesting applications in spintronics and nanoscale magnetism.

Chapter 7

Nanotube Junctions and Nanotube Contact

Much of the research on carbon nanotubes have been carried out with the motivation to generate devices, such as sensors, transistors, nanomagnets etc, and hence to find a feasible way that contribute to the objectives of miniaturization. Attempts to design and fabricate nanodevices from carbon nanotubes have exploited several properties discovered recently, some of them reviewed in the previous chapters. In this chapter, we treat the contact properties of carbon nanotubes. First we examine the 3D grid or network structures of SWNTs. The atomic and electronic structure, stability, and energetics of the junctions are studied for different magnitudes of contact forces pressing the tubes towards each other and hence inducing radial deformations. Three dimensional grid structure formed by SWNTs are considered as a possible framework in device integration.

As a second, the microscopic aspects of the contact between carbon nanotubes and metal electrode are investigated. The contact between a s-SWNT and metal electrodes shows that the electronic structure and potential depend strongly on the type of metal.

7.1 A theoretical study of crossed and parallel carbon nanotube junctions and three-dimensional grid structures

Single-wall carbon nanotubes have been considered as a major nanostructure for future nanoscale electronics[10, 213, 215, 240, 252]. Not only various devices to be fabricated from SWNTs, but also SWNT based interconnects have been of interest[210, 238]. Recent theoretical analyses have shown that electronic devices together with their metallic interconnects can, in principle, be fabricated on a single tube[111]. Parallel, cross and Y junctions of carbon nanotubes, because of their unusual physical properties have been studied experimentally and theoretically[154, 253, 254, 255, 256, 257, 258, 259, 260, 261, 262, 263, 264, 265, 266, 267]. Based on generalized tight-binding molecular dynamics (MD) calculations Menon and Srivastava[253] proposed that stable T junction of SWNTs can form the smallest prototypes of microscopic metal-semiconductor-metal contact. Yildirim *et al.*[154] investigated the character of link between tubes in SWNT ropes under pressure. In addition to the Van der Waals packing they found two more different phases with local minima where the linkage is provided by C-C bonds between adjacent parallel zigzag SWNTs. However, similar interlinking C-C bonds did not form between the (6,6) parallel tubes even if they are deformed under a very high pressure. Terrones *et al.*[262] have fabricated stable junctions of various geometries (+,X,T,Y) *in-situ* in a transmission electron microscope. Electron beam exposure at high temperatures induced structural defects which promoted the joining of tubes. Classical MD calculations have been carried out to simulate various junctions of SWNT[261, 262]. Employing empirical potential MD, Krasheninnikov *et al.*[263] simulated the bombardment of nanotubes and demonstrated that crossed nanotubes can be welded. Recently, Yoon *et al.*[258] presented first-principles study of deformation and quantum electronic conductance of junctions formed by two crossed (5,5) metallic SWNTs. Despite, high contact forces, the C-C bonds between these tubes did not form to link the junction.

The conductance through nanotube junctions has been also a subject of interest. Using an atomic force microscope, Postma *et al.*[257] manipulated SWNTs to create a junction such as buckles and crossings within individual metallic SWNT connected to metallic electrodes. They showed that these manipulated structures behave as tunnel junctions. By changing the angular alignment of the atomic lattices at the SWNT-graphite contact it has been shown that the contact resistance can be varried by more than an order of magnitude in a controllable and reproducible manner, indicating that momentum conservation also dictates the junction resistance[256]. Buldum and Lu[260] carried out electron transport calculations through the junction of two crossing SWNTs. By rotating one of the tubes they found that intertube conductance is strongly dependent on the atomic registry between two tubes. It is now well understood that the junctions of SWNTs exhibit novel electronic properties so that they can be ideal nanostructures to fabricate robust molecular scale electronics[255, 259]. As a kind of nanotube contact, the geometry of telescopic arrangement of two shells of a MWNT have been recently considered for calculating inter-shell currents [268]. They find a trend of quasi-linear increase in the inter-shell conductance with the increase in the length of overlap region.

All previous studies have indicated the importance of nanotube junctions in device applications and brought about issues to be addressed both theoretically and experimentally. In particular, the description of the atomic structure of the contact between two tubes as a function of contact forces (or uniaxial stress), and electronic energy structure and electronic potential have needed a detailed *ab-initio* analysis. It is now important to know under what circumstances crossed-nanotubes remain attached (or welded) to each other and the junction becomes conductor. Also questions as to the roles of the atomic registry, forces pressing the tubes to induce radial deformation and point defects at the contact in forming junctions have remained to be clarified.

In this section, we present a detailed, first-principles analysis of the junction of crossed and parallel semiconducting SWNTs in different atomic registries as a function of uniaxial stress pressing the tubes. We examined their energetics, stability and electronic properties. As a first-step in three dimensional (3D) device

integration based on SWNTs, we also examined a 3D grid made by periodically stacking of SWNTs. Our results are summarized as follows: (i) The intertube interactions and resulting electronic properties are strongly dependent on the radial deformation of the tubes at the contact. They do not vary continuously, but exhibit various phases depending upon the strength of the contact forces. (ii) A vacancy created at the contact promotes the linking through sp^3-like bonds forming between tubes. (iii) These sp^3-like bonds link crossing tubes not only mechanically, but also electronically, and may survive even after the contact forces are released.

7.1.1 Computational model and method

Two crossed tube (also a crossbar structure) are modelled by parallel rows of (8,0) tubes along x-direction which are placed on a similar but perpendicular rows of (8,0) tubes along y-direction. This way, a 2D square grid of crossed tubes are generated. These grids are repeated periodically along z-direction with a vacuum spacing of 10 Å between grids. Owing to this large vacuum spacing and supercell lattice parameters $a = b$ =12.76 Å=(3×lattice parameter of (8,0) tube, c_{SWNT}) along the x- and y-directions the coupling of adjacent junctions of the grids is expected to be small. However, the tube sides between two adjacent junction can be affected from the radial deformation of the contact. In a crossbar having free ends, the circular cross section of the bare tube is expected to be recovered after some distance from the junction. As for the junction of parallel tubes, they are modelled by two infinite parallel (8,0) SWNTs in contact.

Normally, two crossed or parallel, stress free tubes are linked with very weak Van der Waals interaction with a spacing $s_{VdW} \sim 3.3$ Å. Then, the distance from the top of one tube to the bottom of the other one, $D = D_{VdW} \cong s_{VdW} + 2R_1 + 2R_2$, where R_1 and R_2 are radii of free tubes. In order to create contact beyond Van der Waals linkage, carbon atoms located at the top and bottom of the junction are fixed at a given distance, $D < D_{VdW}$ as indicated in Fig. 7.1. This situation is equivalent to generate contact forces $F_p(D)$ which press two tubes towards each other. Rest of the atoms in the supercell are relaxed to

minimize the total energy. At the end, the tubes in contact are deformed radially to have elliptical cross sections and a spacing $s(D)$ between the tubes is achieved after the relaxation. By changing D different contact forces $F_p(D)$ yielding different spacings $s(D)$ are obtained to examine the effect of the deformation at the junction. In the force-free calculations, all the atoms in the supercell have been relaxed.

We considered two different atomic registries at the contact as described in Fig. 7.1: (i) H-H registry where a hexagon on one tube lies over a hexagon on the other tube; (ii) B-H configuration where one C-C bridge-bond along the axis of the tube faces a hexagon on the other tube at the center of contact. By removing the vacuum spacings between adjacent 2D grids, 3D grid structures (where each tube is now in contact with two perpendicular tubes from above and below) have been constructed. We used 5 **k**-points within the Monkhorst-Pack[83] special **k**-point scheme in the sampling of the Brillouin zone of 2D grid. For 3D grid structure 14 special **k**-points have been used.

Since our main objective is to reveal the electronic properties of SWNT junctions, we carried out an extensive analysis for the quantum transport of electrons. To this end, we used nonequilibrium Green's function formalism together with an empirical tight-binding method to investigate the electron transport from one finite tube to the other one through the junction. Each finite tube is attached to a different reservoir. The details of the method are explained in Section V.

7.1.2 Atomic and electronic structures of junctions

7.1.2.1 Junctions of crossed SWNTs

We considered 2D grids having either H-H or B-H atomic registry at the contact region. For the H-H registry, we studied only one junction which has D=12.53 Å . The relaxed junction together with C-C bonds connecting two SWNTs is illustrated in Fig. 7.2. The circular cross sections of tubes are significantly deformed. The deformation energy is calculated as the difference between the total

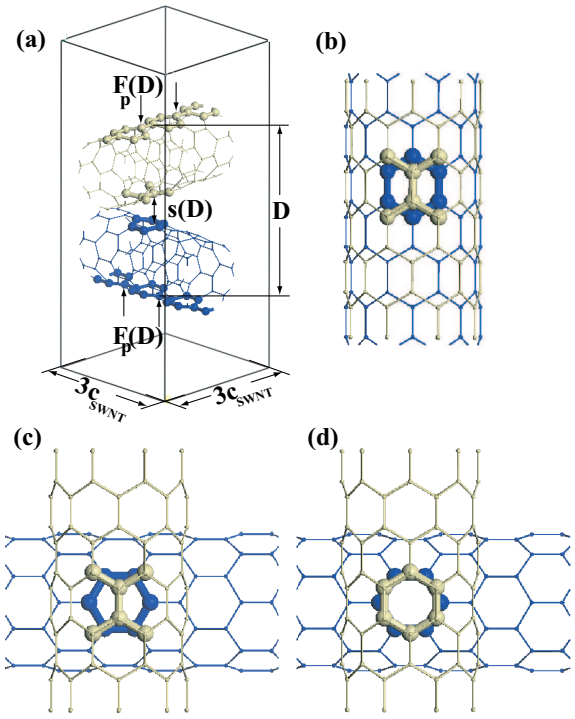

Figure 7.1: (a) Supercell used to simulate a junction of two crossed tubes. $F_p(D)$ is the contact force generated due to a fixed distance $D < D_{VdW}$, and $s(D)$ is optimized spacing between the surfaces of two SWNTs at the contact. (b) Bridge-Hollow (B-H) atomic registry between two parallel zigzag SWNT, where the C-C bonds of top SWNT along its axis face the hexagon of the bottom SWNT. (c) Same as (b) for the crossbar structure. (d) Hexagon-Hexagon (H-H) atomic registry for the crossbar structure. The lattice parameter of the bare (8,0) tube is $c_{SWNT} = 4.25$ Å.

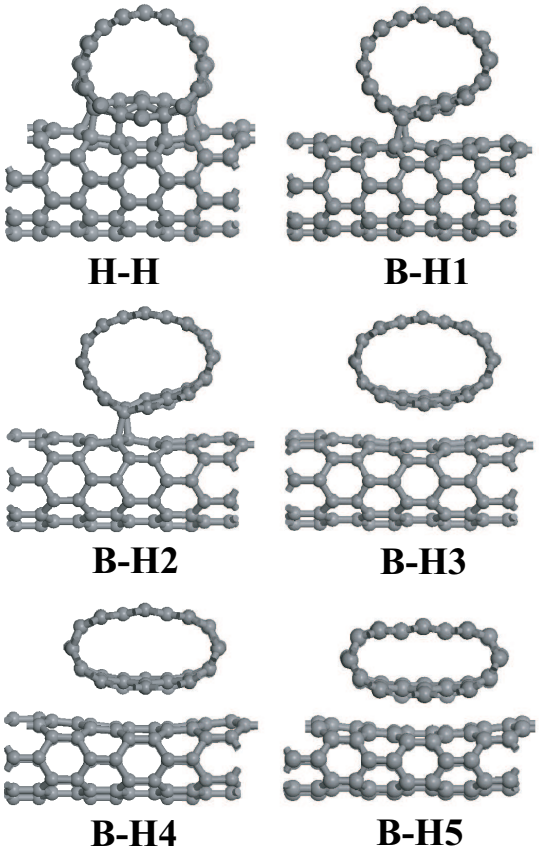

Figure 7.2: Relaxed atomic structures of two crossed $(8,0)$ SWNTs with different atomic registries (H-H and B-H). B-H junction has been studied for five different spacing values of $s(D)$ labelled by B-H1, B-H2, B-H3, B-H4, and B-H5.

energy of two non-interacting bare tubes and the total energy of crossed ones and is found to be 19.1 eV per supercell (or per 6 unitcells of SWNT). The electronic band structure of the corresponding 2D grid structure in the H-H registry is semiconducting and has a band gap of $\sim$0.3 eV.

Junctions of crossed (8,0) tubes in B-H registry have been treated for five different values of D as illustrated in Fig. 7.2. As one goes from junction B-H1 to B-H5, the distance D has decreased gradually (12.35, 11.95, 11.55, 10.35, and 9.15 Å , respectively). While D is reduced from 12.35 Å to 9.65 Å, some physical properties have displayed irregular changes. Figure 7.3 shows variations of the spacing, energy and contact forces with D; namely $s(D)$, $E_T(D)$ and $F_p(D)$,

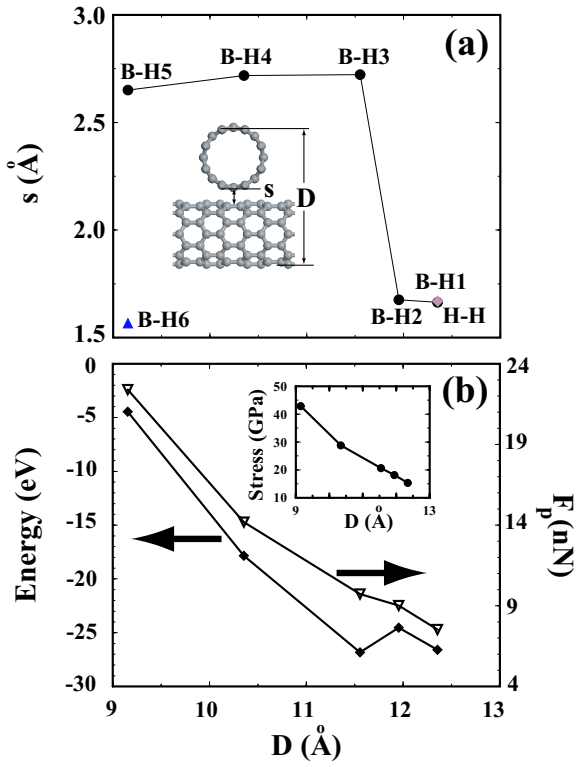

Figure 7.3: (a) Variation of relaxed spacing s, between two crossed nanotubes and (b) its energy (shown by diamonds) and contact force F_p (shown by triangles) as a function of D. The stress per supercell and atomic configuration of the junction are shown by insets. In (a) filled circles, light diamond and triangle indicate B-H, H-H registries and B-H registry including single vacancy, respectively. In (b) diamonds and triangles are joined by lines as a guide to the eye; but the detailed structure of possible local minima are omitted.

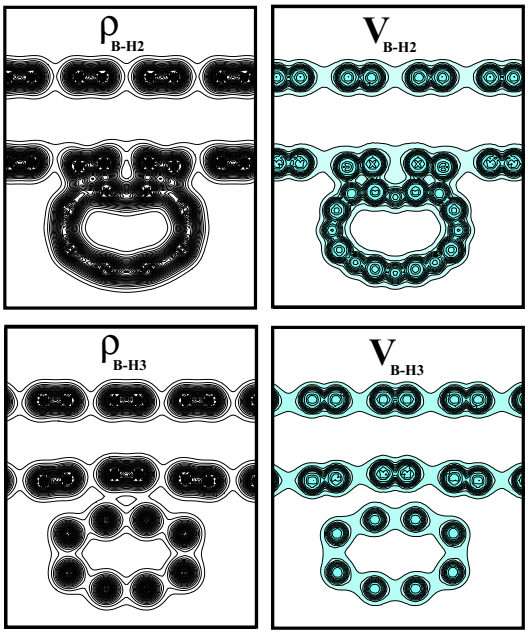

Figure 7.4: Contour plots of total charge density ρ_T and SCF electronic potential V_e of B-H2 and B-H3 junctions. In the right panels the potential energy in the white regions is higher than the Fermi energy, *ie.* $\Phi_B > 0$.

respectively. It should be noted that $F_p(D) = 0$, for values of D that make E_D a local minimum. The changes of the spacing, bonding and atomic structure, as well as the electronic structure are nontrivial, even paradoxical. For example, B-H1 and B-H2 junctions have small spacings ($s(D) \sim 1.7$ Å), which allow bond formation between the crossed tubes. The tubes by themselves display high curvature where the C-C bonds can form between their surfaces. On the other hand, in spite of smaller D and stronger F_p in the B-H3 - B-H5 junctions, their spacings $s(D)$ increase to ~ 2.7 Å and the interlinking bonds at the contact are broken. This situation arises due to the flattening of the curved tube surfaces at the junction. While contact atoms in B-H1 and B-H2 geometries are forming sp^3-like bonds between the tube surfaces, the flattened surfaces of B-H3 - B-H5 junctions behave more graphite like with large intertube spacings and finite potential barrier $\Phi_B(z = s/2) = V_e(z = s/2) - E_F > 0$ (where V_e is electronic potential energy).

Depending on the value of $s(D)$ and the presence of interlinking bonds, we distinguish two different types of junctions. Junctions such as B-H1 and B-H2

have established electronic contact between the tubes, while in B-H3 - B-H5 junctions $s(D)$ increases and interlinking bonds at the contact are broken. These cases can be analyzed by charge density, $\rho_T(\mathbf{r})$ and electronic potential energy, $V_e(\mathbf{r})$ contour plots as shown in Fig. 7.4. For example, small spacing $s(D)\sim$1.6 Å of B-H2 junction allows the formation of C-C bonds between the surfaces of two SWNTs. These interlinking bonds are easily distinguished in Fig. 7.4. Whereas in the B-H3 junction $s(D)$ has increased to $\sim$2.7 Å, and a finite potential barrier Φ_B has developed between two tubes.

Important features of the electronic structure of the junctions are revealed from the electronic band structure of the corresponding 2D grid structure along k_x- and k_y-direction. The grid formed of H-H junctions is a semiconductor with a band gap of E_g =0.3 eV in spite of the C-C bonds which connect crossing SWNTs. Similarly, the 2D grids of B-H1 and B-H2 junctions are semiconductor, but the band gap gets gradually smaller. It is 0.17 eV in the former, but is reduced to 0.1 eV in the latter. The gap is closed in B-H3 and B-H4 structures owing to relatively stronger deformation of tubes at the contact. Interestingly, upon further decreasing of D, the gap opened again and hence 2D grid becomes again a semiconductor. The metallicity at the intermediate levels of deformation is due to the radial deformation of each tube at the contact. Because of $\sigma^* - \pi^*$ hybridization[105, 111, 118], the conduction band of the π^*-singlet states dips below the Fermi level of both SWNT. First closing, then opening of the band gap of the 2D grid structure is a behavior specific to the junction of crossed (8,0) tubes. Note that the metallization of the grid is due to relatively short distance (approximately one unit cell of SWNT) between two adjacent nodes. If the edges of the squares of the grid were taken long enough, the central regions of SWNT between two nodes would be unaffected and remain undeformed in spite of the severe radial deformation at the contacts. Under these circumstances the 2D grid would maintain its gap. On the other hand, the edges of the 2D grid made by metallic SWNTs (such as armchair tubes) is expected to remain metallic no matter what the character of the junction is. The conductivity is then controlled by the contact resistance of the metallic tubes.

7.1.2.2 Effect of vacancy and carbon impurity

Crossbars have been produced by the exposure of the junction to the electron beam, where one generates several imperfections[261, 262]. As a possible imperfection we considered the effect of a vacancy existing on one of the tubes at the contact region. In spite of a high deformation and small D in the B-H5 junction the spacing between the tubes has been rather large. After creating a vacancy on the surface of one of the tubes the bonding character near the vacancy has been changed from sp^2 to sp^3-like configuration, thereafter the spacing has decreased and eventually an interlinking bond has formed. It appears that an imperfection like a vacancy at the contact provides an electronic charge distribution and atomic structure which are suitable for linking of two tubes. The linkage and eventually welding (or merging) of two tubes at the junction can take place by the creation of a large number of vacancies or divacancies. Interestingly, we found that the 2D grid having a single vacancy at the contact is semiconducting with a band gap E_g ∼0.25 eV.

The effect of vacancy is further examined in Fig. 7.5 by comparing total charge density and SCF-potential in a plane bisecting $s(D)$ between the tubes at the junction. In the absence of vacancy B-H5 junction has low ρ_T, but $V_e > E_F$ in the same plane. A finite barrier Φ_B develops, and prevents electrons from the ballistic motion between the tubes. The situation is, however different if a vacancy is incorporated to one of the tubes at the contact. In the region of the interlinking C-C bond induced by the vacancy, we see high charge density and low potential. This situation is reminiscent of the fact that the interlinking C-C bond made an orifice or hole through the potential barrier. Such an orifice can allow the ballistic electron transfer if its diameter is large so that an effective barrier does not develop due to size effects.

A single carbon atom placed between two tubes and on top of the mutual axial bonds crossing at the contact can form four directional and strong bonds. The interlinking of the tubes is found to be favorable energetically. We found the total energy of the whole system is lowered by 4.6 eV. This means that an energy of 4.6 eV is required to disconnect the crossed (8,0) tubes linked by a

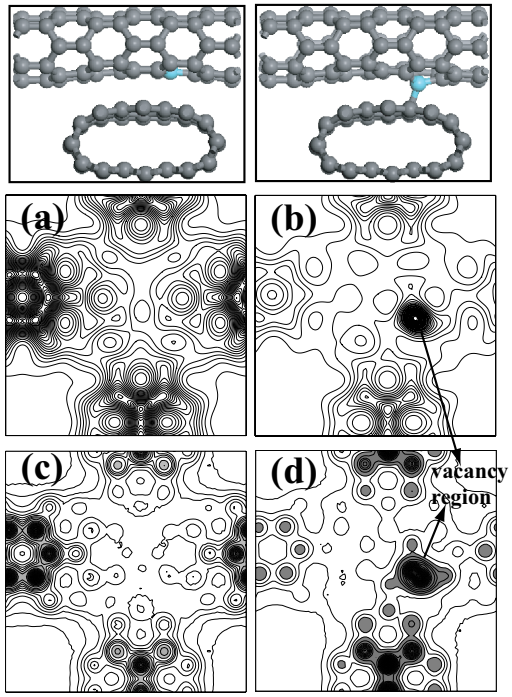

Figure 7.5: Relaxed atomic structure, total charge density ρ_T and SCF-electronic potential V_e of junction of crossed SWNTs. Left panels: B-H5 contact; right panels: B-H5 type contact including a single carbon vacancy. (a) and (b) are charge density contour plots on a lateral plane bisecting the spacing s between tubes. (c) and (d) are the same for electronic potential energy. While $V_e > E_F$ at the contact and hence $\Phi_B > 0$ in (c), the potential barrier is collapsed and an orifice is formed between two tubes through the contact in (d).

single carbon atom.

7.1.2.3 Parallel tubes

The junctions made by parallel tubes may display a behavior which is slightly different from the crossing SWNTs. Earlier Yildirim *et al.*[154] examined the interlinking of SWNTs forming a 2D hexagonal lattice under pressure. In addition to the interlinking of tubes via Van der Waals attractive interactions under zero pressure, they found two different local minima of the Born-Oppenheimer surface at different ranges of applied pressure. In the phases corresponding to these minima, C-C bonds have formed to link the tubes in one direction in the first minimum and in two directions in the second minimum. The present structure and model differs from those of Yildirim *et al.*[154], since only two parallel tubes are considered in contact. Two free SWNTs are expected to be linked by the Van der Waals interaction with $s_{VdW} \sim 3.3$ Å and $D_{VdW} \cong s_{VdW} + 2R$. By constraining them with $D < D_{VdW}$, we see that interlinking bonds are easily formed between two tubes for low F_p. In contrast to what one sees in the junctions of crossing tubes, these bonds continue to exist even under strong contact forces. The spacing $s(D)$ is in the range of ~ 1.6 Å no matter what the value of D is. Each interlinking bond pulls and connects two C atoms, one from each tube and change the local sp^2-type bonding to sp^3-like bonding configuration (See Fig. 7.6).

7.1.2.4 Free junctions

Having examined the energetics and atomic structure of junctions of crossing and parallel tubes, we next address the question as to what happens if the contact force is released and hence the tubes are left free. It is important to know whether the junction survives or the linking of tubes ceases. To this end, we optimized B-H2 and B-H3 junctions after $F_p(D)$ is released (or the constraint due to D is lifted). Note that under contact forces, the former had interlinking bonds, but the latter had relatively larger $s(D)$ whereby interlinking bonds were broken. Once the F_p is released from the B-H2 junction, the deformation of SWNTs steadily

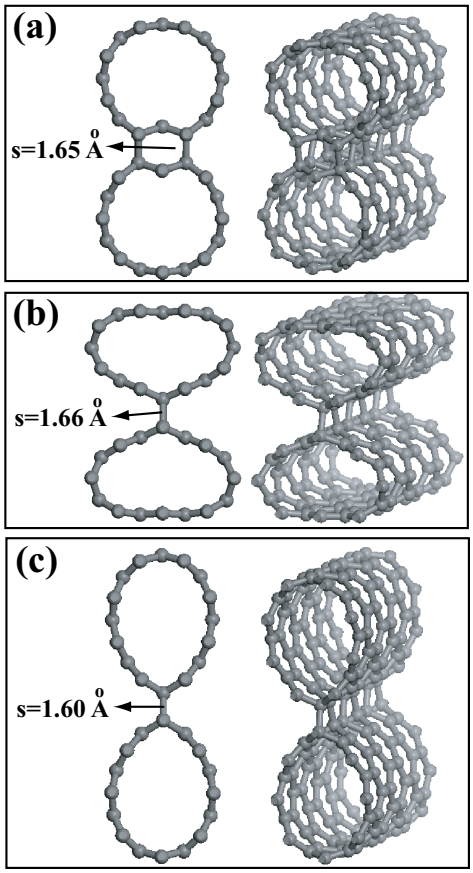

Figure 7.6: Relaxed atomic structure of the junctions between two parallel tubes under different contact force or D. (a) Large D and hence weak deformation. (b) Small D hence strong deformation. (c) Relaxed junction after the contact force in (b) is released. Parallel tubes have B-H registry.

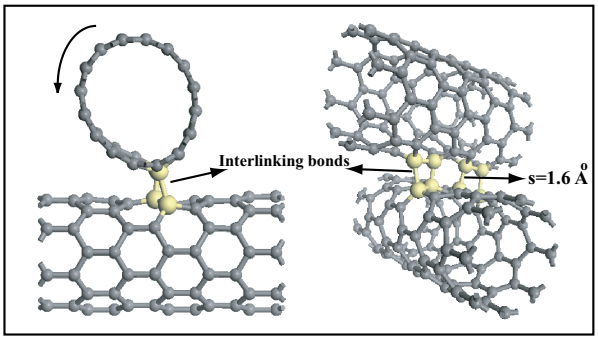

Figure 7.7: Relaxed atomic structure of a junction B-H2 after the contact forces F_p are released.

relaxed to reassume their original bare circular shape. After the full relaxation the C-C bonds continued to link two SWNTs, but the form of the cross section at the contact region has changed and the upper tube has rotated as shown in Fig. 7.7. The curvature increased locally at both ends of interlinking C-C bonds to comply with the sp^3-like bond configuration. It appears that B-H2 type junction forming under weak F_p can provide a connection between crossed SWNTs as a local minimum. However, the B-H3 junction behaves differently upon lifting of the contact forces. Without being captured in any local minimum, cross sectional deformation is gradually eliminated and eventually two SWNTs become disconnected. In the case of parallel junctions two tubes remained connected with interlinking C-C bonds as shown in Fig. 7.6c even after the contact force is released.

In closing this section we note that Yoon *et al.*[258] investigated the junction of crossed (5,5) SWNTs by performing a constrained total energy minimization within a supercell structure, in which only the positions of the atoms near the junction are relaxed while fixing the center-to-center intertube distance at the boundaries to produce the desired contact force. By using the Landauer-Büttiker[270, 271] formula they calculated intertube and intratube conductance as a function of contact force. These calculations[258] of crossed nanotube junctions differ from the present one in many respects. First of all the (5,5) metallic tubes considered by Yoon *et al.*[258] do not form the interlinking C-C bonds between the tubes. Consequently, the large spacing ($s \cong 3.35$ Å) occurring in the absence of the contact force, is reduced only to $\sim$2.5 Å under strong contact

force. Although this spacing is still too large to form C-C interlinking bonds, it may allow a significant wave function overlap of individual tubes at the Fermi level and hence may enhance the tunnelling current as in fact found by Yoon *et al.*[258] In the present study (8,0) zigzag tubes can form C-C bonds at the contact which, in turn, may lower or even collapse the tunnelling barrier. For the same reason the variation of s with F_p is more complex and varies from 3.35 Å (Van der Waals linking not included in this study) to ∼1.6 Å. Our work also differs from the earlier one by the constrains which create the contact force between crossed tubes. Similar to the experimental condition using an Atomic Force Microscope, we pressed the tubes from top and bottom (namely by fixing only a few atoms designated in Fig. 7.1 at a desired distance) and relaxed the rest of the atoms. As a result, the deformation of the tubes are more realistic, in particular for the case of strong F_p.

7.1.3 3D grid structure

The 3D grids of SWNTs add an additional dimension to the planar structures and may be of use in 3D integration and other similar applications such as forming a 3D periodic framework for the artificial crystal structure of giant molecules. Here we studied a 3D grid made of a supercell containing 6 unit cells of the $(8, 0)$ SWNT. As described in Sec. II, our model for the 3D grid structure shown in Fig. 7.8 is generated by stacking the B-H1 junctions along the z-axis. The contact force is imposed by fixing the supercell parameter along z-axis at a specific value, which leads to certain deformation of tubes upon relaxation. Owing to the initial structure and the supercell parameters, the SWNTs along y-axis form interlinking bonds with the SWNTs along x-axis from only one side. At the other (opposite) side of SWNTs the spacing s between adjacent tubes is large and does not allow any interlinking bonds. Accordingly, a potential barrier develops which prevents the ballistic electron transfer along z-axis. Such a one-sided linking of tubes at the junction appears to be circumstantial, however. Under different F_p either two-sided linkings or two-sided detached junctions with large s may occur.

The electronic band structure shown in Fig. 7.8 confirms the situation that the

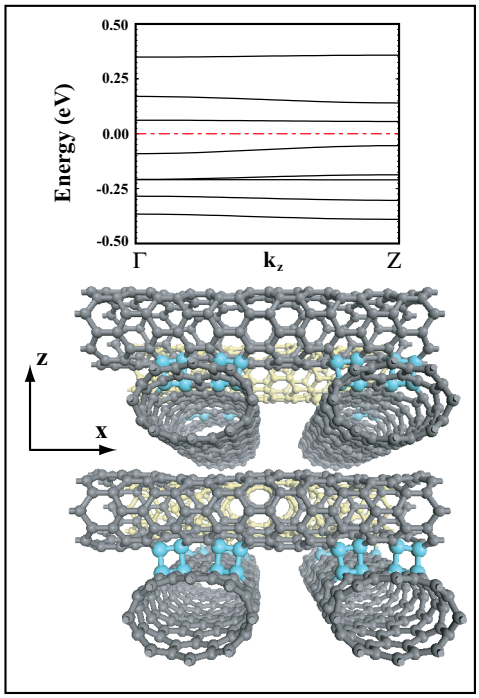

Figure 7.8: Energy band structure along the z-axis shown by inset, and relaxed atomic structure of the corresponding 3D grid of the $(8, 0)$ zigzag tubes.

3D grid structure is electronically disconnected along z-axis. It has a band gap of 0.15 eV, and flat bands. We, however, note that the electronic and mechanical properties of grid structure can be tuned by changing the supercell parameters. The electronic and mechanical linking of SWNTs along x-, y-, and z-directions depend on the contact forces inducing radial deformation, and on the lateral lattice parameters. Upon releasing the contact force, the interlinking bonds can provide stability and may lead to metallic properties. Nevertheless, the model discussed here demonstrates that stable 3D grid and crystal structure can, in principle, be formed from SWNTs. These 3D grid structures can be modified by external agents, such as stress, modulating absorption of molecules and atoms. For example, through decoration of transition metal atoms or magnetic molecules the grid can gain magnetic properties. 3D grids made by armchair tubes have metallic interconnects between nodes.

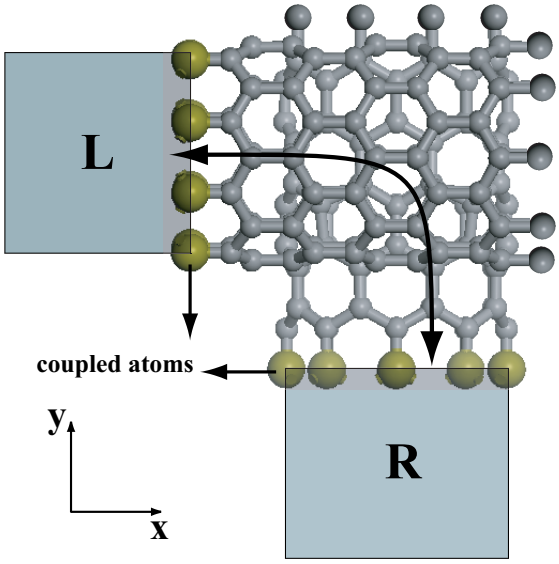

Figure 7.9: An atomistic model which describes the electronic transport through the junction. **L** and **R** are reservoirs where finite tubes forming the junction are coupled to.

7.1.4 Electron transport

The rapid advances in the measurements of electrical conductance of individual molecular- and atomic-sized devices require commensurate advances in the theoretical understanding of the detailed microscopic mechanisms. Modelling of a single element of nanodevices is needed to provide interpretations to predict device characteristics. Several approaches have been developed to calculate the quantum conductance in nanostructures, based on semiempirical (tight-binding, Hückel) models. More recently, a variety of first-principles formulations have appeared. *Ab-initio* approaches have also been extensively used to characterize the electrical transport properties of nanostructures.

In the present study to analyze the conductance properties of junctions of two SWNTs we used Green's function technique combined with Landauer-Büttiker formalism and a parameterized tight binding model [269]. The junction is taken to be coupled to two semi-infinite electrodes (reservoirs) from the end surfaces L and R as depicted in Fig. 7.9.

The conductance through the junction is given by the Landauer type formula [270, 271] in terms of the Green's functions of the junction and the coupling of the junction to the electrodes [137];

$$G = \frac{2e^2}{h}\mathrm{Tr}(\Gamma_L G^r \Gamma_R G^a) \tag{7.1}$$

where G^r and G^a are the retarded and advanced Green's functions of the conductor and Γ_L and Γ_R are the coupling functions of the conductor to the electrodes. The retarded Green's function is given by the expression

$$G^r = (\epsilon - H - \Sigma_L - \Sigma_R)^{-1} \tag{7.2}$$

where H is the Hamiltonian of the conductor region, and Σ_L, Σ_R are the self-energy terms due to the electrodes. The self-energies and the coupling functions are related through $\Gamma_{L(R)} = -2\mathrm{Im}\Sigma_{L(R)}$. In this approach the properties and the effects of the electrodes are represented by the self energy terms which we have parameterized by the corresponding line-width functions $(\Gamma_{L(R)})_{ij} = \gamma\delta_{ij}$, where the indices run through the orbitals of the surface atoms at the contacts. Such parameterization of self-energy terms corresponds to the approximation of wide-band limit [272] where the level shifts, $\mathrm{Re}\Sigma_{L(R)}$, are neglected and the linewidths are taken as energy-independent constant, γ, for every level of the surface atoms. After a few trials, in our calculations we chose $\gamma = 0.5$ fixed, which provides a sensible broadening of conduction channels shown in Fig. 7.10.

Within the tight-binding model all these functions are $4n \times 4n$ matrices (n is the number of atoms in the junction region) expressed in terms of s, p_x, p_y, p_z parametrization of carbon as given in Ref. [269]. Here, the selection of range for a suitable nearest neighbor interactions in the matrix elements $< \varphi_{i,n}(\mathbf{r})|H|\varphi_{j,m}(\mathbf{r} - \mathbf{R}_{ij}) >$ (or setting a cutoff distance so that $R_{ij} < R_{cutoff}$ yields nonzero interatomic interaction) and the appropriate scaling factor of energy parameters are essential. To this end, we examined the distribution of interatomic distances in these structures. Figure 7.10(a) shows the ordering of interatomic distance R_{ij} in the B-H2 junction. Here we can clearly distinguish three nearest neighbor distances; namely the first nearest neighbor distance with $\mathrm{R}_{ij} < 1.75$ Å, and second and third nearest neighbor distances with $\mathrm{R}_{ij} < 2.91$

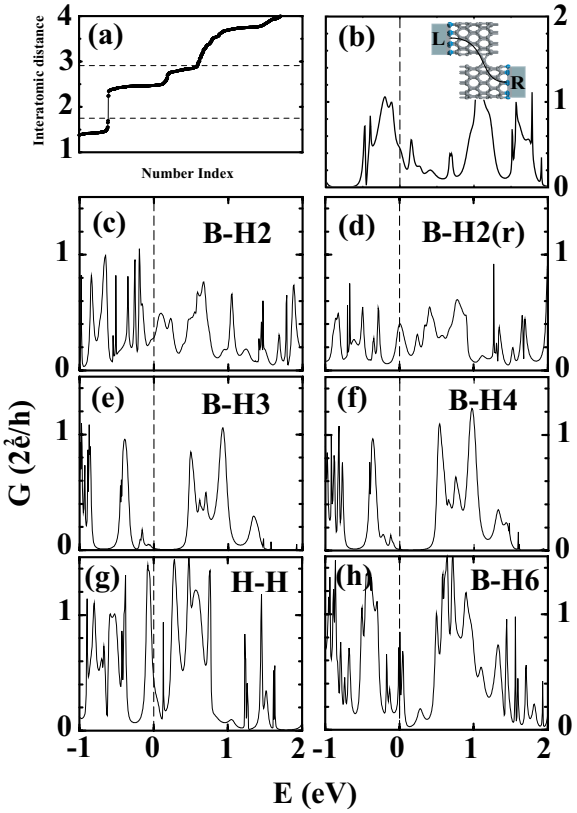

Figure 7.10: Calculated conductance G versus energy E for various junctions. (a) Distribution ordering of interatomic distances in the B-H2 junction *i.e.* R_{ij} versus number index of sorted distances. Dashed line at 1.75 Å and 2.91 Å correspond to the domains of tight-binding parametrization; (b) B-B junction of two parallel tubes connected by a carbon atom; (c) B-H2 junction of crossed tubes. (d) B-H2 junction relaxed after contact forces are released; (e) B-H3 junction; (f) B-H4 junction; (g) Junction having H-H registry; (h) B-H6 junction which is B-H5 including a single vacancy. In all plots coupling parameter is fixed at $\gamma = 0.5$. Zero of energy is set at the Fermi level.

Å. Then, Slater-Koster Hamiltonian parameters of the tight-binding model are as follows: The on-site energies are $\epsilon_s = -7.3$ eV for the s-orbital and $\epsilon_p = 0$ for the triply-degenerate p-orbitals. The nearest neighbor pairs determined by the condition that the interatomic distance R_{ij} being less than 1.75 Å are assigned the hopping parameters $V_{ss\sigma} = -4.30$ eV, $V_{sp\sigma} = 4.98$ eV, $V_{pp\sigma} = 6.38$ eV, and $V_{pp\pi} = -2.66$ eV. Further interactions are taken into account up to $R_{ij} = 2.91$ Å which covers all the 2nd and 3rd nearest neighbors pairs by using scaled parameters $V_{ss\sigma} = -0.18\alpha$, $V_{sp\sigma} = 0$, $V_{pp\sigma} = 0.35\alpha$, and $V_{pp\pi} = -0.10\alpha$ with the scaling parameter $\alpha = (3.335/R_{ij})^2$. This set of tight-binding parameters were successfully used earlier[269, 273] to calculate electronic properties of carbon nanotubes having deformed cross-sections. The original derivation of these empirical tight-binding parameters was performed by fitting to the *ab-initio*-calculated band structure of bulk graphite[274]. The similar sp^2 coordination of atoms both in graphite and in SWNT makes this parameterization reasonably valid for SWNTs as well. To test the tight-binding model we have calculated ballistic conductance of infinite (5,5) and (8,0) SWNTs and found agreement with earlier calculations.

Using the above model we made conductance calculations for junction of parallel tubes connected with a carbon atoms, B-H2, force-free B-H2, B-H3, B-H4, H-H and B-H6 (*i.e.* the B-H5 junction which has a vacancy) configurations. Figure 7.10 shows the intertube equilibrium conductances of these systems. All conductance values for these structures do not exceed unit quantum of conductance $G_0 = 2e^2/h$.

In Fig. 7.10b, despite a large separation (~ 2.2Å) between two parallel tubes, significant intertube conductance, $0.5G_0$, is achieved through the carbon atom that connects the tubes. The existence of the extra C atom between the tubes provides a ballistic channel for the conduction, however, the scattering mechanisms and the effect of the contact resistance limit its value below unit quantum of conductance. The contact geometry of two parallel SWNTs that we studied can be contrasted to that of the telescopic arrangement of double wall carbon nanotubes (DWNT) as considered in Ref. [268]. In the latter case, although the distance between the walls is comparable to our case, the intertube conductance

they calculate is more than two orders of magnitude smaller due to the potential barrier between the walls of DWNT. In that case the system is in tunnelling regime.

The contact force dependence of the intertube conductance in (5,5) crossed nanotube junctions was investigated in calculations by Yoon *et al.*[258], and a strong dependence on the contact force was calculated. On the contrary, in the present study using (8,0) zigzag tubes, intertube conductance is inversely proportional with contact force. For B-H2 structure we calculated the equilibrium conductance as 0.28 G_0. Conductance plots for B-H3 and B-H4 junctions support the previous conclusions reached through the analysis of contact structure and electronic potential. Hence the intertube conductance of highly compressed junctions is negligible due to a wide Φ_B intervening between tubes. The conductance of the junction which was relaxed after constraints on the B-H2 lifted and hence F_P was released increases to 0.40 G_0. A slight increase of G can be attributed to the reduced deformation of contact in the absence of the constraints. The conductance of H-H junction on the Fig. 7.10g is comparable to those of B-H2 and B-H2(r). The B-H5 junction, with a large s and finite Φ_B between tubes, has $G \sim 0$. There is an empty gap of ~ 0.5 eV for ballistic conductance. However, upon creation of vacancies, the potential barrier has collapsed and the calculated conductance increased to a value close to 0.8 G_0. We note that the model used in calculating G in Fig. 7.9 has short arms of (8,0) SWNT leading to the junction. These short arms, which are also deformed under F_p appear to be conductor, in spite of the fact that a long bare (8,0) is a semiconductor.

7.2 Electronic structure of the contact between carbon nanotube and metal electrodes

The switching of the current in a s-SWNT at room temperature by an external electric field has been utilized to fabricate a new field effect transistor (FET). [213, 214, 215] The interaction between s-SWNT and metal electrode, and the Schottky barrier, Φ_B formed thereof have been proposed as the origin of FET operation.

Model calculations have been carried out to provide further understanding of experimental I-V characteristics.[275, 276] The SWNT-electrode interaction and resulting electronic structure are crucial for the electron transport and hence for all device properties. This letter presents an analysis of the self-consistent field (SCF) electronic potential and electronic energy structure of a zigzag (8,0) SWNT side-bonded to either gold or molybdenum electrodes.

A metal electrode is presented by a slab consisting of five atomic planes. First, the lattice parameters of the slab have been changed slightly to match to that of the SWNT. Induced strains along the directions perpendicular to the axis of SWNT have been determined by using bulk Poisson's ratio. Then the calculated stress is minimized by varying the lattice parameters of the SWNT-adsorbed slab. Finally, all atomic positions except those at the bottom two planes of slab have been fully relaxed. The lattice parameter of the Au (Mo) substrate along the SWNT axis expanded (contracted) by 1.5%(2.7%) upon the relaxation. Mo atoms in the close proximity of SWNT have significant perpendicular displacements. In the study of the effect of radial deformation, the SWNT is pressed between two metal electrodes, each made of three atomic planes having fixed atomic positions and 2D periodicity lattice matched to the tube. Note that the supercell geometry gives rise to a continuous contact of infinite extension, but it can provide accurate prediction of the electronic structure and atomic positions, which are crucial to determine the Fermi level pinning and band diagram of finite semiconductor-metal heterostructures.

We start by summarizing our results for the adsorption of individual Au and Mo atoms, since the character of their bonding determines the interaction between SWNT and corresponding metal electrodes.[220] The adsorption geometry is determined first by placing single Au or Mo atom at different possible adsorption sites (i.e. above the center of hexagon, H-site; just above a carbon atom, T-site; and above the axial or zigzag C-C bond, A-, and Z-sites) and then by optimizing the atomic structures. We found that the binding energy of an individual Au atom is, in general, weak and ranges between 0.3-0.5 eV depending on the adsorption site. In contrast, the bonding of an individual Mo atom at the H-site is rather strong and involves significant charge transfer.

The contact on the gold electrode is formed by placing the s-SWNT on the Au(100) surface, so that a surface Au atom faces the center of the hexagon. The Au-SWNT distance, **s**, was initially 2.2 Å, but it increased to 3.18 Å as a result of full structure optimization. The interaction energy E_i is calculated by subtracting the total energies of SWNT alone and metal electrode alone from the total energy of the electrode+SWNT system. For the Au, we found E_i to be very small and repulsive (-48 meV per supercell). The equilibrium position may correspond to a local shallow minimum, but it shall be further stabilized by Van der Waals interaction. This situation implies a weak Au-SWNT interaction which is characterized by physisorption.

The effect of Au electrode on the band structure of the bare SWNT may be deduced from the single Au atom adsorbed on the SWNT. Adsorbed single Au does not induce any significant change in the bands of the bare tube; the form of the band gap remains unaltered. Au gives rise to a single isolated band. The effect on the electronic structure can be revealed for the LDOS calculations. The LDOS calculated for two Au atoms at different sites (one is at the contact just below the SWNT hexagon; the second being farthest to SWNT mimics the clean Au surface) in Fig 7.11(a) have finite state density at the Fermi level. These two LDOS's are similar; there are only minute changes. Whereas the LDOS of the carbon atoms at the contact still has a band gap. The Fermi level lies near the top of the valence band of SWNT and complies with a small Φ_B in the hole doping picture. The LDOS at the carbon atom which is farthest from the metal electrode displays a state distribution similar to that of the carbon atom at the contact region. Calculated total charge density of SWNT bonded to the metal electrode, E, i.e. $\rho[SWNT+E]$, and difference charge density, $\Delta\rho = \rho[SWNT+E]-\rho[E]-\rho[SWNT]$, shows minute charge rearrangement. These results indicate that the weak Au electrode-SWNT interaction does not induce significant changes in the electronic structure. The SCF electronic potential between SWNT and Au electrode, $V_e(\mathbf{r}) = V_{ion}(\mathbf{r}) + V_H(\mathbf{r}) + V_x(\mathbf{r})$, is presented on a vertical plane and also on a horizontal plane bisecting **s** in Fig 7.11(a) and (b). The shaded area shows that the electronic potential energy at the contact yields a potential barrier $\Phi_c = V_e - E_F > 0$. At the contact midway between SWNT and Au(100) surface

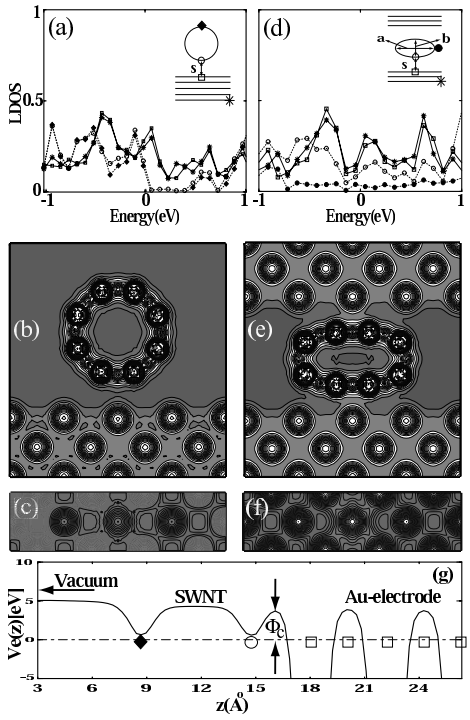

Figure 7.11: (a) LDOS at different Au and C atoms of the (8,0) zigzag SWNT side bonded to the Au(100) surface. The location of atoms are described by inset. The zero of energy is taken at the Fermi energy E_F. State densities shown by empty circle and filled diamonds correspond to 6 neighboring carbon atoms. Other densities are for single atoms. (b) Contour plots of the SCF electronic potential, $V_e(\mathbf{r})$, on a vertical plane. (c) Same as in (b) on a horizontal plane bisecting $\mathbf{s}$. In the dark gray regions $V_e(\mathbf{r}) > E_F$. (d), (e) and (f) correspond to the radially deformed (8,0) SWNT pressed between two 3-layer Au(100) slabs with $b/a = 0.47$ as shown by inset. State densities shown by empty circles in (d) correspond to 6 neighboring carbon atoms. Other densities are for single atoms. (g) Variation of $V_e(z)$ on a perpendicular line passing through the center of SWNT.

Φ_c is calculated to be $\sim$ 3.9 eV, that is comparable with the calculated work function ($\Phi \sim 5$ eV) of Au-slab. Fig. 7.11(g) shows the variation of $V_e(z)$ on a line passing through the center of the SWNT and perpendicular to the Au(100) surface. The effective potential barrier $\Phi_{c,eff}$, can be even higher owing to the increased confinement of electrons at the contact region. Therefore, electrons which are transferred from the metal to the semiconducting SWNT has to tunnel a potential barrier $\Phi_{c,eff}(\mathbf{r})$.

By pressing the s-SWNT between two Au slabs, hence by imposing a radial deformation on the tube (see the inset in Fig 7.11(d)) we examined the electronic structure and the contact potential. Normally, the semiconducting tubes undergo an insulator-metal transition, since the π^*-singlet states in the conduction band are lowered because of increased $\pi^* - \sigma^*$ hybridization at the high curvature site and eventually overlap with the valence band.[111, 113, 131] In the present case, at a radial deformation, $\epsilon_r = b/a = 0.47$, the state density of SWNT+electrode system near E_F has increased partly due to increased state density of the metallized s-SWNT. The spacing **s** has decreased to 2.6 Å, and eventually potential barrier has collapsed (i.e. $V_e < E_F$) at specific sites at the contact (see Fig 7.11(e) and (f)). Under these circumstances, the electron from the SWNT can be ballistically transferred to the gold electrodes.

The above situation is, however, different in the case of s-SWNT side-bonded to the Mo(110) surface as shown in Fig 7.12(a). Upon relaxation, the tube has rotated slightly so that C atoms tend to approach to Mo atoms. The interaction energy E_i has been calculated to be $\sim$3.5 eV. The LDOS at the Mo atom interacting with the C atoms of the SWNT is different from that at the clean Mo(110) surface. Moreover, the LDOS at the carbon atom closest to the Mo surface has finite state density at E_F. In particular, the peak near E_F is associated with the C-Mo bond states and hence may be identified as the metal induced gap states (MIGS). The LDOS of the C atoms farthest from the contact has a band gap near E_F. This situation indicates that the site of SWNT forming contact is conducting, while the opposite site farthest from the contact remains semiconducting. Owing to the strong Mo-C bond, the spacing between SWNT and Mo electrode is smaller (**s**=1.96 Å) than that with the Au electrode. The strong

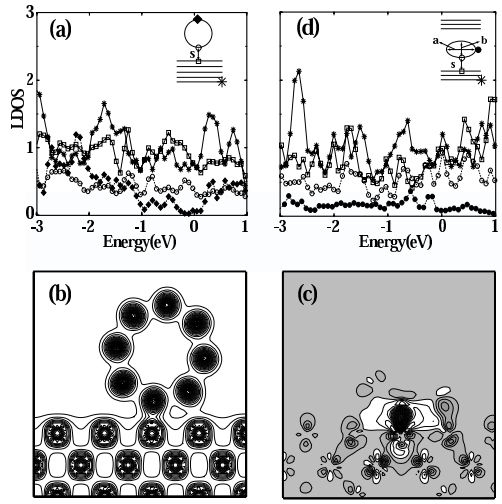

Figure 7.12: (a) LDOS at different Mo and C atoms of the (8,0) zigzag SWNT side bonded to the Mo(110) surface. The location of atoms are described by inset. The zero of energy is taken at the E_F. State densities shown by empty circles and filled diamond correspond to 8 neighboring carbon atoms, Others are for single atoms. (b) Contour plots of the total SCF charge density on a vertical plane. (c) Difference charge density showing the charge depleted (white) regions and charge accumulate (black) regions. (d) LDOS corresponding to the (8,0) SWNT radially deformed between two 3-layer Mo(110) slabs with $b/a = 0.56$ as shown by the inset. State densities shown by empty circles correspond to 10 neighboring carbon atoms.

C-Mo bond formation is clarified by the calculated total SCF charge density in Fig 7.12(b). The difference charge density $\Delta\rho$ presented on a vertical plane in Fig 7.12(c) shows the strong charge transfer to the C-Mo bonds. The electronic potential calculated on the horizontal plane bisecting **s** and also on a line from SWNT to the Mo(110) surface through the contact show that $V_e(\mathbf{r}) < E_F$ at the contact region. Accordingly, a potential barrier, Φ_c does not form at the extended contact between the SWNT-Mo electrode. The radial deformation on the s-SWNT induced by squeezing it between two Mo(110) electrodes gives rise to the metallization of the tube and hence to the increase of state density at E_F.

7.3 Discussions

Junctions with different registry and radial deformation have been considered. Two tubes which are normally under a weak and attractive Van der Waals interaction can be further linked by pressing them towards each other. Compressing tubes radially induces deformation and changes the circular cross section into elliptical one. We showed that two parallel $(8, 0)$ tubes can be linked by C-C bonds between the tubes under weak as well as strong contact forces. The junctions of crossed nanotubes are studied by using a 2D grid model for a wide range of contact forces. It has been shown that certain physical properties do not vary continuously with the contact forces. The C-C bonds interlinking the tubes can form under relatively weak contact forces. These bonds survive even after the contact forces are released. However, strong forces induce significant radial deformation and give rise to flattening of the tube surfaces. Once the surfaces becomes locally planar at the contact, the curvature effects diminish. At the end, interlinking bonds are broken and the spacing between chemically inactive flat surfaces increases as in graphite layers. Under these circumstances a finite potential barrier between tubes hinders ballistic electron transport from one tube to other. The potential barrier collapses if linking bonds between the tubes are present.

The formation of interlinking bonds can be enhanced by making the contact

chemically active. This can be achieved by implementing imperfections, such as substitutional impurities with valencies different from four (such as B, N, P etc.) or more conventionally by creating vacancies and divacancies. A single carbon atom between tube surfaces can also provide the interlinking. A single vacancy created on one of the tube surfaces makes the junction chemically active and establishes an sp^3-like bonding configuration. As a result, the potential barrier is collapsed through interlinking bonds. Our results related to junctions with vacancy explain how the stable crossbar structures can be fabricated by *in-situ* processes. An alternative process to make crossbar, T and other types of junctions is to weld the tubes at the junction site by the chemisorption of atoms, which make stable chemisorption bonds. Here we mention Ti atom, which is easily adsorbed and also can make thick coating of SWNTs. Calculation of quantum ballistic conductance through various junctions confirm the analysis based on potential energy and atomic structure for the behavior of the contact as a function of the contact force.

We also examined the 3D grid structure of tubes by using only limited supercell size consisting of 3×3 unit cells of $(8, 0)$ zigzag tube laterally. Our results indicate that formation of linking bonds, stability and variation of electronic structure depend on the applied contact force. We believe that 2D and 3D grid structures can render a framework to integrate SWNT-based devices or functionalization by adsorption of molecules.

A large spacing and sizable potential barrier between the tube and metal electrode, $\Phi_c \sim 3.9eV$ are characteristics of the contact made with the Au surface. This explains why the devices made from Au electrodes have high contact resistance. Here, weak coupling of electronic states cannot lead to MIGS, and the (8,0) SWNT is identified to be semiconducting even after the contact has been set with the Au surface. Because of weak coupling and hence finite Φ_c, the s-SWNT-Au contact is reminiscent of the metal-oxide-semiconductor (MOS) junction. A small Φ_B is estimated for the p-type character. Upon radial deformation, **s** decreases and eventually Φ_c collapses. Similar features have been observed recently in STM studies using multi-wall carbon nanotube tip and Au(111) sample.[277]

However, Φ_c has disappeared due to strong coupling between the states of s-SWNT and Mo(110).[278] The height of the Schottky barrier Φ_B that forms at the SWNT-Mo(110) junction having a finite contact region followed by a free s-SWNT depends on the position where the Fermi level is pinned in the gap of s-SWNT. A crude estimate based on the LDOS suggests that $\Phi_B \sim 0.4$ eV for the p-type character. The small cross section of the tube does not allow us to identify a band diagram across the diameter. But the bands are normally bent along the axis of the s-SWNT and the height of the barrier is monitored by the applied gate voltage. Finally, we note that the electronic properties of present metal-SWNT junctions, in particular the Fermi level pinning exhibit marked differences from those of metal-Si heterostructures, which are known to be insensitive to the type of metal.

Chapter 8

Hydrogen Storage of Carbon Nanotubes

Fuel cells have been a real challenge for clean and efficient source of energy in diverse fields of applications in different size and capacity range. Once hydrogen molecule is chosen as potential fuel, its storage, easy discharge for consumption and dissociation into hydrogen atoms in the fuel cell to produce the desired electromotive force involve several problems to be solved. Dillon *et al.*[22] have pioneered the idea that nanotubes can be efficient, cheap and rechargeable storage medium for small-scale fuel cells and they estimated 5-10 weight percent (*wp*) H_2 adsorption in single-wall carbon nanotubes (SWNT). Later, Ye *et al.*[279] and Liu *et al.*[280] obtained H_2 storage capacities of 8.2 and 4.2 *wp*, respectively. Unfortunately, recent studies further exploring this idea have come up with controversial conclusions[281, 282, 283, 284, 285, 286]. In the mean time, adsorption of alkali atoms on SWNTs have been proposed to enhance the H_2-uptake[286, 287]. Nevertheless, carbon nanotubes have high surface-volume ratio and their functionalization to render them feasible for hydrogen storage through coverage of suitable adatoms has remained to be explored.

In this Chapter, to clarify controversial issues related to the storage of hydrogen molecule on carbon nanotubes we first addressed following questions: (*i*) Can

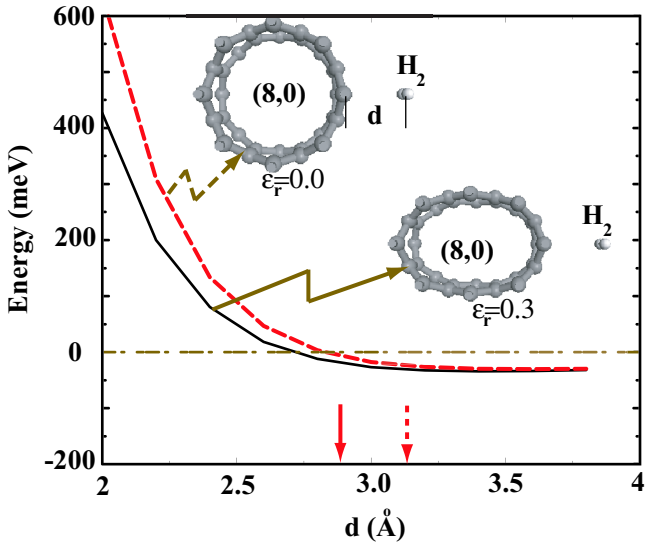

Figure 8.1: Variation of chemical interaction energy E_C between SWNT and H_2 molecule as a function of distance d between them. Two cases, namely adsorption to bare and radially deformed SWNT are shown by dashed and continuous lines, respectively. In calculating both curves, atomic structures corresponding to $d \rightarrow \infty$ have been used without relaxation. Dash-dotted line indicate zero of chemical interaction energy. Optimized distance for two cases are indicated by arrows.

H_2 molecule be adsorbed on the SWNT? (*ii*)What is the nature and strength of the bonding? (*iii*)Can the strength of the bonding be modified either by changing the curvature of the surface or by the coadsorption of metal atoms? Then, we examined whether the functionalization of SWNTs by transition metal elements can promote the H_2-uptake and give rise to the dissociation of H_2. To answer all these questions we investigated the interaction between H_2 molecule and bare, radially deformed and foreign atom adsorbed SWNTs by carrying out calculations within DFT[37, 290]. Our results not only advance our understanding of H_2 adsorption on carbon nanotubes, but also suggest new ways for efficient hydrogen storage. Recently, Taner *et al.* found that every Ti atom adsorbed on hexagonal site of SWNT can hold up to 4 H_2 molecule and they obtained 8% *wp* hydrogen with this system [288]. They suggests that Ti doped nanotubes are better systems for hydrogen storage mechanisms.

Our calculations have been carried out using first-principles plane wave

method and ultrasoft pseudopotentials[89, 241] within Generalized Gradient Approximation (GGA)[122]. Adsorption and dissociation of H_2 is treated within the supercell geometry with lattice parameters a_{SC}=20 Å, b_{SC}=20 Å and c_{SC}=4.26 Å. The lattice parameter of the SWNT along its axis, c is taken to be equal to c_{SC}. Certain systems are treated in double supercell with $c_{SC} = 2c$ to reduce the adsorbate-adsorbate interaction. All atomic positions (SWNT and adsorbate), as well as the lattice parameter of the supercell, c_{SC} are optimized by minimizing total energy, E_T, atomic forces and the stress of the system. Brillouin zone is sampled by $1 \times 1 \times 23$ special **k**-points ($1 \times 1 \times 11$ for double cells) using the Monkhorst-Pack scheme[83]. The calculations involving the graphite-adsorbate systems are carried out by $4\times4\times1$ special **k**-point sampling. Bloch wave functions are expanded by plane waves with the kinetic energy $\hbar^2|\mathbf{k}+\mathbf{G}|^2/2m < 400$ eV. The weak attractive Van der Waals (VdW) interaction becomes crucial in calculating binding energies of weak physisorption bonds, but is not well represented in DFT using GGA[291]. Therefore, in the case of physisorption, the contribution of weak and attractive VdW interaction energy, E_{VdW}, to the binding is obtained from the Slater-Kirkwood approximation[192] using the asymptotic form of the Lifshitz's equation[189]. This approach, however, cannot be suitable to determine the contribution of VdW interaction in the chemisorption of molecules. Nevertheless, in the chemisorption regime the VdW interaction is dominated by the chemical interaction. In the present calculations we take the zigzag (8,0) SWNT as a prototype tube.

8.1 Adsorption of H2 on bare and radially deformed SWNT

To clarify whether H_2 can form stable bonding on the outer or inner surface of a SWNT, we calculated the chemical interaction energy between H_2 and the outer surface of the (8,0) SWNT at different sites (*i.e.* H-site, above the hexagon; Z- and A-site above the zigzag and above the axial C-C bonds; T-site, a bridge site between two adjacent zigzag C-C bonds) as a function of spacing d. The chemical

interaction energy is obtained from the expression, $E_C(d)$=E_T[H_2+SWNT,d]-E_T[SWNT]-E_T[H_2], in terms of the total energies of bare nanotube (E_T[SWNT]), free H_2 (E_T[H_2]), and H_2 attached to SWNT at a distance d (E_T[H_2+SWNT,d]). Here $E_C < 0$ corresponds to an attractive interaction. The stable binding occurs at the minimum of $E_C(d) + E_{VdW}(d)$, the negative of it is denoted as the binding energy E_b. The binding is exothermic when $E_b > 0$. In Fig. 8.1 we show the variation of $E_C(d)$ calculated for unrelaxed atomic structures at the H-site. Once the atomic structure of both SWNT and H_2 molecules are relaxed the minimum value of $E_C(d)$ is found to be -27 meV at $d_0 = 3.1$Å at the H-site. Minimum values of $E_C(d)$ calculated for A-, Z-, and T-sites are also very small and comparable to that of H-site. We expect that as n or radius R of SWNT increases the calculated $|E_C(d)|$ slightly decreases. Similar DFT calculations by Han and Lee [292] found that $E_C(d)$ of H_2 with a vertical orientation at the H-site of a (10,0) SWNT has a minimum value of 34 meV at d_0=3.44 Å. The long range VdW interaction energy calculated for the H-site at d_o is E_{VdW} ∼-30 meV. Then the binding energy associated with H_2 molecule adsorbed at H-site is calculated to be E_b ∼57 meV. This is a small binding energy and indicates physisorption[293].

Previous studies[281, 282] revealed that the physisorption of individual H_2 molecules with $E_b > 0$ cannot occur on the inner wall of SWNT. Hydrogen molecules prefer to stay either at the center of the tube or to form some cylindrical shells inside depending on radius of the tube. Owing to increased H-H interaction at high coverage, even the atomic hydrogen cannot form stable structure when it is adsorbed to the inner wall of small radius tube. For (8,0) tube we found that H_2 is trapped and stabilized at the center of the tube with a repulsive interaction energy $E_C = +0.34$ eV. The implementation of H_2 inside the tube having radius in the range of 3 Å is expected to be hindered by this repulsive interaction.

Earlier it has been shown that binding energy of foreign atoms adsorbed on SWNT increase with increasing curvature[113]. Tada *et al.*[294] have argued that the potential barrier associated with the dissociative adsorption of H_2 on SWNT is lowered with increasing curvature of the tube. It has been proposed that the potential barrier for the dissociation of H_2 adsorbed in the interstitial region between tubes can be lowered by applying radial deformation to the rope

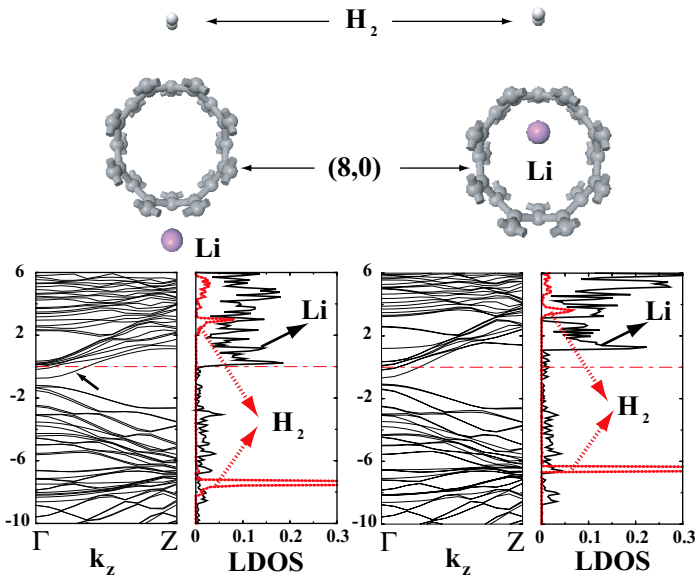

Figure 8.2: Atomic configuration, energy band structure and LDOS calculated for the coadsorption of H_2 molecule and single Li atom. Two cases correspond to Li atom chemisorbed on the external and internal surface of the (8,0) zigzag SWNT. Zero of energy is set at the Fermi level, E_F. LDOS calculated at Li and H_2 are shown by continuous and dotted lines, respectively. Metallized SWNT bands are indicated by arrows.

or SWNT[295]. It is known that under radial deformation the circular cross section changes and consequently the curvature varies at different locations on the surface. Motivated with those effects of curvature, we examine whether the attractive interaction energy E_C can be enhanced by changing the curvature of the tube via radial deformation. Radial deformation is realized by pressing the tube between two ends of a given diameter. It, in turn, changes the circular cross section of the bare tube with radius R_o to an elliptical one with major and minor axes $2a$ and $2b$, respectively. The atomic structure of (8,0) tube is optimized under radial strain $\epsilon_r = (R_o - b)/R_o \simeq 0.3$ by fixing row of carbon atoms at the end of minor axis. The deformation is reversible so that the tube goes back to its original, undeformed form upon the release of radial strain[105, 131]. The deformation energy (that is the difference between the total energies of deformed and undeformed SWNTs) is calculated to be E_D =1.4 eV per unit cell. We examined whether the binding energy of H_2 molecule changes under the radial deformation of SWNT. Figure 8.1 shows the variation of $E_C(d)$ for H_2 approaching toward the high curvature site of the tube (*i.e.* one end of the major axis) at the H-site. The minimum value of the attractive interaction, E_C is -30 meV and occurs at d_o=2.9 Å. For ϵ_r =0.25, we also obtained very small enhancement of $E_C(d)$. Hence, the enhancement of the binding energy of H_2 due to curvature effect is negligibly small due to relatively large d_o. This result also suggests that the physisorption energy does not vary significantly depending on the radius of SWNT. The minimum of $E_C(d)$ is small and does not vary significantly relative to the adsorption site. This suggests that the chirality of the tube has negligible effect on the physisorption energy. Apparently, the binding of H_2 on the outer surface of SWNT is weak and the corresponding physisorption energy is small. The binding cannot be enhanced by increasing the curvature locally through radial deformation. Curvature effect or radial deformation may be significant at small d when H_2 is forced towards SWNT surface. Present results are in line with the work by Kostov *et al.*[296].

8.2 Coadsorption of hydrogen molecule and Lithium atom on SWNT

Next, we examine whether the binding of H_2 is enhanced by the coadsorbed foreign atoms. To this end we first consider Li atom adsorbed on the (8,0) SWNT, since the adsorption of an alkali atom has been proposed to enhance the H_2-uptake[286, 287]. Li atom is chemisorbed at the H-site, 1.5 Å above the surface of SWNT with a binding energy of 0.8 eV. Self-consistently calculated electronic structure shown in Fig. 8.2 reveals that chemisorbed Li atoms donate their $2s$-valence electrons to the lowest conduction π^*-band so that the semiconducting (8,0) SWNT (having band gap E_g =0.6 eV) becomes metallic. This is a behavior common to the other alkali atoms adsorbed on SWNTs[220]. In order to examine the indirect effect of coadsorbed Li we considered H_2 as attached at the opposite site to Li. The optimized structure of the physisorbed H_2 is shown in Fig. 8.2 together with relevant structural parameters. We found E_C has a minimum value of -35 meV at d_o =3.4 Å. Similar study has been also performed for Li atom adsorbed on the inner wall of SWNT while H_2 is on the external wall directly above the coadsorbed Li as shown in Fig. 8.2. In this adsorption configuration minimum value of E_C practically did not change. The local density of states calculated on Li atom and H_2 refuse the possibility of any significant interaction between adsorbates. As a result, our calculations for both external and internal adsorption of Li rule out any indirect effect of coadsorbed Li to enhance the binding of H_2 on SWNT. The occupation of empty conduction band by the alkali electrons and hence metallization of SWNT did not affect the bonding of H_2. These results are in agreement with the first principles calculations by Lee *et al.*[298]. However, the effect of Li on the adsorption of H_2, whereby H_2 is attached directly to Li atom is found significant. The minimum value of E_C has increased to -175 meV, while d_o decreased to 2.1 Å. Briefly, the coadsorption of Li does not have any indirect effect on the binding of H_2, but the energy associated with direct binding to Li is enhanced. The nature of bonding remains physisorption in direct and indirect cases.

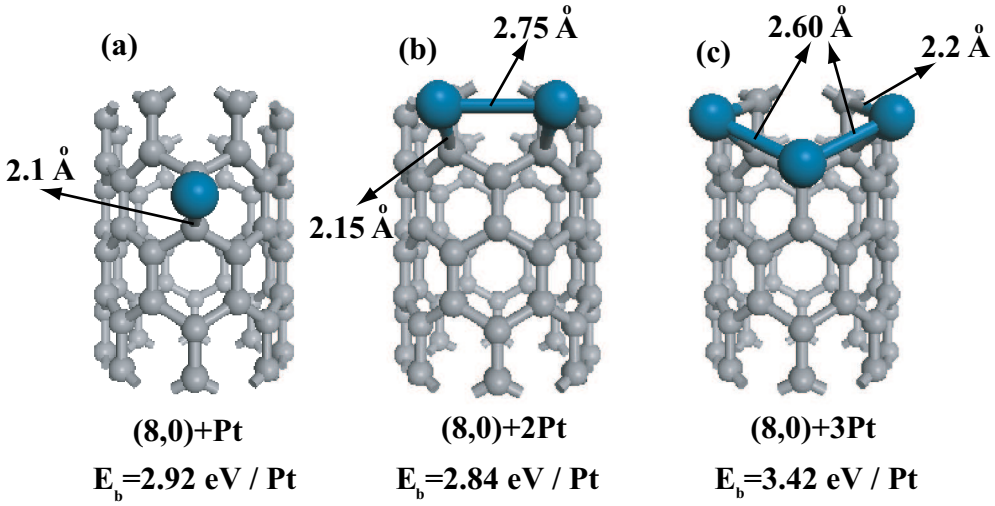

Figure 8.3: (a) Atomic configurations for single, double and triple Pt atoms adsorbed on the (8,0) SWNT. Average binding energy of adsorbed Pt atoms E_b and bond distances are indicated.

8.3 Coadsorption of Hydrogen molecule and Platinum atom on SWNT

A single transition metal atom adsorbed on the outer surface of SWNT has shown interesting properties, such as high binding energy and magnetic ground state with high net magnetic moment. For example, transition element atoms (Ti, V, Cr, Mn, Fe, Co, Pt, *etc.*) have crucial adsorption states on nanotubes[220] and some of them (Ti, Ni, Pd) form continuous or quasi-continuous metal coating on the SWNT[211, 238, 297]. As for Pt atom, it is known to be a good catalyst in various chemical processes. While SWNTs offer high surface/volume ratio, the interaction between H_2 and Pt atom adsorbed on SWNT may be of interest. Now we investigate the character of the bonding between H_2 and Pt adsorbed on SWNT and address the question of how many H_2 molecules can be attached to an adsorbed Pt atom and how strong is the binding.

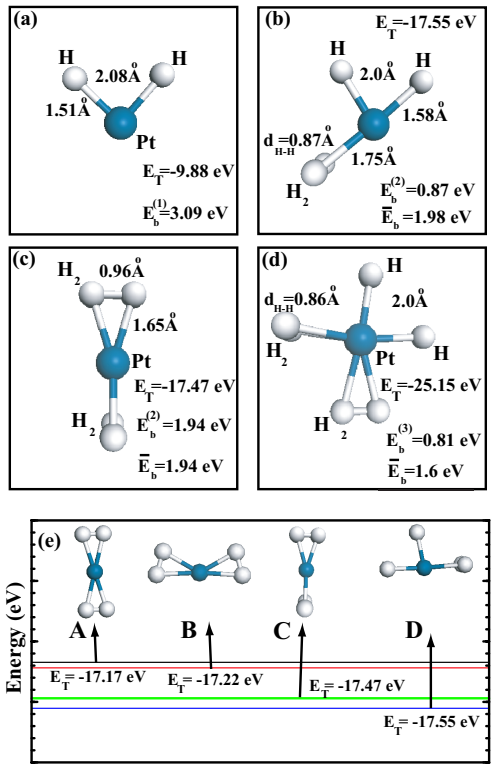

Figure 8.4: Optimized binding configuration of H_2 molecules adsorbed to a free Pt atom. (a) Dissociative adsorption of a single H_2 molecule. (b) The first H_2 is dissociatively, second H_2 molecularly adsorbed. (c) Two H_2 are molecularly adsorbed. (d) Two H_2 are molecularly, one H_2 dissociatively adsorbed (e) Four different configurations related with the adsorption of two H_2 to the same free Pt atom. Binding energy of the n^{th} H_2 molecule adsorbed to Pt atom, $E_b^{(n)}$; average binding energy per H_2, $\overline{E}_b$, total energy with respect to constituent atoms E_T and bond distances are indicated.

8.3.1 Adsorption of Pt atoms on SWNT

We first examine the adsorption of Pt atom(s) on (8,0) SWNT. The character of the bonding has been investigated by placing Pt atoms on the A-sites of (8,0) tube (that is known to yield highest binding energy[220]) and then by optimizing the structure. Three different adsorption configuration have been examined, namely one, two and three Pt atoms adsorbed on the adjacent sites to represent a small cluster on SWNT as described in Fig. 8.3. Calculated binding energies of Pt atoms have increased as the number of Pt atoms increases from one to three in the same neighborhood. On the other hand, the C-Pt distance gradually increases with increasing number of Pt atoms adsorbed in the same neighborhood. This paradoxical situation can be understood by the increasing Pt-Pt coupling, which happens to retract electronic charge from C-Pt bonding derived by the Pt-3d and C-2p orbitals.

8.3.2 Adsorption of H2 to a free Pt atom

We now consider the interaction between H_2 molecules and a free Pt atom. Optimized binding structures are shown in Fig. 8.4. Upon approaching to a free Pt atom, single H_2 molecule dissociates and form PtH_2 with Pt-H bond distance d_{Pt-H}=1.51 Å and d_{H-H}=2.08 Å. The total energy E_T relative to the energies of free Pt and H atoms is calculated -9.88 eV. The binding energy relative to H_2 molecule and free Pt atom (namely, $E_b^{(1)}$=E_T[H_2]+E_T[Pt]-E_T[Pt+2H]) is $E_b^{(1)}$=3.09 eV. As for the adsorption of H_2 to PtH_2, there are several minima on the Born-Oppenheimer surface: The first minimum corresponds to a configuration in Fig. 8.4(b) where PtH_2 preserves the dissociated configuration while second H_2 is molecularly adsorbed. Even if H-H interaction of adsorbed H_2 is weakened and hence the H-H distance has increased to 0.87Å, we identify it as molecular adsorption. We denote this configuration as PtH_2-H_2. The adsorbed H_2 molecule is perpendicular to the plane of PtH_2. The binding energy of the second H_2 to PtH_2 (namely, $E_b^{(2)}$=E_T[H_2]+E_T[Pt+2H]-E_T[Pt+2H+H_2]) is calculated to be 0.87 eV. Under these circumstances the average binding energy per

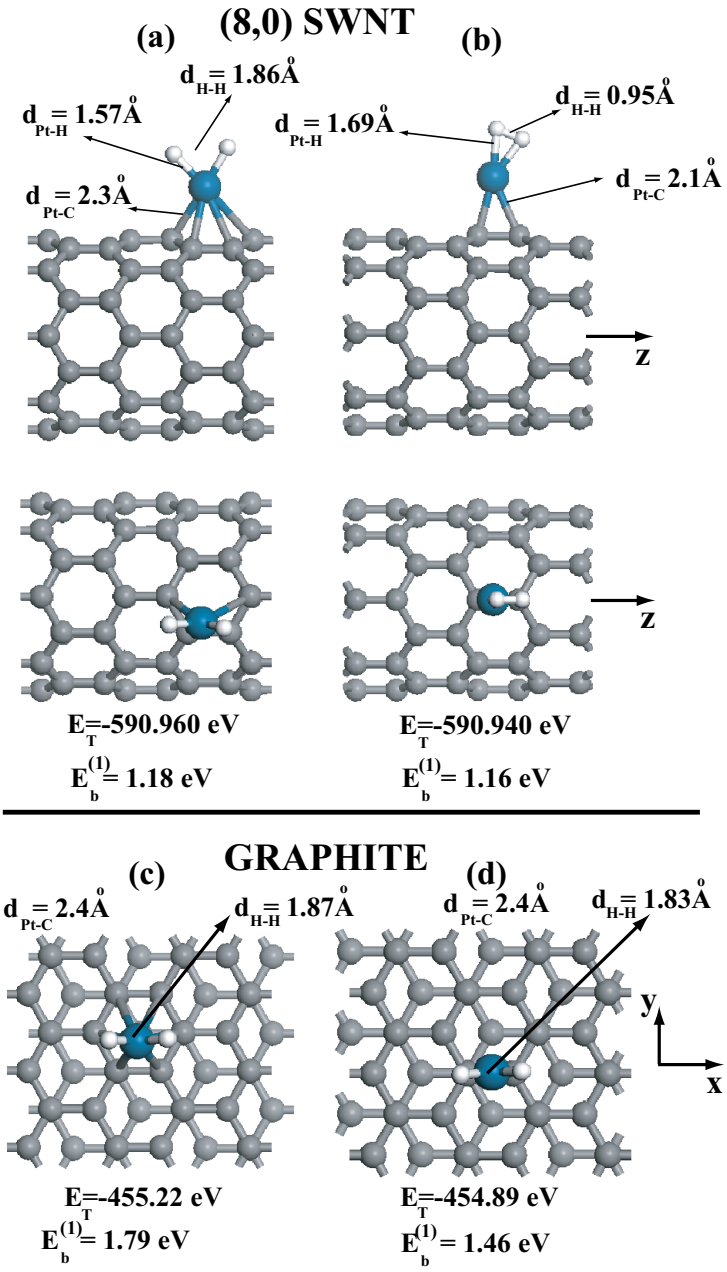

Figure 8.5: Optimized geometry for a single H_2 molecule adsorbed to a single Pt atom. (a) Pt atom is adsorbed near the H-site of (8,0) SWNT (side and top view) (b) Pt at the A-site (bridge position) of (8,0) SWNT (side and top view) (c) Pt atom is adsorbed near the H-site of the graphite surface (d) Pt atom at the A-site of graphite. E_T is the total energy relative to the constituent free C, Pt and H atoms.

H_2 is $\overline{E}_b$=1.98 eV. In the second configuration, identified as Pt-2H_2 as shown in Fig. 8.4(c), both H_2 are molecularly adsorbed. As H-H molecular bonds are weakened, d_{H-H} is increased to 0.96Å and all Pt-H bonds have uniform length with d_{Pt-H} =1.65Å. Here adsorbed H_2 molecules are perpendicular. The binding energy of each molecules is calculated to be 1.94 eV slightly less then the average binding energy in PtH_2-H_2 configuration. The configuration PtH_2-2H_2 shown in Fig. 8.4(d) involves the adsorption of three H_2 molecules; one dissociatively, remaining two are molecularly adsorbed. Here Pt-H_2 planes of two molecularly adsorbed H_2 are perpendicular. The binding energy of the third H_2 relative to the energy of PtH_2-H_2 in Fig. 8.4(b) is found to be $E_b^{(3)}$=0.81 eV. Accordingly, the average binding energy of each H_2 is $\overline{E}_b$=1.6 eV relative to free H_2 and free Pt atom. Fig. 8.4(e) compares four distinct configurations related with the adsorption of two molecules on the same free Pt atom. It appears that these configurations determined by conjugate gradient method correspond to local energy minima and the configuration in Fig. 8.4(b) appears to have lowest energy.

8.3.3 Adsorption of H2 to a Pt atom on SWNT

We deduced two configurations for the adsorption of a single molecule to a Pt atom adsorbed on the (8,0) SWNT as described in Fig. 8.5. While these two chemisorption configurations look dramatically different, their total energies differ only by 20 meV. In the configuration described in Fig. 8.5(a) H_2 is dissociatively adsorbed with binding energy ($E_b^{(1)}$=E_T[H_2]+E_T[SWNT+Pt]-E_T[SWNT+Pt+2H]) 1.18 eV. The H-H and Pt-C distances are 1.86 Å and 2.3 Å, respectively. Whereas in the configuration in Fig. 8.5(b) H_2 is molecularly adsorbed with a significantly weakened H-H bond. H_2 approaching from different directions and angles results in a chemisorption state with binding energy E_b =1.16 eV and Pt-H distance 1.7 Å. The length of H-H bond has increased from 0.75 Å to 0.95 Å upon adsorption[299]. As compared to the configuration of dissociative adsorption in Fig. 8.5(a), in the case of molecular adsorption the Pt-SWNT bond is relatively stronger with shorter d_{Pt-C}=2.1 Å. Notably, while in the first configuration leading to dissociative adsorption in Fig. 8.5(a) Pt atom is

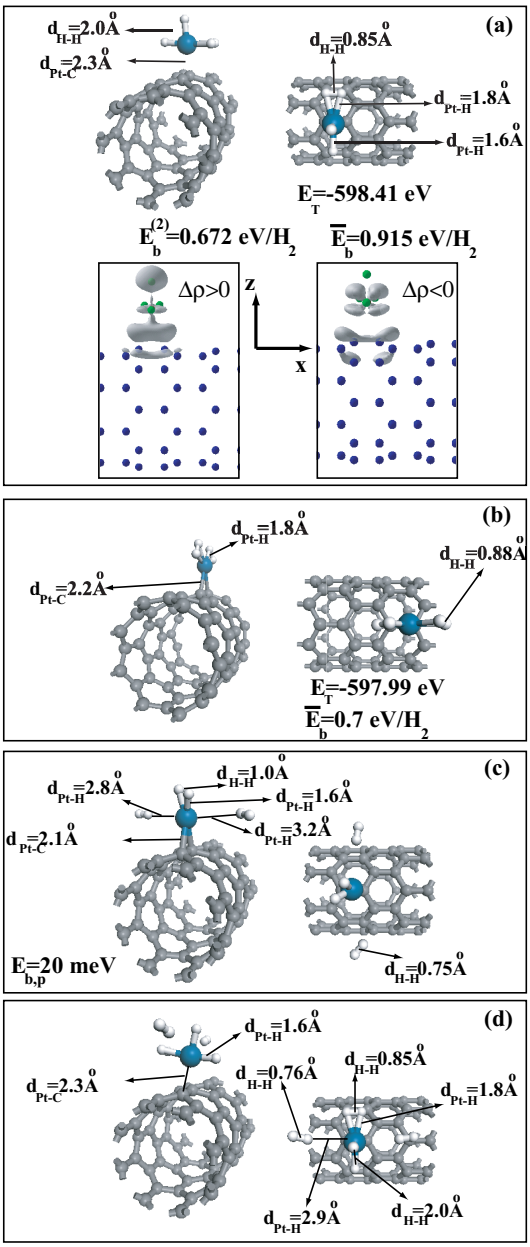

Figure 8.6: Optimized structure of H_2 molecules adsorbed to the Pt atom on the SWNT. (a) One H_2 adsorbed to PtH_2. The inset show the regions of charge depletion ($\Delta\rho < 0$) and charge accumulation ($\Delta\rho > 0$) as a result of the bonding between SWNT and PtH_2+H_2 in (a). (b) Another local minima where two H_2 is molecularly adsorbed to the Pt atom. (c) One H_2 is chemisorbed two H_2 are weakly bound. (d) four H_2.

located near hollow H-site, in the "molecular" adsorption of H_2 in Fig. 8.5(b) Pt atom is adsorbed at the A-site. We also note that because of the Pt-SWNT bond in Fig. 8.5(a) and 8.5(b) the binding energies are smaller than that in Fig. 8.4(a).

Adsorption of H_2 to a single Pt atom attached to the surface of graphite is of interest in order to reveal how the binding energy and binding configuration of H_2 depends on the radius of SWNT. We considered two configuration, namely single Pt atom is adsorbed near hollow H-site, as shown in Fig. 8.5(c) and Pt at the A-site as shown in Fig. 8.5(d). For both location of Pt atom on the graphite surface, H_2 molecule approaching the adsorbed Pt atom is dissociated and eventually formed two Pt-H bonds with individual Pt atom. In this case the binding of Pt with the graphite surface is weaker than that on SWNT, and thus d_{Pt-C} is increased to 2.4Å. Relatively weaker interaction between Pt and graphite surface allows stronger interaction between H_2 and Pt, as in the case of free Pt atom, and hence leads to the dissociation of the molecule. In view of two limiting case in Fig. 8.5, one can expect that dissociation of H_2 may be favored if Pt is adsorbed on SWNTs having large R (or large n).

To answer the questions of how many H_2 molecule can be attached to a single Pt atom we perform a systematic study outlined in Fig. 8.6. First we let a second H_2 approaches to Pt atom on SWNT that already has one H_2 molecule attached as in Fig. 8.5(b). The final optimized geometry of Pt and adsorbed H_2 molecules in Fig. 8.6(a) is similar to the configuration PtH_2-H_2 described in Fig. 8.4(b). This situation is explained by the weakening Pt-C bond between PtH_2 and SWNT shown in Fig. 8.5(a) which is followed by the increase of d_{Pt-C}. First H_2, which was initially chemisorbed to Pt as a molecule (with relatively increased d_{H-H}) has dissociated upon the molecular adsorption of the second H_2. The dissociation of H_2 is an indirect process and is mediated by the weakening of the Pt-C bonding through the molecular adsorption of second H_2. The difference charge density $\Delta\rho(\mathbf{r}) = \rho_T(\mathbf{r}) - \rho_{\mathrm{SWNT}}(\mathbf{r}) - \rho_{\mathrm{PtH_2+H_2}}(\mathbf{r})$ calculated from the difference of total charge density $\rho_T(\mathbf{r})$ of SWNT+PtH_2+H_2 in Fig. 8.6(a) and those of SWNT and PtH_2+H_2 indicates that while the charge of Pt-d_{xy} and C-$p_{x,y}$ orbitals are depopulated, the Ptd_{z^2} and C-p_z orbitals become populated to form Pt-SWNT

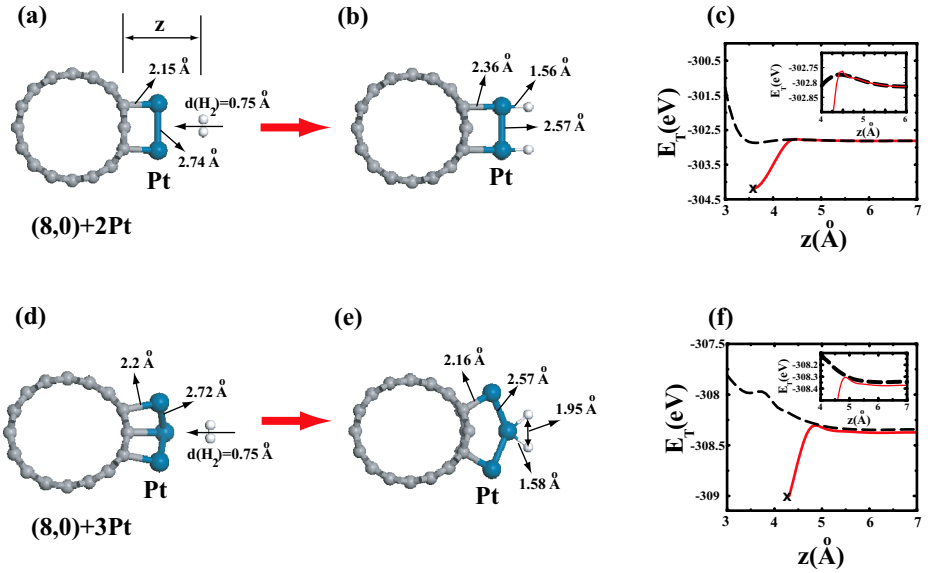

Figure 8.7: Dissociative adsorption of single H_2 on a small Pt cluster adsorbed on SWNT (a). One H_2 is approaching two adjacent Pt atoms adsorbed on SWNT. (b) Optimized geometry after dissociative adsorption of H_2. (c) Variation of total energy with distance z. Dashed curve corresponds to E_T for unrelaxed H_2 and unrelaxed SWNT. Continuous curve corresponds to E_T of the geometry relaxed at certain values of z. (d), (e) and (f) same as (a), (b) and (c) except the Pt cluster consists of 3 Pt atoms. z is the distance from the surface of SWNT. Variation of $E_T(z)$ is amplified by inset.

bond. This result suggests that in a reverse situation the weakening of the Pt-SWNT bond would lead to the transfer of charge from Pt-C bond to Pt-H bonds resulting in increased population of d_{xy}-orbitals that favors the dissociation of H_2. Interestingly, exactly the same configuration has been obtained even when two H_2 molecule approach concomitantly the bare Pt adsorbed on SWNT. Another configuration related with two molecularly adsorbed H_2 is shown in Fig. 8.6(b), which appears to be a local minima on the Born-Oppenheimer surface and has $\sim$0.4 eV less binding energy than that in Fig. 8.6(a). We note that the atomic configuration of PtH_2-H_2 complex in Fig. 8.6(a) does not change significantly even after SWNT is removed and the remaining system is relaxed.

In Fig. 8.6(c), two H_2 approaching from both sites of PtH_2 on SWNT have been attached by weak physisorption bonds resulting in PtH_2+$2H_2$ configuration. Their distances to Pt atom are relatively larger (d_{Pt-H_2}=2.1Å and 3.2Å) than that occurred for molecularly chemisorption of H_2. The latter Pt-H_2 distance is too long and the corresponding binding energy is only $\sim$ 20 meV; the binding energy can increase slightly by the VdW interaction but the adsorbed molecule can desorb and escape from Pt at high-temperature. Note that due to weak interaction between Pt and both H_2 molecules in Fig. 8.6(c) H-H distance of PtH_2 remained small to be associated with H_2 and consequently the Pt-C bond retained its strength with relatively smaller Pt-C distance. The attempts to attach more than three molecules to the Pt atom have failed. For example, as shown in Fig. 8.6(d), from four H_2 brought at the close proximity of Pt atom, only three were attached (one dissociatively chemisorbed, one molecularly chemisorbed, one physisorbed and the forth escaped). At the same time the Pt-SWNT bond has weakened and hence d_{Pt-C} distance has increased to 2.3Å. The binding energy of second H_2 molecule $E_b^{(2)}$ in Fig. 8.6(a); the average binding energy per H_2 in Fig. 8.6(b), $\overline{\mathrm{E}}_b$; the binding energy of the physisorbed H_2 with d_{Pt-H_2} = 3.2 Å, $E_{b,p}$ are indicated. Furthermore, we define the interaction energy between Pt+$n$$H_2$, (with n=2, 3 and 4 where one of H_2 is dissociated) and SWNT in Fig. 8.6(a-c) as E_C[Pt-$n$$H_2$]=$E_T$[SWNT]-$E_T$[Pt+$n$$H_2$+SWNT]. Here the total energies are calculated using the same atomic structures in Fig. 8.6(a-c). Calculated interaction energies for each case are 0.68 eV, 1.88 eV and 0.78 eV, respectively. Using

the similar procedure we also calculated the interaction energy between Pt+H_2 (where H_2 is molecularly adsorbed) and SWNT in Fig. 8.5(a) to be 1.93 eV. Clearly, the variation of these energies with structure and Pt-C distances confirm the above arguments that the dissociation of one of H_2 is followed by the weakening of the bond between Pt and SWNT.

8.3.4 Adsorption of H2 to a small Pt cluster on SWNT

As shown in Fig. 8.7(a-b), the situation is different in the case of interaction between H_2 and a small Pt cluster (consisting of a few Pt atoms adsorbed at close proximity). As H_2 approaches two Pt atoms on SWNT it starts to dissociate at a distance $\sim$ 3.9Å from the surface of SWNT. The optimized configuration is shown in Fig. 8.7(b) where H-H molecular bond is broken and each adsorbed Pt atom formed a Pt-H bonds with d_{Pt-H}=1.56Å. Upon chemisorption d_{Pt-C} increased from 2.15Å to 2.36Å. The dissociation process schematically shown in Fig. 8.7(c) by plotting the variation of total energy E_T as a function of z for two different cases. The dashed curve corresponds to the total energy of SWNT+Pt_2 and H_2 calculated for different H_2-tube distance z by keeping the atomic configuration at $z \to \infty$ unchanged for all z. The continuous curve is obtained by relaxing the atomic configuration at certain values of z. We see that for $z < 4.2$Å E_T starts to lower upon the onset of dissociation. We note very small barrier at about $z \sim 4.5$Å. Upon overcoming this energy barrier, the process is exothermic with an energy gain of $\sim$ 1.2 eV. The continuous curve ended with ($\times$) that corresponds to the equilibrium configuration. As described in Fig. 8.7(d-f), the adsorption of single H_2 on a Pt cluster consisting of three Pt atoms also results in dissociation of the molecule. As the size of cluster increased by inclusion of the third Pt atom, the small potential barrier at $z \sim 4.5$Å is further lowered, the binding energy increased to 1.5 eV. Also one of the Pt atoms which binds both H atom is detached from the SWNT surface. This situation confirms that Pt-SWNT bonds are weakened upon the (molecular or dissociative) adsorption of H_2 to Pt.

The interaction between Pd atoms adsorbed on SWNT and H_2 molecule is

somehow similar to that with Pt atom. However, the latter case leads relatively less strong interaction and smaller binding energies. For example, the interaction between H_2 and a single Pd atom adsorbed on SWNT results in a binding between chemisorption and physisorption with a binding energy of 0.6 eV. In this case, while the H-H bond length is stretched a little from the normal value 0.7 Å to 0.8 Å, the C-Pd bond is stretched from 2.1 Å to 2.2 Å. Small changes after the adsorption of H_2 are manifestations of relatively weak H_2-Pd interaction. In contrast to adsorbed two Pt atom in Fig. 8.7(a) breaking the H_2 molecule, two adsorbed Pd atoms give rise to chemisorption of molecule with more stretched H-H bonds.

8.4 Discussions

In summary, we presented a detailed analysis of the interaction between hydrogen molecule and a SWNT. We found that the binding energy between H_2 and outer surface of a bare SWNT is very weak and the physisorption bond can easily be broken. We showed that the binding of H_2 to the outer surface cannot be enhanced by applying radial deformation to increase curvature effects at the site facing H_2 molecule. In contrast, the interaction between the inner surface of (8,0) tube and H_2 is repulsive which can prevent molecules from entering inside the tube having small radius. The repulsive interaction may turn to be attractive for large tube radius. To promote H_2 uptake on SWNT surface we considered functionalized tubes through adsorption of foreign atoms. The binding energy of H_2 on SWNT surface did not increase significantly by the coadsorption of Li. However, the binding energy increased if H_2 is directly attached to adsorbed Li; yet the nature of the bonding remained physisorption.

The situation with Pt atom, which can make strong chemisorption bonds with the outer surface of SWNT is found to be interesting from the point of view of H_2 storage. We showed that H_2 molecule can form chemisorption bonds with free Pt as well as Pt adsorbed on SWNT. Single H_2 adsorbed on a free Pt atom dissociates and forms two strong Pt-H bonds. On the other hand, while

single H_2 molecule is molecularly chemisorbed to a single Pt atom at the A-site of SWNT surface, it can dissociate if Pt atom adsorbed near the hollow site. The latter configuration is favorable energetically. Even the molecular adsorption of single H_2 can turn dissociative if a second H_2 is molecularly adsorbed to the same Pt atom. The dissociative adsorption is mediated by the weakening of Pt-C bonds either due to a specific location of Pt on SWNT or due to the second H_2 molecularly adsorbed to Pt. Dissociative adsorption of single H_2 to a single Pt atom on the graphite surface suggests that the dissociation of H_2 is favored on SWNTs having large radius. Our analysis suggests that single Pt adsorbed on SWNT can bind up to two H_2 molecules with significant binding energy in the chemisorption range. Beyond two adsorbed H_2, additional H_2 molecule may form very weak physisorption bonds with Pt. Single Pd atom adsorbed on SWNT exhibits similar effects but in relatively weaker manner as compared to that of Pt. Certainly, SWNT surfaces decorated by adsorbed Pt (or Pd) atoms each binding two H_2 molecules (disregarding additional H_2 attached by very weak physisorption bonds) cannot meet the target of 6 *wp* set for a feasible hydrogen storage. However, present results revealed interesting interaction between H_2 and Pt and resulting bonding mechanisms which have led to similar investigations of SWNTs functionalized by other transition elements (in particular Ti, Ni, Cr, V) for more efficient H_2 storage.

Chapter 9

Conclusion

In the present thesis, the structural, magnetic and electronic properties of Functionalized Carbon Nanotubes have been analyzed in detail by applying *ab-initio* plane-wave pseudopotential formalism. We have implemented different kinds of functionalization to nanotubes to obtain new materials which show novel physical and chemical properties. Our computational work will be of interest for experimental studies aiming at new materials to be used in new generation devices. Besides, these approaches necessary to understand: *(i)* how can we generate materials? *(ii)* How can we find interesting properties by using different kind of atoms? *(iii)* Are these new materials appropriate for widely used devices?

Our studies showed that bare Nanotubes are very active materials and their physical and chemical properties are attractive for new ideas about them. They are suitable for the use in potential technological applications. That a (n,m) SWNT can be metallic or semiconducting depending on n and m offers a wide range of options. Moreover, these options are multiplied several times through the functionalization of tubes. Here we dealt with specific cases wherein the properties of the nanotube undergo a dramatic change upon physisorption of foreign atoms. Not only functionalization but also radial deformation has been seen to modify the nanotube properties. A semiconducting nanotube can be metallic under a radial strain which changes the circular cross section into an elliptical one. Even more interesting is that these changes can be tuned reversibly.

For the accuracy, number of **k**-points and value of cutoff wavevector which are taken during calculations are important parameters for first-principles calculations. Cutoff energy necessary to determine number of plane waves which are used during self consistent calculations. Generally in our calculations we use the most appropriate value after we tested its suitably for convergence. In real crystal structure, it is necessary to use infinite number of **k**-points. But for these systems energy change with respect to **k**-points will high for small number of **k**-points. When we increase number of **k**-points we realized that energy change goes to saturate case. For this reason we use most probable number of **k**-points by looking change of energy with respect to **k**-points. For metals, for small number case smearing is important parameter for *ab-initio* calculations. By using smearing we determine how the partial occupancies are set for each wavefunctions. For magnetic systems spin-polarized case is more energetic than the spin-coupled case. For this reason, we also performed spin-polarized calculations for systems which include foreign atoms like O, H, transition metal atoms. We also consider exchange-correlations formalisms during our calculations. We both used LDA and GGA formalisms. However, LDA gives overbinding for binding energies in crystallic systems, GGA gives underbinding with respect to experimental results but electronic properties of systems which is found with GGA formalisms

9.1 Results

The important results that we have obtained from our calculations can be arranged as a conclusion;

1. Oxygenation of carbon nanotubes: atomic structure, energetics and electronic structure:

- The triplet state of the physisorbed oxygen molecule is energetically favorable, whereas the non-magnetic (spin paired) state yields relatively stronger binding energy.
- Results invalidate the hole doping of semiconducting carbon nanotube upon

the physisorption of oxygen. O_2 adsorbed SWNT show dramatic differences depending on the type of the tube. Upon O_2 physisorption, the zigzag SWNT remains semiconducting, while the metallicity of the armchair is lifted for the spin-down bands. The spin-up bands continue to cross at the Fermi level, and make the system metallic only for one type of spin.

2. Energetics and electronic structure of individual atoms adsorbed on carbon nanotubes:

- It is found that the character of the bonding and associated physical properties strongly depend on the type of adsorbed atoms.
- Our results indicate that the properties of SWNTs can be modified by the adsorbed foreign atoms. While the atoms of good conducting metals, such as Zn, Cu, Ag and Au, form very weak bonds, transition metal atoms such as Ti, Sc, Nb and Ta, and group IV elements C and Si are adsorbed with relatively high binding energy.
- Owing to the curvature effect, these binding energies are larger than the binding energies of the same atoms on the graphite surface. We have showed that the adatom carbon can form strong and directional bonds between two SWNTs.

3. High Conducting nanowires obtained from metal-atom coverage of carbon nanotubes:

- We have shown that a semiconducting single-wall carbon nanotubes, SWNT can be covered uniformly by titanium atoms and form a complex but regular atomic structure. However, the other transition-metal atoms can not uniformly covered on SWNT. The circular cross section changes to a square-like form, and the system becomes metallic with high state density at the Fermi level and with high quantum ballistic conductance.

- We also found that the net magnetic moment of Titanium covered SWNT can be dramatically altered by the stress applied along axial direction. *Ab-initio* spin-density-functional calculations show that titanium atoms can make a uniform coverage on SWNT with a net magnetization. Infinite Ti covered nanotube is found to be metallic and ferromagnetic. We also found that high Ti coverage decrease the net magnetic moment of system.

- We showed that Ga can form stable metallic linear and zigzag monatomic chain structures. The interaction between individual Ga atom and SWNT leads to a chemisorption bond involving charge transfer.

- Ga nanowires produced by the coating of carbon nanotube templates are found to be stable and high-conducting.

4. Nanotube Junctions and Nanotube Contacts:

- Under relatively weak contact forces the tubes are linked with intertube bonds which allow a significant conductance through the junction. These interlinking bonds survive even after the contact forces are released and whole structure is fully relaxed. Upon increasing contact force and radial deformation the tube surfaces are flattened but the interlinking bonds are broken to lead to a relatively wider intertube spacing. The intertube conductance through such a junction diminish because of finite potential barrier intervening between the tubes. The linkage of crossing tubes to form stable junctions is enhanced by a vacancy created at the contact.

- The contact between a s-SWNT and metal electrodes shows that the electronic structure and potential depend strongly on the type of metal. The s-SWNT is weakly side-bonded to the gold surface with minute charge rearrangement and remains semiconducting. A finite potential barrier forms at the contact region. In contrast, molybdenum surface forms strong bonds resulting significant charge transfer and metallicity at the contact. The radial deformation of the tube lowers the potential barrier at the contact and increases the state density at the Fermi level.

5. Hydrogen Storage of Carbon Nanotubes:

- Interaction between bare nanotube and hydrogen molecule is low. For this reason H_2 molecule can make weak physisorption bonds with bare SWNT.
- Even if Li atom adsorbed on SWNT surface, the nature of the bonding remained as physisorption.
- When single Pt atom adsorbed on the surface of bare SWNT, single H_2 molecule make chemisorbtion bond with Pt atom.
- Dissociation of H_2 molecule occurs only in case nanotube have large radius.
- Single Pt adsorbed on SWNT can bind up to two H_2 molecules with significant binding energy in the chemisorption range. When third and forth H_2 molecules exist around Pt atom after first and second H_2 molecule interact with Pt, they can stay in physisorption case.

9.2 Suggestion and Remarks

Half-Metallicity (HM) is a novel physical property for material systems. Because spin-dependent devices are of current interest. Nanotubes can be functionalized by using foreign atoms to obtain half-metallic properties. We created chain structures on (8,0) SWNT by using TM atoms. This work is in progress. Early electronic structures that we obtained for this work have showed that there are HM property for TM chain doped Nanotube structures. Actually there is no %100 percent polarization but there is high contribution to majority spin with respect to minority spin.

The other important and interesting subject that in progress is Hydrogen storage. In this case hydrogen adsorption is investigated for carbon nanotubes having TM atoms like Ti, Fe, Co, V *etc.* attached to the surface.

This Thesis based on the following articles:

- "Oxygenation of carbon nanotubes: Atomic structure, energetics, and electronic structure ", **S. Dag**, O. Glseren, T. Yildirim, and S. Ciraci, **Phys. Rev. B 67, 165424 (2003)**.

- "Systematic study of adsorption of single atoms on a carbon nanotube", E. Durgun, **S. Dag**, V. M. K. Bagci, O. Glseren, T. Yildirim, and S. Ciraci, **Phys. Rev. B 67, 201401 (R) (2003)**.

- "High-conducting magnetic nanowires obtained from uniform titanium-covered carbon nanotubes", **S. Dag**, E. Durgun, and S. Ciraci, **Phys. Rev. B 69, 121407 (2004)**.

- "A comparative study of O2 adsorbed carbon nanotubes", **S. Dag**, O. Glseren and S. Ciraci, **Chem. Phys. Lett. 380, Issues 1-2, 1-5 (2003)**.

- "Electronic structure of the contact between carbon nanotube and metal electrodes", **S. Dag**, O. Glseren, S. Ciraci, T. Yildirim , **Appl. Phys. Lett. 83, Issue 15, 3180-3182, (2003). (This study highlighted in Nano Today, December 2003.)**

- "Functionalized carbon nanotubes and device applications", S. Ciraci, **S Dag**, T Yildirim, O Glseren and R T Senger **J. Phys.: Condens. Matter 16, 29 R901-R960** (2004).

- "Energetics and Electronic Structures of Individual Atoms Adsorbed on Carbon Nanotubes", E. Durgun, **S. Dag**, S. Ciraci, O. Gulseren, **J. Phys. Chem. B 108(2); 575-582 (2004)**.

- "Theoretical study of Ga-based nanowires and the interaction of Ga with single-wall carbon nanotubes", E. Durgun, **S. Dag**, and S. Ciraci, **Phys. Rev. B 70, 155305 (2004)**.

- "Theoretical study of crossed and parallel carbon nanotube junctions and three-dimensional grid structures", **S. Dag**, R. T. Senger and S. Ciraci, **Phys. Rev. B 70, 205407, (2004)**.

- "Coverage and Strain Dependent Magnetization of titanium coated carbon nanotubes", **S. Dag** and S. Ciraci **Phys. Rev. B 71, 165414 (2005)**.
- "Adsorption and dissociation of hydrogen molecule on carbon nanotubes", **S. Dag**, Y. Ozturk, S. Ciraci, T. Yildirim, **Phys. Rev. B (in press)**.

Bibliography

[1] S. Iijima, Nature **354**, 56 (1991).

[2] S. Iijima, T. Ichihashi, Nature (London) **363**, 603 (1993).

[3] D. S. Bethune, C. H. Kiang, M. S. de Vries, G. Gorman, R. Savoy, J. Vazquez, R. Beyers, Nature (London) **363**, 605 (1993).

[4] M. S. Dresselhaus, G. Dresselhaus and P.C. Eklund, Science of Fullerenes and Carbon Nanotubes (Academic Press Inc., San Diego, 1996); T.W. Ebbesen, Physics Today **49**, nr. 6, 26-32 (June 1996), C. Dekker, Physics Today **52**, nr. 5, 22-28 (May 1999).

[5] R. Saito , G. Dresselhaus and M. S. Dresselhaus 1998 Physical Properties of Carbon Nanotubes (London: Imperial College)

[6] A. Thess, R. Lee, P. Nikolaev, H. Dai, P. Petit, J. Robert, C. Xu, Y. Hee Lee, S. Gon Kim, D. T. Colbert, G. Scuseria, D. Tomnek, J. E. Fischer, and R. E. Smalley, Science **273**, 483 (1996).

[7] S. J. Tans, A. R. M. Vershueren, C. Dekker, Phys. Rev. Lett. **84**, 2941 (2000).

[8] R. Martel, T. Schmidt, H. R. Shea, T. Hertel, Ph. Avouris, Appl. Phys. Lett. **73**, 2447 (1998).

[9] R. D. Antonov, A. T. Johnson, Phys. Rev. Lett. **83**, 3274 (1999).

[10] C. Zhou, J. Kong, H. Dai, Appl. Phys. Lett. **76**, 1597 (2000).

[11] J. W. G. Wildöer, L. C. Venema, A. G. Rinzler, R. E. Smalley, C. Dekker, Nature, **391**, 59 (1998).

[12] T. Ando, T. Nakanishi, R. Saito, J. Phys. Soc. Jpn. **67**, 1704 (1997).

[13] P. L. Mceuen, M. Bockrath, D. H. Cobden, Y. -G. Yoon, S. G. Louie, Phys. Rev. Lett. **83**, 5098 (1999).

[14] S. J. Tans, C. Dekker, Nature, **404**, 834 (2000)

[15] T. Odom, P. Kim, J.-L. Huang and Ch. Lieber, Nature **391**, 62 (1998).

[16] L. C. Venema, V. Meunier, Ph. Lambin, and C. Dekker, Phys. Rev. B **61**, 2991 (2000).

[17] Image gallery of the group of C. Dekker, http://www.mb.tn.tudelft.nl/.

[18] Ph. Lambin, A. Fonseca, J.P. Vigneron, J.B. Nagy and A.A. Lucas, Chem. Phys. Lett. **245**, 85 (1995).

[19] Z. Yao, H.W.Ch. Postma, L. Balents and C. Dekker, Nature **402**, 273 (1999).

[20] B.I. Yakobson and R.E. Smalley, American Scientist **85**, 324 (1997).

[21] S. J. Tans, M. H. Devoret, H. Dai, A. Thess, R. E. Smalley, L. J. Geerligs and C. Dekker, Nature, **386**, 474 (1997).

[22] A. C. Dillon, K. M. Jones, T. A. Bekkendahl, C. H. Kiang, D. S. Bethune and M. J. Heben, Nature, **386**, 377 (1997).

[23] Z. F. Ren et al., Science, **282**, 1105 (1998).

[24] B.W. Smith, M. Monthioux, and D.E. Luzzi, Nature **396**, 323 (1998).

[25] S. Berber, Y. -K. Kwon, and D. Tomnek, Phys. Rev. Lett. **84**, 4613 (2000).

[26] P.C. Collins, M.S. Arnold, and Ph. Avouris, Science **292**, 706 (2001).

[27] M. Kociak, A. Yu. Kasumov, S. Guron, B. Reulet, I. I. Khodos, Yu. B. Gorbatov, V. T. Volkov, L. Vaccarini, and H. Bouchiat , Phys. Rev. Lett. **86**, 2416 (2001).

[28] J. Kohanoff and N. Gidopoulos *Densit Functional Theory: basics, new trends and applications*

[29] M. Born and J. R. Oppenheimer, Ann. der Phys. **84**, 457 (1927).

[30] D. M. Ceperley, Phys. Rev. B **18**, 3126 (1978); D. M. Ceperley, B. J. Alder, Phys. Rev. Lett. **45**, 566 (1980).

[31] E. Zaremba and W. Kohn, Phys. Rev. B **13**, 2270 (1976).

[32] See, e.g., N. H. March in *Theory of the inhomogeneous electron gas*, eds. S. Lundqvist and N. H. March (Plenum, NY, 1983).

[33] C. F. von Weiszäcker, Z. Phys. **96**, 431 (1935).

[34] F. Perrot, J. Phys: Condens. Matter **6**, 431 (1994); L.-W. Wang and M. P. Teter, Phys. Rev. B **45**, 13397 (1992).

[35] E. Smargiassi and P. A. Madden, Phys. Rev. B **49**, 5220 (1994).

[36] M. Foley and P. A. Madden, Phys. Rev. B **53**, 10489 (1996).

[37] P. Hohenberg and w. Kohn, Phys. Rev. B **136**, B864 (1964).

[38] M. Levy, Phys. Rev. A **26**, 1200 (1982).

[39] A. Theophilou, J. Phys. C **12**, 5419 (1979); N. Hadjisavvas and A. Theophilou, Phys. Rev. A, **32**, 720 (1985); W. Kohn, Phys. Rev. A, **34**, 737 (1986); N. I. Gidopoulos, P. G. Papaconstantinou and E. K. U. Gross, Phys. Rev. Lett. **88**, 033003 (2002).

[40] E. K. U. Gross, J. F. Dobson, and M. Petersilka in *Density Functional Theory*, ed. R. F. Nalewajski, Springer Series "Topics in Current Chemistry" (Springer, Berlin, 1996); see also E. Runge and E. K. U. Gross, Phys. Rev. Lett. **52**, 997 (1984); M. Petersilka, U. J. Gossmann and E. K. U. Gross, Phys. Rev. Lett. **76**, 1212 (1996).

[41] A. Görling, Phys. Rev. A **54**, 3912 (1996); Phys. Rev. Lett. **85**, 4229 (2000).

[42] W. Kohn and L. J. Sham, Phys. Rev. **140**, A1133 (1965).

[43] D. C. Langreth and J. P. Perdew, Phys. Rev. B **15**, 2884 (1977).

[44] U. von Barth and L. Hedin, J. Phys. C **12**, 5419 (1979).

[45] S. H. Vosko, L. Wilk, and and M. Nussair, Can. J. Phys. **58**, 1200 (1980).

[46] R. O. Jones and O. Gunnarsson, Rev. Mod. Phys. **61**, 689 (1989).

[47] See, e.g., G. D. Mahan, *Many Particle Physics*(Plenum, NY, 1990).

[48] J. P. Perdew and A. Zunger, Phys. Rev. B **23**, 5048 (1981).

[49] M. Gell-mann and K. A. Brückner, Phys. Rev. **106**, 364 (1957).

[50] J. P. Perdew and Y. Wang, Phys. Rev. B **46**, 12947 (1992).

[51] J. A. Alonso and L. A. Girifalco, Solid State Commun. **24**, 135 (1977); Phys. Rev. B **17**, 3735 (1978).

[52] O. Gunnarsson and R. O. Jones, Phys. Rev. Scr. **21**, 394 (1980); J. Chem. Phys. **72**, 5357 (1980); O. Gunnarsson, M. Johnson, and B. I. Lundqvist, Phys. Rev. B **20**, 3136 (1979).

[53] A. R. Denton and N. W. Ashcroft, Phys. Rev. A **39**, 4701 (1989); A. R. Denton, P. Nieleba, K. J. Runge, and N. W. Ashcroft, Phys. Rev. Lett. **64**, 1529 (1990).

[54] J. F. Lutsko and M. Baus, Phys. Rev. Lett. **64**, 761 (1990).

[55] D. J. Singh, Phys. Rev. B **48**, 14099 (1993).

[56] L. Hedin, Phys. Rev. **139**, A796 (1965).

[57] V. I. Anisimov, J. Zaanen, and O. K. Andersen, Phys. Rev. B **44**, 943 (1991).

[58] S. -K. Ma and K. A. Bruekner, Phys. Rev. **165**, 18 (1968).

[59] D. C. Langreth and M. J. Mehl, Phys. Rev. Lett. **47**, 446 (1981); Phys. Rev. B **28**, 1809 (1983).

[60] E. K. U. Gross and R. M. Dreizler, Z. Phys. A **302**, 103 (1981).

[61] J. P. Perdew, Phys. Rev. Lett. **55**, 1665 (1985).

[62] S. K. Ghosh and R. G. Parr, Phys. Rev. A **34**, 785 (1986).

[63] C. Filippi, C. J. Umrigar, and M. Taut, J. Chem. Phys. **100**, 1295 (1994).

[64] J. P. Perdew and Y. Wang, Phys. Rev. B, **33**, 8800 (1986).

[65] J. P. Perdew, Phys. Rev. B, **33**, 8822 (1986).

[66] J. P. Perdew and Y. Wang, Phys. Rev. B, **45**, 13244 (1991).

[67] A. D. Becke, Phys. Rev. A, **38**, 3098 (1988).

[68] C. Lee, W. Yang, R. G. Parr, Phys. Rev. B **37**, 785 (1988).

[69] J. P. Perdew, K. Burke, and M. Ernzerhof, Phys. Rev. Lett. **77**, 3865 (1996); **78**, 1396 (1997)(E).

[70] E.H. Lieb, and S. Oxford, Int. J. Quan. Chem., **19**, 427 (1981).

[71] A. D. Becke, J. Chem. Phys. **84**, 4524 (1986).

[72] Y. Zhang and W. Yang, Phys. Rev. Lett. **80**, 890 (1998); J. P. Perdew, K. Burke, and M. Ernzerhof, *ibit* **80**, 891 (1998).

[73] M. Ernzerhof and G. E. Scuseria, J. Chem. Phys. **110**, 5029 (1999).

[74] M. Levy and J. P. Perdew, Int. Quantum Chem. **49**, 539 (1994).

[75] C. Kittel, Introduction to Solid State Physics. (John Wiley and Sons, New York, 1996).

[76] A. Baldereschi, Phys. Rev. B **7**, 5212 (1973); D. J. Chadi, M. L. Cohen, Phys. Rev. B **8**, 5747 (1973); H. J. Monkhorst, J. D. Pack, Phys. Rev. B **13**, 5188 (1976); **16**, 1748 (1977).

[77] Stefano de Gironcoli, Phys. Rev. B 51, 6773 (1995).

[78] C. L. Fu, k. M. Ho, Phys. Rev. B 28, 5480 (1983).

[79] N. Marzari, D. Vanderbilt, A. De Vita, M. C. Payne, Phys. Rev. Lett. 82, 3296 (1999).

[80] M. Methfessel and A. T. Paxton, Phys. Rev. B 40, 3616 (1989).

[81] Payne, M.C.; Teter, M. P.; Allan, D. C.; Arias, T. A. ; Joannopoulos, J. D. "Iterative Minimization Techniques for Ab-initio Total Energy Calculations: Molecular Dynamics and Conjugate Gradients", Rev. Mod. Phys., **64**, 1045 (1992).

[82] Srivastava, G. P.; Weaire, D. "The theory of the cohesive energies of solids", Advances in Physics, **26**, 463 (1987).

[83] Monkhorst, H. J.; Pack, J. D. "Special points for Brillouin-zone integrations", Phys. Rev., B13, 5188-5192 (1976). Monkhorst, H. J.; Pack, J. D. ""Special points for Brillouin-zone integrations"a reply", Phys. Rev., B16, 1748-1749 (1977).

[84] W. E. Pickett, Comput. Phys. Rep. **9**, 115 (1989)

[85] D. R. Hamann, M. Schlüter, C. Chiang, Phys. Rev. Lett. 43, 1494 (1979).

[86] G. Kerker, J. Phys. C 13, L189 (1980).

[87] A. Zunger, M. L. Cohen, Phys. Rev. B 18, 5449 (1978); 20, 4082 (1979).

[88] L. Kleinman, D. M. Bylander, Phys. Rev. Lett. 48, 1425 (1982).

[89] D. Vanderbilt, Phys. Rev. B 41, 7892 (1990).

[90] K. Laasonen, A. Pasquarello, R. Car, C. Lee and D. Vanderbilt, Phys. Rev. B 47, 10142 (1993).

[91] M. P. Teter, M. C. Payne, and D. C. Allan, Phys. Rev. B **40**, 12255 (1989).

[92] P. Pulay, Chem. Phys. Lett. **73**, 393 (1980).

[93] R.E. Smalley et al. "Growth mechanisms for single-wall carbon nanotubes in a laser-ablation process." Appl. Phys. A, **72**, 573 (2001).

[94] E. Joselevich, C.M. Lieber. "Vectorial Growth of Metallic and Semiconducting Single-Wall Carbon Nanotubes." Nano. Lett. **2**, 1137 (2002).

[95] K.H. Lee, J.M. Cho, W. Sigmund. "Control of growth orientation for carbon nanotubes." Appl. Phys. Lett. **82**, 448 (2003).

[96] M. S. Dresselhaus, G. Dresselhaus, Ph. Avouris, "Carbon Nanotubes: synthesis, structure, properties and applications" Springer-Verlag NewYork, c(2001).

[97] R. A. Jishi, M. S. Dressehaus, and G. Dresselhaus, Phys. Rev. B, **47**, 16671 (1995).

[98] P. C. Euklund, J. M. Holden, and R. A. Jishi, Carbon **33**, 959 (1995)

[99] R. A. Jishi, L. Venkataraman, M. S. Dresselhaus, and G. Dressehaus, Chem. Phys. Lett. **209**, 77 (1993)

[100] R. Saito, G. Dresselhaus, M.S. Dresselhaus. "Physical Properties of Carbon Nanotubes." Imperial College Press. page 27, (1999)

[101] J. R. Hauptmann, *Spin Transport in Carbon Nanotubes*, Ph.D Thesis, 2003.

[102] S. Ciraci, A. Buldum and I. Batra, J. Phys: Condens. Matter **13**, 537 (2001).

[103] S. Frank, P. Poncharal, Z. L. Wang and W. A. Heer, Science **280**, 1744 (1998).

[104] M. Ouyang, J. Huang, C.L. Cheung and C.M. Lieber, Science **292**, 702 (2001).

[105] O. Gülseren, T. Yildirim and S. Ciraci, Phys. Rev. **65**, 153405 (2002).

[106] J.C. Charlier, T.W. Ebbesen, Ph. Lambin, Phys. Rev. B**53**, 11108 (1996).

[107] L. Chico, M.P. Lopez Sancho and M.C. Munoz, Phys. Rev. Lett. **81**, 1278 (1998).

[108] P.G. Collins, A. Zettl, H. Bando, A. Thess and R.E. Smalley Science **278**, 100 (1997).

[109] M. Bockrath, D.H. Cobden, P.L. McEuen, N.G. Chopra, A. Zettl, A. Thess and R.E. Smalley, Science **275**, 1922 (1997).

[110] A. Bezryadin, A.R.M. Verschueren, S.J. Tans, and C. Dekker, Phys. Rev. Lett. **80**, 4036 (1998).

[111] Ç. Kılıç, S. Ciraci, O. Gülseren and T. Yildirim, Phys. Rev. B **62**, 16345 (2000).

[112] H.S. Sim, C.J.Park and K.J. Chang, Phys. Rev. B **63**, 073402 (2001).

[113] O. Gülseren, T. Yildirim and S. Ciraci, Phys. Rev. Lett. **87**, 116802 (2001).

[114] N. Hamada, S. Sawada and A. Oshiyama, Phys. Rev. Lett. **68**, 1579 (1992).

[115] L.C. Venema, J.W. Janssen, M.R. Buitelaar, J.W.G. Wildöer, S.G. Lemay, L.P. Kouwenhoven and C. Dekker, Phys. Rev. B **62**, 5238 (2000).

[116] T.W. Odom, J. Huang, P. Kim and C.M. Lieber, J. Phys. Chem. B **104**, 2794 (2000).

[117] C.T. White, D.H. Robertson and J.W. Mintmire, Phys. Rev. B **47**, 5485 (1993).

[118] X. Blase, L.X. Benedict, E.L. Shirley and S.G. Louie, Phys. Rev. Lett. **72**, 1878 (1994).

[119] C.L. Kane and E.J. Mele, Phys. Rev. Lett. **78**, 1932 (1997).

[120] A. Kleiner and S. Eggert, Phys. Rev. B **63**, 073408 (2001).

[121] A. Kleiner and S. Eggert, Phys. Rev. B **64**, 113402 (2001).

[122] J. P. Perdew and Y. Wang, Phys. Rev. B **46**, 6671 (1992); J.P. Perdew, J.A. Chevary, S.H. Vosko, K.A. Jackson, M.R. Pederson, D.J. Singh, and C. Fiolhais, Phys. Rev. B **46**, 6671 (1992).

[123] D. Sanchez-Portal, E. Artacho, J.M. Soler, A. Rubio, and P. Ordejon, Phys. Rev. B **59**, 12678 (1999).

[124] D.H. Robertson, D.W. Brenner and J.W. Mintmire, Phys. Rev. B **45**, 12592 (1992).

[125] G. G. Tibbets, J. Cryst. Growth **66**, 632 (1984).

[126] K.N. Kudin, G.E. Scuseria and B.I. Yakobson, Phys. Rev. B **64**, 235406 (2001).

[127] W. Kim, H. C. Choi, M. Shim, Y. Li, D. Wang, and H. Dai, Nano Lett. **2**, 703 (2002).

[128] H. Yorikawa and S. Muramatsu, Phys. Rev. B **52**, 2723 (1995).

[129] J.W. Mintmire, B.I. Dunlap and C.T. White, Phys. Rev. Lett. **68**, 631 (1992).

[130] H. Yorikawa and S. Muramatsu, Solid State Comm. **94**, 435 (1995).

[131] O. Gülseren, T. Yildirim, S. Ciraci, C. Kilic, Phys. Rev. B **65**, 155410 (2002).

[132] C. J. Park, Y. H. Kim, K. J. Chang, Phys. Rev. B **60**, 10656 (1999).

[133] M.S. Dresselhaus, Nature, **391**,19 (1998).

[134] C. T. White and J.W. Mintmire, Nature **394**, 29 (1998).

[135] J.-C. Charlier and Ph. Lambin, Phys. Rev. B **57**, R15037 (1998).

[136] J.W. Mintmire and C.T. White, Phys. Rev. Lett. **81**, 2506 (1998).

[137] S. Datta. *Electronic Transport in Mesoscopic Systems*, Cambridge University Press (1995).

[138] W. Liang, M. Bockrath, D. Bozovic, J.H. Hafner, M. Tinkham, H. Park, *Fabry-Perot interference in a nanotube electron waveguide*, Nature **411**, 665 (2001).

[139] J. Appenzeller, R. Martel, P. Avouris, H. Stahl, U.T. Hunger, B. Lengeler. "Phase-coherent transport in ropes of single-wall carbon nanotubes." Phys. Rev. B, **64**, 121404 (2001).

[140] A. Bachtold, M.S. Fuhrer, S. Plyasunov, M. Forero, E.H. Anderson, A. Zettl, P.L. McEuen. "Scanned Probe Microscopy of Electronic Transport in Carbon Nanotubes." Phys. Rev. Lett, **84**, 6082 (2000).

[141] P.J. de Pablo, C. Gomez-Navarro, M.T. Martinez, A.M. Benito, W.K. Maser, J. Colchero, J. Gomez-Herrero, A.M. Baro. "Performing current versus voltage measurements of single-walled carbon nanotubes using scanning force microscopy." Appl. Phys. Lett. **80**, 1462 (2002).

[142] R. Landauer, Z. Phys. B **68**, 217 (1987).

[143] M.M.J. Treacy, T.W. Ebbesen, and J.M. Gibson, Nature (London), **381**, 678 (1996).

[144] R.S. Ruoff, J. Tersoff, D.C. Lorents, S. Subramoney, and B. Chan, Nature (London) **364**, 514 (1993).

[145] N.G. Chopra, L.X. Benedict, V.H. Crespi, M.L. Cohen, S.G. Louie, and A. Zettl, Nature (London), **377**, 135 (1995).

[146] A. Rochefort, P. Avouris, F. Lesage, D. R. Salahub, Chem. Phys. Lett. **297**, 45 (1998).

[147] A. Rochefort, P. Avouris, F. Lesage, and D.R. Salahub , Phys. Rev. B **60**, 13824 (1999).

[148] L. Liu, C.S.Jayanthi, M. Tang, S.Y. Wu, T.W. Tombler, C. Zhou, L. Alexseyev, J. Kong and H.Dai, Phys. Rev. Lett. **84**, 4950 (2000).

[149] T.W. Tombler, C. Zhou, L. Alexseyev, J. Kong, H. Dai, L. Liu, C.S. Jayanthi, M. Tang, and S. Wu, Nature **405**, 769 (2000).

[150] S.A. Chesnokov, V.A. Nalimova, A.G. Rinzler, R.E. Smalley and J.E. Fischer, Phys. Rev. Lett. **82**, 343 (1999).

[151] P.E. Lambert, P. Zhang and V. Crespi, Phys. Rev. Lett. **84**, 2453 (2000).

[152] E.D. Minot, Y. Yaish, V. Sazonova, J-Y. Park, M. Brink, P.L. McEuen, Phys. Rev. Lett. **90**, 156401 (2003).

[153] J.P. Salvetat, G.A.D. Briggs, J. Bonard, R.R. Bacsa, A.J. Kulik, T. Stöckli, N.A. Burnham and L. Forró, Phys. Rev. Lett. **82**, 944 (1999).

[154] T. Yildirim, O. Gülseren, Ç. Kılıç and S. Ciraci, Phys. Rev. B **62**, 12648 (2000).

[155] L. Yang, M.P. Anantram, J. Han and J.P. Lu, Phys. Rev. B **60**, 13874 (1999).

[156] L. Yang and J. Han, Phys. Rev. Lett. **85**, 154 (2000).

[157] W. Shen, B. Jiang, B.S. Han and S. Xie, Phys. Rev. Lett. **84**, 3634 (2000).

[158] V. Lordi and N. Yao, J. Chem Phys. **109**, 2509 (1998).

[159] M.F. Yu, T. Kowalewski and R.S. Ruoff, Phys. Rev. Lett. **85**, 1456 (2000).

[160] M.S.C. Mazzoni and H. Chacham, Appl. Phys. Lett. **76**, 1561 (2000).

[161] P. Delaney, H.J. Choi, J. Ihm, S.G. Louie and M.L. Cohen, Nature **391**, 466 (1998); P. Delaney, H.J. Choi, J. Ihm, S.G. Louie and M.L. Cohen, Phys. Rev. B **60**, 7899 (1999).

[162] A. N. Andriotis, M. Menon, D. Srivastava, and G. Froudakis, Phys. Rev. B **64**, 193401 (2001).

[163] S. Dag, Y. Öztürk and S. Ciraci (to be published).

[164] A.M. Rao, *et. al.* Appl. Phys. A: Mater. Sci. Process. **64**, 231 (1997).

[165] U.D. Venkateswaren, A.M. Rao, E. Richter, M. Menon, A. Rinzler, R.E. Smalley, and P.C. Eklund, Phys. Rev. B **59**, 10928 (1999); A.K. Sood, P.V. Teredesai, D.V.S. Muthu, R. Sen, A. Gavindaraj, and C.N. Rao, Chem. Phys. Lett. **319**, 296 (2000); P.V. Teredesai, A.K. Sood, D.V.S. Muthu, R. Sen, A. Govindaraj, and C.N.R. Rao, Chem. Phys. Lett. **310**, 296 (2000).

[166] M.J. Peters, L.E. McNeil, J.P. Lu, and D. Kuhn, Phys. Rev. B **61**, 5939 (2000).

[167] J. Tang, L.C. Qin, T. Sasaki, M. Yudasaka, A. Matsushita, and S. Iijima, Phys. Rev. Lett. **85**, 1887 (2000).

[168] T. Yildirim, O. Gülseren, and S. Ciraci, Phys. Rev. B. **64**, 075404 (2001).

[169] J. Kong, N. R. Franklin, C. Zhou, M. G. Chapline, S. Peng. K. Cho, and H. Dai, Science **287**, 622 (2000).

[170] P. G. Collins, K. Bradley, M. Ishigami, and A. Zettl, Science, **287**, 1802 (2000).

[171] O. Gülseren, T. Yildirim, and S. Ciraci, Phys. Rev. B **66**, 121401 (2002).

[172] K. A. Dean, and B. R. Chalamala, J. Appl. Phys. **85**, 3832 (1999); *ibid*, Appl. Phys. Lett. **76**, 375 (2000).

[173] P. M. Ajayan, T. W. Ebbesen, T. Ichihashi, S. IIjima, K. Tanigaki, and H. Hiura, Nature **362**, 522 (1993).

[174] T. W. Ebbesen, P. M. Ajayan, H. Hiura, and K. Tanigaki, Nature **367**, 519 (1994).

[175] K. Morishita, and T. Takarada, Carbon **35**, 977 (1997).

[176] S. H. Jhi, S. G. Louie, and M. L. Cohen, Phys. Rev. Lett. **85**, 1710 (2000).

[177] S. M. Lee, Y. H. Lee, Y. G. Hwang, J. R. Hahn, and H. Kang, Phys. Rev. Lett. **82**, 217 (1999).

[178] D. C. Sorescu, K. D. Jordan, and P. Avouris, J. Phys. Chem. B **105**, 11227 (2001).

[179] X.Y. Zhu, S.M. Lee, Y.H. Lee, and T. Frauenheim, Phys. Rev. Lett. **85**, 2757 (2000).

[180] C-Y, Moon, Y-S, Kim, E-C, Lee, Y-G, Jin, and K. J. Chang, Phys. Rev. B **65**, 155401 (2002).

[181] N. Park, S. Han, and J. Ihm, Phys. Rev. B **64**, 125401 (1999).

[182] D. J. Mann and M. D. Halls, J. Chem. Phys. **116**, 9014 (2002).

[183] A. Ricca and J. A. Drosco, Chem. Phys. Lett. **362**, 217 (2002).

[184] P. Hohenberg and W. Kohn, Phys. Rev. **136**, B864 (1964); W. Kohn and L. J. Sham, Phys. Rev. **140**, A1133 (1965).

[185] G. Kern, G. Kresse, and J. Hafner, Phys. Rev. B **59**, 8551 (1999).

[186] Y. Baskin and L. Meyer, Phys. Rev. **100**, 544 (1955).

[187] A. Janotti, S.H. Wei, and D.J. Singh, Phys. Rev. B **64**, 174107 (2001).

[188] J. Furthmüller, J. Hafner, and G. Kresse, Phys. Rev. B **50**, 15606 (1994).

[189] E. M. Lifshitz, Zh. Eksp. Teor. Fiz. **29**, 94 (1956) (Sov. Phys. JETP **2**, 73 (1956)).

[190] J. N. Israelachvili, *Intermolecular and Surface Forces* (Academic, London 1985).

[191] S. Ciraci, E. Tekman, A. Baratoff, and I. P. Batra, Phys. Rev. B **46**, 10411 (1992).

[192] T. A. Halgren, J. Am. Chem. Soc. **114**, 7827 (1992).

[193] K.P. Huber and G. Herzberg, *Molecular Spectra and Molecular Structure. IV. Constants of Diatomic Molecules* (Van Nostrand Reinhold, New York, 1979).

[194] H. Ulbricht, G. Moos, and T. Hertel, Phys. Rev. B **66**, 075404 (2002).

[195] Y. Wu, N. Marzari, and R. Car (unpublished).

[196] I.W. Chiang, B.E. Brinson, R.E. Smalley, J.L. Margrave, and R. H. Hauge, J. Phys. Chem. B **105**, 1157 (2001).

[197] S. Dag, O. Gülseren, T. Yildirim and S. Ciraci, Phys. Rev. B **67** (2003) 165424.

[198] S. P. Chan, G. Chen, X. G. Gong, and Z. F. Liu, Phys. Rev. Lett. **90** (2003) 086403.

[199] V. Derycke, R. Martel, J. Appenzeller, and Ph. Avouris, Appl. Phys. Lett. **80** (2002) 2773.

[200] V.M.K. Bagci, O. Gülseren, T. Yildirim, Z. Gedik, and S. Ciraci, Phys. Rev. B**66**, 045409 (2002).

[201] S. Iijima, T. Ichihashi, and Y Ando, *ibid* **356**, 776 (1992).

[202] M. S. Dresselhaus, G. Dresselhaus, and P. C. Eklund, *Science of Fullerenes and Carbon Nanotubes* (Academic Press, San Diego, 1966).

[203] N. Agräait, J.G. Rodrigo, and S. Vieira, Phys. Rev. B**47**, 12345 (1993).

[204] H. Ohnishi, Y. Kondo, and K. Takayanagi, Nature (London) **395**, 783 (1998).

[205] A.I. Yanson, G.R. Bollinger, H.E. Brom, N. Agräit, and J. M. Ruitenbeek, Nature (London) **395**, 783 (1998).

[206] S. Ciraci and E. Tekman, Phys. Rev B**40**, R11969 (1989);E. Tekman, S. Ciraci, Phys. Rev B**43**, 7145 (1991); H. Mehrez, S. Ciraci, A. Buldum and I.P. Batra, Phys. Rev. B**55**, R1981 (1997).

[207] A. Buldum, S. Ciraci, C.Y. Fong, J. Phys.: Condens. Matter **12**, 3349 (2000); A. Buldum, D.M. Leitner, and S. Ciraci, Europhys. Lett. **47**, 208 (1999).

[208] A. Ozpineci and S. Ciraci, Phys. Rev. B**63**, 125415 (2001).

[209] O. Gulseren, F. Ercolesi and E. Tosatti, Phys. Rev. Lett. **80** 3775 (1998); E. Tosatti and S. Prestipino, Science **289**, 561 (2000).

[210] H. Dai, E.W. Wong, Y.Z. Lu, S. Fan, C.M. Lieber, Nature(London) **375**, 769 (1995); W.Q. Han, S.S. Fan, Q.Q. Li, Y.D. Hu, Science **277**, 1287 (1997).

[211] Y. Zhang and H. Dai, Appl. Phys. Lett. **77**, 3015 (2000); Y. Zhang, N.W. Franklin, R.J. Chen, and H. Dai, Chem. Phys. Lett. **331**, 35 (2000).

[212] C. Zhou, J. Kong, and H. Dai, Phys. Rev. Lett. **84**, 5604 (2000).

[213] S.J. Tans, A.R.M. Verscheuren and C. Dekker, Nature (London), **393**, 49 (1998); A. Bachtold, P. Hadley, T. Nakanishi, and C. Dekker, Science **294**, 1317 (2001); T. Nakanishi, A. Bachtold and C. Dekker, Phys. Rev B **66**, 073307 (2002).

[214] H.T. Soh, C. Quate, A.F. Morpurgo, C.M. Marcus, J. Kong and H. Dai, Appl. Phys. Lett. **75**, 627 (1999); C. Zhou, J. Kong, and H. Dai, Appl. Phys. Lett. **76**, 1597 (2000).

[215] R. Martel, V. Derycke, C. Lavoie, J. Appenzeller, K.K. Chan, J. Tersoff, and Ph. Avouris, Phys. Rev. Lett. **87** 256805 (2001); Ph. Avouris, R. Martel, V. Derycke and J. Appenzeller, Physica, B **323**, 6 (2002).

[216] I.O. Kulik, T. Hakioglu, and A. Barone, Europ. Phys. Journal, B**30**, 219 (2002).

[217] X.X. Zhang, G.H. Wen, S. Huang, L. Dai, R. Gao, and Z.L. Wang, Journal of Magnetism and Magnetic Materials, **231**, L9 (2001); B.C. Satishkumar, A. Govindaraj, P.V. Vanitha, A.K. Raychaudhuri, and C.N.R. Rao, Chem. Phys. Lett. **362**, 301 (2002).

[218] T. Yildirim, O. Gülseren, and S. Ciraci, Phys. Rev. B**64**, 075404 (2001); O. Gülseren, T. Yildirim, and S. Ciraci, Phys. Rev. B**66**, 121401 (2002).

[219] S. Dag, O. Gülseren, T. Yildirim, and S. Ciraci, Phys. Rev. B**67**, 165424 (2003)

[220] E. Durgun, S. Dag, V.M.K. Bagci, O. Gülseren, T. Yildirim, S. Ciraci, Phys. Rev. B**67**, R201401 (2003); E. Durgun, S. Dag, S. Ciraci, O. Gülseren, J. Phys. Chem. B **108(2)**, 575 (2004).

[221] T. A. Halgren, J. Am. Chem. Soc. **114**. 7827 (1992).

[222] C. E. Moore, *Atomic Energy Levels* U.S. National Bureau of Standards, Washington D.C. 1971.

[223] P. Soderlind, O. Eriksson, J.M. Wills, and A.M. Boring, Phys. Rev. B **48**, 5844 (1993).

[224] J. Friedel, The Physics of Metals, edited by J. M. Ziman (Cambridge University Press, New York, 1969); D.G. Pettifor, in Solid State Physics, edited by H. Ehrenreich and D. Turnbull (Academic, New York, 1987). Vol. **40**, p43.

[225] R. J. Baierle, S. B. Fagan, R. Mota, A.J.R. Silva, and A. Fazzio, Phys. Rev. B **64**, 085413 (2001).

[226] N. Agraït, G. Rubio, and S. Vieira, Phys. Rev. Lett. **74**, 3995 (1995).

[227] C-K. Yang, J. Zhao, and J. P. Lu, Phys. Rev. B(R) **66**, 041403 (2002).

[228] C.C. Kaun, B. Larade, H. Mehrez, J. Taylor, H. Guo, Phys. Rev. B **65**, 205416 (2002).

[229] B. L. Altshuler and A. G. Aronov in *Electron-electron interaction in disordered systems*, Eds: A. L. Efros and M. Pollak, Elsevier Amsterdam (1985).

[230] C. Kilic, S. Ciraci, O. Gülseren, and T. Yildirim, Phys. Rev. B **62**, 16345 (2000).

[231] O. Gülseren, T. Yildirim, and S. Ciraci, Phys. Rev. B **68**, 115419 (2003).

[232] C-K. Yang, J. Zhao and J. P. Lu, Phys. Rev. Lett. **90**, 257203 (2003).

[233] G. A. Prinz, Science, **282**, 1660 (1998).

[234] P. Ball, Nature (London) **404**, 918 (2000).

[235] S. A. Wolf, *et al.*, Science, **294**, 1488 (2001).

[236] R. A. de Groot, *et al.*, Phys. Rev. Lett. **50**, 2024 (1983).

[237] W.E. Pickett and J.S. Moodera, Phys. Today **54**, 39 (2001).

[238] S. Dag, E. Durgun and S. Ciraci, Phys. Rev. B **69**, 121407(R) (2004).

[239] R. Landauer, Z. Phys. B, **68**, 217 (1987); R. Landauer, Phys. Lett. **85A**, 91 (1981); C. C. Kaun, B. Larade, H. Mehrez, J. Taylor and H. Guo, Phys. Rev. B **65**, 205416 (2002).

[240] For a comprehensive review on the electronic and transport properties of SWNTs see: S. Ciraci, A. Buldum and I. P. Batra, J. Phys. Condens. Matter **13**, 537 (2001); S. Ciraci, S. Dag, T. Yildirim, O. Gülseren and R. T. Senger, J. Phys. Condens. Matter **16**, R901 (2004).

[241] Numerical computations have been carried out by using VASP software: G. Kresse and J. Hafner, Phys. Rev. B **47**, 558 (1993); G. Kresse and J. Furthmuller, *ibid* B **54**, 11169 (1996).

[242] H. Mehrez and S. Ciraci, Phys. Rev. B **56**, 12632 (1997).

[243] M. R. Sørensen, M. Brandbyge and K. W. Jacobsen, Phys. Rev. B **57**, 3283 (1998).

[244] D. Sanchéz-Portal, E. Artacho, J. Junquera, P. Ordejón, A. Garcia, J. M. Soler, Phys. Rev. Lett. **83**, 3884 (1999).

[245] H. Hakkinen, R. N. Barnett, U. Landman, J. Phys. Chem. B **103**, 8814 (1999).

[246] F. D. Tolla, A. D. Corsa, J. A. Torres, and E. Tosatti, Surf. Sci. **947**, 454 (2000).

[247] P. Sen, S. Ciraci, A. Buldum and I. P. Batra, Phys. Rev. B **64**, 195420 (2001).

[248] S. Tongay, E. Durgun and S. Ciraci (App. Phys. Lett.)

[249] W. T. Geng and K. S. Kim, Phys. Rev. B **67**, 233403 (2003).

[250] B. L. Altshuler and A. G. Aronov, Electron-Electron Interaction in Disorded Systems, edited by A. L. Efros and M. Polale (Elsevier, Amsterdam 1985).

[251] S.W. Ip, R. Sridhar, J.M. Toguri, T.F. Stephenson, A.E.M. Warner, Materials Science and Engineering,**A224**, 31 (1998).

[252] C. Dekker, Phys. Today, **52**, No 5, 22 (1999).

[253] M. Menon, D. Srivastava, Phys. Rev. Lett. **79**, 4453 (1997).

[254] G. Treboux, P. Lapstun, and K. Silverbrook, Chem. Rev. Lett. **306**, 402 (1999).

[255] M. S. Fuhrer, J. Nygård, L. Shih, M. Forero, Y-G. Yoon, M. S. C. Mazzoni, H. J. Choi, J. Ihm, S. G. Louie, A. Zettl, P. L. Mceuen, Science **288**, 494 (2000).

[256] S. Paulson, A. Helser, M. B. Nardelli, R. M. Taylor II, M. Falvo, R. Superfine, and S. Washburn, Science **288**, 494 (2000).

[257] H. W. Ch. Postma, M. deJonge, Z. Yao, and C. Dekker, Phys. Rev. B **62**, R10653 (2000).

[258] Young-Gui Yoon, Mario S. C. Mazzoni, H. J. Choi, J. Ihm, S. G. Louie, Phys. Rev. Lett. **86**, 688 (2001).

[259] M. Ouyang, J. -L. Huang, C. L. Cheung, and C. M. Lieber, Science **291**, 97 (2001).

[260] A. Buldum, J. P. Lu, Appl. Surf. Sci. **219**, 123 (2003).

[261] A. Pérez-Garrido, A. Urbina, Carbon **40**, 1227 (2002).

[262] M. Terrones, F. Banhart, N. Grobert, J. -C. Charlier, H. Terrones, P. M. Ajayan, Phys. Rev. Lett., **89**, 075505 (2002).

[263] A. V. Krasheninnikov, K. Nordlund, J. Keinonen, F. Banhart, Phys. Rev. B **66**, 245403 (2002).

[264] J. W. Janssen, S. G. Lemay, L. P. Kouwenhoven, C. Dekker, Phys. Rev. B, **65**, 115423 (2002).

[265] A. Nojeh, G. W. Lakatos, S. Peng, K. Cho, R. F. W. Pease, Nanolett. **3**, 1187 (2003).

[266] A. Buldum and J. P. Lu, Appl. Surf. Science, **215**, 123 (2003).

[267] F. Cleri, P. Keblinski, I. Jang, S. B. Sinnott, Phys. Rev. B, **69**, 121412(R) (2004).

[268] A. Hansson and S. Stafström, Phys. Rev. B **67**, 075406 (2003).

[269] J. -C. Charlier, Ph. Lambin, and T. W. Ebbesen, Phys. Rev. B **54**, 8377 (1996).

[270] R. Landauer, Philos. Mag. **21**, 863 (1970).

[271] M. Buttiker, Phys. Rev. Lett., **57**, 1761 (1986).

[272] A. P. Jauho, N. S. Wingreen, and Y. Meir, Phys. Rev. B **50**, 5528 (1994).

[273] M. B. Nardelli and J. Bernholc, Phys. Rev. B **60**, R16338 (1999).

[274] D. Tomanek and S. G. Louie, Phys. Rev. B **37**, 8327 (1988).

[275] A. Rochefort, M. Di Vientra, P. Avouris, Appl. Phys. Lett. **78**, 2521 (2001).

[276] S. Heinze, J. Tersoff, R. Martel, V. Derycke, J. Appenzeller and Ph. Avouris, Phys. Rev. Lett **89**, 106801 (2002).

[277] M. Luna, P. J. de Pablo, J. Colchero, J. Gomez-Herrero, A. M. Baro, H. Tokumoto, S. P. Jarvis, Ultramicroscopy **96**, 83 (2003).

[278] E. Tekman and S. Ciraci, Phys. Rev. B**43**, 7145 (1991); S. Ciraci, Theory of tip-sample interactions, in *Scanning Tunneling Microscopy III* edited by R. Wiesendanger and H.-J. Güntherodt (Springer-Verlag 1993).

[279] Y. Ye, C.C. Ahn, C. Witham, B. Fultz, J. Liu, A.G. Rinzler, D. Colbert, K.A. Simith, R.E. Smalley, Appl. Phys. Lett. **74**, 16 (1999).

[280] C. Liu, Y.Y. Fan, M. Liu, H.T. Cong,H.M. Cheng, M.S. Dresselhaus, Science **286**, 1127 (1999).

[281] S.M. Lee, Y.H. Lee, Appl. Phys. Lett. **76**, 20 (2000).

[282] Y. Ma, Y. Xia, M. Zhao, and M. Ying, Phys. Rev. B **65**,155430 (2002).

[283] F. Darkrim, D. Levesque, J. Chem. Phys. **109**, 12 (1998)

[284] K.A. Eklund, P.C. Williams, Chem. Phys. Lett. **320**,352 (2000).

[285] M. Siraishi, T. Takenobu, A Yamada, M. Ata, H. Kataura, Chem. Phys. Lett. **358**, 213 (2002).

[286] P. Chen, X. Wu, J. Lin, K.L. Tan, **285**, 91 (1999).

[287] P. Dubot and P. Cenedese, Phys. Rev. B **47**, 208 (1999).

[288] T. Yildirim and S. Ciraci Phys. Rev. Lett. **94**, 175501 (2005).

[289] This work is based on Y. Öztürk's M.S. Thesis, Bilkent University 2003 (Unpublished)

[290] W. Kohn and L.J. Sham, Phys. Rev. **140**, A1133 (1965).

[291] W. Kohn, Y. Meir, and D.E. Makarov, Phys. Rev. Lett. **80**, 4153 (1998).

[292] S. S. Han and H. M. Lee, Carbon **42**, 2169 (2004).

[293] As pointed out in Ref.[291], VdW interaction is poorly represented by LDA, and even worst by GGA. In the calculation of E_b=E_C+E_{VdW}, E_C may include a small portion of E_{VdW}. Nevertheless, since E_b is already small the amount related with double counting is expected to be in the range of accuracy achieved by present DFT calculations.

[294] K. Tada, S. Furuya and K. Watanabe, Phys. Rev. B **63**, 155405 (2001).

[295] S.-P. Chan, G. Chen, X.G. Gong, and Z.-F. Liu, Phys. Rev. Lett. **87**, 205502 (2001).

[296] M. K. Kostov, M. W. Cole, and J. C. Lewis, arxiv.cond-mat 0007034v1. For this paper, the interaction between H_2 and a SWNT surface has been calculated by using 2- and 3- body particles. The range of calculated energy is in agreement with the present results.

[297] S. Dag and S. Ciraci, Phys. Rev. B **71**, 165414 (2005).

[298] E.-C. Lee, Y.-S. Kim, Y.-G. Jim and K.J. Chang, Phys. Rev. B **66**, 073415 (2002).

[299] Since, the bond distance of H_2 is extended by 20%, the H-H interaction is weaker than that in free H_2. For d_{H-H} $\sim$1Å the adsorption may be considered as an intermediate stage between molecular and atomic adsorption.

Chapter 10

Vitae

Sefa Dag was born on February 17, 1977 in Mersin Turkey. He finished Gazipaşa primary school in 1987. After that He attended Salim Yılmaz secondary school and subsequently Salim Yılmaz high school between 1987 and 1992. Sefa Dag began his undergraduate studies in the Physics Engineering Department of Hacettepe University in 1993 and received his B.S. degree in 1998 with first-class honors degree. For his graduate studies he has preferred the Physics department of Bilkent University receiving his M.Sc. degree in 2000. He pursued his Ph.D. degree at the same department. He received his Ph.D. from Bilkent University Physics Department in 2005. Both his M.Sc. and Ph.D. theses work are carried out under the supervision of Professor Salim Ciraci in the area of theoretical Condensed Matter Physics and Nanoscience. His intensive research efforts on nanotubes and nanowires has revealed a variety of properties which make important contributions to the fields of nanoscience and nanotechnology. The main objective of his research in these fields is to find new modifications to the pristine nanotube and nanowires to render them functionally active for the various applications. Currently, Sefa Dag will work as a postdoctoral research fellow at the Center of Nanophase Materials Department of Oak Ridge National Laboratory in Tennessee, United States of America.

He has more than 23 published papers in internationally recognized journals. He is also invited to give talks at the international conferences. Besides, he also

worked with the computational groups in the Physics Department of UC-DAVIS and NIST in the USA.

" *It is a pleasure to get my Ph.D. from the Bilkent University. The research opportunities offered to me here were of the same caliber of those available in the USA. I know that I used this chance in a good way.*"